Astrophysical and cosmological background signals from the radio to the microwaves

Tiziana Trombetti

Department of Physics and Earth Science

University of Ferrara

A thesis submitted for the degree of

Ph.D. in Physics

A.Y. 2014/15 - 2016/17

PhD student: Dr.ssa Tiziana Trombetti

Supervisor: Dr. Carlo Burigana

PhD Coordinator: Prof. Vincenzo Guidi

PhD Committee: Prof. Alessandro Cardini
Prof. Angelo Di Canto
Prof. Nicola Vittorio

Defense: 28/02/2018

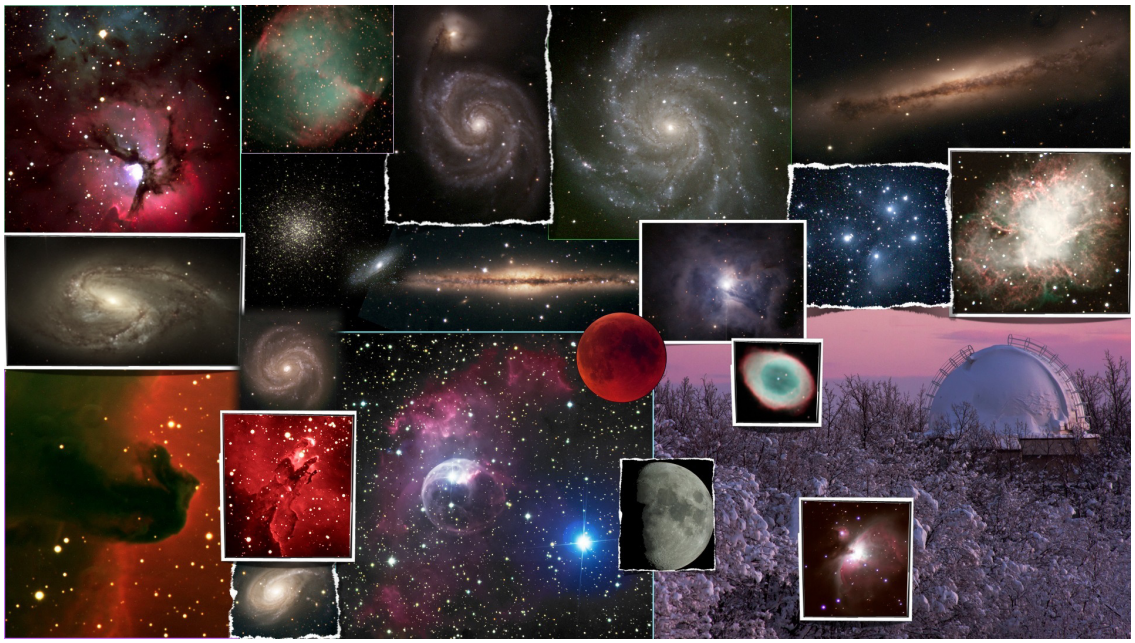

Sometimes one Universe is too big to be explored ...
Sometimes hundreds of universes are too rare to live in ...
Time travel is the key ... now we need to find where the lock is ...

Tzj =]!

To ...

... the most extraordinary person in my life, *Ivan Bruni*, who was on my side every single moment throughout these years, independently on my mood. In this work permeates also his delicate essence and soul. To *Balú*, my hairy pallet, rained from the sky for my delight, to *Midori*, my small black bumbler kitty, appeared from the forest as an elf to enliven my days, to *Ponzio*, the soft kitty ball with the strength of a lion, to *Loiano* mountains, whose landscapes gave me seasonal breathtaking emotions, to the *60cm* and the *152cm* reflector telescopes, who let me travel in time and space all over the Universe, to *Chukino*, my sweet small donkey, to *Davide*, my precious and wise friend, to *Loriana* and *Paolo*, my extraordinary neighbours, to *Mervi*, my amazing Finnish flatmate in Oslo, to the *snow*, a company increasingly common in recent times. I turn my thoughts also to all my petite neighborhood who believe in me.

To ...

... my family, above all to *Patrizia*, my mother, to *brj*, my near and far twin, to *Letizia* and *Maria*, my ghost-mothers, each of them for having supported me in different ways, being always present.

To ...

... my friends, and remarkably to *Theo*, to *Tina*, to *Giada* and *Claudio*, to *Enzo*, to *Peppe*, to *Simone*, to *Roberto*.

To ...

... my fantastic supervisor *Carlo Burigana* and to all the unique people met during this inspiring and never-ending adventure.

Finally ...

... to all those who know me, colour and enjoy my days but whose names are not explicitly revealed here.

Acknowledgements

This thesis work has been performed at INAF, Istituto di Astrofisica Spaziale e Fisica Cosmica di Bologna and Istituto di Radioastronomia sede di Bologna. Partial supports by ASI through the ASI/INAF agreement n. I/072/09/0 and n. 2014-024-R.0/R.1 for the *Planck* LFI Activity of Phase E2, through the contract I-022-11-0 LSPE, through the contract I/016/07/0 COFIS and by MIUR through PRIN 2009 grant no. 2009XZ54H2 are acknowledged.

I acknowledge the use of the ESA *Planck* Legacy Archive (PLA) and of the Legacy Archive for Microwave Background Data Analysis (LAMBDA, supported by the NASA Office of Space Science). Some of the results in this work have been derived using the HEALPix (Górski et al. 2005) package. The use of computing facilities at NERSC (U.S.A.) and at INAF–IASF Bologna is acknowledged.

It is a pleasure to thank the many colleagues of the *Planck*, Cosmic ORigins Explorer (CORE) and Square Kilometre Array (SKA) Collaborations, the teams for the proposals (2014 APRS – ATNF proposal C2922, Semester: April, 2014 – and 2015OCTS/C2922) and observational campaigns at Australia Telescope Compact Array (ATCA) for constructive discussions and collaborations, and the staff at the ATCA site, Narrabri (NSW), for the valuable support (ATCA is part of the Australia Telescope funded by the Commonwealth of Australia for operation as a National Facility managed by CSIRO).

Preface

The Cosmic Microwave Background (CMB) represents one of the landmark evidence of the Hot Big Bang theory, predicted in 1922 by Alexander Friedmann. The CMB is the thermal radiation originated in the primordial Universe due to the tight coupling between matter and radiation. It was only after the baryon photon decoupling, when the first neutral atoms formed and the Universe became transparent, that this radiation freely streamed toward us diffused at Last Scattering Surface (LSS). The CMB provides a wide number of observables in which modern cosmology finds its basis to probe the very early stages of the Universe. Indeed, since CMB discovery in 1964, and in particular in the past two decades, the improved measurements in temperature fluctuations achieved an unprecedented accuracy in constraining the majority of the cosmological parameters values. In early 1990's, the COsmic Background Explorer (COBE) satellite discovered the CMB anisotropies and inaugurated the "precision cosmology" era measuring the CMB absolute temperature and spectrum. Although anticipated by a fine, joint analysis of CMB anisotropy upper limits at small scales and galaxy surveys, it was only around ten years later that the idea of a ΛCDM Universe, driven by a dark energy component compatible with a standard cosmological constant, took place owing to the discovery of the recent cosmic acceleration through SNIa observations and the flatness of the Universe thanks to the Balloon Observations Of Millimetric Extragalactic Radiation and Geophysics (BOOMERanG) CMB anisotropy experiment. Soon after this mission, the Degree Angular Scale Interferometer (DASI) experiment probed, for the first time, the E-mode polarization anisotropies. In subsequent years, the Wilkinson Microwave Anisotropy Probe (WMAP) through its detailed all sky anisotropy maps sensitively improved the cosmological parameters determination and by accurate measure of the cross-correlation between temperature and E-mode polarization anisotropy probed the essentially adiabatic nature of primordial perturbations. The CMB polarization pattern mainly originates from the scattering of CMB photons off free electrons in an anisotropic radiation field. Polarization magnitude at large angular scales (corresponding to multipoles

$\ell \lesssim 10$) is more related to the reionization era, mainly associated to the epoch during which the first cosmic structures reheated the cosmological plasma. The cosmological reionization era occurred at the end of the "dark ages", when the first luminous sources emerged, and its beginning is identified, to first approximation, by the Thomson scattering optical depth, the so called τ-parametrization. The evolution of the ionization fraction plays a fundamental role in the knowledge of the feedback mechanisms affecting cosmic structures at different epochs, and is traced by various types of observations. Remarkably, at large angular scales, cosmological reionization amplifies not only the E-mode polarization but also the B-mode polarization, thus offering a second multipole window, complementary to that corresponding to the first acoustic peak, for the detection of the stochastic field of primordial gravitational waves.

Since the time of last scattering, the CMB signal is affected by various sources of contamination, typically in the form of diffuse or discrete emission, superimposed to the primordial signal. Hence, to extract the wealth of informations encoded in the CMB a complete knowledge of the different foreground components and their precise removal from the data is crucial. Important sources of (mainly diffuse) foreground come from the Solar System while others, as synchrotron, bremsstrahlung and dust emission, comes from the Milky Way. Signals from extragalactic radio sources and dust emission dominated galaxies are compelling as well, particularly at small angular scales. In order to disentangle these sources and separate them in microwave maps on a physically motivated basis, it is necessary to measure and characterize their Spectral Energy Distribution (SED), polarization properties and possible variability, at least for radio sources. For these reasons, it is unavoidable to carry on multifrequency observations with different instruments, both coeval and at different epochs.

The purpose of this thesis is to jointly investigate a set of selected topics on the basis of the cosmological analysis of CMB and radio surveys including astrophysical foreground limitation. The recent release of *Planck* data, in synergy with the Second *Planck* Catalog of Compact Sources and radio data (ATCA), represents an optimal observational framework to extract information about extragalactic foregrounds and to predict their impact on future CMB projects aimed at B-mode detection.

Understanding the energetic involved in the various epochs of the evolving Universe, from the early stages to the structure formation phase, is an intriguing aspect of classical and modern cosmology. The CMB B-mode anisotropies, induced by primordial gravitational waves generated during the inflationary epoch, are related to the energy scale of inflation. On the other

hand, the departure from a perfect blackbody is predicted by some main unavoidable mechanisms in the cosmic plasma, as energy dissipation processes at early times ($z \gtrsim 10^5$) resulting in Bose-Einstein like distortions and late epoch mechanisms ($z \lesssim 10^4$), before or after the recombination era, generating Comptonization and free-free distortions, the reionization process being likely the most remarkable example in astrophysical cosmology. In this thesis, I explore intriguing cosmological themes that could be studied with present and forthcoming CMB and radio projects. The role of future dipole spectrum analyses is deeply discussed as a way to investigate on dissipation processes and to set constraints on the cosmic far-infrared background, which amplitude is related to the dust-obscured star-formation phase of galaxy evolution. The Square Kilometre Array will trace the neutral hydrogen distribution and the neutral-to-ionized transition state at the reionization epoch through the redshifted 21-cm line, observable at frequencies of about 0.1–0.2 GHz. This phase is also traced by the diffuse free-free emission, but also at higher frequencies, the range around some GHz likely being the most promising. Also, the quadratic dependence of free-free emission on baryon density implies that its amplitude is related to matter clumping and then to the nature of dark matter particles via their effect on the power spectrum at small scales.

Finally, my thesis work involves essential keys in modern cosmology and astrophysics, such as data analysis tools for foreground cleaning, parameter estimation, radio source SED fitting and intensity distribution analysis as well as theoretical and numerical methods for predicting CMB spectral distortions, Boltzmann codes for CMB and power spectra fluctuations evolutions, numerical codes for the evaluation of sources Poissonian fluctuations, Monte Carlo simulations to address the impact of observational issues, some of them originally implemented, others adapted and/or interfaced to deal with the scientific problems here briefly introduced.

Contents

Preface v

List of Figures xiii

List of Tables xxv

1 Microwaves space observations: from *Planck* legacy to the future 1

1.1 Introduction . . . 1

1.2 *Planck* Mission: instrument and systematics . . . 2

1.3 Astrophysical foregrounds . . . 6

1.3.1 Catalogs of sources and clusters of galaxies . . . 7

1.3.2 Galactic diffuse components . . . 9

1.4 *Planck* cosmological implications . . . 12

1.4.1 The Integrated Sachs-Wolfe effect . . . 12

1.4.2 The ISW probed through the CMB-LSS cross-correlation . . . 13

1.4.3 Parametrization of early and late ISW and data analysis . . . 15

1.4.4 CMB low multipoles anomalies . . . 17

1.4.5 Features in the primordial fluctuations . . . 18

1.4.6 Primordial non-Gaussianity . . . 20

1.5 WMAP and *Planck* joint data analysis . . . 22

1.5.1 Low-ℓ data . . . 23

1.5.2 Foreground mitigation and analysis . . . 25

1.5.3 Cosmological parameters . . . 27

1.6 CMB mission proposals in ESA context . . . 29

1.7 The PIXIE mission . . . 33

1.8 The LiteBIRD mission . . . 35

1.9 The CORE mission . . . 37

2 Radio facilities and extragalactic source characterization 41

2.1 Introduction . . . 41
2.2 The Atacama Large Millimeter/submillimeter Array . . . 42
2.3 The Australian Telescope Compact Array . . . 44
2.4 Scientific case . . . 47
2.5 Observations . . . 49
2.6 Data reduction . . . 51
2.6.1 Imaging and flux density measurements . . . 53
2.7 Data analysis . . . 54
2.7.1 Fit procedures . . . 54
2.7.2 Spectral properties . . . 56
2.7.3 Linear polarization fraction . . . 62
2.7.4 Polarization angle: cm- and mm-wavelength regime behaviour . . . 63
2.7.5 Circular polarization . . . 67
2.8 Source counts in polarization . . . 67
2.9 Variability . . . 69
2.10 Conclusions . . . 72

3 Polarization properties of extragalactic sources at Planck frequencies 75

3.1 Introduction . . . 75
3.2 Outline of the method . . . 79
3.3 Validation . . . 81
3.4 Results . . . 87
3.4.1 Radio sources . . . 87
3.4.2 Dusty galaxies . . . 88
3.4.3 Power spectra . . . 89
3.5 Conclusions . . . 91

4 Square Kilometre Array and CMB spectral distortions 95

4.1 Introduction . . . 95
4.2 The Square Kilometre Array . . . 96
4.3 The SKA science . . . 97

4.4 SKA precursors . . . 102
4.5 SKA pathfinders . . . 103
4.6 SKA contribution to future CMB spectrum experiments . . . 104
4.7 Dark Matter models and free-free emission . . . 106
4.7.1 Exploiting various models . . . 109
4.7.2 Results . . . 110
4.7.3 Astrophysical confusion noise . . . 111
4.8 SKA contribution to future B-mode projects . . . 113

5 Observer peculiar motion effects in microwave and radio surveys 117
5.1 Introduction . . . 117
5.2 Radio dipole . . . 119
5.3 The CMB dipole: forecasts for CORE in the ideal case . . . 120
5.4 Parametric model for potential foreground and calibration residuals in total intensity . . . 123
5.5 The CMB dipole: forecasts for CORE including potential residuals . . . 126
5.6 Measuring Doppler and aberration effects in different maps . . . 128
5.6.1 Boosting effects on the CMB fields . . . 128
5.6.2 Going beyond the CMB maps . . . 131
5.6.3 Estimates of the Doppler and aberration effect . . . 133
5.7 Differential approach to CMB spectral distortions and the CIB . . . 138
5.7.1 The CMB dipole . . . 138
5.7.2 The CIB dipole . . . 141
5.7.3 Beyond the dipole . . . 142
5.7.4 Detectability . . . 146
5.8 Simulation results for CMB spectral distortions and CIB intensity . . . 148
5.8.1 Ideal case: perfect calibration and foreground subtraction . . . 150
5.8.2 Including potential foreground and calibration residuals . . . 154
5.8.2.1 Monte Carlo results at about 1° resolution . . . 154
5.8.2.2 Application of masks . . . 156
5.8.2.3 Varying assumptions on potential foreground and calibration residuals . . . 157
5.8.3 Summary of simulation results . . . 160

5.9 Discussion and conclusions 160
Appendix 5.A Likelihoods of CMB dipole parameters 165
Appendix 5.B Rms values from Monte Carlo simulations: ideal case 169
Appendix 5.C Ideal case at high resolution 172
Appendix 5.D Rms values from Monte Carlo simulations: including potential residuals 173
Appendix 5.E Results for different assumptions on potential foreground and calibration residuals 173

Conclusions **181**

References **187**

List of Figures

1.1 Residual EE auto-power spectra of systematic effects from the HFI pre-2016 E2E (end-to-end) simulations computed on 50 % of the sky (colours specified in the top left panel apply to all panels). The purple line (ADC NL total residual) shows the sum of all effects associated with ADC nonlinearity. The dark blue line (ADC NL - Analogue-to-digital converter nonlinearity - no distortion) shows the level without the dominant dipole distortion. The plots show also the F-EE fiducial model from best-fit *Planck* 2015 cosmological parameter (252) (black curves). The 100-GHz and 143-GHz model scaled to 353 GHz with a dust SED is shown as dashed and dotted lines, respectively. From (262). 5

1.2 Sensitivity (the flux density at 90% completeness) of the PCCS2, compared with PCCS, ERCSC, WMAP and others. For the LFI channels, the sensitivities refer to the full sky. For the HFI channels, the 90% completeness limits plotted for the PCCS were evaluated in a selected extragalactic zone; the regions of sky to which the 90% completeness limits apply are similar but not identical to those of the PCCS2. From (244). 8

1.3 Distribution of PSZ2 clusters with associated redshift in the mass-redshift (M500 – z) plane compared to SPT and ACT catalogues. Black circles: PSZ2 clusters; red (green) filled circles: common SPT/PSZ2 (ACT/PSZ2) clusters. Red (green) empty squares: the remaining SPT (ACT) clusters not detected by *Planck*. See also the text. From (258). 9

1.4 Stokes Q and U polarization parameters for the synchrotron at 30 GHz (upper line) and thermal dust at 353 GHz (bottom line). From (237). 10

1.5 Brightness temperature rms as a function of frequency and component for temperature (left), where each component is smoothed to an angular resolution of 1° FWHM and the lower and upper edges of each line are defined by masks covering respectively 81% and 93% of the sky, and polarization (right), where the corresponding smoothing scale is 40′ and the sky fractions are 73% and 93%. From (237). 11

1.6 Map (thermodynamic temperature in K) of the recovered ISW anisotropies (left) and its corresponding estimated error per pixel (right), from the combination of the *Planck* SEVEM CMB map and all the LSS tracers. The error map structure is determined by the sky coverage of the different surveys. The total signal-to-noise of the ISW map cannot exceed, obviously, a value of ≈ 4. The signal-to-noise is higher near the Galactic poles, with values of ≈ 2. From (51). 14

1.7 One-dimensional posteriors for $A_{e\mathrm{ISW}}$ and $A_{l\mathrm{ISW}}$. In the left column, only *Planck* temperature and low multipole polarization APS (*Planck* TT + lowP) were used. The plots in the right column use also the *Planck* polarization APS at high multipoles (*Planck* TT, TE, EE + lowP). From (56). 16

1.8 Posterior probabilities of Δ (solid line for the standard mask with $f_{sky} \simeq 90\%$, and dashed line for an extended mask with $f_{sky} \simeq 40\%$). From (51). 18

1.9 PPS simulated for various oscillatory models parametrized with an amplitude, a frequency and a phase (for the Linear oscillation models I have the scale-dependence index as further parameter). Left: Log-spaced oscillations models for different values of the frequency oscillation parameter. Middle: Linear oscillation models for different values of the scale-dependence index. Right: Step oscillation models for different values of the frequency and phase parameters. From (51). 19

1.10 Frequency dependence of polarized synchrotron and dust emission derived with the template fitting approach described. Green line shows a pure power law from the WMAP Ka band up to the *Planck* 353 GHz band, allowing to appreciate the flattening of dust emission in agreement with a grey body. See also the text. 27

1.11 PIXIE observatory and mission concept. The instrument is maintained at 2.725 K and is surrounded by shields to block radiation from the Sun or Earth. It observes from a 660 km polar sun-synchronous terminator orbit. The rapid spin and interferometer stroke efficiently separate Stokes I, Q, and U parameters independently within each pixel to provide a nearly diagonal covariance matrix. 33

1.12 Angular power spectra for unpolarized, E-mode, and B-mode polarization in the cosmic microwave background. The dashed red line shows the PIXIE sensitivity to B-mode polarization at each multipole moment $\ell \sim 180\,\mathrm{deg}\,/\theta$. The sensitivity estimate assumes a 4-year mission and includes the effects of foreground subtraction within the cleanest 75% of the sky combining PIXIE data at frequencies $\nu < 600$ GHz. Red points and error bars show the response within broader ℓ bins to a B-mode power spectrum with amplitude $r = 0.01$. PIXIE will reach the confusion noise (blue curve) from the gravitational lensing of the E-mode signal by cosmic shear along each line of sight, and has the sensitivity and angular response to measure even the minimum predicted B-mode power spectrum at high statistical confidence. 34

1.13 The LiteBIRD sensitivities compared to the primordial B-mode for different values of r from 0.1 down to 0.001 and the contamination from the lensing to the B-mode pattern. 36

1.14 The LiteBIRD band locations centre and the sensitivities for each band. It is also shown the contamination from synchrotron and dust emissions, the CMB signal and the most suitable cosmological frequency channels. 36

2.1 Maps in total intensity (colours) and polarization (contours) for AT20GJ0408-7507 at 5.5, 24 and 38 GHz. The two-lobe structure is resolved at the higher frequencies. The eastern lobe appears to be strongly depolarized. 55

2.2 Spectra in total intensity and polarization, polarization fraction and polarization angle for some objects of the faint PACO sample, observed in September 2014 and March-April 2016 campaigns. Error bars are not displayed since they are smaller than the symbols. Total intensity: red plus signs show observations, solid magenta lines the fitting curves, orange crosses the median PACO flux densities (July 09-August 10), brown triangles the AT20G observations (best epoch 2004-2008). Polarization (flux density): black plus signs refer to observations, black filled downwards triangles show upper limits, solid blue lines the best fit curves, green diamonds the AT20G observations (best epoch 2004-2008). Data of September 14 and March-April 16 only campaigns: linear polarization fractions (purple asterisks and upper limits reported as downwards pointing purple filled triangles); circular polarization fraction (violet circles) and upper limits (downward triangles); polarization angle (PA) (black diamonds). 57

2.3 Radio colour-colour diagrams for (from left to right) total intensity and polarized flux density. Symbols identify the spectral type in total intensity: plus for flat-spectrum, asterisks for steep-spectrum, diamonds for peaked-spectrum. Colours refer to the spectral shape between 5.5 and 18 GHz: red for steep-spectrum, blue for flat-spectrum, and green for peaked-spectrum sources. . . . 60

2.4 Spectra in total intensity and polarization with GLEAM observations between 72 and 231 MHz (orange plus), current observations in total intensity (red plus) and polarization (black plus and downward triangles), fits in total intensity and polarization (red and black solid curves). The SUMSS (209) flux density at 843 MHz is shown for comparison, but not used in the fit procedures. For each object, spectral indices (in total intensity) $\alpha_{0.2}^{0.4}$, $\alpha_{2.5}^{5.5}$ and α_{28}^{38} are provided. Is also reported the spectral classification in terms of estimated synchrotron components (see 2.7.3). 61

2.5 Left panel: median polarization fraction behaviour with frequency (at 2.1, 5.5, 9, 18, 24, 33 and 38 GHz) for all the sources (black), for steep sources (red), for peaked (green) and flat ones (blue). Right panel: the same as left panel but for: '1C' sources (red), for '2-3C' sources (green) and for sources with more than 3 components (blue, labelled '>3C'). The errors on median values are given by $1.253 \times \mathrm{rms}/\sqrt{N}$, where rms is the standard deviation around the mean and N is the number of the data (at a given frequency) for a given class of objects (left panel) and the number of detected sources (right panel) (16). 64

2.6 Distribution of the polarization fraction at 18 GHz. Errors and upper limits correspond to a 1σ level. The black circles refer to the sample studied in this analysis, the red plus signs to the full AT20G bright sample. The corresponding fit by a log-normal distribution for each dataset is reported with a solid lines of the same color. 69

2.7 Differential source counts at 20 GHz in polarization (black circles) and upper limits (black downward triangles). Ffor comparison, are shown the polarimetric data estimates from the survey (202), shallower than the present one ($S_{20\,\mathrm{GHz}} > 500$ mJy) combined with the full AT20G catalogue (blue diamonds) and upper limits (blue downward triangles). The curves show the model predictions: blue for the 'conservative' case and red for the 'optimistic' case. Solid lines represent the total number counts; dotted lines are for steep-spectrum sources (classified at low frequencies); dashed lines are for flat objects (flat-spectrum radio quasars, i.e. FSRQs and BL Lacs). 71

2.8 Mean variability indices in total intensity *vs.* time lag at the observed frequencies (different colours). Variability measurements for the faint PACO sample are also displayed. 73

3.1 Distribution of the polarized signals of PCCS2 radio sources and dusty galaxies compared with those of control fields (signals within a radius of FWHM/2 from the corresponding centers). The total flux density limits for radio sources are those listed in Table 3.7. For dusty galaxies at 353 GHz we have kept the same limit as for radio sources (784 mJy). At 217 GHz, $S_{\mathrm{lim,dusty}} = 300$ mJy (see text). 84

3.2 Median polarization degrees for radio sources at *Planck* frequencies with their errors (blue data points), and upper limits (90% and 68% confidence) for dusty galaxies (red arrows). The solid blue line shows the minimum χ^2 value of the median polarization degree of radio sources, assumed to be frequency independent. The dashed and dot-dashed lines show the 68% and 95% limits, respectively. 89

3.3 Polarization E/B-mode power spectra of radio sources and of dusty galaxies compared with the CMB E-mode and B-mode for four values of the tensor to scalar ratio $r = 0.01, 0.003, 0.001, 0.0003$ (from top to bottom); see text and legend for details. Since unresolved point sources contribute, on average, equally to E- and B-mode, their total power spectra have been divided by a factor of 2. 90

4.1 SKA overall project timeline. 97

4.2 Left panel: distorted spectra in equivalent thermodynamic temperature vs. λ (cm) with late energy injection $\Delta\varepsilon/\varepsilon_i \simeq 4y = 5{\times}10^{-6}$ plus an early/intermediate energy injection $\Delta\varepsilon/\varepsilon_i = 5 \times 10^{-6}$ ($\sim$ 20 times smaller than current upper limits) at the "time" Comptonization parameter $y_h = 5, 1, 0.01$ (bottom to top; the cases at $y_h = 5$ and 1 are very similar at short λ; solid lines) plus a FF distortion with $y_B = 10^{-6}$ (dashes). $y_h = y$, but assuming electron temperature equal to the radiation one and computing the integral from the energy injection time to the current time. Right panel: FF distortion in SKA2 frequency range by two astrophysical reionization histories (a *late* phenomenological model is also displayed for comparison). Inset: models absolute differences; vertical lines: ranges of SKA1 configurations. 107

4.3 Evolution of clumping factor for three values of k_{max}. 110

4.4 Brightness temperature relative excess predicted at current time as function of the wavelength assuming the $y_B(x)$ value properly evaluated at each frequency in the entire range. Upper panel: suppression model for $k_{max} = 200$ and 1000 and without the correction due to the IGM density contrast. Bottom panel: comparison between the three considered reionization histories for $k_{max} = 500$. 111

4.5 The CMB B-mode polarization angular power spectrum for different tensor-to-scalar perturbation ratios (from 1 to 3×10^{-4}; solid black lines), lensing (blue dots), and estimates of potential residual of Galactic foregrounds (at 70 GHz) and angular power spectrum from polarized radio sources (at 100 GHz) below different detection thresholds in polarized flux density (green dashes; from top to bottom, 100 mJy and 10 mJy, representative of thresholds achievable, respectively, in current and future CMB experiments, and 100 μJy representative of potential improvement discussed here). Red long dashes show typical potential residuals from Galactic polarized dust emission extrapolated from 353 GHz assuming an error of 0.01 in the dust grain spectral index. Blue dashes show typical potential residuals from Galactic polarized synchrotron emission extrapolated from 30 GHz assuming an error of 0.02 in the synchrotron emission spectral index. Cyan dashes show an estimate of AME angular power spectrum assuming a polarization degree of 2%. See also the text. 116

5.1 Map of the CMB dipole used in the simulations, corresponding to an amplitude $A = 3.3645\,\mathrm{mK}$ and a dipole direction defined by the Galactic coordinates $b_0 = 48.24°$ and $l_0 = 264.00°$. The map is in Galactic coordinates and at a resolution of $\simeq 3.4$ arcmin, corresponding to `HEALPix` $N_{\mathrm{side}} = 1024$. 121

5.2 Instrumental noise map and *Planck* Galactic mask (extended to cut out ±30° of the Galactic plane) employed in the simulations. The noise map corresponds to 7.5 μK.arcmin, as expected for the 60-GHz band. The Map is in Galactic coordinates and at resolution of $\simeq 3.4$ arcmin, corresponding to `HEALPix` $N_{\mathrm{side}} = 1024$. 122

5.3 Sky residual and calibration error maps (in Galactic coordinates) in the 60-GHz band employed in the simulations. Their amplitudes correspond to the pessimistic case, $E_{\mathrm{for}} = 0.64$ and $E_{\mathrm{cal}} = 0.064$, for maps at resolution `HEALPix` $N_{\mathrm{side}} = 1024$. 126

5.4 $1\,\sigma$ errors as function of `HEALPix` $N_{\rm side}$ values for the parameters A, b_0, l_0, and T_0: dipole-only (solid black line); dipole+noise (green dot-dashed line); dipole+noise+mask (red dotted line); and dipole+noise+mask+systematics (blue dashed line). The chosen frequency channel is 60 GHz and the noise map corresponds to $7.5\,\mu$K.arcmin. I adopted the *Planck* Galactic mask extended in order to cut out $\pm 30^\circ$ of the Galactic plane. The systematics correspond to the pessimistic expectation of calibration errors and sky (foreground, etc.) residuals. Notice that the pixelization error, due to the finite map resolution, is dominant over the noise for any $N_{\rm side}$. While the impact of noise and systematics is negligible, the effect of reducing the effective sky fraction is important. 127

5.5 Achievable precision in estimating the velocity through aberration and Doppler effects in an ideal experiment (with $f_{\rm sky} = 1$ and limited by cosmic variance only) for different maps. *Left:* as a function of $\ell_{\rm max}$. *Right:* as a function of $\ell_{\rm min}$ (with fixed $\ell_{\rm max} = 5000$). *Bottom:* for individual bins with $\Delta\ell = 200$. It emerges that: (i) the first hundred ℓs are not important for achieving a high S/N; and (ii) the non-CMB diffuse maps exhibit low precision and are not very useful for measuring β. Note that for simplicity no primordial B-modes are assumed (constraints turn out to be very weakly sensitive to this choice). . . . 134

5.6 Similar to the left panel of Fig. 5.5 but for realistic experiments and assuming $f_{\rm sky} = 0.8$. Bottom right panel gives the precision combining all temperature and polarization maps, also in the case of an ideal experiment (no instrumental noise and $f_{\rm sky} = 1$). 135

5.7 Spectrum of dipole (in equivalent thermodynamic, or CMB, temperature) expressed as the difference between that produced by a distorted spectrum and that corresponding to the blackbody at the current temperature T_0. Thick solid lines (or thin three dots-dashes) correspond to positive (or negative) values. *Left*: the case of BE distortions for $\mu_0 = -2.8 \times 10^{-9}$ (representative of adiabatic cooling; green dots, note the opposite signs with respect to the cases with positive μ_0), $\mu_0 = 1.4 \times 10^{-5}$, 1.4×10^{-6} (representative of improvements with respect to FIRAS upper limits), $\mu_0 = 1.12{\times}10^{-7}$, $2.8{\times}10^{-8}$, and $1.4{\times}10^{-9}$ (representative of primordial adiabatic perturbation dissipation). *Right*: the case of Comptonization distortions for $u = 2 \times 10^{-6}$ (upper curves) and $u = 10^{-7}$ (lower curves), representative of imprints by astrophysical or minimal reionization models, respectively. 140

5.8 Expected behaviour of the dipole spectrum. The upper lines show the spectrum of the (pure) CIB dipole, while the lower lines show the spectrum coming from the dipole pattern computed from the CIB distribution function added to the blackbody (at temperature T_0) distribution function, minus the dipole pattern computed by the blackbody distribution function. Thick solid lines (or thin three dots-dashes) correspond to positive (or negative) values. The analytic representation of the CIB spectrum by (124) is adopted here, considering the best-fit amplitude and the range of $\pm 1\,\sigma$. 142

5.9 *Top row*: maps of the dipole, quadrupole and octupole computed assuming a CMB blackbody spectrum at the current temperature T_0, for reference. In all other cases I provide the maps of the dipole (*second row*), quadrupole (*third row*), and octupole (*bottom row*) at three different frequencies (namely 60, 145, and 600 GHz, from left to right), in terms of the difference between the pattern computed for a BE distortion with $\mu_0 = 1.5 \times 10^{-5}$ and that computed for a blackbody at the present-day temperature T_0. 143

5.10 The same as in Fig. 5.9, but for the case of a Comptonization distortion with $u = 2 \times 10^{-6}$. 144

5.11 The same as in Fig. 5.9, but for the case of the CIB with amplitude set at the best-fit value found by FIRAS. More precisely, I display the temperature pattern of the CIB distribution function added to the blackbody one, minus the temperature pattern coming from the blackbody. 145

5.12 Angular power spectrum of the dipole map, derived from the difference between distorted spectra and the current blackbody spectrum versus CORE sensitivity. The CORE white noise power spectrum (independent of multipole, shown as the black upper solid curve and with diamonds for different frequency channels) and its rms uncertainty (for $\ell = 1$, using dots, and for $\ell = 2$, using dashes) are plotted in black. The cross (asterisk) displays aggregated CORE noise from all channels (up to 220 GHz). Are also shown, for comparison, the LiteBIRD white noise power spectrum (red solid curve and diamonds for different frequency channels). *Left*: BE distortions for $\mu_0 = -2.8 \times 10^{-9}$ (representative of adiabatic cooling), $\mu_0 = 1.4 \times 10^{-5}$, 1.4×10^{-6} (representative of improvements with respect to FIRAS upper limits), $\mu_0 = 1.12 \times 10^{-7}$, 2.8×10^{-8}, and 1.4×10^{-9} (representative of primordial adiabatic perturbation dissipation). For $\mu_0 = 1.4 \times 10^{-5}$ I show also the angular power spectrum of the quadrupole map. *Right*: Comptonization distortions for $u = 2 \times 10^{-6}$ (upper solid curve for the dipole map and bottom dashed curve for the quadrupole map) and $u = 10^{-7}$ (lower solid curve for the dipole map), representative of imprints by astrophysical and minimal reionization models, respectively. 146

5.13 The same as in Fig. 5.12, but comparing the two above cases of Comptonization distortions with the two above cases of BE distortions with the largest values of μ_0. 147

5.14 The same as in Fig. 5.12, but for the CIB (assuming the model from (124)). Also shown is the quadrupole signal (dashes). The different values of I_0 in Eq. (5.31) are the best-fit values and deviations by $\pm 1\,\sigma$. 147

5.15 Marginalised likelihoods, and 68% and 95% contours of the parameters A, b_0, l_0, and T_0 at $N_{\rm side} = 128$ (red) and at $N_{\rm side} = 1024$ (blue): top left, dipole only; top right, dipole+noise; bottom left, dipole+noise+mask; and bottom right, dipole+noise+mask+systematics. The reference frequency channel is 60 GHz and the noise is $7.5\,\mu$K.arcmin. The mask used here is the *Planck* Galactic mask extended to cut out $\pm 30^\circ$ of the Galactic plane. The level of systematics correspond to the pessimistic expectation of calibration errors and sky residuals. 165

5.16 Marginalised likelihoods, and 68% and 95% contours of the parameters A, b_0, l_0, and T_0. Input maps are at $N_{\rm side} = 1024$, with noise, mask and residuals (calibration errors and sky residuals). *Top*: 100 GHz with optimistic (left) and pessimistic (right) systematics. *Bottom*: 220 GHz with optimistic (left) and pessimistic (right) systematics. 167

5.17 Marginalised likelihoods, and 68% and 95% contours of the parameters A, b_0, l_0, and T_0. Input maps are dipole-only, at 60 GHz and at $N_{\rm side} = 1024$. On the left: blackbody. On the right: Bose-Einstein (chemical potential $\mu_0 = 1.4\times10^{-5}$). 168

List of Tables

1.1 Main systematic effects in *Planck* data. 4

1.2 Main characteristics of LFI full mission maps. [a] Calculated from the main beam solid angle of the effective beam, $\Omega_{\rm eff}$ = mean(Ω). These values are used in the source extraction pipeline. [b] Noise rms computed after smoothing to 1 deg. [c] Sum of the error determined from the absolute and relative calibration. [d] Estimated rms values over the full sky and after full mission integration. Not included here are gain reconstruction uncertainties, estimated to be of order 0.1%. From (237). 6

1.3 Main characteristics of HFI full mission maps. [a1] Number of bolometers whose data were used in producing the channel map. [b1] FWHM of the Gaussian whose solid angle is equivalent to that of the effective beams. [b2] FWHM of the elliptical Gaussian fit. [b3] Ratio of the major to minor axis of the bestfit Gaussian averaged over the full sky. [c1] Estimate of the noise per beam solid angle, as given in *b1*. [c2] Estimate of the noise in intensity scaled to 1 deg assuming that the noise is white. [c3] Estimate of the noise in polarization scaled to 1 deg assuming that the noise is white. [d] Calibration accuracy (at 545 and 857GHz, the 5% accounts for the model uncertainty). [e] According to the (34) model, whose uncertainty is estimated to be at the 20% level (also for constant νI_ν). [e2] Zero level correction to be applied on zodiacal light corrected maps. From (237). 7

1.4 Abbreviations for the several datasets (and combinations thereof) employed throughout this analysis. 24

1.5 Best-fit scaling coefficients and χ^2 values for WMAP9 low ℓ polarization frequencies, obtained using the processing mask. The χ^2 values are in N_p unit, and the S+N estimates are computed outside of the processing mask, leaving N_p good pixels in the maps. The χ^2_N values assume only the noise covariance matrix. Differences between these two approaches are weak. Last columns report $\tilde{\chi}^2$ values, in $\mathcal{N}_p$ unit, for both S+N and N, computed outside of the P06 mask used for parameter estimation, leaving $\mathcal{N}_p = 4510$ good pixels. Here, the scaling coefficients derived in the processing mask have been assumed, estimated separately for S+N and N: the scalings quoted in the first two columns are for the former case, though the latter produces figures that are well within errors. 25

1.6 Parameter estimates from *Planck* high TT+ *Planck* lensing either in combination with the low-ℓ datasets analyzed (second to fourth column) or alone (fifth column). In the former cases, use of *Planck* lowT is understood. The last three columns report the shifts (in units of σ) in the parameters with respect to WMAP9 lowP + *Planck* high TT + *Planck* lensing. 28

1.7 LiteBIRD specifications. The second column gives the FWHM resolution of the beam. ΔT and ΔP are the instrumental noise 1 σ sensitivities in a 1 arcminute side pixel. . . . 37

1.8 Proposed CORE-M5 frequency channels. The sensitivity is estimated assuming $\Delta\nu/\nu = 30\,\%$ bandwidth, 60 % optical efficiency, total noise of twice the expected photon noise from the sky and the optics of the instrument being at 40 K. The second column gives the FWHM resolution of the beam. This configuration has 2100 detectors, about 45 % of which are located in CMB channels between 130 and 220 GHz. Those six CMB channels yield an aggregated CMB sensitivity of 2 μK.arcmin (1.7 μK.arcmin for the full array). 40

2.1 Summary of ALMA Receivers. [a]Receiver Noise over 80% of the radio frequency band. [b] Temperature at any RF Band. [c]DSB receiver noise temperature is given for Bands 9 & 10. 43

2.2 ALMA Sensitivity Goals for the 12-m Array. [a]Bandwidth = 8 GHz, two polarizations, 64 antennas in one minute. [b]Bandwidth = 1 km s^{-1} (equivalent Doppler spread at line frequency), two polarizations. [c]One Jansky (Jy) = 10^{-26} W m^{-2} Hz^{-1}. 44

2.3 Observing Parameters for the 6km Compact Array. [a] Field of view (full width at half power). [b] System temperature at high elevation under reasonable weather conditions (they are weather dependent). [c] Signal which doubles the system temperature. [d] Within FWHM primary beam. [e] HPBW in R.A. for the 6 km array for all but the 3 mm band, for which the H214 array is assumed. [f] Theoretical rms noise; one frequency; dual orthogonal polarization; natural weighting. This is the 1 σ Gaussian-noise level. [g] For the array listed in the same column. This is the 1 σ Gaussian-noise level. 47

2.4 Continuum brightness temperature sensitivity after 12 hr integration for bandwidth described in Table 2.3 and for various arrays. 48

2.5 Distribution of sources per spectral type in total intensity and in polarization. 'NA' refers to the three objects classified in total intensity but missing a spectral fit in polarization. Last row and column gives the total for a given spectral class. 58

2.6 First, second (median), and third quartiles of spectral indices in total intensity and in polarization for different frequency ranges. We give values for the full sample and for the three main spectral classes, as classified in total intensity. . . 59

2.7 First, second (median) and third quartiles of the polarization fraction at each observed frequency given by the Kaplan-Meier estimator, taking into account the upper limits, for the full sample and for the steep- and peaked-spectrum sources. The last row reports probabilities for the null hypothesis (i.e. the two samples are drawn from the same parent distribution) given by the Kolmogorov-Smirnov test performed on the steep and peaked groups, considering together 5.5 and 9 GHz, the 18 − 38 GHz frequency interval and all the frequencies, respectively. 65

2.8 Median plus I and III quartile values of cm-wavelengths RMs. The upper set of values refers to the observed RMs, the lower to the RMs at the source for the ones with known redshift. For each group is given total sources number in parenthesis, if < 10 is provided only the median value. RMs are in rad/m^2. . . . 66

2.9 The same as Table 2.8 but for mm-wavelengths. 66

2.10 Distribution of the polarization fractions at 18 GHz for the full sample. 68

2.11 Euclidean normalized differential source counts at 20 GHz in polarization obtained in this paper via the convolution of the distribution of the polarization fraction at 18 GHz with the model (102). 70

2.12 Mean variability indices in total intensity and in polarization (last row). 72

3.1 Comparison of the median polarization degrees, $\Pi_{\rm IDA} = (P/S)_{\rm median}$, at 44 GHz yielded by the IDA method with those measured by (167) at 43 GHz, within the flux density range $S_{\rm range}$. The errors on $\Pi_{\rm IDA}$ correspond to the 16th and 84th percentiles of the polarization degree distribution divided by $N_{\rm bin}^{1/2}$, $N_{\rm bin}$ being the number of sources in the bin, $N_{\rm PCCS2}$ is the number of them with polarization measurements in the PCCS2, D is the KS statistics. The last column gives the probability of the null hypothesis (the distribution of signals of sources and control fields are drawn from the same parent distribution) given by the one-sided KS test. The bottom line refers to the full sample. 82

3.2 Comparison of the median polarization degrees, Π, at 100 GHz yielded by the IDA method with those measured by (6) at 86 GHz. The columns have the same meaning as in Table 3.1. The bottom line refers to the full sample. 82

3.3 Median polarization degrees, $\Pi_{\rm IDA} = (P/S)_{\rm median}$, at 30 GHz of PCCS2 radio sources in the region specified in Sect. 3.2. The columns have the same meaning as in Table 3.1. The first bin is the faintest for which the test detected a significant signal. 85

3.4 Same as in Table 3.3 but at 44 GHz. 85

3.5 Same as in Table 3.3 but at 100 GHz. 86

3.6 Same as in Table 3.3 but at 143 GHz. 86

3.7 Median polarization degrees of radio sources at the *Planck* polarization-sensitive frequencies. 86

4.1 Parameters for SKA (Adapted from SKA-TEL-SKO-DD-001Revision:1, SKA1 System Baseline Design, P. E. Dewdney et al. 2013). 98

4.2 Parameters for the SKA precursors and pathfinders described in the text (adapted from SKA-TEL-SKO-DD-001Revision:1, SKA1 System Baseline Design, P. E. Dewdney et al. 2013). 104

5.1 Aberration and Doppler effects with CORE. $f_{\rm sky} = 0.8$ for all experiments (and $f_{\rm sky} = 1$ in the ideal cases) in order to make comparisons simpler. For CORE and LiteBIRD $\sigma^P = \sqrt{2}\sigma^T$, while for *Planck* see the 2015 values. The combined channel estimates are effective values that best approximate Eq. (5.19) in the ℓ range of interest. Note that CORE will have S/N ≥ 5 in 14 different frequency bands. Also, by combining all frequencies, CORE will have similar S/N in TT, $TE + ET$ and EE. 136

5.2 Average values of $\sqrt{|\Delta\chi^2|}\,\mathrm{sign}(\Delta\chi^2)$ from a Monte Carlo simulation at $N_{\rm side} = 64$, full-sky coverage, adopting perfect foreground subtraction and calibration, and considering each of the 19 frequency channels. 151

5.3 The same as in Table 5.2, but considering all 171 independent combinations of pairs of different frequency channels. 152

5.4 The same as in Table 5.2, but considering each of the 19 frequency channels independently and all 171 independent combinations of pairs of different frequency channels. 153

5.5 Average values of $\sqrt{|\Delta\chi^2|}\,\mathrm{sign}(\Delta\chi^2)$ from a Monte Carlo simulation at $N_{\rm side} = 64$, with full-sky coverage, adopting $E_{\rm for} = 10^{-2}$ and $E_{\rm cal} = 10^{-4}$, and considering each of the 19 frequency channels. 155

5.6 The same as in Table 5.5, but considering all 171 independent combinations of pairs of different frequency channels. 156

5.7 The same as in Table 5.5, but considering each of the 19 frequency channels independently and all 171 independent combinations of pairs of different frequency channels. 157

5.8 Values of $\sqrt{|\Delta\chi^2|}\,\mathrm{sign}(\Delta\chi^2)$ for a single realization at $N_{\rm side} = 64$, using the *Planck* mask-76 extended to exclude regions at $|b| \leq 30^\circ$. I adopt $E_{\rm for} = 10^{-2}$ and $E_{\rm cal} = 10^{-4}$, and consider each of the 19 frequency channels and all 171 independent combinations of pairs of different frequencies. 158

5.9 Predicted improvement in the recovery of the distortion parameters discussed in the text with respect to FIRAS for different calibration and foreground residual assumptions. This table summarizes the results derived with approach (c). "P06" stands for the *Planck* common mask, while "P06ext" is the extended P06 mask. When not explicitly stated, all values refer to $E_{\rm cal}$ and $E_{\rm for}$ at $N_{\rm side} = 64$. 161

5.10 68 % confidence levels of the parameters A, b_0, l_0, and T_0 from Fig. 5.15. . . . 166

5.11 68 % confidence level of the parameters A, b_0, l_0, and T_0 at 60, 100, 145 and 220 GHz (see Fig. 5.16 for the likelihoods at 100 and 220 GHz). 168

5.12 68 % confidence level of the parameters A, b_0, l_0, and T_0 of Fig. 5.17. 168

5.13 Rms values of $\sqrt{|\Delta\chi^2|}\ \mathrm{sign}(\Delta\chi^2)$ from a Monte Carlo simulation at $N_{\mathrm{side}} = 64$, full sky, adopting perfect foreground subtraction and calibration, and considering each of the 19 frequency channels. 169

5.14 The same as in Table 5.13, but considering all 171 independent combinations of pairs of different frequency channels. 170

5.15 The same as in Table 5.13, but considering each of the 19 frequency channels and all 171 independent combinations of pairs of different frequency channels. . 171

5.16 Values of $\sqrt{|\Delta\chi^2|}\ \mathrm{sign}(\Delta\chi^2)$ for a single realization at $N_{\mathrm{side}} = 512$, for the full sky, adopting perfect foreground subtraction and calibration, and considering each of the 19 frequency channels and all 171 independent combinations of pairs of different frequencies. 172

5.17 Rms values of $\sqrt{|\Delta\chi^2|}\ \mathrm{sign}(\Delta\chi^2)$ from a Monte Carlo simulation at $N_{\mathrm{side}} = 64$, full sky, adopting $E_{\mathrm{for}} = 10^{-2}$ and $E_{\mathrm{cal}} = 10^{-4}$, and considering each of the 19 frequency channels. 173

5.18 The same as in Table 5.17, but considering all 171 independent combinations of pairs of different frequency channels. 174

5.19 The same as in Table 5.17, but considering each of the 19 frequency channels and all 171 independent combinations of pairs of different frequency channels. . 175

5.20 Values of $\sqrt{|\Delta\chi^2|}\ \mathrm{sign}(\Delta\chi^2)$ for a single realization at $N_{\mathrm{side}} = 64$, using *Planck* mask-76 extended to exclude regions at $|b| \leq 30°$. I adopt $E_{\mathrm{for}} = 10^{-3}$ and $E_{\mathrm{cal}} = 10^{-4}$, and consider each of the 19 frequency channels and all 171 independent combinations of pairs of different frequencies. 176

5.21 Values of $\sqrt{|\Delta\chi^2|}\ \mathrm{sign}(\Delta\chi^2)$ for a single realization at $N_{\mathrm{side}} = 64$, using *Planck* mask-76 extended to exclude regions at $|b| \leq 30°$. I adopt $E_{\mathrm{for}} = 10^{-2}$ and $E_{\mathrm{cal}} = 10^{-3}$ at $\nu \leq 295\,\mathrm{GHz}$ and $E_{\mathrm{cal}} = 10^{-2}$ at $\nu \geq 340\,\mathrm{GHz}$, and consider each of the 19 frequency channels and all 171 independent combinations of pairs of different frequencies. 177

5.22 Values of $\sqrt{|\Delta\chi^2|}\ \mathrm{sign}(\Delta\chi^2)$ for a single realization at $N_{\mathrm{side}} = 64$, using *Planck* mask-76 extended to exclude regions at $|b| \leq 30°$. I adopt $E_{\mathrm{for}} = 10^{-3}$ and $E_{\mathrm{cal}} = 10^{-3}$ at $\nu \leq 295\,\mathrm{GHz}$ and $E_{\mathrm{cal}} = 10^{-2}$ at $\nu \geq 340\,\mathrm{GHz}$, and consider each of the 19 frequency channels and all 171 independent combinations of pairs of different frequencies. 178

5.23 Values of $\sqrt{|\Delta\chi^2|}\ \mathrm{sign}(\Delta\chi^2)$ for a single realization at $N_{\mathrm{side}} = 256$, using *Planck* mask-76 extended to exclude regions at $|b| \leq 30°$. I adopt $E_{\mathrm{for}} = 10^{-3}$ and $E_{\mathrm{cal}} = 10^{-3}$ at $\nu \leq 295\,\mathrm{GHz}$ and $E_{\mathrm{cal}} = 10^{-2}$ at $\nu \geq 340\,\mathrm{GHz}$, and consider each of the 19 frequency channels and all 171 independent combinations of pairs of different frequencies. 179

1

Microwaves space observations: from *Planck* legacy to the future

1.1 Introduction

Since the discovery of the CMB in 1964, and in particular in the past two decades, the improved measurements in temperature fluctuations achieved an unprecedented accuracy in constraining the majority of the cosmological parameters values. The CMB is one of the observational evidence of the Hot Big Bang theory together with the cosmic expansion (88) and the primordial nucleosynthesis (245), and represents a powerful tool of investigation in a cosmological context. The presence of small CMB temperature anisotropies would have been, as realized, the seeds for galaxy formation, hence, a direct probe of the formation and evolution of the structures we observe today (89).

In early 1990's the COsmic Background Explorer (COBE) satellite, a NASA mission aimed at the exploitation of the microwave background absolute temperature, inaugurated the "precision cosmology" era determining the CMB spectrum temperature of 2.725 K (92, 195) and then discovering the CMB temperature fluctuations of few tens of μK on angular scales larger than 7°, the so called anisotropies.

Already in 1990, (109) argued that a positive cosmological constant is necessary to explain new observations of very large scale structures in a spatially flat cosmology. However, it was only ten years later that the idea of a ΛCDM Universe, driven by a dark energy component compatible with a standard cosmological constant, took place owing to the discovery of the recent cosmic acceleration through SNIa observations and the flatness of the Universe thanks to the

Balloon Observations Of Milimetric Extragalactic Radiation and Geophysics (BOOMERanG) CMB anisotropy experiment. In this Universe, CDM governed expansion until a recent epoch, while now it is dominated by a cosmological constant, also able to account for the lack of fluctuations in the CMB and the large number of certain kinds of objects found at high redshift. Soon after this mission, the Degree Angular Scale Interferometer (DASI) experiment probed for the first time the polarization anisotropies. In the following years, the Wilkinson Microwave Anisotropy Probe (WMAP) sensitively improved the determination of cosmological parameters through its detailed all sky anisotropy maps.

The great amount of available and forthcoming data coming from balloon-borne experiments, such as the mentioned NASA COBE and WMAP satellites, to recent space borne experiments, as the *Planck* mission up to future microwaves (and radio) projects will allow to explore the key aspects of cosmology and fundamental physics in the coming decades.

Indeed, the wealth of information encoded in the CMB has significantly helped cosmology to turn into a precision science, and allowed us to describe cosmic evolution starting from its very primordial stages. The linear polarization pattern of CMB anisotropies (164) has been generated in two distinct cosmological epochs. The recombination era ($z \simeq 1100$) during which, as the Universe expanded and cooled, the diffusion length of photons in an increasingly neutral medium became large enough to reveal the quadrupole moment of the local anisotropy pattern at the last scattering surface (LSS). The Universe then became almost neutral and transparent to radiation, since Thomson scattering, the main physical process involved, was no longer efficient in coupling matter and radiation. Much later, during the early phases of galaxy and star formation, photoionizing radiation able to escape from the bound structures was injected in the intergalactic medium that became ionized again (reionization epoch). During this period, free electrons interacted, through Thomson scattering, with CMB photons once more. Owing to the size of the Hubble horizon at reionization, this new contribution is only seen at large angular scales, as a characteristic bump at low multipoles ($\ell \lesssim 10$) in the pure polarization CMB spectra, as well as in the temperature to polarization correlation.

1.2 *Planck* Mission: instrument and systematics

Planck[1] is a project of the European Space Agency (ESA) and a third generation mission

[1] *Planck* hosted instruments provided by two scientific Consortia funded by ESA member states (in particular the lead countries: France and Italy) with contributions from NASA (USA), and telescope reflectors provided in a

in terms of precision cosmology, designed for the CMB anisotropy analysis. The satellite, launched in 2009, was equipped with a Gregorian dual reflector telescope of 1.5m diameter, whose focal plane were able to collect the microwave photons owing to two wide band cooled receiver arrays, the Low Frequency Instruments (LFI) made up of radiometers operative at 20 K, and the High Frequency Instruments (HFI) composed of bolometers working at 100 mK. Together, the two instruments scanned the sky in 9 frequency bands, performing respectively 8 and 5 nearly all sky surveys: LFI at 30, 44 and 70 GHz and HFI at 100, 143, 217, 353, 545, 857 GHz, with telescope optical axis pointing at 85° from the spin axis (250, 318). It orbited around the L2 Lagrangian point, scanning the sky while spinning at 1 rpm in almost great circles with a full width half maximum (FWHM) resolution ranging from 33.3′ to 4.3′ from 30 GHz to 857 GHz, and a final sensitivity per FWHM^2 resolution element spanning $\sim 2 - 14\ \mu$K/K in terms of $\delta T/T$ for frequencies $\nu \leq 353$GHz.

The *Planck* instruments attained maps of CMB anisotropies on the whole sky with an unprecedented sensitivity and resolution, whose scientific exploitation has been based on the combined LFI and HFI data analysis. Hence, besides the so called cosmic variance limit, an intrinsic error which has an impact on, primarily, the low multipoles, the main goal of *Planck* has been the accurate measure of the CMB temperature fluctuations.

To look at this extremely faint signal, it is crucial the almost optimal control of systematics effects, one of the main task in data reduction and interpretation (211, 251, 270, 350). They can be additive or multiplicative spurious contributions independent of the sky signal, or coupled with the sky signal and related with the observational strategy. Furthermore, in the microwaves, different kinds of astrophysical contamination emissions can, in principle, veil the cosmological information. This foreground signal can be diffuse, coming from the Solar System and from the Galaxy, or discrete, due to extragalactic sources at various cosmic distances.

Table 1.1 lists the main systematic effects in *Planck* according to their source and summarizes their control and residual impact on science.

Tables 1.2 and 1.3 report the main characteristics of LFI and HFI. Fig. 1.1 shows potential residuals for the EE auto-power spectra of systematic effects for HFI. The level of systematics effects has been in line with expectations, therefore confirmed the belief of a full science exploitation owing to the CMB signal.

collaboration between ESA and a scientific Consortium led and funded by Denmark.

Category	Effect	Notes – Control/Removal
Effects coupled with sky		
	Main beam distortions	Relevant in both temperature and polarization maps. Accounted for in window function for angular power spectrum estimation.
	Nearly-lobes pickup	Optical response at angles < 5 degrees from the main beam. Main effect from Galaxy and point sources. Accounted through simulations.
	Side-lobes pickup	Galaxy and CMB dipole pickup by main and sub-reflector spillovers. Small effect on temperature maps, relevant effect for polarization study, particularly at large angular scales. Accounted through simulations.
	Polarization angle uncertainty	Uncertainty in the polarization angle in-flight measurement.
	Bandpass mismatch	Affects primarily radiometric detectors. Negligible impact on temperature. Corrected in polarization at map level exploiting source measurements (e.g. Crab Nebula).
	Imperfect photometric calibration	Optics, receiver noise properties changes, and other non-idealities. Adaptive smoothing algorithm using beam characterization, 4-K reference load voltage output, temperature sensor data.
	Pointing	Uncertainties in pointing reconstruction, thermal changes affecting focal plane geometry. Small impact on anisotropy measurements.
	Receiver time response	In HFI, bolometer memory is coupled with beam shape. Filters, window function.
Detectors		
	Cosmic ray hits	Affect bolometric detectors. Timelines cleaning via template fitting.
	$1/f$-type noise	Affects radiometric and bolometric detectors. In LFI, $1/f$ contribution limited to max 3% by differential measurement strategy. De-striping/map-making algorithms.
	Orthomode transducer cross-polarization	In LFI, imperfect polarization separation. Negligible impact.
Electronics		
	1-Hz spikes	Affects LFI data. Removed from timelines by template fitting.
	Analogue-to-digital converter nonlinearity	Reduced/removed through template fitting.
Thermal*		
	300K fluctuations	In principle affect both instruments. Inherent hardware stability is compliant with scientific requirements.
	20K fluctuations	Affect mainly LFI. Inherent hardware stability is compliant with scientific requirements.
	4K fluctuations	Affect both instruments. Inherent hardware stability is compliant with scientific requirements.

⋆ A combination of differential measurement strategy (specifically for LFI) with calibration and de-striping further reduce the effect.

Table 1.1: Main systematic effects in *Planck* data.

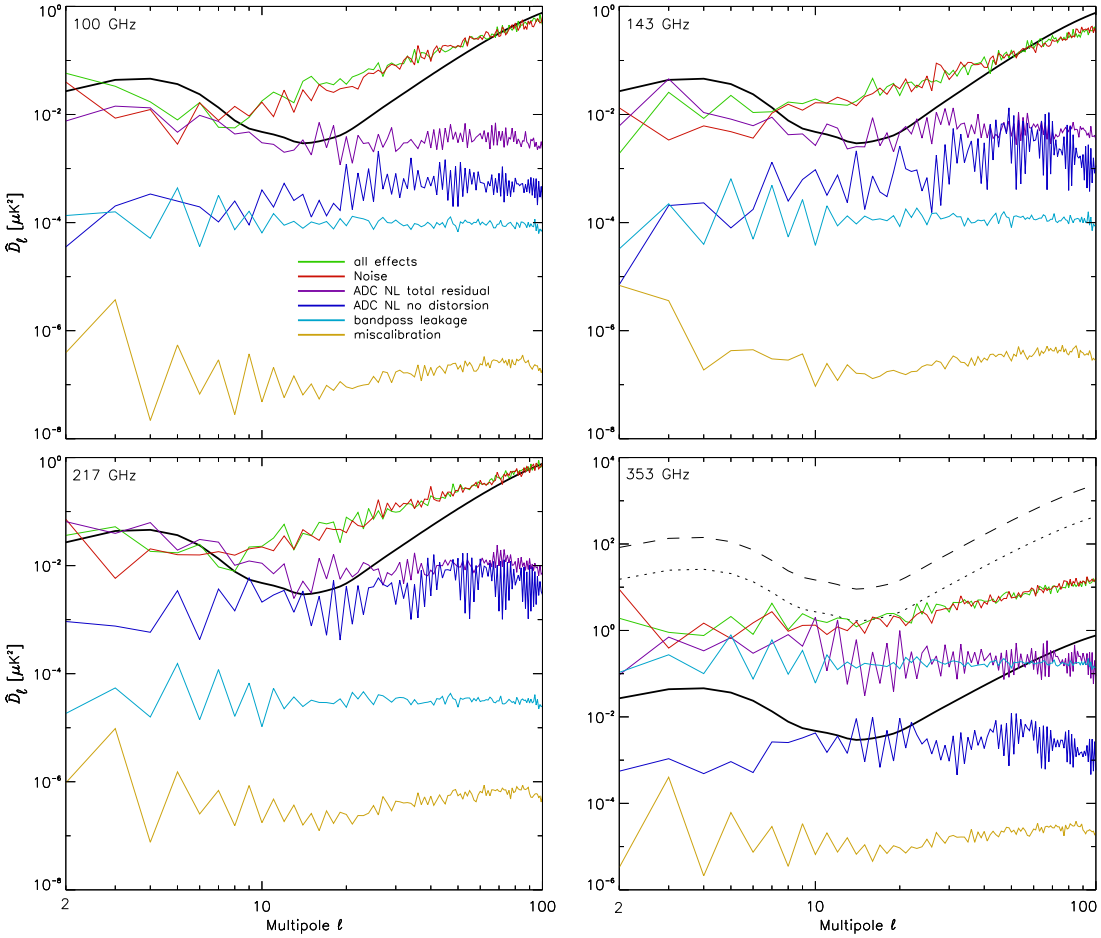

Figure 1.1: Residual *EE* auto-power spectra of systematic effects from the HFI pre-2016 E2E (end-to-end) simulations computed on 50 % of the sky (colours specified in the top left panel apply to all panels). The purple line (ADC NL total residual) shows the sum of all effects associated with ADC nonlinearity. The dark blue line (ADC NL - Analogue-to-digital converter nonlinearity - no distortion) shows the level without the dominant dipole distortion. The plots show also the F-*EE* fiducial model from best-fit *Planck* 2015 cosmological parameter (252) (black curves). The 100-GHz and 143-GHz model scaled to 353 GHz with a dust SED is shown as dashed and dotted lines, respectively. From (262).

Characteristic	Frequency band		
	30 GHz	44 GHz	70 GHz
Centre frequency [GHz]	28.4	44.1	70.4
Effective beam FWHM[a] [arcmin]	32.29	27.00	13.21
Effective beam ellipticity[a]	1.32	1.04	1.22
Temperature noise (1 deg)[b] [μK_{CMB}]	2.5	2.7	3.5
Polarization noise (1 deg)[b] [μK_{CMB}]	3.5	4.0	5.0
Overall calibration uncertainty[c] [%]	0.35	0.26	0.20
Systematic effects uncertainty in Stokes I^d [μK_{CMB}]	0.19	0.39	0.40
Systematic effects uncertainty in Stokes Q^d [μK_{CMB}]	0.20	0.23	0.45
Systematic effects uncertainty in Stokes U^d [μK_{CMB}]	0.40	0.45	0.44

Table 1.2: Main characteristics of LFI full mission maps. [a] Calculated from the main beam solid angle of the effective beam, Ω_{eff} = mean(Ω). These values are used in the source extraction pipeline. [b] Noise rms computed after smoothing to 1 deg. [c] Sum of the error determined from the absolute and relative calibration. [d] Estimated rms values over the full sky and after full mission integration. Not included here are gain reconstruction uncertainties, estimated to be of order 0.1%. From (237).

1.3 Astrophysical foregrounds

The analysis of the microwave to sub-mm sky plays a crucial role not only for the cosmological information contained in the CMB but also for the wealth of astrophysical information it provides. The *Planck* Collaboration has recently released maps in temperature at nine frequency bands between 30 and 857 GHz and seven bands in polarization up to 353 GHz, reprocessing the data from the Low and High Frequency Instruments. To extract relatively bright variable sources, the diffuse Zodiacal Light Emission and solar system bodies, a comparison between data taken at different times or maps derived from different surveys is performed, since signal dependence on time and/or on the relative observer-source or -interplanetary dust cloud positions. The separation of all the other astrophysical emissions and of CMB anisotropies is carried out on maps averaged over advantageous sets of surveys applying different point-like sources and diffuse emissions dedicated filters, possibly complemented by external catalogs, and algorithms exploiting frequency dependence and angular correlation, where feasible in

Characteristic	Reference frequency ν [GHz]						
	100	143	217	353	545	857	Notes
Number of bolometers	8	11	12	12	3	4	*a*1
Effective beam FWHM$_1$ [arcmin]	9.68	7.30	5.02	4.94	4.83	4.64	*b*1
Effective beam FWHM$_2$ [arcmin]	9.66	7.22	4.90	4.92	4.67	4.22	*b*2
Effective beam ellipticity ε	1.186	1.040	1.169	1.166	1.137	1.336	*b*3
Noise per beam solid angle [μK$_{\rm CMB}$]	7.5	4.3	8.7	29.7	–	–	*c*1
[kJy sr^{-1}]	–	–	–	–	9.1	8.8	*c*1
Temperature noise [μK$_{\rm CMB}$ deg]	1.29	0.55	0.78	2.56	–	–	*c*2
[kJy sr^{-1} deg]	–	–	–	–	0.78	0.72	*c*2
Polarization noise [μK$_{\rm CMB}$ deg]	1.96	1.17	1.75	7.31	–	–	*c*3
Calibration accuracy [%]	0.09	0.07	0.16	0.78	1.1(+5)	1.4(+5)	*d*
CIB monopole prediction [MJy/sr]	0.0030	0.0079	0.033	0.13	0.35	0.64	*e*
Zodiacal light level correction [K$_{\rm CMB}$]	4.3×10^{-7}	9.4×10^{-7}	3.8×10^{-6}	3.4×10^{-5}	–	–	*e*2
[MJy/sr]	–	–	–	–	0.04	0.12	*e*2

Table 1.3: Main characteristics of HFI full mission maps. [a1] Number of bolometers whose data were used in producing the channel map. [b1] FWHM of the Gaussian whose solid angle is equivalent to that of the effective beams. [b2] FWHM of the elliptical Gaussian fit. [b3] Ratio of the major to minor axis of the bestfit Gaussian averaged over the full sky. [c1] Estimate of the noise per beam solid angle, as given in *b1*. [c2] Estimate of the noise in intensity scaled to 1 deg assuming that the noise is white. [c3] Estimate of the noise in polarization scaled to 1 deg assuming that the noise is white. [d] Calibration accuracy (at 545 and 857GHz, the 5% accounts for the model uncertainty). [e] According to the (34) model, whose uncertainty is estimated to be at the 20% level (also for constant νI_ν). [e2] Zero level correction to be applied on zodiacal light corrected maps. From (237).

combination with templates at other frequency bands.

1.3.1 Catalogs of sources and clusters of galaxies

The Second *Planck* Catalogue of Compact Sources (PCCS2), both Galactic and extragalactic, consists of (many tens of thousands) sources detected in single-frequency maps, combined from all *Planck* mission data over the entire sky (see Fig. 1.2).

Compact sources detected at lower (higher) frequencies are assigned to the PCCS2 (PCCS2 or PCCS2E sub-catalogues, depending on their sky positions). The PCCS2 covers most of the sky and allows to extract subsamples at higher reliabilities than the target 80% integral relia-

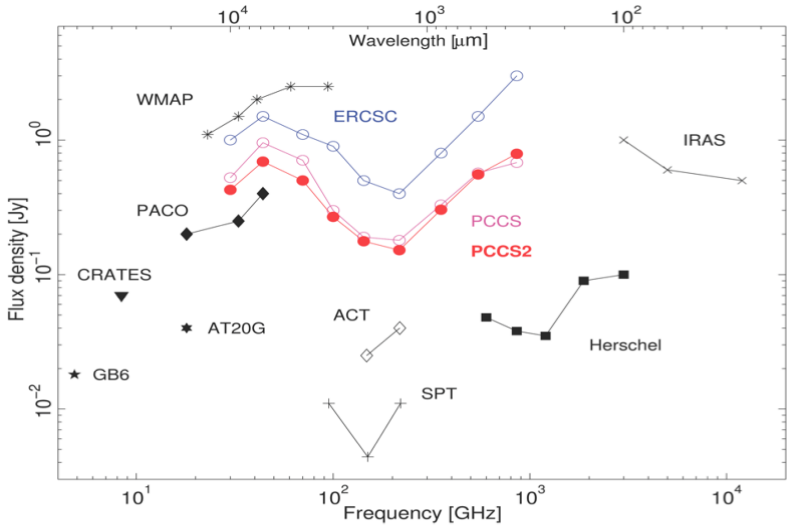

Figure 1.2: Sensitivity (the flux density at 90% completeness) of the PCCS2, compared with PCCS, ERCSC, WMAP and others. For the LFI channels, the sensitivities refer to the full sky. For the HFI channels, the 90% completeness limits plotted for the PCCS were evaluated in a selected extragalactic zone; the regions of sky to which the 90% completeness limits apply are similar but not identical to those of the PCCS2. From (244).

bility of the catalogue. The PCCS2E contains sources whose detection reliability is affected by diffuse emission. Both catalogs include polarized flux densities, or upper limits, and orientation angles at frequencies 30 GHz $\leq \nu \leq$ 353 GHz for many hundreds sources. The spectral index proves the source nature: the low or high frequency channels are dominated by synchrotron or dusty galaxies sources. A significant steepening at $\nu \sim 50$ GHz is found in blazar spectra and the bright tail of extragalactic source counts at high frequency (at least for $\nu \leq 217$ GHz) is dominated by synchrotron emitters, not by dusty galaxies.

In Chapter 3, I will present an original analysis of the polarization properties of extragalactic sources at *Planck* frequencies.

The Second *Planck* catalog of SZ galaxy clusters (PSZ2), with 1653 detections, is the largest SZ-selected sample and the deepest all-sky catalogue of galaxy clusters. The objects have been analyzed with observations in other wavebands (radio to IR, optical and X-rays) and 1203 of them have counterparts in datasets external to *Planck*. A population of low-redshift X-ray under-luminous clusters has been revealed by SZ selection. They appear in optical and SZ surveys with consistent mass properties, but are almost absent in ROSAT X-ray selected samples. Fig. 1.3 compares PSZ2 with deeper SZ catalogs obtained with South Pole and

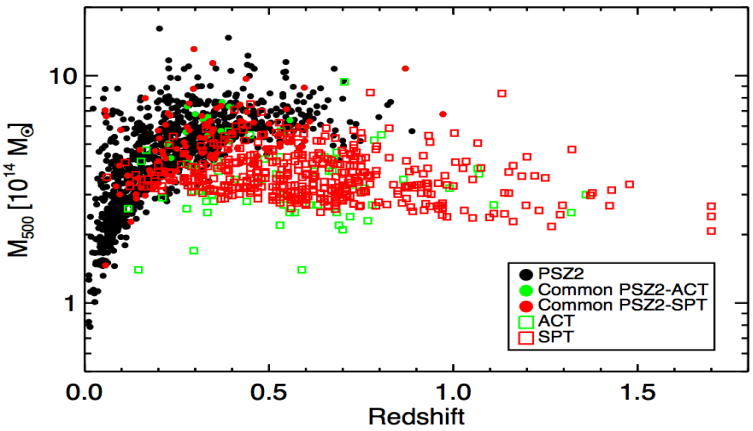

Figure 1.3: Distribution of PSZ2 clusters with associated redshift in the mass-redshift (M500 – z) plane compared to SPT and ACT catalogues. Black circles: PSZ2 clusters; red (green) filled circles: common SPT/PSZ2 (ACT/PSZ2) clusters. Red (green) empty squares: the remaining SPT (ACT) clusters not detected by *Planck*. See also the text. From (258).

Atacama Cosmology Telescopes (SPT and ACT) on selected areas. Microwave and X-ray cluster data have been jointly used to independently constrain cosmological parameters. In particular, the evolution of galaxy cluster abundance in mass and redshift set constraints on matter density fluctuation normalization, mean matter density, dark energy density, its equation of state and on extensions of the minimal cosmological model, including e.g. massive neutrinos and modified gravity.

Integrated information on cluster physics and cosmological evolution comes from the Comptonization parameter, y, fluctuations over all-sky *Planck* maps (250) other than observing it as SZ effect towards specific clusters. The analysis of sub-millimeter/far-IR background fluctuations, carried out mainly in selected *Planck* areas, proves high-z galaxy evolution and star formation history (247). These themes are also probed by large scale CMB polarization, sensitive to cosmic reionization history (237, 326) related to structure and star formation/evolution and their production of ionizing photons in the intergalactic medium.

1.3.2 Galactic diffuse components

In *Planck* data, the component separation between astrophysical diffuse objects and CMB anisotropies has been carried out with four different algorithms at each frequency band. Two of them, SEVEM and COMMANDER, are designed in real space while NILC in real and harmonic (needlet) space and SMICA in harmonic or needlet domain. The resultant CMB cleaned

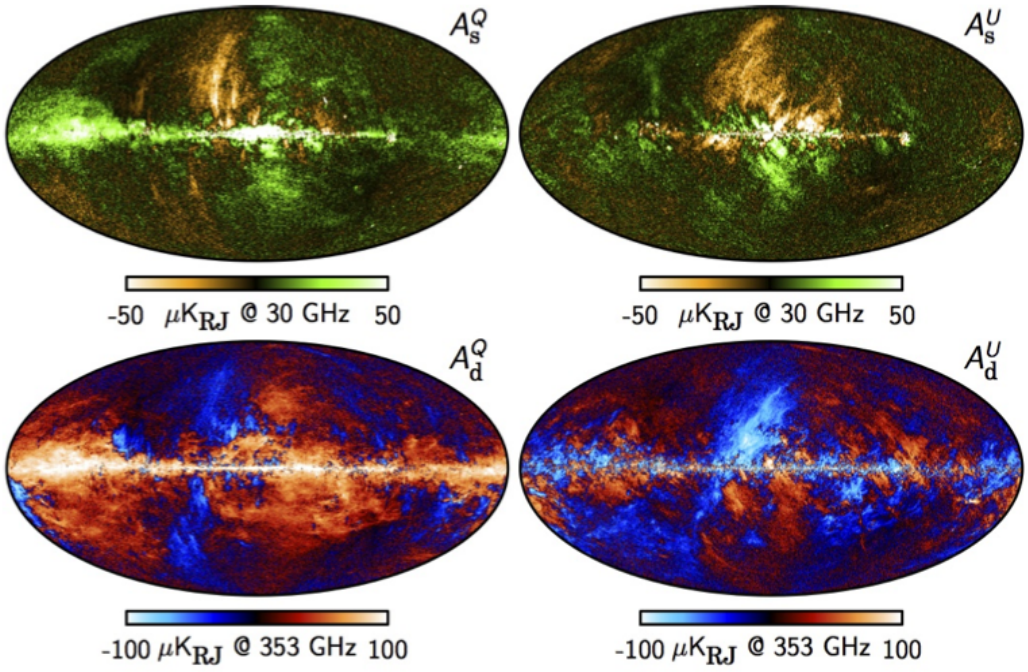

Figure 1.4: Stokes Q and U polarization parameters for the synchrotron at 30 GHz (upper line) and thermal dust at 353 GHz (bottom line). From (237).

maps agree strikingly but the commander method revealed to be remarkably appropriate to describe the astrophysical emissions across the sky, mostly because of its a priori knowledge of the parameters able to characterize the foregrounds through real space Bayesian methods.

In temperature, *Planck* and WMAP (30) data were merged together with 408 MHz (341) maps in oder to extract, besides CMB, synchrotron, spinning and thermal dust, free free and CO emissions. In polarization, only synchrotron and thermal dust emissions have been separated from the other diffuse astrophysical components and are illustrated in Fig. 1.4 in terms of Q and U Stokes parameters maps.

In a region close to the Galactic centre at low frequencies, the *Planck* community revealed the presence of a remarkable foreground emission, the so called “haze”, whose nature is still partly unknown.

From the various source maps it is possible to quantify the contribution of each component to sky fluctuations, displayed in Fig. 1.5. A remarkable result of *Planck* is the assessment of the microwave sky complexity, calling for even more frequency channels for future CMB projects aimed at precise characterization of all components and of tiny CMB polarization fea-

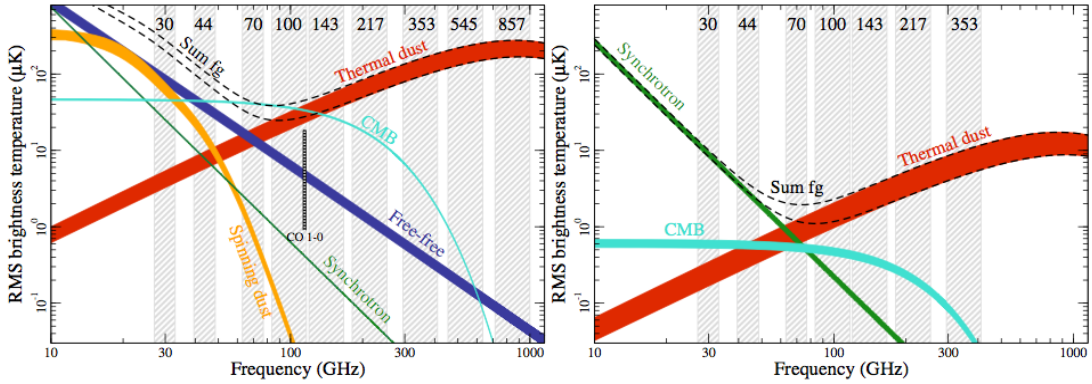

Figure 1.5: Brightness temperature rms as a function of frequency and component for temperature (left), where each component is smoothed to an angular resolution of 1° FWHM and the lower and upper edges of each line are defined by masks covering respectively 81% and 93% of the sky, and polarization (right), where the corresponding smoothing scale is 40′ and the sky fractions are 73% and 93%. From (237).

tures, such as primordial B-modes. Note also the change of paradigm with respect to WMAP results in the relative weights of the various components. In temperature, synchrotron emission fluctuations are less than those of both free-free and spinning dust emissions around 30 GHz. The angular power spectrum (APS) of synchrotron and dust polarized emissions has been properly characterized on various wide sky areas (238) and the synchrotron frequency behavior has been studied as function of the Galactic latitude (254). Polarized emission from Galactic dust, the main foreground above 70 GHz, is important (and sometimes underestimated in previous analyses) essentially everywhere in the sky. *Planck* maps provided new insights into interstellar dust physics and a precise determination of the contamination level in the CMB APS (241) for polarization experiments, allowing for a proper analysis of BICEP2 and *Keck* array observations (36).

Moreover, taking into account different sky areas, it has been possible an accurate determination of synchrotron and dust polarized emissions APS (238), where the synchrotron was regarded as a function of the Galactic latitude (243). At frequencies $\nu > 70$ GHz, the Galactic polarized dust is the main foreground contamination. Fig. 1.5 evidences the brightness temperature rms as a function of frequency and component for temperature and polarization.

1.4 *Planck* cosmological implications

Beyond this investigation, latest measurements of CMB in temperature and polarization from *Planck* satellite (252), complemented at smaller scales by recent ground-based experiments (36, 94, 137, 322) and combined with other cosmological information coming from e.g. type-Ia supernovae, galaxy and galaxy cluster surveys, have reached high precision in estimating all the parameters that describe the current so-called standard cosmological model. Far from representing a fully, physically exhaustive interpretation of the Universe properties, the cosmological constant plus cold dark matter (ΛCDM) model phenomenologically describes reasonably well existing data with a simple set of six parameters. The integrated Sachs-Wolfe effect, discussed in Sect. 1.4.1, represents a remarkable example of the success of current cosmology, since a such intrinsically weak predicted signal is clearly recognized in two classical cosmological probes, like CMB anisotropies and galaxy surveys, and in their cross-correlations. Looking at fine signatures in the CMB it is possible to derive more hints on early Universe and inflationary paradigm as well as to carry out a sort of laboratory tests to constrain particle and fundamental physics.

1.4.1 The Integrated Sachs-Wolfe effect

The late integrated Sachs-Wolfe (ISW) effect (200, 278, 289) is a secondary anisotropy in the cosmic microwave background (CMB), which is caused by the interaction of CMB photons with the time-dependent gravitational potential of the evolving cosmic large-scale structure (LSS). It can be generated under several scenarios affecting the late evolution of the structures: a cosmological constant, dark energy (DE) (83), modified gravity (161), or spatial curvature (173).

Precisely, the early ISW is generated after recombination (since the energy density of relativistic matter is still considerable at that time): it adds in phase with the Sachs-Wolfe primary anisotropy, increasing the height of the first acoustic peaks. Besides, the effect on the APS, C_ℓ (being ℓ the multipole of the spherical harmonic expansion), is suppressed by the factor $\rho^2_{\rm rad}(\eta_{\rm rec})/\rho^2_{\rm m}(\eta_{\rm rec})$: increasing the radiation energy density with respect to that of matter near recombination will give a larger early ISW effect. The late ISW effect is active at more recent time, when dark energy starts to play a role and the gravitational potentials are decreasing, focusing on scales corresponding to galaxy clusters, where gravitational perturbations start growing and CMB photons get redshifted by the time-dependent gravitational potentials. The

potentials causing the late ISW also give rise to the weak lensing distortions which is the interplay between these two effects results in a non-Gaussian correlation between small and large angular scales, which is encoded in the lensing-induced bispectrum.

The optimal detection (83) of the ISW effect is made by the cross-correlation of the CMB temperature anisotropies with tracers of the gravitational potential, like, for instance, galaxy catalogues. The first detection (46) was made using WMAP data and radio and X-ray galaxy catalogues. After this work, several analyses followed providing additional evidence of the ISW detection using different surveys and correlation techniques. The ISW signal is very weak (an ideal LSS tracer could provide a detection of up to $\approx 8\,\sigma$), and, therefore, its capability to constrain cosmological parameters, is very limited. Nevertheless, using the ISW signal alone it is possible to constrain some cosmological parameters, by fixing the remaining ones to their standard value, thus helping to confirm the standard ΛCDM model. Examples of these determinations are, for instance, (see e.g. the estimation of the DE density parameter (255) $\Omega_\Lambda \approx 0.67$, with an error of about 20%; the compatibility of the DE equation of state parameter with the expected value for a ΛCDM scenario (333) or the setting of upper limits on spatial flatness of a few per cent (190)).

1.4.2 The ISW probed through the CMB-LSS cross-correlation

The four CMB maps (239) produced by *Planck* (`COMMANDER`, `NILC`, `SEVEM`, `SMICA`) have been cross-correlated with several tracers of the LSS. In the first release, the NRAO VLA Sky Survey (NVSS) radio-galaxy catalogue, the photometric luminous galaxy (SDSS-CMASS/LOWZ), and the photometrically-selected galaxies (SDSS-MphG) from the Sloan Digital Sky Survey (SDSS) were considered. Two additional catalogues from the Wide-Field Infrared Survey Explorer (WISE) were added to the analysis of the second release: one based on star-forming galaxies (WISE-GAL), and another one based on active galactic nuclei (WISE-AGN). Considering the full cross-correlations of the CMB with all the LSS tracers, the latest results provided a total ISW detection of around $3\,\sigma$, as expected for the standard ΛCDM model. The NVSS catalogue already provides by itself a similar detection level.

The most novel result provided by *Planck* was its capability to provide a detection of the ISW without relying on external tracers of the LSS, thanks to its reliable estimation of the gravitational potential through the lensing suffered by the CMB photons (253). The cross-correlation of this map with the CMB one, or, equivalently, the specific shape of the ISW-

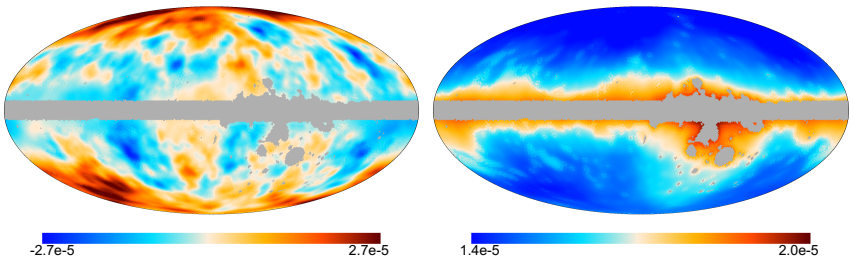

Figure 1.6: Map (thermodynamic temperature in K) of the recovered ISW anisotropies (left) and its corresponding estimated error per pixel (right), from the combination of the *Planck* SEVEM CMB map and all the LSS tracers. The error map structure is determined by the sky coverage of the different surveys. The total signal-to-noise of the ISW map cannot exceed, obviously, a value of ≈ 4. The signal-to-noise is higher near the Galactic poles, with values of ≈ 2. From (51).

lensing bispectrum, reported a detection of the ISW at around $\approx 3\,\sigma$. When all the LSS tracers are combined, the total ISW detection is $\approx 4\,\sigma$, also in good agreement with the ΛCDM model.

Assuming the standard ΛCDM model, the statistical ISW captured in the CMB-LSS cross-correlation can be used to estimate a map of the ISW anisotropies caused by the gravitational potential traced by each of the LSS probes (21). Fig. 1.6 shows the ISW fluctuation maps obtained from the full cross-correlation of the *Planck* SEVEM CMB map with NVSS, WISE-AGN, WISE-GAL, SDSS-CMASS/LOWZ, SDSS-MphG, and the *Planck* lensing LSS tracers.

All these results were obtained without using CMB polarization information (except for the estimation of the *Planck* lensing map). In principle, including polarization could increase the ISW detection (129) around a 15%, however, the current CMB polarization data from *Planck* is high-pass filtered at the largest angular scales ($\gtrsim 5°$), which are the most important ones in this context. Including the large scale polarization is, perhaps, the most important remaining aspect within the context of the ISW study, at least, from the CMB side. On the other side, future galaxy surveys like *Euclid* (188), J-PAS (29), or LSST (193) among others, will provide accurate galaxy catalogues, probing very large volumes, allowing to perform, for instance, a tomographic ISW detection.

A complementary approach consists in stacking the CMB fluctuations in the position of known structures, such as voids and clusters, as done initially on WMAP data (146) using a catalogue (GR08) of super-structures from SDSS. An anomalous ISW signal, incompatible with the standard ΛCDM model was found, confirmed in the *Planck* analyses, showing that the intensity of the detected signal ($\approx -11\,\mu$K for voids, and $\approx +8.5\,\mu$K for clusters) and the

scale at which that signal is maximum ($\approx 3.5^\circ$ for voids, and $\approx 4.5^\circ$ for clusters) are, indeed, unexpected.

At these scales, the current CMB *Planck* polarization map still retains certain signal, despite the high-pass filtering and, therefore, it can be used to test further the nature of this anomalous signal. The key point is that, if this signal is caused by the ISW effect, and, therefore, originated by a gravitational secondary CMB anisotropy, a negligible contribution of the CMB polarization is expected. In fact, no associated polarization is found in *Planck* data, although the diminishing of the signal caused by the high-pass filtering limits any strong conclusion. Anyway, the current polarization data are not in contradiction with assuming that the emission coming from these GR08 structures provides an anomalous ISW signal. Studying the stacked fluctuations of the *Planck* lensing map on the GR08 positions also supports this hypothesis. Indeed, at least for the voids, a clear correlation between the lensing gravitational potential and the position of the super-structures is found.

1.4.3 Parametrization of early and late ISW and data analysis

The ISW amplitude can be parametrized in terms of $A_{e\mathrm{ISW}}$ and $A_{l\mathrm{ISW}}$, which rescale the contribution of the ISW to the temperature anisotropies. A Markov-chain Monte-Carlo (MCMC) analysis making use of the publicly available code `cosmomc` (189) with a baseline standard ΛCDM model was performed imposing flat priors on the parameters (56). It was also performed a check of the impact of a Gaussian prior $A_{l\mathrm{ISW}} = 1.00 \pm 0.25$, denoted by the "prior" label in the following plots and tables, consistent with the 68% confidence level (C.L.) bounds on the same parameter from the estimation of the ISW-lensing bispectrum induced on the Gaussian CMB anisotropies which has been obtained by cross-correlating the *Planck* CMB maps with the *Planck* map of the lensing potential. The analysis was based on various datasets, in particular: the high-ℓ *Planck* temperature and temperature+polarization APS in the range $30 \leq \ell < 2500$ (hereafter TT and TT, TE, EE, respectively) in combination with the low-ℓ *Planck* temperature and polarization APS in the range $2 \leq \ell < 30$ (lowP); the WMAP APS including both temperature and polarization up to $\ell = 1200$.

Planck TT + lowP data provide tighter constraints than WMAP on the early ISW ($A_{e\mathrm{ISW}} = 1.064^{+0.042}_{-0.043}$ vs. $A_{e\mathrm{ISW}} = 1.007^{+0.056}_{-0.058}$ at 68% C.L.), and present a 1σ evidence of $A_{e\mathrm{ISW}} \neq 1$ that is stable when considering the extensions of the ΛCDM model shown in Fig. 1.7. Regarding the late ISW, *Planck* data place a constraint $A_{l\mathrm{ISW}} < 1.14$ at 95% C.L.: *Planck* alone does

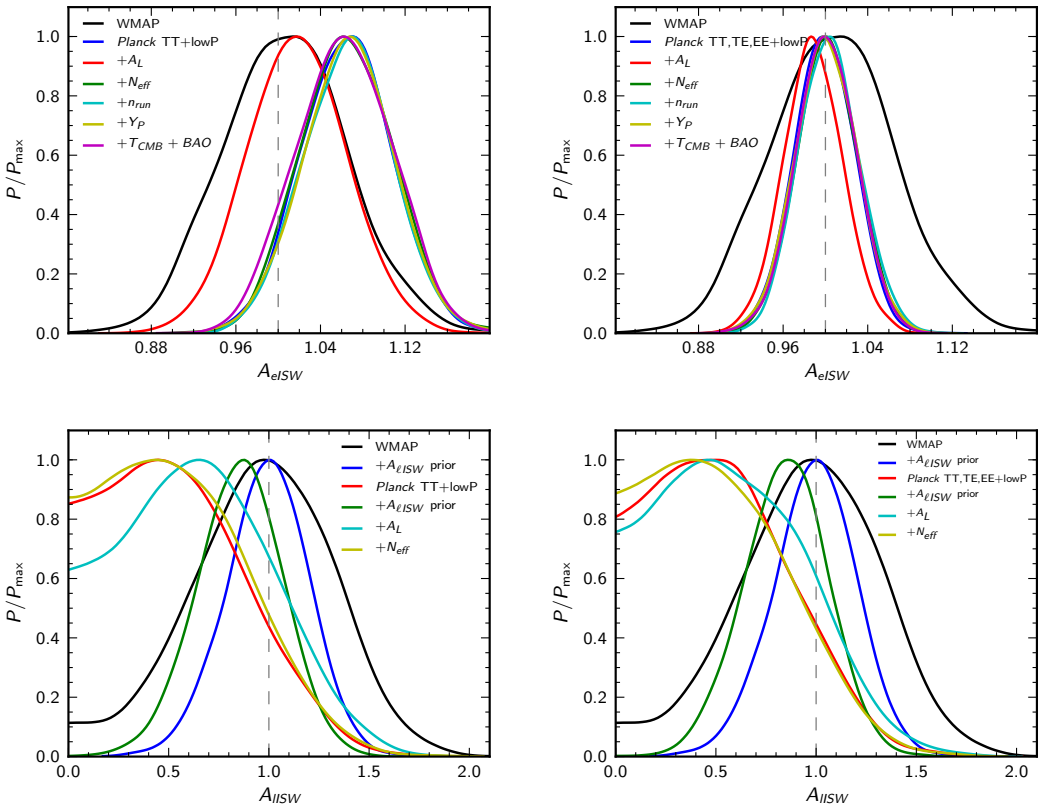

Figure 1.7: One-dimensional posteriors for $A_{e\mathrm{ISW}}$ and $A_{l\mathrm{ISW}}$. In the left column, only *Planck* temperature and low multipole polarization APS (*Planck* TT + lowP) were used. The plots in the right column use also the *Planck* polarization APS at high multipoles (*Planck* TT, TE, EE + lowP). From (56).

not improve significantly the constraint on $A_{l\mathrm{ISW}}$ with respect to WMAP data (which give $A_{l\mathrm{ISW}} = 0.958^{+0.391}_{-0.317}$ at 68% C.L.).

As expected, the late ISW affects angular scales that are dominated by cosmic variance, rather than by instrumental noise. Adding the prior on $A_{l\mathrm{ISW}}$ coming from CMB temperature anisotropies-weak lensing correlations gives a $\sim 4\sigma$ detection $A_{l\mathrm{ISW}} = 0.85 \pm 0.21$. Accounting for the recent *Planck* polarization data at high ℓ, the evidences for a non-standard value of $A_{e\mathrm{ISW}}$ disappear. Using also the small scale polarization APS does not change the results obtained for $A_{l\mathrm{ISW}}$: their effect is to tighten the upper bounds obtained considering only the TT + lowP APS.

1.4.4 CMB low multipoles anomalies

It is usually stated that the six parameters of the ΛCDM model (160, 245, 252) are enough to describe the large scale Universe. However, some features are not well captured, and anomalies occur for instance at the largest CMB angular scales (78) These anomalies (32, 76, 77, 79, 108, 149, 159, 293, 304) deserve particular attention. The low variance anomaly (151) is a closely related observation (149) so that the terms "lack of power" and "lack of correlation" are used as synonymous.

In the ΛCDM cosmology, the lack of power is referred to the two-point correlation function of CMB temperature anisotropies for angles $\gtrsim 60°$, as originally noted with COBE[1] data(159) and then confirmed by the WMAP team already in their first year release (304). This feature was associated to missing power in the quadrupole (32). WMAP-3yrs and WMAP-5yrs data were then used to show (76, 77) that a lack of correlation occurs only in 0.03% of the ΛCDM realizations. A subsequent analysis (108) confirmed the anomaly using WMAP-5yrs data, and, at the same time, found, with a Bayesian approach, that the ΛCDM model cannot be excluded. WMAP 7 and 9 yrs data have been subsequently analyzed (293) and (149), where the lack of correlation was studied against the Galactic masking. *Planck* 2013 and WMAP-9yrs data (79) confirmed for this anomaly a significance at the level of 99.97%. Similar results were obtained in *Planck* 2015 data (242). One intriguing feature of this anomaly is that it is more significant at high Galactic latitude (149, 242). It is intriguing to demonstrate its simple statistical fluke nature or its possible fundamental origin (150, 152).

Lack of power at large angular scales is a typical manifestation of early departures from slow–roll, which follow naturally the emergence from an initial singularity. As explained in (106, 176, 177), when this occurs the PS approaches in the infrared the limiting behaviour

$$\mathcal{P}(k) = A\,\frac{k^3}{(k^2+\Delta^2)^{2-n_s/2}}\,, \tag{1.1}$$

which brings along a new physical scale Δ. An infrared depression of the APS presents itself naturally in string theory, in orientifold vacua with high–scale supersymmetry breaking.

In these models a scalar field emerges at high speed from an initial singularity, then bounce against a steep exponential potential before attaining an eventual slow–roll regime. The key ingredient is the steep exponential, whose logarithmic slope is predicted by string theory (107),

[1] http://lambda.gsfc.nasa.gov/product/cobe/

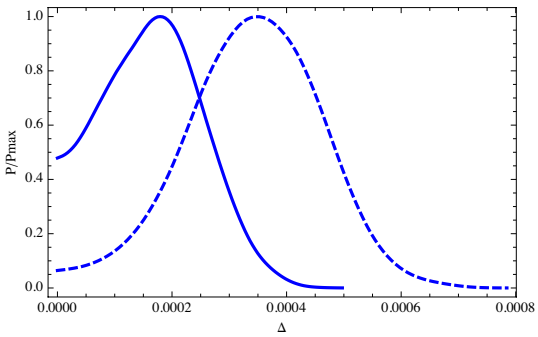

Figure 1.8: Posterior probabilities of Δ (solid line for the standard mask with $f_{sky} \simeq 90\%$, and dashed line for an extended mask with $f_{sky} \simeq 40\%$). From (51).

and a number of exactly solvable systems provide explicit realizations of this peculiar dynamics.

The results of a Bayesian analysis extended to all standard cosmological parameters and based on *Planck* 2013 data are shown in Fig. 1.8, where posteriors for Δ are given for two choices of the Galactic mask: the standard mask, with $f_{sky} \simeq 90\%$ (solid line), and an extended mask with $f_{sky} \simeq 40\%$. For the latter choice, the estimated value is

$$\Delta = (0.340 \pm 0.115) \times 10^{-3}\,\mathrm{Mpc}^{-1}\,. \tag{1.2}$$

Interestingly, Δ in eq. (1.2) differs from 0 at 99% C.L. Moreover, in analogy with the lack of power anomaly, Fig.1.8 shows that the significance of this result increases sizeably for a larger Galactic mask.

In conclusion, the considerations inspired by string theory, and in particular by the supersymmetry breaking mechanism (10, 13, 14, 15, 310) and the related cosmological dynamics, (107) provided the original motivation for the present analysis. The resulting scenario would associate Δ to the onset of the inflationary phase, and as I have demonstrated my estimates appear compatible with this interpretation. Collecting more information on low multipoles of CMB APS the infrared tail of the APS might tell us something more definite about how an inflationary regime was originally attained.

1.4.5 Features in the primordial fluctuations

The most recent CMB data by the *Planck* satellite (252) are in excellent agreement with the assumption of adiabatic primordial scalar perturbation with nearly scale-invariant PS, described

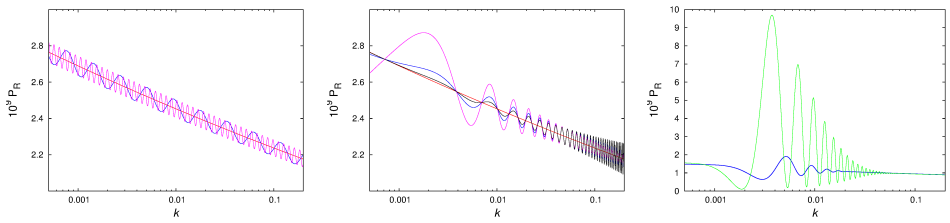

Figure 1.9: PPS simulated for various oscillatory models parametrized with an amplitude, a frequency and a phase (for the Linear oscillation models I have the scale-dependence index as further parameter). Left: Log-spaced oscillations models for different values of the frequency oscillation parameter. Middle: Linear oscillation models for different values of the scale-dependence index. Right: Step oscillation models for different values of the frequency and phase parameters. From (51).

by a simple power law with spectral index n_s very close to (albeit different from) unity (249). It would be produced in the simplest inflationary scenario, in which a single minimally-coupled scalar field slowly rolls down a smooth potential. In spite of this, models that account for localized 'features' in the PPS could provide a better fit to data with respect to a smooth power-law spectrum. These features could be produced in inflationary models with departures from the near-scale-invariant-power-law spectrum of the standard simplest scenario, and observable signatures would be in the CMB anisotropy temperature APS and in the matter PS from galaxy surveys. Three classes of models have been analyzed, and Fig. 1.9 displays the corresponding PPS shapes.

The inflationary class of models are:

(i) Log-spaced oscillations model assumes an oscillation in proper time affecting the amplitude of curvature perturbation during the inflationary expansion (producing features periodic in $\ln k$). It is the case of models with no-Bunch-Davies initial condition (93), or in the bouncing inflationary scenario(38) or also in the axion monodromy inflation (127). (ii) Linear oscillation model includes effects from a possible boundary on effective field theory (where I assume new physics which occurs at one moment in time, such as a discontinuity in single-field inflation (305) or a sharp turn in multi-field inflation (299)). (iii) Step oscillation model assumes a briefly interruption of the slow-roll. For instance it can happen by a phase transition, a burst of resonant particle production, a sudden turn in field space or a step in the inflation potential (3). It is found to be essentially a power-law with superimposed oscillations localized only in a

limited range of wavenumbers. It is noteworthy that this kind of models is able to produce oscillation at very high-ℓ, and it is very interesting looking to the CMB temperature anisotropies glitches in correspondence of $\ell = 22$ and $\ell = 40$, first observed by the WMAP experiment and later confirmed by the *Planck* satellite.

The results show that using the CMB data alone there is no-evidence of improving the concordance with data and agree with the more recent results of the *Planck* Collaboration (249). Instead, using the combined dataset of CMB SDSS-DR11 data, a positive Bayesian evidence for the inflationary log-spaced oscillation and step oscillation models has been discovered. Updating this analysis with final *Planck* data will be very interesting to confirm or discard these kinds of models.

1.4.6 Primordial non-Gaussianity

The study of primordial non-Gaussianity (PNG) provides a powerful tool to shed light on early Universe mechanisms for the generation of primordial perturbations (24, 62). Different inflationary models predict different *amplitudes*, *shapes*, and *scale dependence* of PNG. As a result, PNG allows to discriminate between models that can show degeneracies on the basis of an APS-only analysis.

One of the main goals of these analyses is to constrain the amplitude and shape of PNG using the angular bispectrum of CMB anisotropies, related via *linear* radiation transfer to the primordial bispectrum, $B_\Phi(k_1, k_2, k_3)$, defined by:

$$\langle \Phi(\vec{k}_1)\Phi(\vec{k}_2)\Phi(\vec{k}_3)\rangle = (2\pi)^3\delta^{(3)}(\vec{k}_1 + \vec{k}_2 + \vec{k}_3)B_\Phi(k_1, k_2, k_3)\,; \tag{1.3}$$

here Φ is the primordial potential defined in terms of the comoving curvature perturbation ζ on super-horizon scales by $\Phi \equiv (3/5)\zeta$. The bispectrum measures the correlation among three perturbation modes, and it is expected to be zero for Gaussian perturbations. In general, the bispectrum can be written as:

$$B_\Phi(k_1, k_2, k_3) = f_{\rm NL}F(k_1, k_2, k_3)\,, \tag{1.4}$$

where $f_{\rm NL}$ is the so-called "nonlinearity parameter", a dimensionless parameter measuring the amplitude of non-Gaussianity. The functional dependence of $F(k_1, k_2, k_3)$ on the type of triangle formed by k_1, k_2, k_3 defines the *shape* of the bispectrum (17). Even in the simplest models of inflation, consisting of a single slowly-rolling scalar field, some level of PNG is predicted

(2, 197), but this is too small to be detectable in CMB and LSS surveys. Large level of PNG can be produced however in multi-field scenarios, or in single-field models with non-standard Lagrangians and deviations from Bunch-Davies vacuum, and in many other cases. Each of the scenarios outlined above predicts different shapes, the main of which are briefly described below[1].

Local shape, where the signal peaks in "squeezed" triangles ($k_1 \ll k_2 \simeq k_3$). This shape is typically generated in multi-field models of inflation.

Equilateral shape, peaking on equilateral bispectrum triangles($k_1 \approx k_2 \approx k_3$). Examples of this class include single-field models with non-canonical kinetic term (63), such as e.g. Dirac-Born-Infeld (DBI) inflation (301), models characterized by more general higher-derivative interactions of the inflaton field, and models arising from effective field theories (64).

Folded (flattened) shape, peaking on isosceles, nearly degenerate triangles. Examples of this class include e.g. single-field models with non-Bunch-Davies vacuum.

Orthogonal shape, which is generated, e.g., in single-field models of inflation with a non-canonical kinetic term, or with general higher-derivative interactions. Notably, the folded shape described above can be obtained as a linear combination of equilateral and orthogonal shapes. In light of this, actual measurements of PNG generally focus on local, equilateral and orthogonal templates.

Having computed the CMB angular bispectrum templates arising from the various primordial shapes, non-Gaussianity estimation consists essentially in fitting such templates to the 3-point function of the data in order to measure the best-fit amplitude parameters $f_{\rm NL}$. This apparently straightforward approach actually presents many statistical and numerical complications. Such issues arise mainly from the huge number of modes (triangles) which contribute to the signal for high resolution experiments like *Planck* and WMAP, and from spurious mode couplings owing to sky-cut and anisotropic instrumental noise. Several numerical techniques have been successfully tested in the literature and implemented by the *Planck* team in order to address these issues. This gave rise to several independent, but ultimately equivalent, *Planck* bispectrum analysis pipelines, the so called modal, binned and separable template-fitting estimators, that were individually applied to the data (49, 120, 121, 183, 217). *Planck* papers on PNG (246, 248) describe all details of the analysis, including validation tests carried on data

[1]It must be noted that many but not all models are included in the previous classification. For example, models with a temporary breaking of slow-roll conditions generate strongly scale-dependent, oscillatory shapes that cannot be approximated by a combination of local, equilateral and orthogonal templates.

and simulations, descriptions of the various pipelines, and constraints on a much larger set of shapes than the three discussed here.

The final *Planck* results for the local, equilateral and orthogonal shapes, from the 2015 combined analysis of temperature and polarization data, are as follows:

$$f_{\rm NL}^{\rm local} = +0.8 \pm 5.0 \; ; \quad f_{\rm NL}^{\rm equil.} = -4 \pm 43 \; ; \quad f_{\rm NL}^{\rm ortho.} = -26 \pm 21 \; . \tag{1.5}$$

The main conclusion from *Planck* PNG analysis is that consistency with Gaussianity is found in all cases (including shapes not considered here). *Planck* bispectrum constraints lead to important implications for inflationary model building, such as a lower bound on the sound speed in effective single field inflation theory, or limits on the curvaton decay fraction, and so on. In light of the current results, the simplest slow-roll single field inflationary paradigm has passed its most stringent and accurate test to date (although alternative, more complex, possibilities, while constrained, are by no means ruled out yet). *Planck* has extracted nearly all the possible PNG information from CMB data. Even an ideal, noiseless temperature+polarization experiment would improve on current error bars by at most a factor 2.

1.5 WMAP and *Planck* joint data analysis

The onset of the reionization epoch mainly determines the Thomson optical depth τ between the observer and the CMB LSS, one of the six cosmological parameters of the standard ΛCDM model (252). All primary CMB angular power spectra are affected by reionization in having their amplitude suppressed by a factor $e^{-2\tau}$. Such a suppression, which equally affects intensity and polarization spectra, arises due to re-scattering of photons by free electrons and is effective at all scales but the largest ones that were outside the horizon at reionization; hence the "bump" at low ℓ's. This loss in anisotropy power at non-zero τ is clearly degenerate with the amplitude of primordial scalar fluctuations A_s which source CMB anisotropy. On the other hand, only polarization spectra inherit the characteristic low ℓ increase, or bump, mentioned above, whose amplitude is $\propto \tau^2$. This unique signature is exploited to disentangle τ and A_s and better infer the value of both these ΛCDM model parameters.

The first estimate of τ from CMB measurements was provided by the Wilkinson Microwave Anisotropy Probe (WMAP). In the nine-year legacy results, the WMAP collaboration reports $\tau = 0.089 \pm 0.014$ (160). *Planck* (237) has shown (252, 260, 268) that the WMAP estimate is likely biased high due to residual dust polarization, imperfectly accounted for by the simple

dust model the WMAP team employed, since they lacked of tracers based on direct observations. *Planck*'s 353 GHz channel, on the other hand, is an ideal monitor of dust polarization. Considering still WMAP large-scale polarization, but using the 353 GHz channel to mitigate dust, τ shifts down to 0.075±0.013 (268). The 2015 analysis of *Planck* reports $\tau = 0.067 \pm 0.023$ using only *Planck* low-resolution data (from the 70 GHz channel of its low frequency instrument) and priors on cosmological parameters fixed by small-scale CMB information (260). More recently, the Planck collaboration has published a new estimate of $\tau = 0.055 \pm 0.009$ (262) using only low-ℓ polarization *EE* cross-spectra built from the 100 and 143 GHz channels of the high frequency instrument[1], unlike the *Planck* 2015 low-ℓ results that also make use of TT and TE information. This new value is fully compatible with the previous one from *Planck* and displays a smaller uncertainty.

This study shows how the choice of existing low-multipole polarization data impacts cosmological parameter estimates, by looking at different combinations of the public low- and high-ℓ datasets provided by WMAP9[2] and *Planck*[3]. In particular, this analysis is focussed on the impact of using the *Planck* 353 GHz channel as a dust tracer to clean also the large-scale WMAP9 polarization (187).

It is important to analyze the impact of the dust cleaning procedure on the so-called "low-ℓ anomaly", i.e. the tension between the values of the primordial perturbations amplitude estimated from the low- ($\ell < 30$) and high- ($\ell \geq 30$) ell portions of the TT power spectrum. The low-ell anomaly has been found to drive the differences in parameter values obtained from distinct subsets of the high-ℓ data (4, 257). Even though the significance of these shifts is low, it is nevertheless interesting to assess how much the low-ℓ anomaly that causes them depends on the choice of low-ℓ polarization data. By comparing parameter estimates obtained from the low- and high-ℓ datasets, we can test the robustness of the anomaly to the low resolution cleaning procedure for polarized dust, as well as of the particular choice of the high-ℓ datasets.

1.5.1 Low-ℓ data

At low multipoles ($\ell < 30$), it is accounted for the standard joint temperature-polarization, pixel-based machinery for the likelihood, as done in the 2015 *Planck* release (260). Thus, the

[1] The new products, and the associated analysis pipelines, presented in (262) are referred to as "pre-2016".

[2] I use the products available at the Legacy Archive for Microwave Background Data Analysis, LAMBDA (http://lambda.gsfc.nasa.gov/).

[3] Planck Legacy Archive (http://www.cosmos.esa.int/web/planck/pla).

Name	Description
Planck lowT	*Planck* Commander temperature map ($\ell < 30$).
WMAP9 lowP	WMAP9 polarization maps dust-cleaned using WMAP team's model ($\ell < 30$).
WMAP353 lowP	WMAP9 polarization maps dust-cleaned using the *Planck* 353 GHz map ($\ell < 30$).
Planck lowP	*Planck* polarization maps dust-cleaned using the *Planck* 353 GHz map ($\ell < 30$).
WMAP/*Planck* lowP	Noise-weighted WMAP and *Planck* polarization maps (353-cleaned, $\ell < 30$).
Planck high TT	*Planck* high-ℓ TT likelihood ($30 \leq \ell \leq 2500$).
WMAP9 high TT	WMAP9 high-ℓ TT likelihood ($30 \leq \ell \leq 1200$).
Planck lensing	*Planck* lensing likelihood ($40 \leq \ell \leq 400$)
high-ℓ priors	Gaussian priors derived from a joint likelihood using *Planck* lowT, *Planck* lowP and *Planck* high TT: $\omega_b = 0.022222 \pm 0.00023,\ \omega_c = 0.1197 \pm 0.0022,\ 100\theta = 1.04085 \pm 0.00047, n_s = 0.9655 \pm 0.0062$.

Table 1.4: Abbreviations for the several datasets (and combinations thereof) employed throughout this analysis.

low-ℓ datasets always consist of low resolution ($N_{\rm side} = 16$ in the Hierarchical Equal Area iso-Latitude Pixelation (HEALPix) scheme [1]) maps of temperature and polarization anisotropies, and of the related noise covariance matrices.

As low-ℓ temperature data, it is always employed the *Planck* `Commander` CMB map, obtained combining the *Planck* observations between 30 and 857 GHz (237, 239), the 9-year WMAP observations between 23 and 94 GHz (30), and the 408 MHz sky maps from (156), as described in (239, 260, 262) (see also (114, 115) for a description of the `Commander` component-separation algorithm). The `Commander` map covers 94% of the sky and will hereafter be denoted as "*Planck* lowT".

For low-ℓ polarization, three different datasets, all based on WMAP9 data are considered; two of them are augmented by also considering information from *Planck* low-resolution polarization maps. Each temperature and polarization low-ℓ dataset is summarized in Table 1.4.

[1] `http://healpix.jpl.nasa.gov/`; see also (144).

ν	α	β	$N_{\rm p}$	$\chi^2_{\rm S+N}$	$\chi^2_{\rm N}$	$\tilde{\chi}^2_{\rm S+N}$	$\tilde{\chi}^2_{\rm N}$
Ka	0.315 ± 0.003	0.0031 ± 0.0004	5720	1.026	1.045	1.012	1.029
Q	0.163 ± 0.003	0.0039 ± 0.0004	5742	0.9830	1.004	0.9778	0.995
V	0.047 ± 0.003	0.0076 ± 0.0004	5894	0.9627	0.977	0.9606	0.974

Table 1.5: Best-fit scaling coefficients and χ^2 values for WMAP9 low ℓ polarization frequencies, obtained using the processing mask. The χ^2 values are in $N_{\rm p}$ unit, and the S+N estimates are computed outside of the processing mask, leaving $N_{\rm p}$ good pixels in the maps. The $\chi^2_{\rm N}$ values assume only the noise covariance matrix. Differences between these two approaches are weak. Last columns report $\tilde{\chi}^2$ values, in $\mathcal{N}_{\rm p}$ unit, for both S+N and N, computed outside of the P06 mask used for parameter estimation, leaving $\mathcal{N}_{\rm p} = 4510$ good pixels. Here, the scaling coefficients derived in the processing mask have been assumed, estimated separately for S+N and N: the scalings quoted in the first two columns are for the former case, though the latter produces figures that are well within errors.

1.5.2 Foreground mitigation and analysis

To minimize the impact of polarized foregrounds, it is implemented a template fitting procedure such that each linear polarization map $\mathbf{m}_\nu = [\mathbf{Q}_\nu, \mathbf{U}_\nu]$, ($\mathbf{Q}_\nu, \mathbf{U}_\nu$ being the Stokes parameters maps at frequency band ν) is masked by the WMAP9 processing mask (30) and used to find two scaling coefficients α_ν and β_ν, assumed constant over the available sky, that minimize the form $\chi^2_{\rm S+N} = \tilde{\mathbf{m}}^{\rm T}_\nu \mathbf{C}^{-1}_\nu \tilde{\mathbf{m}}_\nu$, with $\tilde{\mathbf{m}}_\nu = \mathbf{m}_\nu - \alpha_\nu \mathbf{t}_{\rm S} - \beta_\nu \mathbf{t}_{\rm d}$, $\mathbf{t}_{\rm S}$ and $\mathbf{t}_{\rm d}$ being the templates for synchrotron and dust emissions, chosen as the WMAP9 K-band and the *Planck* 353 GHz maps, respectively. The covariance matrix $\mathbf{C}_\nu = \mathbf{S} + \mathbf{N}_\nu$ is taken as the sum of the signal[1], $\mathbf{S}$, and noise, $\mathbf{N}_\nu$, matrices, and the signal matrix is built through harmonic expansion (320) assuming the WMAP 9-year fiducial model. Nonetheless, using in its place the *Planck* 2015 fiducial induces negligible differences in the estimated scaling coefficients. The WMAP team has used a similar procedure to derive their scaling coefficients, although neglecting the CMB signal in the $\mathbf{C}_\nu$ matrices. Their approximation induces only differences that lie well within the error budget. In Table 1.5 I describe the $\chi^2_{\rm N}$ figures I find assuming $\mathbf{C}_\nu \equiv \mathbf{N}_\nu$ only.

Once α_ν and β_ν are found, the foreground-reduced polarization maps $\hat{\mathbf{m}}_\nu$ are obtained as:

$$\hat{\mathbf{m}}_\nu = (\mathbf{m}_\nu - \alpha_\nu \mathbf{t}_{\rm S} - \beta_\nu \mathbf{t}_{\rm d})/(1 - \alpha_\nu - \beta_\nu)\,, \tag{1.6}$$

[1] We use thermodynamic temperature units so each channel has the same signal covariance matrix.

and the associated noise covariances $\hat{\mathbf{N}}_\nu$ are:

$$\hat{\mathbf{N}}_\nu = \left(\mathbf{N}_\nu + \delta\alpha_\nu^2\,\mathbf{F}_\mathrm{S} + \delta\beta_\nu^2\,\mathbf{F}_\mathrm{d}\right)/(1-\alpha_\nu-\beta_\nu)^2\,, \tag{1.7}$$

where $\delta\alpha$ and $\delta\beta$ are the standard errors associated with the estimated scalings, and $\mathbf{F}_{\mathrm{s,d}} \equiv \mathbf{t}_{\mathbf{s,d}}\mathbf{t}_{\mathbf{s,d}}^{\mathrm{T}}$ are, respectively, the covariance contributions for synchrotron and dust emission, built from the outer products of the corresponding templates. Table 1.5, lists the values for the scaling coefficients assuming the processing mask. Fixing them, the table shows χ^2 values outside of WMAP's cosmological P06 mask which leaves about 73% of the sky. Fitting the coefficients for K_a, Q and V and their 1σ errors, the best fist estimate for the synchrotron spectral index is -3.152 ± 0.019 and for the dust spectral index is 1.332 ± 0.024 (1σ errors). These values are robust to the fitting procedure employed, as well as to my assumptions for errors in the templates. In particular, adding the calibration errors quoted for the WMAP9 and *Planck* 353 GHz frequency maps to standard errors evaluate for the scalings, a synchrotron spectral index of -3.154 ± 0.022 and a dust spectral index of $1.332 \pm 0.025$are derived. Furthermore, these results are stable including WMAP W channel.

Remarkably, the synchrotron spectral index is in agreement at 1σ with the one derived by the WMAP team applying the template fitting method to polarization maps. On the contrary, they found a steeper dust spectrum, with an index ranging from 1.41 to 1.5. The previous fit is then repeated for comparison, but only accounting the rescaling coefficients in the WMAP channels specified above and including calibration uncertainties. For the synchrotron spectral index the results are very similar (-3.152 ± 0.022). The dust spectral index, on the other hand, is found to be 1.420 ± 0.091, in agreement with WMAP team results. Clearly, these resulta for the dust including the *Planck* 353 GHz frequency map are driven by highest frequencies. It is interesting to note that a grey body spectrum with dust grain temperature $T_{dg} = 19.6\,\mathrm{K}$ and grain emissivity index $\beta_{dg} = 1.59$, as found in (241) at intermediate and high Galactic latitudes, predicts an effective spectral index of 1.33 between 93 GHz and 353 GHz and of 1.52 between 33 GHz and 93 GHz, in agreement with the results described above. The spectral indices derived with this template fitting procedure applied to WMAP and *Planck* 353 GHz polarization maps provide an evidence of the grey body spectrum of Galactic thermal dust emission. Fig. 1.10 shows the frequency dependence of polarized synchrotron and dust emission derived with the template fitting approach described above in terms of both antenna and thermodynamic or (CMB) temperature.

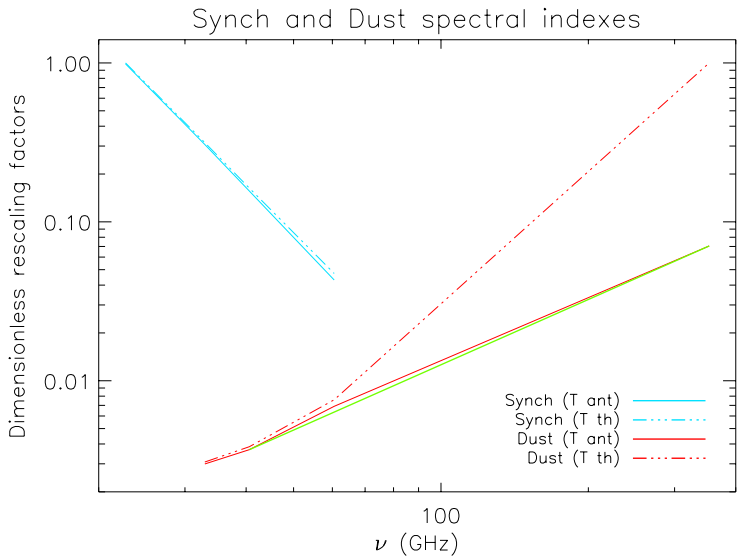

Figure 1.10: Frequency dependence of polarized synchrotron and dust emission derived with the template fitting approach described. Green line shows a pure power law from the WMAP Ka band up to the *Planck* 353 GHz band, allowing to appreciate the flattening of dust emission in agreement with a grey body. See also the text.

1.5.3 Cosmological parameters

In this section, I focus on the impact of low-ℓ and high-ℓ CMB data aimed at the estimation of cosmological parameters, starting from the choice of the large-scale polarisation data. Cleaning WMAP polarization data with the *Planck* 353 GHz dust template yields a significantly lower value of τ with respect to the same data cleaned using WMAP9 dust model. This choice also affects estimates of the scalar amplitude A_s through its degeneracy with τ.

Precisely, combining the WMAP and *Planck* 70 GHz polarization data, and cleaning with the *Planck* dust template, $\tau = 0.066^{+0.012}_{-0.013}$; this value is very stable against the inclusion of high-ℓ data (including *Planck* lensing) and is in remarkable agreement with the *Planck* low-ℓ only estimate $\tau = 0.067 \pm 0.023$, as well as being consistent with the more recent value $\tau = 0.055 \pm 0.009$ obtained by the *Planck* collaboration using the large-scale polarisation data from the high-frequency instrument (262). Note also the remarkable consistency with the estimate $\tau = 0.066^{+0.025}_{-0.026}$ obtained disregarding the low-ℓ information and using *Planck* high TT and *Planck* lensing data, that independently measure $A_s e^{-2\tau}$ and A_s, and thus allow an indirect determination of the optical depth[1].

[1] See (141) for a theoretical model predicting a value of τ in agreement with those discussed in this section.

Low-ℓ dataset (all of them include *Planck* high TTand *Planck* lensing)							
Parameter	[1] WMAP9 lowP	[2] WMAP353 lowP	[3] WMAP/*Planck* lowP	[4] no low-ℓ data	$\frac{[2]-[1]}{\sqrt{\sigma^2_{[2]}+\sigma^2_{[1]}}}$	$\frac{[3]-[1]}{\sqrt{\sigma^2_{[3]}+\sigma^2_{[1]}}}$	$\frac{[4]-[1]}{\sqrt{\sigma^2_{[4]}+\sigma^2_{[1]}}}$
$\Omega_b h^2$	0.02238 ± 0.00022	0.02222 ± 0.00021	0.02224 ± 0.00021	$0.02223^{+0.00026}_{-0.00027}$	-0.53	-0.45	-0.43
$\Omega_c h^2$	0.1169 ± 0.0017	0.1190 ± 0.0017	0.1187 ± 0.0017	0.1189 ± 0.0027	$+0.87$	$+0.77$	$+0.65$
100θ	1.04127 ± 0.00043	1.04096 ± 0.00044	1.04101 ± 0.00043	$1.04101^{+0.00052}_{-0.00053}$	-0.50	-0.43	-0.39
τ	$0.084^{+0.011}_{-0.012}$	0.062 ± 0.012	$0.065^{+0.010}_{-0.012}$	$0.066^{+0.025}_{-0.026}$	-1.3	-1.2	-0.64
$\log[10^{10} A_s]$	$3.095^{+0.020}_{-0.022}$	3.055 ± 0.023	3.060 ± 0.020	3.064 ± 0.045	-1.3	-1.2	-0.61
n_s	0.9723 ± 0.0052	0.9665 ± 0.0053	0.9673 ± 0.0051	0.9657 ± 0.0078	-0.78	-0.68	-0.71
$10^9 A_s \exp[-2\tau]$	1.866 ± 0.012	1.876 ± 0.012	1.874 ± 0.011	$1.875^{+0.015}_{-0.016}$	$+0.62$	$+0.54$	$+0.50$
H_0 [km/s/Mpc]	68.59 ± 0.77	67.61 ± 0.80	67.74 ± 0.76	$67.7^{+1.2}_{-1.3}$	-0.89	-0.79	-0.64
Ω_m	0.2975 ± 0.0098	0.310 ± 0.011	0.309 ± 0.010	0.310 ± 0.017	$+0.89$	$+0.79$	$+0.66$

Table 1.6: Parameter estimates from *Planck* high TT+ *Planck* lensing either in combination with the low-ℓ datasets analyzed (second to fourth column) or alone (fifth column). In the former cases, use of *Planck* lowT is understood. The last three columns report the shifts (in units of σ) in the parameters with respect to WMAP9 lowP + *Planck* high TT + *Planck* lensing.

I note that, even if τ and $\log(10^{10} A_s)$ are the more influenced parameters by the cleaning of the polarization maps, other base parameters are also affected, albeit to a lesser extent. This is especially evident when the *Planck* high TT and *Planck* lensing are used jointly with the low-ℓ polarization data: while τ and $\log(10^{10} A_s)$ shift by roughly 1.2σ between the *Planck* 353 GHz and WMAP dust model cleanings, the estimates of the other base parameter shift by an amount between $\sim 0.4\sigma$ (for θ) and 0.8σ (for $\Omega_c h^2$).

Detailed information can be found in Table 1.6, that reports the parameter evaluation derived by combining different low-ℓ polarization datasets (including the case where none at all is employed) with *Planck* high TT and *Planck* lensing, as well as the corresponding parameter shifts with respect to the WMAP9 lowP + *Planck* high TT + *Planck* lensing case. The Hubble constant value coming from the WMAP9 lowP + *Planck* high TT +*Planck* lensing combination is also $\sim 1\sigma$ lower than the corresponding value from datasets cleaned with the *Planck* dust templates. In general, polarization datasets cleaned with the *Planck* 353 GHz channel lead to H_0 values systematically higher than the corresponding quotation with WMAP9 lowP. This contributes to increase the tension with local measurements of H_0 (282).

As for the role of the high-ℓ dataset, this analysis confirms the existence of the so-called "low-ℓ anomaly", i.e., the fact that the value of the amplitude parameter $\mathcal{A}_s$ estimated by the

low-ℓ data is lower, at the $\sim 2\sigma$ level, than the one measured from the high-ℓ data. This anomaly is not affected by the cleaning procedure used on the large-scale polarization. The low-ell anomaly has been found to drive the shifts in parameter values obtained from different multipole ranges (4, 257), implying that these shifts are not affected by the choice of low-ell polarization data. On the other hand, values of the amplitude $\mathcal{A}_s$ are fairly consistent between the WMAP and *Planck* high-ℓ TT datasets, as well as with *Planck* lensing.

1.6 CMB mission proposals in ESA context

The theory of inflation, originally proposed as a solution of the cosmological horizon, smoothness and monopole problems, seems to be a good explanation for the Gaussian nature of primordial perturbations and the density perturbations nearly scale invariant spectrum. Moreover, it implies that gravitational waves should originate from scalar field perturbations, whose amplitude is expressed in terms of the parameter $r = T/S$, i.e. the ratio between the amplitudes of primordial tensor and scalar perturbations.

To reveal the primordial inflationary B-modes, it is crucial to observe the sky looking for the reionization bump at $\ell = 2 - 10$ and the recombination epoch at LLS for $\ell = 20 - 100$ (angular scales larger than $\simeq 1°$). The main requirements for a B-modes detection mission, to reveal a tensor to scalar ratio $T/S \sim 10^{-3}$, are an improvement in sensitivity of a factor ~ 100 with respect to *Planck* a control of systematics effects of the order of few tens of nK and an accurate understanding of polarized foregrounds at the level of 1 %. This objective is potentially achievable by different class of missions, all of them recently proposed to ESA

In 2009, in response to the ESA Cosmic Vision 2015-2025 call for Proposals, a medium class space mission has been presented, B-Pol (97), aimed at detecting the primordial gravitational waves occurred during the inflationary epoch on cosmological scales through the detection of the so-called primordial B-mode polarization, thus confirming the quantum origin of the CMB fluctuations. It was designed to host six broad frequency bands detectors, from 45 GHz to 353 GHz, Moreover, CMB anisotropies appear linearly polarized, thus the measured spectra contain two more quantities for each pointing direction in the sky, the Stokes parameters Q and U. A linear combination of these parameters allows us to define, in Fourier space, the E-mode (gradient component) and B-mode (curl component) polarization patterns and to identify, together with temperature anisotropies, four power spectra according to a Gaussian model, C^{TT}, C^{EE}, C^{BB}, C^{TE}, the latter being the temperature polarization cross correlation.

1. MICROWAVES SPACE OBSERVATIONS: FROM *PLANCK* LEGACY TO THE FUTURE

The polarization of the CMB is due to Thomson scattering of anisotropic photons off free electrons at last scattering surface and is characterized by a very low signal peaking at multipole $\ell \sim 100$, which correspond to the angle subtended by the photons mean free path at last scattering. On the other hand, at large angular scales (small multipoles), polarization is related to the Universe reionization epoch, which induces a re-scattering of photons and provides informations about its thermal history during at the end of the so called dark ages.

In December 2010, a new proposal has been submitted to ESA to trace the polarization in the microwaves (321), the Cosmic Origin Explorer, COrE. The spacecraft, designed to host 15 frequency bands from 45 GHz to 795 GHz with angular resolution comparable to *Planck* and a sensitivity from 10 to 30 times better than *Planck* is addressed to look for primordial gravitational waves generated during inflation up to $r \geq 10^{-3}$ at more than 3 σ level, corresponding to an energy scale of inflation of few$\times 10^{15}$. Another objective of COrE should be the detection of CMB gravitational lensing power spectrum with extremely high precision allowing the determination of the absolute neutrino masses better than in laboratory experiments, the search for primordial non-Gaussianities, the map of galactic magnetic fields in regions of diffuse emission and the determination of a very deep compact sources catalogue.

As already seen in Sect.1.5.1, at frequencies above 250 GHz, the contamination of cold dust grains of interstellar medium, characterized by a temperature $T \simeq 20$ K, becomes dominant over CMB anisotropies, but its knowledge is still partial and roughly described by empirical models. This emission is partially polarized, thus potentially observable by COrE.

One of the goal of COrE is the characterization of the gravitational lensing B-modes, thus it requires an unprecedented detailed description of the foregrounds, with an accuracy around or better $5\mu\text{K} \cdot \text{arcmin}$. Concerning Galactic and extragalactic science, COrE can detect myriad of polarized or not new IR compact sources.

Few years later, in May 2013, a large class mission has been proposed to ESA, PRISM, The Polarized Radiation Imaging and Spectroscopy Mission (12) as a full sky, high sensitivity and resolution observer, in total intensity and polarization, from the microwaves to the IR. The instrument is designed to measure the absolute spectrum of sky emission more than three orders of magnitude better than COBE/FIRAS. PRISM consists of two instruments: (*i*) A high angular resolution polarimetric imager with a 3.5 m usable diameter telescope, cooled to below 10K in order to maximally reduce the photon noise due to the thermal emission of the mirrors. This instrument will map the intensity and polarization anisotropies on the whole sky in 32 broad frequency bands between 30 GHz (1 cm) and 6 THz (50 microns) with

unprecedented sensitivity and with an angular resolution ranging from about 17 arcminutes to about 6 arcseconds; (*ii*) a lower angular resolution (1.4°) spectrometer that will compare the sky frequency spectrum to a nearly perfect reference blackbody and measure the absolute sky emission over the same frequency range.

PRISM will have a major impact on Galactic astrophysics by providing a unique set of all-sky maps. The PRISM data will extend Herschel dust observations to the whole sky, map the absolute sky intensity and polarized emission with high sensitivity in more than 20 different frequency bands, and also map emission lines key to quantifying physical processes in the interstellar medium. The survey will have the sensitivity and angular resolution required to map dust polarization down to sub-arcminute resolution even at the Galactic poles.

Because of its broad frequency coverage and extreme stability, PRISM will be able to detect B-modes at 5σ for $r = 5 \times 10^{-4}$, even under pessimistic assumptions concerning the complexity of the astrophysical foreground emissions that must be reliably removed. It will be able to separate and filter out the majority of the lensing signal due to gravitational deflections. Hence, PRISM will perform the best possible measurement of primordial CMB B-mode polarization, and the best possible measurement of the corresponding inflationary tensor perturbations achievable through CMB observations. Their data will also provide unique clues to study the interstellar medium, the Galactic magnetic field and star formation.

Furthermore, the excellent agreement between the microwave sky emission and the perfect blackbody observed by the COBE FIRAS instrument is rightfully highlighted as a crucial confirmation of Big Bang cosmology. However theory predicts that at higher sensitivity this agreement breaks down. Energy injection at any redshift z $\lesssim$(few)$\times 10^6$ superimposes spectral distortions relative to a perfect CMB blackbody spectrum. The PRISM absolute spectrometer will measure the spectrum more than three orders of magnitude better than FIRAS. y-distortions from the re-ionized gas as well as from hot clusters constitute a certain detection. However, μ-distortions and more general spectral distortions have the potential to uncover decaying dark matter and to probe the primordial power spectrum on very small scales that cannot be measured by other means, being contaminated by the nonlinearity of gravitational clustering at late times.

A secondary, but also important, objective is the collection of high quality survey full-sky data for a large variety of applications by the astronomical community. The hundreds of intensity and polarization maps of PRISM spanning over two decades in frequency will constitute a legacy archive useful for almost all branches of astronomy for decades to come.

1. MICROWAVES SPACE OBSERVATIONS: FROM *PLANCK* LEGACY TO THE FUTURE

PRISM will deliver a well calibrated and fully characterized spectro-polarimetric survey of the full sky from 50 μm to 1 cm. The spectral resolution will range from about 0.5 GHz to 15 GHz at 1.4° angular resolution, and from $\delta\nu/\nu \simeq 0.025$ to 0.25 at the diffraction limit of a 3.5m telescope (from $\sim$ 6" to 17').

COrE+ (Cosmic Origins Explorer +) in an ESA medium-class space mission,proposed in 2015, called to investigate Cosmic Origins through high sensitivity, full sky observations of the polarized microwave and sub-millimeter sky between 60 and 600 GHz. With these observations we will explore the origin of stars and cosmic structures on large scales. The primary science goal of COrE+ is to investigate the physics of the very early Universe, which is the source of the entire cosmic web we observe today. The energy scale for this new physics is $\sim 10^{16}$ GeV, more than 12 orders of magnitude beyond the energy scales accessible to the Large Hadron Collider (LHC) at CERN, and it will be probed by ultra-precise observations of the B mode polarization of the CMB radiation. This is also the energy scale where quantum gravity effects start to become relevant. Long wavelength gravity waves have not yet been detected, despite a vigorous sub-orbital observation programme that has been actively pursued for more than a decade. Cosmic inflation does not provide a unique prediction for the amplitude of the primordial tensor mode, parameterized by the tensor-to-scalar ratio. A precise measurement of, or upper bound on r is essential for constraining inflationary physics. Knowledge of r will substantially restrict the field of inflationary models allowed by current observations. Present constraints on inflationary models rely mainly on measurements of the primordial scalar mode power spectrum, which is well measured by *Planck* and ground-based CMB experiments and unlikely to improve substantially in the future. Because of the uncertainty in the expected value of r, it is not possible to predict which experiment will deliver a first statistically significant detection. However, the comprehensive study of the CMB polarization is a scientific imperative that requires observations by a space mission with exquisite sensitivity, matching control of systematic errors, and broad frequency coverage. Any tentative detection by a suborbital experiment will require a confirmation from space because of ambiguities in the removal of galactic foreground contamination. Compared to proposed experiments with a lower budget and faster schedule, COrE+ is designed as the ultimate experiment for probing inflation from CMB polarization observations, an objective that cannot be achieved by any other means.

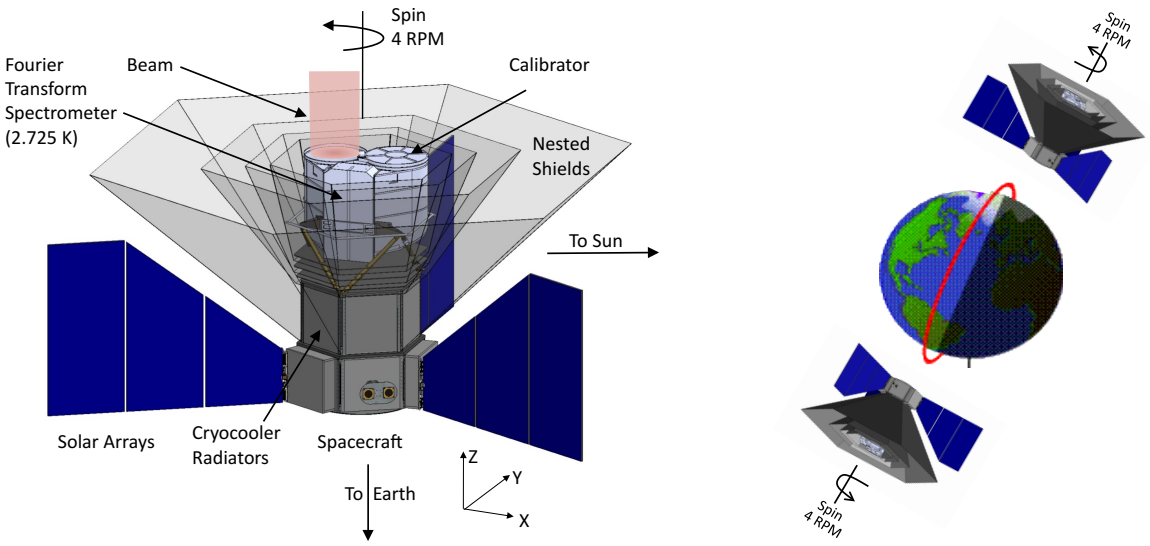

Figure 1.11: PIXIE observatory and mission concept. The instrument is maintained at 2.725 K and is surrounded by shields to block radiation from the Sun or Earth. It observes from a 660 km polar sun-synchronous terminator orbit. The rapid spin and interferometer stroke efficiently separate Stokes I, Q, and U parameters independently within each pixel to provide a nearly diagonal covariance matrix.

1.7 The PIXIE mission

The Primordial Inflation Explorer (PIXIE) is an Explorer-class mission submitted to NASA aimed at the CMB mapping in absolute intensity and linear polarization and the diffuse astrophysical foregrounds over the full sky, from 30 GHz to 6 THz (1 cm to 50 μm wavelength), to derive high signal to noise ratio polarization maps of the CMB and every Galactic foreground. The spacecraft will spin from a low Earth orbit at 4 RPM around the spin axis (see Fig. 1.12).

PIXIE uses a polarizing Michelson interferometer to measure the difference spectrum between two orthogonal linear polarizations from two co-aligned beams (182) to detect inflationary epoch polarization with $r \ll 10^{-3}$. The PIXIE mission concept is an improved version of the FIRAS spectrometer by adding large area detectors, which aims at performing absolute spectroscopy and measuring large-scale CMB B-modes simultaneously. One of its major limitations is the effective resolution of only 2.6°. On the contrary, it is designed to be perfectly symmetric in order to reduce its sensitivity to potential systematics since the rotation of a non circolar beam around a non polarized sky induces a spurious polarization signal. Hence, PIXIE

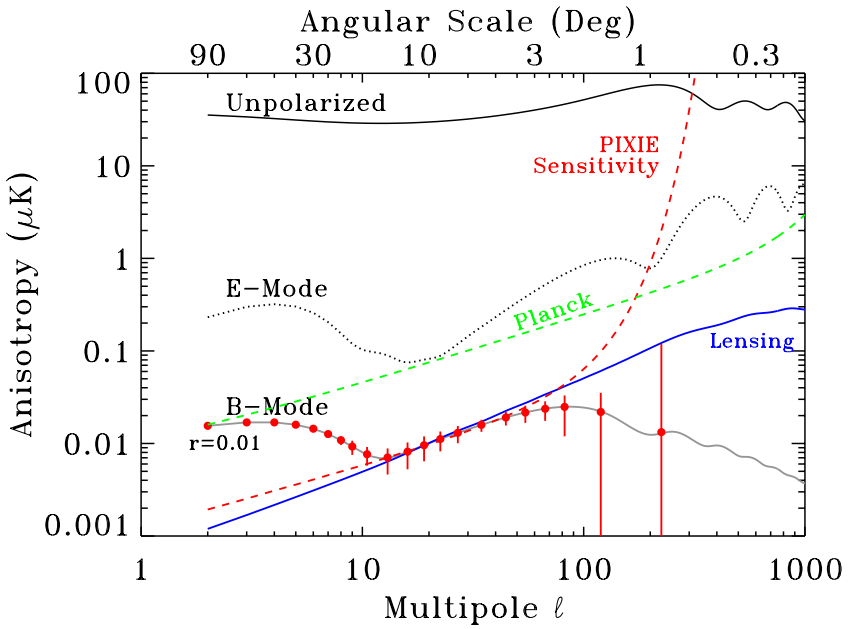

Figure 1.12: Angular power spectra for unpolarized, E-mode, and B-mode polarization in the cosmic microwave background. The dashed red line shows the PIXIE sensitivity to B-mode polarization at each multipole moment $\ell \sim 180\,\mathrm{deg}/\theta$. The sensitivity estimate assumes a 4-year mission and includes the effects of foreground subtraction within the cleanest 75% of the sky combining PIXIE data at frequencies $\nu < 600$ GHz. Red points and error bars show the response within broader ℓ bins to a B-mode power spectrum with amplitude $r = 0.01$. PIXIE will reach the confusion noise (blue curve) from the gravitational lensing of the E-mode signal by cosmic shear along each line of sight, and has the sensitivity and angular response to measure even the minimum predicted B-mode power spectrum at high statistical confidence.

distinctive scheme can gather breakthrough sensitivity both in polarization and spectral distortions (181). Fig. 1.12 shows the PIXIE sensitivity compared to the CMB signal and its main contamination foregrounds, synchrotron and dust.

The huge amount of collected data will allow the exploitation of various Galactic and extragalactic science cases such as large scale scale structure formation and interstellar medium. Nevertheless, it will provide crucial constraints on Universe ionization history and on CIB spectrum and anisotropies. Indeed, PIXIE will trace CIB monopole, dipole and higher order power spectrum to test the matter distribution at z ~ 3. Moreover, more stringent constraints on the optical depth parameter, the gas temperature and the Universe reionization at z ~ 10 will be performed owing to the cross correlation analysis of the temperature polarization anisotropies.

The broad frequency range of the PIXIE data provides rich ancillary science in addition to the primary goal of inflationary science. Thomson scattering of CMB photons from free electrons at the epoch of reionization sources E-mode polarization on large angular scales. The same scattering necessarily distorts the unpolarized CMB away from a blackbody.

The four dominant CMB foreground contamination, synchrotron, polarized dust, free free and electric dipole due to rapidly spinning dust grains emission, are characterized by smooth frequency dependent functions, and then removed in multi-frequency combined observations.

1.8 The LiteBIRD mission

LiteBIRD is a Lite (Light) Satellite for the studies of B-mode polarization and Inflation from cosmic background Radiation Detection at the extremely early universe. LiteBird is a highly-targeted, low-cost Japanese B-mode mission concept, in many respects similar to the B-Pol mission proposed to ESA in 2007. It is designed to detect B-modes at the level of $r \sim 10^{-3}$, a sensitivity that it should be able to achieve assuming that the foregrounds are not too complicated. However, LiteBird lacks the angular resolution needed to make significant contributions to other key science objectives than PRISM and CORE. Its main scientific goal will be the probe of the B-mode range down to one order of magnitude lower than what can be done from the ground. Its main strategy is the focus on r measurements in synergy with ground based super telescopes which are necessary for an accurate subtraction of the lensing contribution to B-mode. Fig. 1.13 illustrate the LiteBIRD sensitivities compared to the primordial B-mode for different values of r from 0.1 down to 0.001 and the contamination from the lensing to the B-mode pattern.

The instrument on board the satellite is equipped with a superconducting detector array cooled to 4 K in order to achieve a target sensitivity of 2 μK·arcmin over 15 frequency bands from 40 GHz to 400 GHz (207). Within the assumption $\Delta\nu/\nu \sim 30\%$, each centre band is chosen according to Fig. 1.14.

LiteBIRD has been formally proposed as a strategic large mission to the ISAS, JAXA in February 2015 and one year later it has started the conceptual design phase-A1. In December 2014, the US team presented the project to the NASA's mission of opportunity to supply the focal plane detectors and the refrigerator system, that were partially covered. Currently, it is in conceptual study phase-A. Other contributions come, or will be likely available, from various European countries, such as UK. LiteBIRD specifications are listed in Table 1.7.

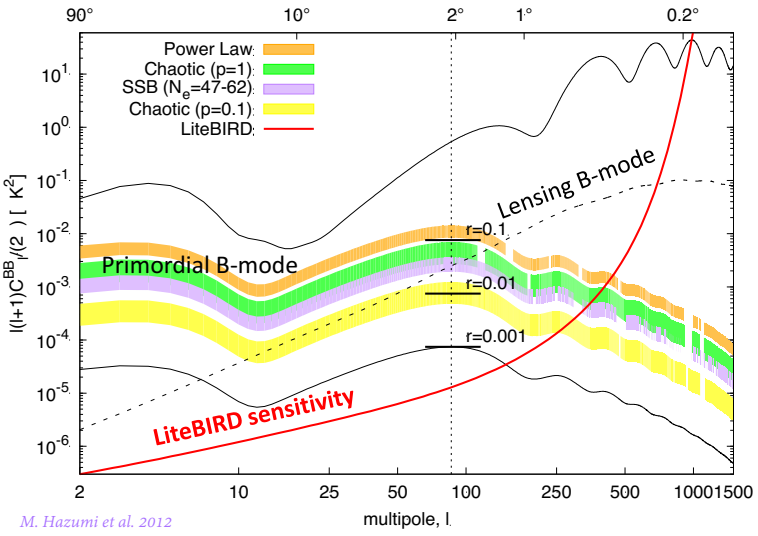

Figure 1.13: The LiteBIRD sensitivities compared to the primordial B-mode for different values of r from 0.1 down to 0.001 and the contamination from the lensing to the B-mode pattern.

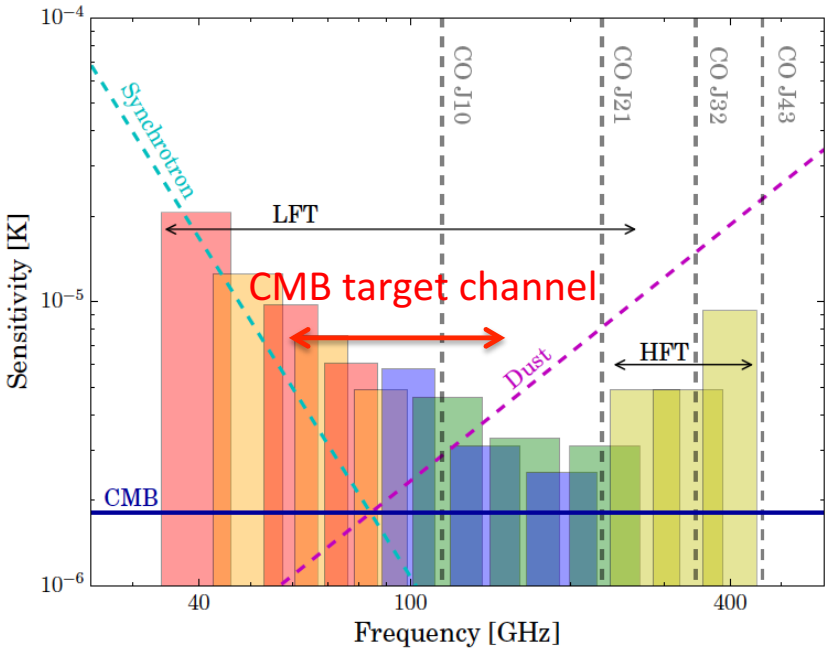

Figure 1.14: The LiteBIRD band locations centre and the sensitivities for each band. It is also shown the contamination from synchrotron and dust emissions, the CMB signal and the most suitable cosmological frequency channels.

Channel [GHz]	Beam [arcmin]	ΔT [μK.arcmin]	ΔP [μK.arcmin]
40	108	42.5	60.1
50	86	26	36.8
60	72	20	28.3
68.4	63	15.5	21.9
78	55	12.5	17.7
88.5	49	10	14.1
100	43	12	17.
118.9	36	9.5	13.4
140	31	7.5	10.6
166	26	7	9.9
195	22	5	7.1
234.9	18	6.5	9.2
280	37	10	14.1
337.4	31	10	14.1
402.1	26	19	26.9

Table 1.7: LiteBIRD specifications. The second column gives the FWHM resolution of the beam. ΔT and ΔP are the instrumental noise 1 σ sensitivities in a 1 arcminute side pixel.

1.9 The CORE mission

Cosmic ORigins Explorer (CORE) is a satellite proposal (105) dedicated to microwave polarization and submitted to the European Space Agency (ESA) in October 2016 in response to a call for future medium-sized space mission proposals for the M5 launch opportunity of ESA's Cosmic Vision programme. The CORE collaboration finalized a collection of papers, *Exploring Cosmic Origins* (ECO), aimed at describing different scientific objectives achievable with the data expected from a mission like CORE, in particular, the mission requirements and design paper (104) and the instrument paper (95) provide a comprehensive discussion of the key parameters of CORE. The paper on extragalactic sources (100) deeply discuss their contribution to the cosmic infrared background (CIB) and the paper on B-mode component separation (280),

focussed on polarization, and the one on mitigation of systematic effects (220) describe potential residuals to be accounted for scientific exploitation. CORE, is designed to fully exploit and provide the definitive maps of the CMB polarization anisotropies at large and medium angular scales. In case of a detection of primordial gravitational waves, CORE will allow a determination of the shape of their spectrum over the largest possible range of cosmological scales. As already said, the signature of the gravitational waves is imprinted at angular scales larger than about one degree in the B-modes of the CMB polarization, which is a specific patterns that cannot be created by ordinary scalar perturbations. However, gravitational lensing of the CMB by intervening massive structures also generates B-modes, peaking on 10 arcmin angular scales. A precise measurement of this lensing effect, required to distinguish between these two sources of B-modes, also provides the opportunity to derive a high fidelity map of dark matter distribution at times and scales inaccessible otherwise, and to address fundamental questions such as the absolute scale of the neutrino masses, with the potential to uncover novel physics. CMB lensing will also provide crucial inputs concerning the early stages of galaxy formation and their arrangement into large-scale structures. These scientific goals can be achieved with extremely sensitive requirements, full sky measurements, an extremely high level of control of instrumental systematic effects and a broad frequency coverage that only a space mission such as CORE can satisfy. CORE is designed to map the full-sky CMB polarization with a mean noise level of approximately 2 μK $\cdot$ arcmin (25 times better than the *Planck* mission in amplitude), with an angular resolution of order 5 arcmin at around 200 GHz. The instrument will host about 19 frequency channels, distributed over a broad frequency range spanning the 60-600 GHz interval, to control astrophysical foreground emission. Indeed, more than 99% of the Galactic emission must be removed from the observed maps, and/or the foreground emission contribution to the angular power spectrum of the observations must be modelled with 10^{-4} accuracy. Another key requirement is the measurement accuracy: all systematic effects will be controlled so that no more than approximately 10^{-4} of the intensity leaks into polarization maps, and that no more than about 1% of E-type polarization leaks into B-type modes. CORE will observe the sky from a large Lissajous orbit around the Sun-Earth L2 Lagrange point on an orbit that offers stable observing conditions and avoids contamination from side lobe pick-up of stray radiation originating from the Sun, Earth, and Moon. The entire sky will be observed repeatedly during four years of continuous scanning, with a combination of three rotations of the spacecraft over different time scales so that each sky pixel is crossed frequently and from many different directions, providing polarization measurements at many different angles. With

about 50% of the sky covered every few days, this scan strategy also provides a powerful mitigation of systematic effects, which is needed to convincingly extract the primordial signal on large angular scales. The baseline measurement concept relies on systematics mitigation and correction with a suitable combination of scanning strategy and data processing. The feasibility of this approach is already supported by a fairly extensive set of simulations carried out by modifying the *Planck* simulation chain. Table 1.8 summarizes the CORE specifications.

Channel [GHz]	Beam [arcmin]	$N_{\rm det}$	ΔT [μK.arcmin]	ΔP [μK.arcmin]	ΔI [μK_{RJ}.arcmin]	ΔI [kJy sr^{-1}.arcmin]	$\Delta y \times 10^6$ [y_{SZ}.arcmin]
60	17.87	48	7.5	10.6	6.81	0.75	−1.5
70	15.39	48	7.1	10	6.23	0.94	−1.5
80	13.52	48	6.8	9.6	5.76	1.13	−1.5
90	12.08	78	5.1	7.3	4.19	1.04	−1.2
100	10.92	78	5.0	7.1	3.90	1.2	−1.2
115	9.56	76	5.0	7.0	3.58	1.45	−1.3
130	8.51	124	3.9	5.5	2.55	1.32	−1.2
145	7.68	144	3.6	5.1	2.16	1.39	−1.3
160	7.01	144	3.7	5.2	1.98	1.55	−1.6
175	6.45	160	3.6	5.1	1.72	1.62	−2.1
195	5.84	192	3.5	4.9	1.41	1.65	−3.8
220	5.23	192	3.8	5.4	1.24	1.85	...
255	4.57	128	5.6	7.9	1.30	2.59	3.5
295	3.99	128	7.4	10.5	1.12	3.01	2.2
340	3.49	128	11.1	15.7	1.01	3.57	2.0
390	3.06	96	22.0	31.1	1.08	5.05	2.8
450	2.65	96	45.9	64.9	1.04	6.48	4.3
520	2.29	96	116.6	164.8	1.03	8.56	8.3
600	1.98	96	358.3	506.7	1.03	11.4	20.0
Array		2100	1.2	1.7			0.41

Table 1.8: Proposed CORE-M5 frequency channels. The sensitivity is estimated assuming $\Delta\nu/\nu$ = 30 % bandwidth, 60 % optical efficiency, total noise of twice the expected photon noise from the sky and the optics of the instrument being at 40 K. The second column gives the FWHM resolution of the beam. This configuration has 2100 detectors, about 45 % of which are located in CMB channels between 130 and 220 GHz. Those six CMB channels yield an aggregated CMB sensitivity of 2 μK.arcmin (1.7 μK.arcmin for the full array).

2

Radio facilities and extragalactic source characterization

2.1 Introduction

Multi-frequency and multi-epoch polarimetric observations of extragalactic radio sources are significantly important in cosmology for several reasons. Radio sources are the most relevant foreground contaminants of the CMB polarization maps on scales up to $\sim$ 30 arcmin up to frequencies of about 100 GHz. A proper characterization of their contribution to the power spectrum in polarization is crucial for a precise assessment of the lensing B-mode signal (5, 154). This, in turn, is essential for the B-modes power spectrum detection and characterization associated with the stochastic background of gravitational waves, the most ambitious goal of current and future CMB projects.

At the same time, radio sources are privileged calibrators for both the polarized intensity and the polarization angle for CMB experiments. Systematic errors due to calibration inaccuracies of the polarization angle are nowadays a limiting factor for CMB polarization experiments. Unfortunately, the number of compact, bright, highly polarized and stable enough extragalactic sources suitable for accurately calibrating CMB polarization maps are rare. New observations with current facilities at millimeter and radio frequencies are crucial for a better characterization of extragalactic radio source properties.

2.2 The Atacama Large Millimeter/submillimeter Array

The ALMA is a gigantic array constructed in the high desert of northern Chile at around 5000 m altitude thanks to a collaboration between North America, Europe and East Asia in cooperation with the Republic of Chile, is one of the most complex astronomical observatory ever built. Because of its extremely high altitude and the limited available oxygen, it is operated from the Operation Support Facility (OSF) at an elevation of 2900 m. Its construction and operations are led by the European Space Agency (ESO), the National Radio Astronomy Observatory (NRAO) and the National Astronomical Observatory of Japan (NAOJ). Even though the antennas are provided by three different vendors, Vertex (North America), AEM consortium (Europe) and Melco (Japan), they share the same specifications (345).

The Atacama array is a radio telescope that observes the sky in the frequency range between 31 GHz and 950 GHz with a typical resolution from 0.2 arcsec to 0.004 arcsec, by means of 66 dish classical Cassegrain antennas of different sizes which provide an unprecedented resolution and sensitivity. Each antenna hosts dual polarization heterodyne receivers that convert the sky signal into a lower frequencies for a straightforward post-processing. Fifty four of them are 12 meters diameter, the remaining have a 7 meters diameter, for a total collecting area of 6600 square meters.

The 12 meters antennas can be spread out to 16 km area such to gather the finer details of the observed sources as a zoom lens, or can be tightly packed into 150 m configuration to have a better sensitivity for extended and fainter objects. Moreover, the instrument is equipped with a compact array (ACA) of twelve 7-m antennas and four 12-m antennas suitable for taking data from large scale structures. Four of the 54 12-m antennas are developed for total power measurements, while the remaining form the Baseline Array (the reconfigurable part of the array). ALMA's most compact configurations is characterized by a resolution ranging from 0.7 arcsec at 675 GHz to 4.8 arcsec at 110 GHz, while for its most extended arrangement, the resolution ranges from 6 mas (milliarcseconds) at 675 GHz to 37 mas at 110 GHz (80).

The highest quality science produced with ALMA will emerge through competitive access over the widest possible user community coordinated via the ALMA Regional Centers (ARCs) whose support is at the basis of the proposal, observation preparation, archiving, distribution, data reduction and data analysis.

ALMA is aimed at the study of the first objects emerged soon after the dark ages billions of years ago, observed today in the millimiter and sub-millimiter bands because of Universe

Band	Frequency (GHz)	T^{a}_{SSB} (K)	T^{b}_{ν} (K)	Configuration
1	31 - 45	17	26	HEMT
2	67 - 90	30	47	HEMT
3	84 - 116	41	60	2SB
4	125 - 163	51	82	2SB
5	163 - 211	65	105	2SB
6	211 - 275	83	136	2SB
7	275 - 373	147	219	2SB
8	385 - 500	196	292	2SB
9	602 - 720	175[c]	261	DSB
10	787 - 950	230[c]	344	DSB

Table 2.1: Summary of ALMA Receivers. [a]Receiver Noise over 80% of the radio frequency band. [b] Temperature at any RF Band. [c]DSB receiver noise temperature is given for Bands 9 & 10.

expansion and at the imaging of the of proto planetary disks. In the nearby Universe, it is also designed to provide the details of stars and planets formation, to recover a complete and excellent map of gas and dust primarily of the Milky Way, to analyze the gas from an erupting volcano of Io (one of the main Jupiter's moon) and studying the origin of the solar wind (317).

Early observations started in October 2011 with proposals for "Cycle 0" and 16 antennas available, each with four receiver bands in two configurations, the Compact Configuration (baselines from 18 m to 125 m) and the Extended Configuration (baselines from 36 m to 400 m). Globally, it operates in both interferometric and single dish mode, providing complete imaging and spectroscopic data. During full operations mode, ALMA Level One Science are the detection of spectral line emission from CO or C^{+} in galaxies as Milky Way at z = 3, the imaging of gas kinematics in a solar-mass protostellar/protoplanetary disk at a distance of 150 pc, allowing the study of the physical, chemical and magnetic field structure of the disk, detect the tidal gaps created by planets undergoing formation and the ability to provide precise images at an angular resolution of 0.1 arcsec (28). Moreover, other fundamental science cases are:

- ⋆ redshifted dust continuum emission from galaxies at z ≥ 10, thus driving the knowledge of galaxy formation;

Frequency (GHz)	Continuum[a] ΔS (mJy[c])	Spectral Line[b] ΔS (mJy)	Beam, 15 km Configuration (arcsec)
110	0.047	7.0	0.038
140	0.055	7.1	0.030
230	0.100	10.2	0.018
345	0.195	16.3	0.012
409	0.296	22.6	0.010
675	1.04	62.1	0.006
850	1.92	101	0.005

Table 2.2: ALMA Sensitivity Goals for the 12-m Array. [a]Bandwidth = 8 GHz, two polarizations, 64 antennas in one minute. [b]Bandwidth = 1 km s^{-1} (equivalent Doppler spread at line frequency), two polarizations. [c]One Jansky (Jy) = 10^{-26} W m^{-2} Hz^{-1}.

- ⋆ measure star-forming galaxies redshift in the Universe through CO emission;
- ⋆ detailed analysis of different galactic environments interstellar medium (ISM) and the probe of cold dust and molecular gas of nearby galaxies;
- ⋆ precise understanding of dense cores gravitational collapse in molecular clouds;
- ⋆ uncover of molecular gas chemical composition that enclose young stars;
- ⋆ observe molecules and dust grains formation in circumstellar shells and envelopes of evolved stars, novae, and supernovae;
- ⋆ allow a better knowledge of dynamical and chemical models of Solar System planets atmospheres and provide unobscured images of cometary nuclei and other Solar System objects.

2.3 The Australian Telescope Compact Array

The ATCA is one of the telescopes operated by the Australia Telescope National Facility (ATNF), an organization developed by the Commonwealth Scientific and Industrial Research Organisation (CSIRO) in April 1990. ATNF supplies open access to different radio telescopes as the 64-m Parkes telescope, the ATCA, the 22-m Mopra telescope, the Long Baseline Array (LBA) and, finally, the Australian SKA Pathfinder (ASKAP), consisting in 36×12-m dishes

currently under construction in Boolardy, Western Australia. ASKAP is expected to observe a 30 square degrees FOV at 1.4 GHz, being a fast 21-cm survey machine designed to carry out large scale HI spectral line, transients and radio continuum surveys of the sky (171).

The ATCA is a radio interferometer made up of six 22-m dishes which constitute 15 baselines in a single configuration. Five antennas (from CA01 to CA05) are movable along a 3-km long east-west track and a 214-m long north-south spur, allowing the hybrid arrays configuration and one (CA06) is fixed at a distance of 3 km from the western end of the track. Thus, the longest possible baseline is 6 km. Each Cassegrain antenna is cryogenically cooled by means of six low noise receivers sampling five frequency range from 1.1 to 105 GHz (λ from 3-mm to 30-cm), while CA06 does not have a 3-mm receiver system (343).

The antennas can be arranged on a limited number of fixed stations with the shortest spacing available of 30 m and the longest 6 km having the minimum grating increment of 15 m. From fall 2006, the standard configurations are:

- ✓ 1 hybrid configuration with a nominal maximum baseline of 75 m (H75);
- ✓ 1 hybrid configuration with a nominal maximum baseline of 168 m (H168);
- ✓ 1 hybrid configuration with a nominal maximum baseline of 214 m (H214);
- ✓ 2 east-west configurations with a maximum baseline of about 375 m;
- ✓ 4 east-west configurations with a maximum baseline of about 750 m;
- ✓ 4 east-west configurations with a maximum baseline of about 1500 m;
- ✓ 4 east-west configurations with a maximum baseline of about 6000 m;

The array is an earth-rotation aperture synthesis radio interferometer. This technique provides a measure of the spatial coherence function of the correlated signal, achieved during a long enough period of time, of the two element interferometers hosted by the antennas array. The ATCA has linear feeds, recording two orthogonal linear polarizations, X and Y (210). The feedhorns are mounted on the optical axis to allow polarization measurements with instrumental polarization below $\sim$ 1% and, conventionally, the Stokes parameters Q and U (and the circular polarization V) can be in error by about 2% of the total intensity value. Measurements of the two linear polarizations phase difference at the receiver by on-line hardware may need further off-line calibration. For an unpolarized source, observing both orthogonal polarisations offers a $\sqrt{2}$ improvement in signal to noise ratio for an intensity image over an image generated

from only one polarization. The signal from the feedhorn is send into a low noise, broadband amplifier.

In radioastronomy, the sensitivity of a telescope is the minimum signal power distinguishable from random noise fluctuations at the output of the receiving system. Usually, it is defined as the spectral power flux density of a source that would produce the same signal power as the noise power. The noise power, due to ground radiation, atmosphere thermal emission variable under different weather conditions, the background radio emission from Milky Way, the receiving amplifier and other system components is typically referred to as equivalent temperature. The temperature due to noise power, the system temperature, T_{sys}, is related to the noise power by the relation $T_{sys} = P_{noise}/k_B\Delta\nu$, with k_B the Boltzmann constant.

The power emitted by a randomly polarized source is received by a radio telescope following $P_{received} = 12AS\Delta\nu$, being A the antenna effective area, S the spectral power flux density and $\Delta\nu$ the frequencies range observed, thus the effective bandwidth. The 12 factor justifies the detector response to only one polarization component of the randomly polarized wave. Since ATCA hosts separated detectors for the two orthogonal polarization, it can detect the total power.

The angular resolution varies depending of the baseline. It increases from longer baselines leaving the point-source sensitivity constant but decreasing the brightness sensitivity proportionally to the beam area (see Table 2.4). At high angular resolution, the telescope is only useful for observing southern objects, while for the lower one, the north-south and hybrid arrays improve the coverage for equatorial sources up to a maximum north-south baseline of 214-m.

Concerning the millimeter observations, the six ACA antennas host 15 mm receivers from 16 to 25 GHz. The 15 mm, 7 mm and 3 mm systems share a common dewar, while separate feed horns are positioned to the Cassegrain focus, thus making impossible simultaneous observations at the three mm bands. The 7 mm system detect signals in the frequency range (30, 50) GHz, and is equipped with feeds and receivers installed into the mm wave receiver packages. Finally, the inner five ATCA telescopes but the CA06 are outfitted with a 3mm receiver and can observe in the range 83 to 105 GHz. A noise diode has been added to CA02 for 3 mm polarization calibration.

Band Name	16 cm	4 cm	15 mm	7 mm	3 mm
Band Code	L/S	C/X	K	Q	W
Frequency Range (GHz)	1.1 - 3.1	3.9 - 11.0	16 - 25	30 - 50	83 - 105
Fractional frequency range	95%	95%	44%	50%	24%
Number of antennas	6	6	6	6	5
Number of baselines	15	15	15	15	10
Primary beam [a]	42' - 15'	12' - 4'	2'	70"	30"
System temperature (K) [b]	45	36	60	112	724
System sensitivity (Jy) [c]	55	43	72	136	1051
Strongest confusing source (mJy) [d]	140 - 24	2.3 - 0.4	–	–	–
Array assumed below	6 km	6 km	6 km	6 km	H214
Synthesized beam [e]	9" - 3"	3" - 1"	0.5"	0.2"	2"
Bandwidth assumed below (GHz)	2	2	2	2	2
Centre frequency assumed below (GHz)	2.1	7.0	17.0	40.0	95.0
Flux sensitivity (mJy/beam) (10 min) [f]	0.04	0.03	0.05	0.09	0.70
Brightness sensitivity (K) (10 min) [g]	0.1	0.1	0.16	0.29	0.02
Flux sensitivity (mJy/beam) (12 hr)	4	3	5	33	83
Brightness sensitivity (K) (12 hr)	0.02	0.01	0.02	0.01	0.002

Table 2.3: Observing Parameters for the 6km Compact Array. [a] Field of view (full width at half power). [b] System temperature at high elevation under reasonable weather conditions (they are weather dependent). [c] Signal which doubles the system temperature. [d] Within FWHM primary beam. [e] HPBW in R.A. for the 6 km array for all but the 3 mm band, for which the H214 array is assumed. [f] Theoretical rms noise; one frequency; dual orthogonal polarization; natural weighting. This is the 1 σ Gaussian-noise level. [g] For the array listed in the same column. This is the 1 σ Gaussian-noise level.

2.4 Scientific case

At high radio frequencies ($\nu > 10\,\mathrm{GHz}$) the bright ($S_{20\,\mathrm{GHz}} \gtrsim 100\,\mathrm{mJy}$) extragalactic radio population is dominated by blazars (BL Lacs and Flat-Spectrum Radio Quasars, FSRQs), interpreted as sources whose relativistic jets are directed very close to the line-of-sight (40). The jets are collimated by intense magnetic fields, the blazar radio emission is synchrotron radiation from a series of blobs along the jet and the observed flux densities are blue-shifted and greatly boosted by relativistic effects.

Band	Array					
	6 km	1.5 km	750 m	EW352	H214	H75
	(K)	(mK)	(mK)	(mK)	(mK)	(mK)
16 cm	0.02	2.1	0.53	0.1	0.1	0.02
4 cm	0.01	1.6	0.4	0.07	0.11	0.01
15 mm	0.02	2.6	0.65	0.12	0.18	0.02
7 mm	0.03	4.8	1.2	0.22	0.33	0.04
3 mm	–	–	–	1.4	2.1	0.24

Table 2.4: Continuum brightness temperature sensitivity after 12 hr integration for bandwidth described in Table 2.3 and for various arrays.

In this scenario, the flat radio spectra are interpreted as the combination of components self-absorbed up to different frequencies. The spectra steepen when the emission becomes optically thin. Young and compact objects are characterised by spectra peaking at high frequencies while older sources are more extended and have spectra steepening at lower frequencies. Occasionally, the spectra may be dominated by a single flaring blob. Measurements of polarimetric properties of radio-loud Active Galactic Nuclei (AGN) at centimetric and millimetric wavelengths carry information on magnetic fields and on the plasma in the inner, unresolved regions of their relativistic jets.

Even if synchrotron radiation can be up to $\simeq 70-80\%$ polarized, the polarization degree of extragalactic sources is rarely observed to be higher than $\sim 10\%$; the median values are $\sim 2.5\%$ at 20 GHz (202) as a result of several depolarization effects. The measured polarized flux is an average of the emission from sub-structures with different orientations of the magnetic field. Further depolarization may be due to amplified differential Faraday rotation being frequency dependent within the bandwidth. As a consequence, polarimetric observations generally require high sensitivities and a detailed knowledge of instrumental properties to perform accurate calibration (204), a delicate procedure at high frequencies. For these reasons, only recently polarimetric surveys of large source samples at $\nu \gtrsim 20$ GHz have become possible, mainly owing to the advent of large bandwidth instruments.

Surveys in polarization available at high radio frequencies, although in a limited frequency coverage around 20 GHz, did not detect any statistically significant relationship between polarization fraction and total flux density or with frequency. On the contrary, various studies

of samples mostly selected at 1.4 GHz and covering broader flux density ranges, reported an increase of the polarization degree with decreasing flux density and with increasing frequency (147, 212, 309, 319, 328), results later challenged (153).

On the whole, our understanding of the high radio frequency polarization properties of extragalactic sources is still limited. This has motivated the new high-sensitivity ($\sigma_P \simeq 0.6$ mJy, a factor $\simeq 2$ better than the AT20G sensitivity) and nearly simultaneous, multi-frequency polarimetric observations over a wide spectral range (5.5 – 38 GHz) whose results are reported here. The faint *Planck*-ATCA Coeval Observations (PACO) sample, a complete sample of AT20G sources with $S_{20\,\mathrm{GHz}} \geq 200$ mJy (201) were observed with the ATCA. The instrumental capabilities were exploited to reconstruct the polarimetric spectral profile to unprecedented detail.

Owing to the completeness of the sample, the high sensitivity and the close-in-time multi-frequency characterisation allows to provide a new statistical assessment of the polarimetric properties of high frequency extragalactic radio sources, analyzing and describing their spectral and polarization behaviour with frequency. Moreover, exploiting the AT20G and PACO observations in total intensity, it is possible to investigate the source variability for 4 – 5 and 8 yr time lags at several frequencies up to 38 GHz.

Subsequently, the previous sample (45) has been extended extracted from the ATCA survey at 20 GHz (218). The PACO faint sample is made up of 159 sources in the South Ecliptic Pole region where *Planck*'s scan circles intersect, providing maximal sensitivity. The new ATCA high sensitivity multi-frequency polarimetric observations comprises 104 faint objects. The frequency coverage was also extended adding polarimetric observations at 2.1 GHz, in order to allow a more comprehensive analysis of rotation measures. Moreover, the high sensitivity polarimetry has allowed a 5 σ detection of the weak circular polarization for $\sim 38\%$ of the data. The observational determination of total intensity spectra was further extended exploiting the GLEAM (GaLactic and Extra-galactic All-sky Murchison Widefield Array) survey data at 20 frequencies between 72 and 231 MHz (165), available for 89 ($\simeq 86\%$) of the sources.

2.5 Observations

The PACO project yielded observations of 464 AT20G sources in 65 epochs between July 2009 and August 2010 in the 5.5 – 39 GHz frequency range with ATCA, nearly simultaneously (within 10 days) with the *Planck* observations. The main goal of the project was to characterize,

in combination with *Planck* data, the total intensity spectra and their variability over a wide frequency range (at least from 5 GHz to 217 GHz, but up to 857 GHz for some sources).

A multi-frequency observing run was dedicated to polarimetry in September 2014 with ATCA (132). The sample was extracted selecting sources (ecliptic latitude < -75 deg) where the satellite scanning strategy implied a better sensitivity.

The 5 extended sources in the sample (i.e. sources larger than the PACO resolution of $\simeq 1$ arcsec) were discarded since the techniques to extract flux densities used for PACO underestimated their flux densities. Initially, the sample was made up by 53 compact sources and recently extended to 104. The new observational campaign has been carried out in March and April 2016, using the same array configuration and, analogously, within three slots in three contiguous days to have the higher frequencies simultaneously observed. In addition, the frequency coverage was expanded with 2.1 GHz polarimetric measurements.

The spectral setup consisted in 3 sets of 2×2 GHz CABB (Compact Array Broadband Backend) bands centred at $5.5 - 9$ GHz, $18 - 24$ GHz and $33 - 38$ GHz, similar to those of the PACO program. In the first campaign, a total of about 12 hr were allocated in three slots of $\simeq 4$ hr each (including overheads and calibration) dedicated to each of the three bands over a period of least three days. Each object was observed for $\simeq 3$ min in two 1.5 min scans at different hour angles for each frequency. The 51 supplementary sources have been observed in all the six bands and first 53 objects was also observed at 2.1GHz, while in the latter the total observing time was approximately 34 hr, including overheads and calibration. The array configuration was H214, a hybrid (antenna are displayed also along the N-S direction) compact array with a nominal spatial resolution ranging from 36 to 5 arcsec in the $5.5 - 38$ GHz range for the 5 most packed antennas. The resolution goes down to $0.5 - 4$ arcsec including also the longest baselines with the sixth antenna, but with a lower sensitivity. A hybrid configuration results in a more homogeneous *uv*-plane coverage of the largest spatial scales in less time. Thus, it provides a better imaging with respect to a non-hybrid solution, at least for point-like objects.

Other observations were carried out in March and April 2016, using the same array configuration (H214) and spectral setup. The compact extragalactic sources at ecliptic latitudes between $-65°$ and $-75°$ become 104. The 51 additional sources were observed in the six CABB bands.

The previous sample have been re-observed at 5.5 and 9 GHz, while at $18 - 24$ and $33 - 38$ GHz were repeated only for 20% of them and the whole sample was observed at 2.1 GHz.

The total observing time was of $\simeq$ 34 hr, including overheads and calibration.

In order to achieve the same sensitivity level of previous observations ($\simeq$ 0.6 mJy), the data have been integrated for 1 min at 2.1, 5.5 and 9 GHz, and for 1.5 min at the higher frequencies. The effective sensitivity reached in polarization at 2.1 GHz was a bit worse than requested, $\simeq$ 1 mJy, due to significant radio-frequency interference (RFI). As done for the September 2014 observations, only data from the 5 closest antennas have been accounted, discarding the baselines with the sixth and farthest antenna, because of the longest baselines larger noise. The synthesized beam size ranges from 90 to 5 arcsec. Weather conditions were good during the whole observing campaign. Were considered only data from the 5 closest antennas in the H214 array configuration, discarding the baselines to the sixth and farthest antenna, because of the high level of noise. The synthesized beam size was $\simeq$ 90 arcsec down to 5 arcsec in the frequency range.

2.6 Data reduction

Data were reduced via the MIRIAD software (294) where each frequency band was treated separately and corrected for the time-dependent instrumental xy-phase variation, by the exploitation of a noise diode signal mounted in one of the feeds of each antenna.

The reference flux density absolute calibrator (at all frequencies) was the source PKS1934-638, a GigaHertz peaked-spectrum (GPS) radio galaxy, stable, unpolarized (at least below 30 – 40 GHz) and the only known source with all these characteristics in the Southern sky, whose last model [1] (231) is stored into MIRIAD. The whole source sample has been re-calibrated to avoid differences with previous data.

Then, to better characterize the source spectra, each 2 GHz-wide frequency band were split in sub-bands but the 2.1 GHz because of the heavy RFI contamination. The sub-bands were calibrated separately. In total intensity, the bands were divided into 512 MHz wide sub-bands but in polarization, in order to limit the $\Delta\nu^{-1/2}$ degradation in sensitivity, the sub-bands were not subdivided.

The sources are known to reveal linear polarization up to $\sim$ 10% (203). Circular polarization of extragalactic radio sources is generally below 0.1 – 0.2%, at least one order of magnitude lower than the linear polarization (277). Hence, the r.m.s. σ_V of the retrieved Stokes parameter

[1] http://www.atnf.csiro.au/observers/memos/AT39.3_124.pdf

is frequently used just as a noise estimator. It was achieved a $5\,\sigma$ detection of circular polarization, V, in $\sim$ 38% of the dataset, i.e. $\sim$ 89% of the objects are manifest this parameter in at least one frequency.

For only $\sim$ 15% of detections, the circular to linear polarization ratio is $\geq$ 20% and the mean circular polarization is substantially smaller than the polarized flux density calibration, which is $\simeq$ 10%. Since the contribution of Stokes V is so small, the polarized emission, P, can be estimated neglecting the V contribution and adopting σ_V as the r.m.s. for Q and U:

$$P = \sqrt{Q^2 + U^2 - \sigma_V^2}\,. \tag{2.1}$$

The σ_V^2 term removes the noise bias on P (339), instead the error associated to the bias correction was negligible and ignored in what follows, so Eq. (2.1) resulted in a mean error of 0.01%. The polarization angle ϕ and fraction m (usually in percentage) are:

$$\phi = \frac{1}{2}\arctan\left(\frac{U}{Q}\right), \tag{2.2}$$

$$m = 100 \cdot \frac{P}{I}, \tag{2.3}$$

where the Stokes I is the total intensity flux density.

Typically, under the assumption of Gaussian noise, the error scales as $1/\sqrt{N}$, N being the number of correlations at a given ν. The errors in total intensity, linear polarization flux density and position angle were computed adopting calibration errors of 2.5% for I and of a conservative 10.0% for the polarization fraction, P, for data between 5.5 and 38 GHz. At 2.1 GHz, due to the aforementioned rfi problems, it was used a 5% in I and a 12.5% in P. The global error on I is indeed given by:

$$\sigma_I^2 = \sigma_V^2 + (0.025\,I)^2. \tag{2.4}$$

The error on the polarized flux density, σ_P, can be derived from the Eq. (2.1). A conservative $\sim$ 10% error in the polarization calibration were adopted, thus :

$$\sigma_P^2 = \frac{Q^2\sigma_Q^2 + U^2\sigma_U^2}{Q^2 + U^2} + (0.1\,P)^2\,, \tag{2.5}$$

$\sigma_{Q,U}$ being the rms errors on Q and U. This estimate of the calibration error is consistent with the differences between flux densities obtained using two different calibrators for reducing the data. From the error propagation law, the global error on the polarization fraction is:

$$\sigma_m^2 = \left(\frac{\sigma_I}{I}\right)^2 + \left(\frac{\sigma_P}{P}\right)^2, \tag{2.6}$$

and that on ϕ is:

$$\sigma_\phi^2 = \frac{Q^2\sigma_U^2 + U^2\sigma_Q^2}{4(Q^2+U^2)^2} + \sigma_{\phi\,\mathrm{CAL}}^2\,, \tag{2.7}$$

where the calibration error on the polarization angle, $\sigma_{\phi,\mathrm{CAL}}$, is added in quadrature. Under the hypothesis that this affects equally Q and U ($\sigma_{Q,\mathrm{CAL}} \simeq \sigma_{U,\mathrm{CAL}} = \sigma_{\mathrm{CAL}}$), $\sigma_{P,\mathrm{CAL}} \simeq 0.1P$ gives $\sigma_{\mathrm{CAL}} = 0.1P/\sqrt{2}$.

Finally, it is easy to derive the relation:

$$\sigma_{\phi,\mathrm{CAL}}^2 \simeq \frac{2\sigma_{\mathrm{CAL}}^2}{4(Q^2+U^2)} \simeq (0.05\,\mathrm{rad})^2\,, \tag{2.8}$$

that implied $\sigma_{\phi,\mathrm{CAL}} \simeq 3°$ and $3.75°$ at 2.1 GHz. This estimation turns out to be consistent with the polarization angle differences obtained by using various calibrators.

2.6.1 Imaging and flux density measurements

To check the assumption of target compactness at all frequencies and the flux density extraction, have been created maps for each Stokes parameter. The detection threshold has been set at 5σ both in I and P, where $\sigma_{I_{\mathrm{map}}}$ was derived from the I region with no emission.

The used task UVFLUX for flux density measurements, in all but few cases, is designed for point-like sources and works directly on visibilities, minimizing artifacts and phase-instabilities which may affect more image-based measurements. Since the sample excludes extended sources (at least up to 20 GHz), it was expected that flux densities provided by UVFLUX and by IMSTAT (the estimation from imaging) had differences no greater than $\sim$ 10% in total intensity (due to residual phase instabilities in the images). Moreover, the source pointing was accurate enough to keep the objects in the phase centre of the *uv*-plane, owing to their belonging to the PACO catalogue in which all positions are known within an accuracy of 1 arcsec.

Afterwards, it has been performed a comparison between the IMSTAT image peak (in mJy/beam) and the UVFLUX flux density estimation (for $\sim$ 90% of the objects) to reveal, in I and P, whether an extended or displaced component is present. The median discrepancies, $\Delta I/I$ and $\Delta P/P$, are $\simeq$ 2.7% and $\simeq$ 4.3%. In total intensity, the relative discrepancy exceeded 10% for $\sim$ 4% of the images and at frequencies greater than 24 GHz they reached the maximum

values between 20% and 25% for 2 objects at 38 GHz. Always, the image peak values were higher than the UVFLUX estimation. Indeed, the sources were barely resolved.

In polarization, the discrepancy was greater than 15% in $\sim$ 11% of the available images and of 20% in $\sim$ 8% of the cases. In particular, the object AT20GJ040848-750720, shown in Fig. 2.1 for 3 frequencies, was characterized by a flux density excess (with respect to UVFLUX) in correspondence of which the image peak reached $\simeq$ 361% at 33 GHz and $\simeq$ 352% at 38 GHz. Furthermore, in Fig. 2.1, polarized emissions are illustrated by contour levels. The object is marginally resolved at the lower frequencies and at the higher frequencies a second component appears that mainly originates the polarized emission. The object AT20GJ0408-7507 is a bright FRII radio galaxy at $z \simeq 0.7$, dominated by two bright lobes having high depolarization, slightly higher in the eastern one.

Thus, given the good matching between the two techniques, the total intensity flux densities have been derived by integrating over a suitable region on I images, while in polarization the flux density has been estimated by the P peak image owing to the emerging point-like component displaced from the phase centre.

2.7 Data analysis

It has been adopted a 5σ level for detections in polarization with a median error of $\simeq$ 0.6 mJy and a detection rate of $\simeq$ 90% for the whole sample. The number of detections was nearly uniform across the observed frequencies (99 sources detected at 5.5 GHz and 94 at 38 GHz). The level of intra-band depolarization was checked by subdividing each 2 GHz-wide band into 1 GHz sub-bands. No systematic differences were found between the two assessments. At 2.1 GHz, due to the impact of RFI, it was not possible to proceed with this check and the detection rate decreased to $\simeq$ 86%.

2.7.1 Fit procedures

To fit source spectra, a double power law has been adopted, both in its convex (Eq. 2.9) or concave (Eq. 2.10) form:

$$S(\nu) = \frac{S_0}{\left(\frac{\nu}{\nu_0}\right)^{-a} + \left(\frac{\nu}{\nu_0}\right)^{-b}}, \tag{2.9}$$

or:

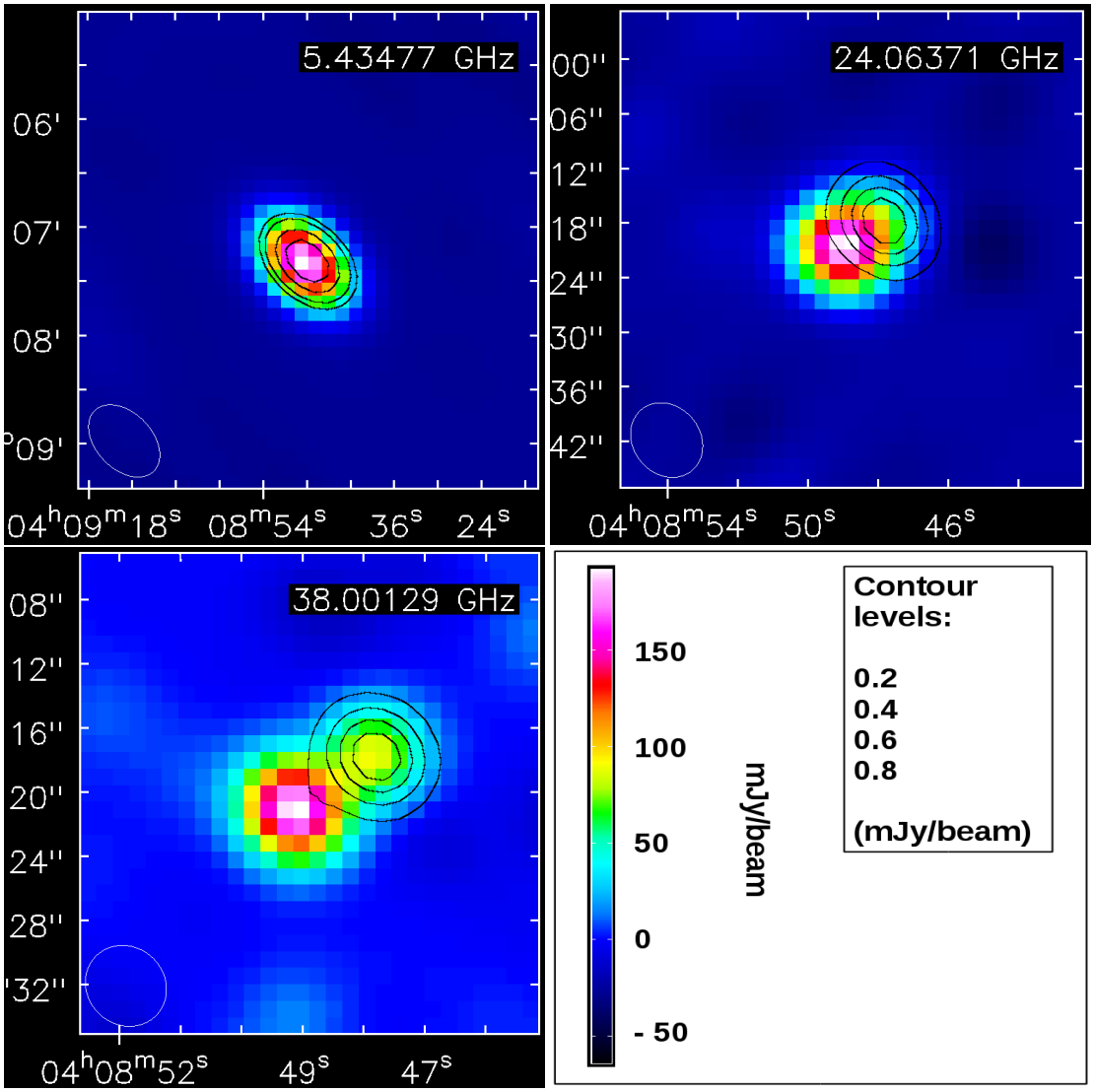

Figure 2.1: Maps in total intensity (colours) and polarization (contours) for AT20GJ0408-7507 at 5.5, 24 and 38 GHz. The two-lobe structure is resolved at the higher frequencies. The eastern lobe appears to be strongly depolarized.

$$S(\nu) = S_0 \left(1 - \frac{1}{\left(\frac{\nu}{\nu_0}\right)^{-a} + \left(\frac{\nu}{\nu_0}\right)^{-b}} \right), \tag{2.10}$$

where S_0, ν_0, a and b are free parameters. In total intensity, Eq. (2.9) satisfied almost the whole sample, Eq. (2.10) only two sources and for two cases it was necessary a triple power law model with 3 additional parameters, i.e. S_1, ν_1 and c:

$$S(\nu) = \frac{S_0}{\left(\frac{\nu}{\nu_0}\right)^{-a} + \left(\frac{\nu}{\nu_0}\right)^{-b}} + \frac{S_1}{\left(\frac{\nu}{\nu_1}\right)^{-b} + \left(\frac{\nu}{\nu_1}\right)^{-c}}. \tag{2.11}$$

In the first run, given the small fraction (less than 10%) of non-detections there were any upper limit when performing the spectral fitting and, in this way, about 85% of the spectra could be successfully fitted. In only three cases (AT20GJ041239-833521, AT20GJ054641-641522, AT20GJ062524-602030), there were any detection in polarization at enough frequencies to get a proper fit.

Similarly to what found for the first sample, most (68%) of our source spectra could be fitted with a double power-law down-turning at high frequencies. An upturning double power-law was required in 15 cases, and a triple power-law in 20 cases. The first dataset showed a median recovered reduced χ^2 of 0.31 and 0.82 for I and P, with a clear conservative error estimate while the second set was characterized by a median values of the reduced χ^2 of 1.12 and 1.89 for I and P, respectively. The spectra for some sources are presented in Fig. 2.2 that shows the fitting curves and, when available, the previous PACO best epoch (2009 – 2010) observations in total intensity, and the AT20G best epoch (2004-2008) observations in total intensity and in polarization. In the lower part of each panel are the polarization fractions (both linear and circular, when detected), followed by the polarization position angles at the different frequencies.

2.7.2 Spectral properties

To minimize fluctuations due to noise, spectral indices were calculated by means of the spectral index $\alpha_{\nu_1}^{\nu_2}$ between the frequencies ν_1 and ν_2, defined as:

$$\alpha_{\nu_1}^{\nu_2} = \frac{\log\left(S(\nu_2)/S(\nu_1)\right)}{\log\left(\nu_2/\nu_1\right)}, \tag{2.12}$$

where $S(\nu_1)$ and $S(\nu_2)$ are the flux densities associated to the two frequencies.

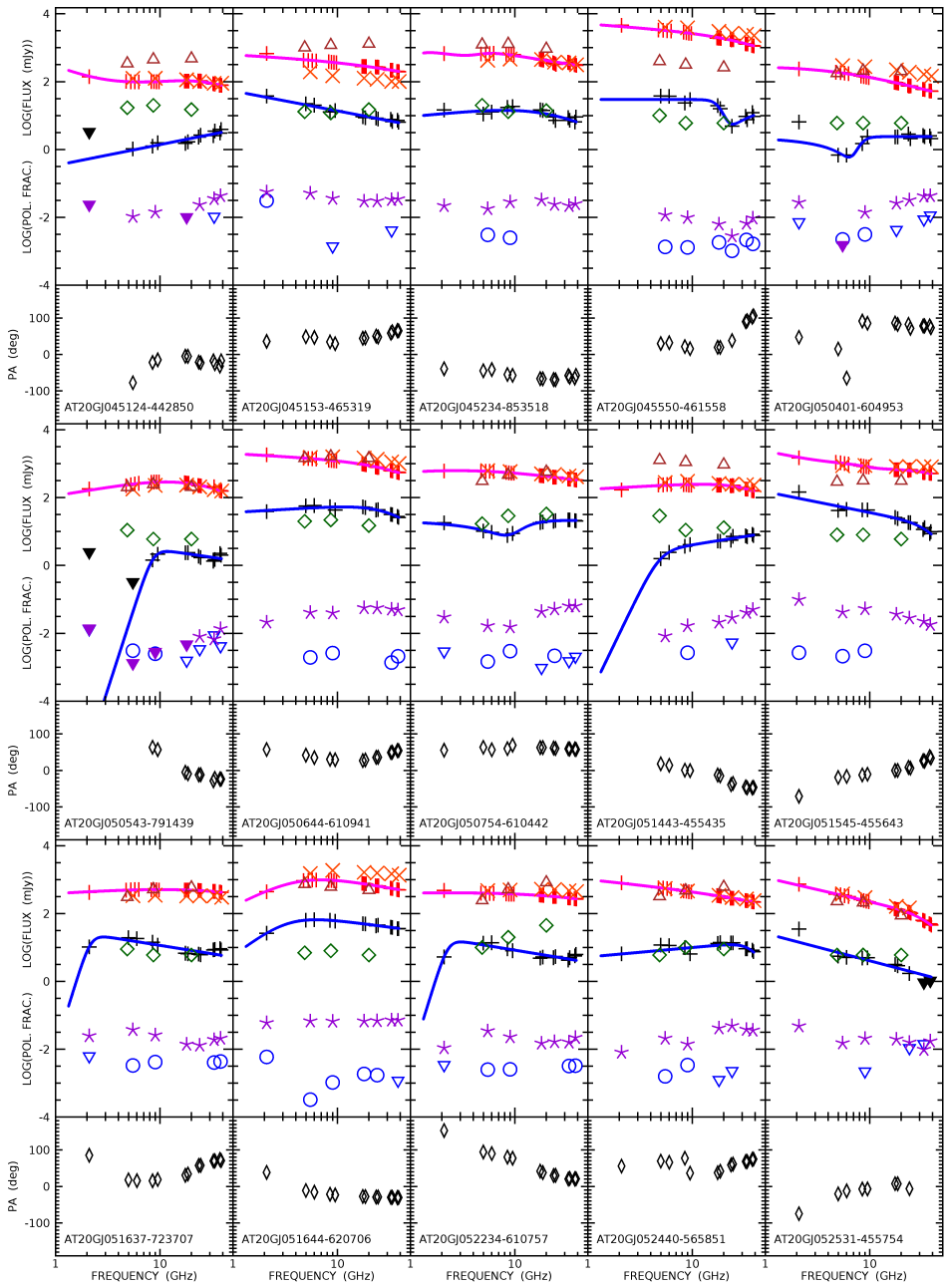

Figure 2.2: Spectra in total intensity and polarization, polarization fraction and polarization angle for some objects of the faint PACO sample, observed in September 2014 and March-April 2016 campaigns. Error bars are not displayed since they are smaller than the symbols. Total intensity: red plus signs show observations, solid magenta lines the fitting curves, orange crosses the median PACO flux densities (July 09-August 10), brown triangles the AT20G observations (best epoch 2004-2008). Polarization (flux density): black plus signs refer to observations, black filled downwards triangles show upper limits, solid blue lines the best fit curves, green diamonds the AT20G observations (best epoch 2004-2008). Data of September 14 and March-April 16 only campaigns: linear polarization fractions (purple asterisks and upper limits reported as downwards pointing purple filled triangles); circular polarization fraction (violet circles) and upper limits (downward triangles); polarization angle (PA) (black diamonds).

Tot. Int. → / Pol. Int. ↓	(In)	(Pe)	(F)	(S)	(U)	
(In)	0	3	0	1	0	4
(Pe)	0	24	4	20	0	48
(F)	0	5	4	4	0	13
(S)	0	5	8	7	0	20
(U)	0	8	5	3	0	16
(NA)	0	1	1	1	0	3
	0	46	22	36	0	

Table 2.5: Distribution of sources per spectral type in total intensity and in polarization. 'NA' refers to the three objects classified in total intensity but missing a spectral fit in polarization. Last row and column gives the total for a given spectral class.

The global reference frequencies have been set selecting 6 frequencies (almost) equally spaced in a logarithmic scale as 2.5, 5.5, 10, 18, 28 and 38 GHz to preserve the equal spacing in logarithmic scale. The spectral classification takes into account $\alpha_{2.5}^{5.5}$ and α_{28}^{38} and identify flat- (F), steep- (S), peaked- (Pe), inverted- (In) and upturning-spectrum (U) object according to $\alpha_{5.5}^{10}$ (or $\alpha_{2.5}^{5.5}$ for the second run) and α_{28}^{38} spectral indices, since the majority of spectral peaks occur around $10-20$ GHz (or below 10 GHz for the second set).

Table 2.5 gives a schematic view of the source classification while Table 2.6 the quartiles of spectral indices distributions. Basically, less than 40% of sources have the same spectral behaviour in total intensity and in polarization, and high- and low-frequency spectral indices are essentially uncorrelated, as shown in Fig. 2.3. The most populated type are peaked (both in I and P) and steep-spectrum sources in total intensity but peaked in polarization. This change in spectral shape toward a peaked- or even an upturning-spectrum in polarization might be the sign of Faraday depolarization which typically lowers the polarization signal at lower frequencies.

Past high frequency flux density measurements may have suffered from the low accuracy of the primary calibrator model. Indeed, the mean high-frequency spectral index of 'PACO faint' sources in total intensity reported in another analysis (45) was flatter by $\delta\alpha \sim 0.3$.

The high-frequency spectral indices steepened at high frequencies and were essentially uncorrelated, although the mean values ($\alpha_{28}^{38} \simeq -0.75$ and $\alpha_{\rm P28}^{38} \simeq -0.80$, respectively) were less steep and closer to each other than found in the first set of data (133). The distribution of

Tot. Int.	2.5 – 5.5 GHz			5.5 – 10 GHz			10 – 18 GHz		
Quart.	Q1	Q2	Q3	Q1	Q2	Q3	Q1	Q2	Q3
All	-0.29	−0.02	0.31	-0.35	−0.11	0.09	-0.46	−0.24	-0.08
Steep	-0.64	−0.33	-0.13	-0.67	−0.37	-0.22	-0.80	−0.46	-0.30
Peaked	0.10	0.32	0.54	-0.04	0.06	0.27	-0.30	−0.14	0.01
Flat	-0.16	−0.01	0.27	-0.25	−0.12	0.06	-0.26	−0.14	-0.05

Tot. Int.	18 – 28 GHz			28 – 38 GHz		
Quart.	Q1	Q2	Q3	Q1	Q2	Q3
All	-0.75	−0.46	-0.27	-1.00	−0.75	-0.44
Steep	-0.91	−0.76	-0.56	-1.56	−1.02	-0.81
Peaked	-0.56	−0.42	-0.28	-0.85	−0.74	-0.56
Flat	-0.33	−0.26	0.09	-0.42	−0.34	-0.20

Pol. Int.	2.5 – 5.5 GHz			5.5 – 10 GHz			10 – 18 GHz		
Quart.	Q1	Q2	Q3	Q1	Q2	Q3	Q1	Q2	Q3
All	-0.28	0.15	0.85	-0.43	−0.06	0.38	-0.61	−0.15	0.34
Steep	-0.46	0.33	0.61	-0.59	−0.06	0.33	-0.74	−0.24	0.29
Peaked	-0.06	0.49	1.04	-0.19	−0.01	0.71	-0.35	−0.06	0.36
Flat	-0.57	−0.21	-0.06	-0.54	−0.29	-0.06	-0.59	−0.33	0.54

Pol. Int.	18 – 28 GHz			28 – 38 GHz		
Quart.	Q1	Q2	Q3	Q1	Q2	Q3
All	-0.98	−0.53	0.02	-1.44	−0.80	-0.03
Steep	-1.00	−0.76	-0.10	-1.47	−0.92	-0.37
Peaked	-0.80	−0.32	0.31	-1.21	−0.73	-0.23
Flat	-1.01	−0.54	0.14	-1.61	−0.68	0.04

Table 2.6: First, second (median), and third quartiles of spectral indices in total intensity and in polarization for different frequency ranges. We give values for the full sample and for the three main spectral classes, as classified in total intensity.

sources among the different spectral types were also very similar, the biggest difference being in the fraction of objects classified as flat-spectrum in total intensity that increased from $\simeq 4\%$ to $\simeq 21\%$.

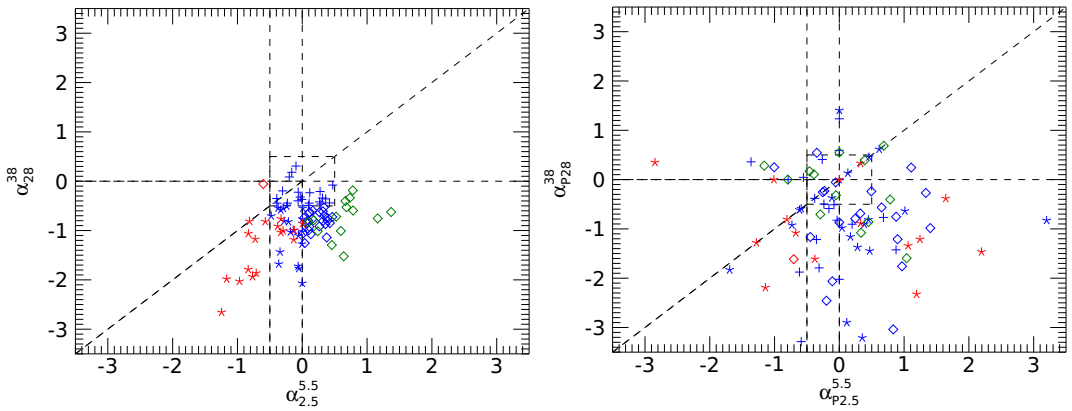

Figure 2.3: Radio colour-colour diagrams for (from left to right) total intensity and polarized flux density. Symbols identify the spectral type in total intensity: plus for flat-spectrum, asterisks for steep-spectrum, diamonds for peaked-spectrum. Colours refer to the spectral shape between 5.5 and 18 GHz: red for steep-spectrum, blue for flat-spectrum, and green for peaked-spectrum sources.

To extend the spectral coverage, it has been exploited the GLEAM (GaLactic and Extragalactic All-sky Murchison Widefield Array) survey data at 20 frequencies between 72 and 231 MHz. The spatial resolution were $\simeq$ 2 arcmin at 200 MHz, similar to the $\sim$ 90 arcsec resolution of the 2.1 GHz observations. There were 89 matching sources ($\simeq$ 86% of our sample) in the GLEAM survey and, since it covers all the sky south of +30° in declination with a mean sensitivity of $\sim$ 10 mJy, and the sample of this investigation were located between −86° and −42°, it could be possible to associate an upper limit of 50 mJy (at 5σ) to those sources without a GLEAM counterpart.

The fitting curves (triple power-laws), although not always successful, generally showed good consistency between ATCA and GLEAM measurements (Fig. 2.2). But while in the range 5.5 GHz – 38 GHz the spectra were consistent with a single emitting region, the GLEAM flux densities were clearly above the extrapolations from higher frequencies in $\sim$ 40% of the cases, strongly suggesting the presence of at least another, generally steeper, component. The joint analysis with polarization data suggested even more complex structures (117) (see subsection 2.7.3).

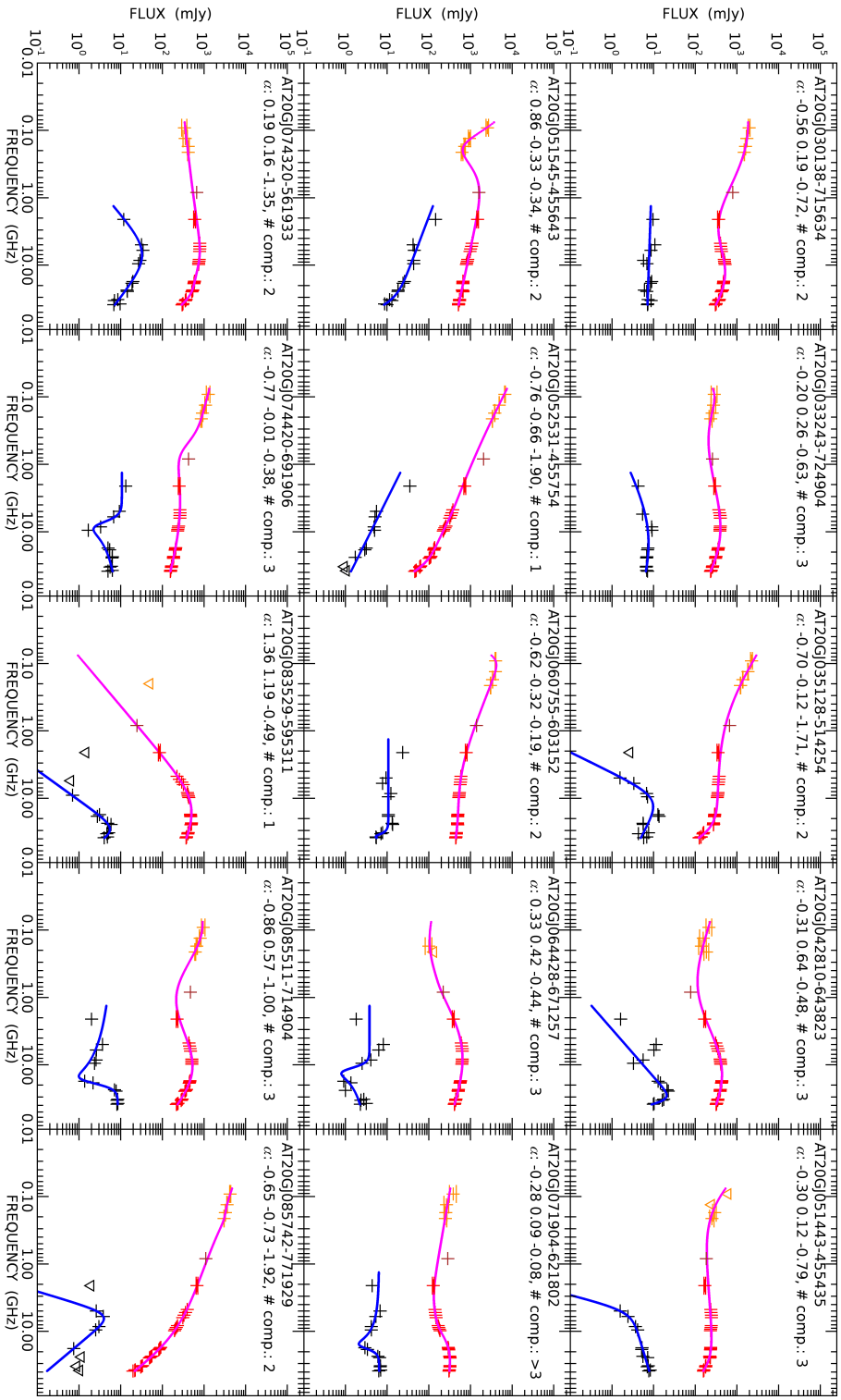

Figure 2.4: Spectra in total intensity and polarization with GLEAM observations between 72 and 231 MHz (orange plus), current observations in total intensity (red plus) and polarization (black plus and downward triangles), fits in total intensity and polarization (red and black solid curves). The SUMSS (209) flux density at 843 MHz is shown for comparison, but not used in the fit procedures. For each object, spectral indices (in total intensity) $\alpha_{0.2}^{0.4}$, $\alpha_{2.5}^{5.5}$ and α_{28}^{38} are provided. Is also reported the spectral classification in terms of estimated synchrotron components (see 2.7.3).

2.7.3 Linear polarization fraction

There is any systematic variation of the mean polarization fraction with either flux density or frequency, down to $\simeq$ 5 GHz, in agreement with previous results. A similar conclusion was reached by (26), who however had measurements only down to 8.4 GHz. On the other hand, claims of a systematic decrease of the polarization fraction with decreasing frequency (6, 8) suggested that Faraday depolarization may work up to $\simeq$ 10 GHz or that the magnetic field is more ordered at high frequencies (328). However the conclusions (6, 8, 290) may be biased towards greater polarization fractions in not having taken into account non-detections (329).

These new observations allowed the extension of polarized intensity spectra down to 2 GHz and a doubled sample. Typically, high detection rate (over 90%) safeguards against any selection bias. Although the polarization fraction declined for several sources drops at lowest frequency, there were any statistical evidence of a decrease of the mean value for the whole sample or for a sub-sample. However, as discussed below, such apparent uniformity may hide a more complex situation. The steep-spectrum objects (36) indeed showed a slight trend, but comparing to the distributions of polarization fraction at 2.1 and 38 GHz, the rejection of the null hypothesis reached the $\simeq 2\sigma$ level. The sample of flat-spectrum objects (22 in total) seemed to reveal an opposite trend, but also in this case the significance was less than 3σ.

Usually, the spectra of the polarization fraction turned out to be less smooth than the total intensity ones. Only about 15% of the sources had an approximately constant polarization fraction over the frequency range. Five sources with smooth total intensity spectra above 2 GHz were characterized by double peaked fractional polarization behaviour, suggesting at least two emission components. The polarization fraction of $\sim$ 15% of the sources had an upturn at 2 GHz, where the emission components seen in the GLEAM data could have yield a substantial contribution. The polarized flux from these components can have drown out the decrease of the polarization fraction of the higher frequency component due to Faraday depolarization. The most straightforward interpretation of these results was that the extension and, correspondingly, the age of emission components increases with decreasing frequency.

On the whole, a joint inspection of total intensity (including GLEAM measurements) and polarization spectra indicated the presence of at least 2 (or sometimes 3) emission components for about 93% of the sources. This was expected for GPS/CSS sources due to their double lobe structure (58, 323). For about the half, the clearest indication could be derived from polarization data. Hence, the sample has been reclassified to distinguish no sign of additional

synchrotron component cases (1C) from hints of $2-3$ synchrotron components (2-3C) or more complicated cases with more than 3 components (>3C) in the spectrum. The latter are quite flat sources in total intensity from 70 MHz up to $\sim$ 30 GHz, where a steepening typically occurred. Among these 17 objects ($\simeq$ 16%), 10 were classified as flat (F).

According to right panel of Fig. 2.5, there is no evidence of linear polarization fraction trends with frequency. Sources 2-3C have a polarization fraction minimum at $\simeq$ 9 GHz, consistent with different emission components at lower and higher frequencies. For the >3C objects, whose spectra show indications of several overlapping synchrotron components, there is a hint of a *decrease* with increasing frequency, rather than of the increase expected of the polarization fraction: the mean values declined from $\simeq 2.1-2.4\%$ at $\leq$ 5.5 GHz to 1.2% at 38 GHz. Moreover, these sources had very large rotation measures (RMs) at mm wavelengths, indicating that their high frequency components were characterized by a really dense and/or a magnetized medium that strongly rotates the polarization angle (232).

2.7.4 Polarization angle: cm- and mm-wavelength regime behaviour

The polarization angle was calibrated to be consistent with those measured by *Planck* and based on the CMB dipole measurements to within $\pm 2^{\circ}$.

It was found evidence of non-zero Faraday rotation for only 2 objects (over a total of 53), since for the overwhelming majority of the sources the rotation measure (RM) dependence with λ^2 had a complex behaviour. Only 9 objects could be described by a linear RM–λ^2 relation at all the frequencies. For these sources, RM estimates were between -72 and 57 rad/m^2, with 4 cases compatible with a low ($\sim \pm 10$ rad/m^2) or a null rotation.

Globally, it was possible to identify two regimes, one at cm-wavelengths and one at mm-wavelengths that were fitted separately, from 2.1 to 9 GHz and from 18 to 38 GHz. The fit was discarded if the reduced $\chi^2 > 2$ (probability < 0.1). Finally, $\sim$ 40% and $\sim$ 57% were successful fits for the low and high frequency regimes, respectively. The corresponding median values of the reduced χ^2 were 0.37 and 0.69.

The medians and quartiles at cm- and mm-wavelengths are reported in Table 2.8 and Table 2.9, for all the acceptable fitted objects and for the 1C, 2-3C and >3C types. The error associated to the estimated RMs could have been large, especially at the higher frequencies because of its dependence on $1/\lambda^2$. Typical uncertainties were of about 9% (low) and 32% (high) frequencies, respectively; thus while at the lower frequencies only 2 ($\sim$ 5%) of the estimated

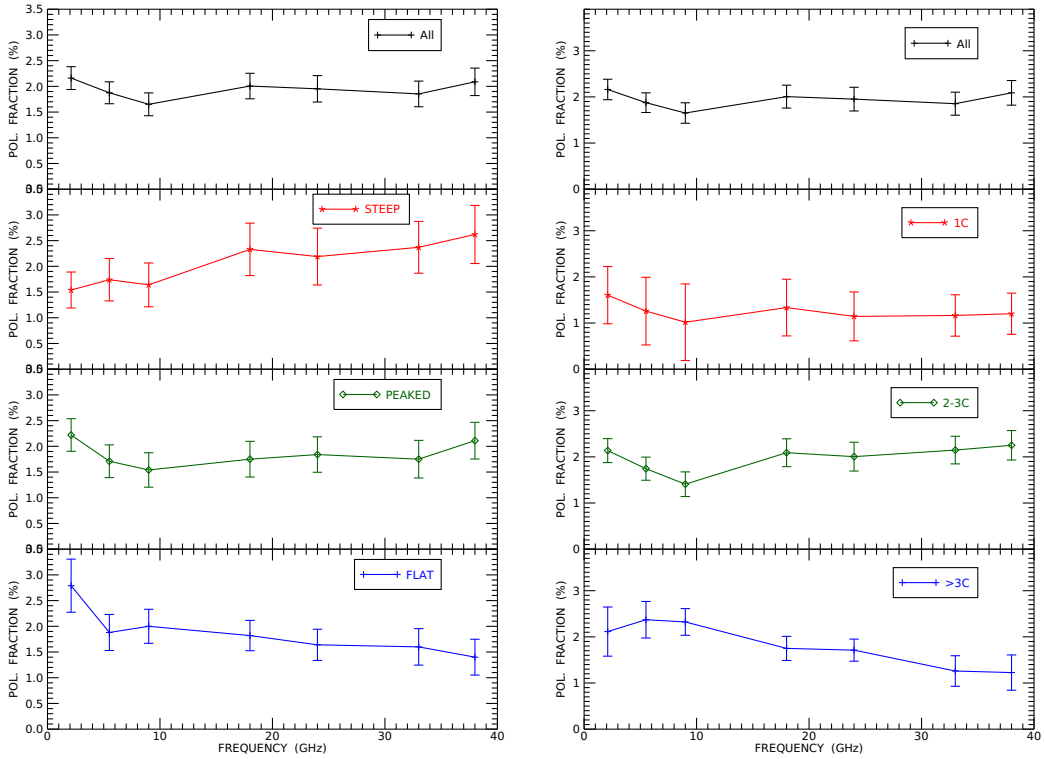

Figure 2.5: Left panel: median polarization fraction behaviour with frequency (at 2.1, 5.5, 9, 18, 24, 33 and 38 GHz) for all the sources (black), for steep sources (red), for peaked (green) and flat ones (blue). Right panel: the same as left panel but for: '1C' sources (red), for '2-3C' sources (green) and for sources with more than 3 components (blue, labelled '>3C'). The errors on median values are given by $1.253 \times \mathrm{rms}/\sqrt{N}$, where rms is the standard deviation around the mean and N is the number of the data (at a given frequency) for a given class of objects (left panel) and the number of detected sources (right panel) (16).

Class.	frequencies (GHz)											
	2.1			5.5			9			18		
	Q1	Q2	Q3	Q1	Q2	Q3	Q1	Q2	Q3	Q1	Q2	Q3
All	1.09	2.16	2.98	0.84	1.88	3.25	0.79	1.65	3.02	0.99	2.01	3.07
Steep	0.95	1.54	2.54	0.81	1.74	3.23	0.95	1.64	3.69	0.87Âă	2.33	3.13
Peaked	1.14	2.22	2.75	0.67	1.71	3.16	0.64	1.54	2.78	0.85	1.75	3.05
Flat	1.73	2.79	3.36	1.09	1.88	3.38	1.19	2.00	2.81	1.35	1.82	2.67
Prob.	(5.5 – 9) GHz			0.825			(18 – 38) GHz			$8.176 \cdot 10^{-4}$		

Class.	frequencies (GHz)								
	24			33			38		
	Q1	Q2	Q3	Q1	Q2	Q3	Q1	Q2	Q3
All	1.06	1.95	2.87	1.17	1.85	3.29	1.20	2.09	3.54
Steep	0.66	2.19	4.28	1.31	2.37	3.84	1.17	2.62	4.00
Peaked	1.26	1.84	2.72	1.25	1.75	2.81	1.31	2.11	3.42
Flat	0.98	1.64	2.45	0.66	1.60	2.08	1.06	1.40	2.11
Prob.	(All freqs.)			0.011					

Table 2.7: First, second (median) and third quartiles of the polarization fraction at each observed frequency given by the Kaplan-Meier estimator, taking into account the upper limits, for the full sample and for the steep- and peaked-spectrum sources. The last row reports probabilities for the null hypothesis (i.e. the two samples are drawn from the same parent distribution) given by the Kolmogorov-Smirnov test performed on the steep and peaked groups, considering together 5.5 and 9 GHz, the 18 – 38 GHz frequency interval and all the frequencies, respectively.

RMs were compatible with a null rotation at the $1\,\sigma$ significance level, this fraction raised to 15% at the higher frequencies.

The median *observed* (i.e. uncorrected for the redshift) values of the RM at low frequency were $\sim 40\,\mathrm{rad/m^2}$ independently of the spectral type. At high frequencies they were larger for the whole sample by a factor ~ 15 (i.e. $\sim 600\,\mathrm{rad/m^2}$) and for 1C or 2-3C objects, and much larger for the >3C objects ($\sim 1100\,\mathrm{rad/m^2}$). Large values of RMs for multi-component sources previously reported suggesting that the youngest, highest frequency components could be characterised by a really dense and/or a magnetized medium that strongly rotates the polarization angle. The RM at the source, $\mathrm{RM_{AGN}}$, are related to $\mathrm{RM_{obs}}$ by (172):

$$RM_{obs} = \frac{RM_{AGN}}{(1+z)^2} + RM_{Gal} + RM_{ion}, \tag{2.13}$$

where RM_{Gal} and RM_{ion} are the contributions of our Galaxy and of Earth's ionosphere, respectively. The Galactic contribution can typically vary from -300 to 300 rad/m^2 depending on the line of sight. The sample was located in a region around the Southern Ecliptic Pole and it was adopted the Galactic Faraday rotation map provided by (225) to have the appropriate correction. The ionospheric contributions was typically found to be $\lesssim 5$ rad/m^2 (172) and could be neglected.

For some sources (44) it was evaluated the redshift and the RM_{AGN} (see Table 2.8 and Table 2.9). The median low-frequency value was around 90 rad/m^2. At high frequencies there was a strong increase of the median RM_{AGN} from 1C to 2-3C to >3C objects (median RM_{AGN} of $\simeq 700$, $\simeq 2400$ and $\simeq 4000$ rad/m^2), but the limited number of 1C and >3C objects prevented any firm conclusion. It was, however, remarkable that the large RMs of >3C objects echo the decrease of their median polarization fraction at mm wavelengths.

All sample (42)			1C (3)			2-3C (31)			>3C (8)		
I	med	III	I	med	III	I	med	III	I	med	III
18	37	58	-	60	-	15	34	53	-	37	-
All sample (23)			1C (2)			2-3C (18)			>3C (3)		
I	med	III	I	med	III	I	med	III	I	med	III
40	94	244	-	335	-	46	84	220	-	122	-

Table 2.8: Median plus I and III quartile values of cm-wavelengths RMs. The upper set of values refers to the observed RMs, the lower to the RMs at the source for the ones with known redshift. For each group is given total sources number in parenthesis, if < 10 is provided only the median value. RMs are in rad/m^2.

All sample (59)			1C (4)			2-3C (50)			>3C (5)		
I	med	III	I	med	III	I	med	III	I	med	III
225	635	1397	-	342	-	283	637	1397	-	1141	-
All sample (27)			1C (2)			2-3C (22)			>3C (3)		
I	med	III	I	med	III	I	med	III	I	med	III
679	2300	5252	-	742	-	716	2351	5191	-	4022	-

Table 2.9: The same as Table 2.8 but for mm-wavelengths.

2.7.5 Circular polarization

Typically, the circularly polarized emission is weak, $\lesssim 0.1\%$ (277), but potentially very interesting because its measurements may allow to gain information on various properties of jets, such as magnetic field strength and topology, the net magnetic flux carried by jets (generated in the central engine), the energy spectrum of radiating particles, and the jet composition, i.e. whether jets are mainly composed of electron-positron pairs or electron-proton plasma (287).

The most obvious candidate for explaining circular polarization of compact radio sources is intrinsic emission, but the expected level under realistic conditions appears to be too low to explain the observed polarization (338). Some authors (227) pointed out that magnetic fields computed from the circular polarization, assuming it is intrinsic, are usually so high to cause a turnover in the intensity spectrum through synchrotron self-absorption at a considerably higher frequency than observed. The most promising mechanism is Faraday conversion, a birefringence effect that converts linear to circular polarization.

At two frequencies (5.5 and 9 GHz), more than 50% of the sources were detected and evaluated median values of the circular polarization fractions, $m_{\rm V}$, finding $m_{\rm V\,median} = (0.23 \pm 0.01)\%$ and $(0.27 \pm 0.02)\%$, respectively. In literature, the median $m_{\rm V}$ of a sample selected at 4.85 GHz is $\simeq (0.05 \pm 0.02)\%$. The derived larger values may arise because of the higher selection frequency, thus on a overwhelming majority of blazars objects. It has been found that these objects have larger circular polarization fractions than radio galaxies (277).

2.8 Source counts in polarization

Fig. 2.7 shows the differential source counts in polarization at 20 GHz obtained through the convolution of the total intensity differential source counts (102) with the polarization fractions distribution at 18 GHz. In Table 2.10 and in Fig. 2.6 are reported the observed distribution (black circles). In each bin uncertainties are derived assuming a Poisson statistics and solid line is the fit assuming a log-normal distribution:

$$f(\Pi) = \text{const} \cdot \frac{1}{\sqrt{2\pi}\,\sigma\Pi} \exp^{-\frac{1}{2} ln(\Pi/\Pi_m)^2/\sigma^2}, \tag{2.14}$$

where const= 0.96, $\sigma = 0.76$ and $\Pi_m = 2.00$, i.e. the median value of the distribution. The reduced χ^2 value is 0.21. In Table 2.11 and in Fig. 2.7 (black circles) the differential source counts in polarization are plotted. Since there is no evidence of a correlation between the total

intensity flux density and the polarization fraction, the number counts $n(P) \equiv dN/dP$ can be determined by:

$$n(P) = \int_{S_0=P}^{\infty} \mathcal{P}\left(m = \frac{P}{S}\right) n(S) \frac{dS}{S}, \tag{2.15}$$

where $n(S)$ is the assumed source counts in total intensity, $\mathcal{P}$ is the probability density distribution for the polarization fraction m, i.e. $\Pi/100$. Note that in each bin in P the integration over S is truncated at $S_0 = P$, which corresponds to the maximum degree of the polarization fraction (i.e. $m = 1.0$). These results are compared with source counts provided by (202) (blue diamonds) via a MCMC simulation of the whole AT20G catalogue and with the model (329) (red and blue lines, referred to the lower and upper level expected). Since the sample is mainly composed by blazars (BL Lacs and FSRQs), typically labelled as 'flat', and represent the dominant population at 20 GHz (dashed lines), there is a good agreement with the limits on the counts provided by the model. Hence, given the assumptions on the median polarization fraction of steep–spectrum radio sources higher than current findings, an overestimate of source number counts in polarization below 10 mJy can be (at least partially) explained. Note that Eq. (2.15) assumes independence of the polarization fraction from the total flux density. However, it is possible that another population with different polarization properties becomes increasingly important with decreasing flux density.

Π (per cent)	Probability	lower uncert.	upper uncert.
0.600	0.2404	0.0453	0.0453
1.800	0.2644	0.0446	0.0446
3.000	0.1843	0.0381	0.0470
4.200	0.0721	0.0222	0.0317
5.400	0.0321	0.0153	0.0253
6.600	0.0160	0.0104	0.0211
7.800	0.0160	0.0104	0.0211
9.000	<0.01843		
10.200	<0.00801		
11.400	0.0080	0.0066	0.0184

Table 2.10: Distribution of the polarization fractions at 18 GHz for the full sample.

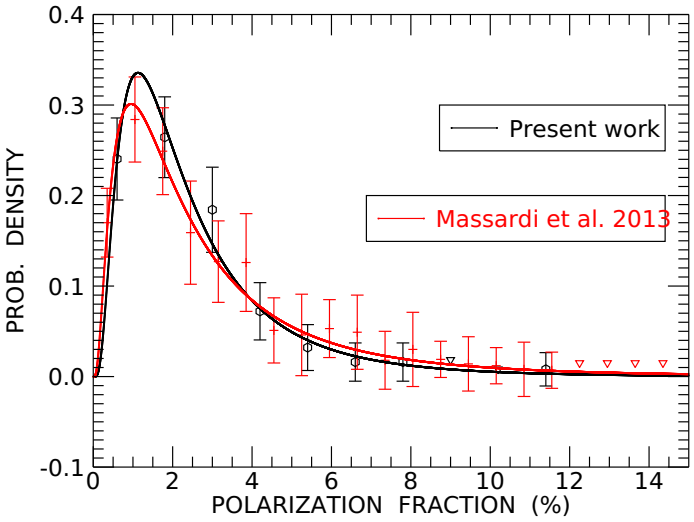

Figure 2.6: Distribution of the polarization fraction at 18 GHz. Errors and upper limits correspond to a 1σ level. The black circles refer to the sample studied in this analysis, the red plus signs to the full AT20G bright sample. The corresponding fit by a log-normal distribution for each dataset is reported with a solid lines of the same color.

2.9 Variability

Taking into account the PACO and the AT20G measurements, the 53 sources analysed in the first run were characterized by at least three epochs of observations in total intensity and two epochs in polarization (no polarization data from PACO). The AT20G data were taken between 2004 and 2008, the PACO data between July 2009 and August 2010 and the present sample in September 2014. The typical global time span about eight years. In several cases all the frequencies were observed two or three times. In many more cases the observations have been repeated for only a subset of frequencies.

Only PACO observations for at least 4 frequencies carried out within several months have been considered. This catalogue reports for each 2 GHz frequency band 4 flux densities, one for each 512 MHz sub-band. Before performing any temporal average, the median value for the 4 chunks must be accounted. The error associated to the averaged PACO flux densities σ_{PACO}, is given by:

$$\sigma_{\mathrm{PACO}} = \sqrt{\sigma^2_{\mathrm{max}} + \sigma^2_{\langle S \rangle_{\mathrm{PACO}}}}\,, \tag{2.16}$$

log [$P(Jy)$]	$S^{5/2}n(S)$ (Jy$^{3/2}$sr^{-1})	lower uncert.	upper uncert.
-2.897	0.0667	0.0007	0.0007
-2.692	0.0760	0.0011	0.0011
-2.486	0.0869	0.0017	0.0017
-2.281	0.1011	0.0025	0.0025
-2.075	0.1198	0.0039	0.0039
-1.870	0.1426	0.0061	0.0061
-1.664	0.1662	0.0094	0.0094
-1.459	0.1856	0.0142	0.0142
-1.253	0.1978	0.0209	0.0209
-1.048	0.1987	0.0299	0.0299
-0.842	0.1886	0.0417	0.0519
-0.637	0.1734	0.0549	0.0766
-0.431	0.1580	0.0726	0.1199
-0.226	0.1447	0.0996	0.2034
-0.020	0.1337	0.1297	0.3606
0.185	<0.31886		
0.391	< 0.64841		
0.596	<1.31855		

Table 2.11: Euclidean normalized differential source counts at 20 GHz in polarization obtained in this paper via the convolution of the distribution of the polarization fraction at 18 GHz with the model (102).

were $\sigma_{\max}$ is the maximum error for 512 MHz sub-bands and $\sigma_{\langle S\rangle_{\rm PACO}}$ the error associated to the average of the PACO fluxes in the selected epochs, $\langle S\rangle_{\rm PACO}$. The AT20G data were collected at 4.86, 8.64 and 20 GHz with the old ATCA correlator set with a 2×128 MHz contiguous bands for each frequency. It was possible to compare these observations with the sample of this study at 5.5, 9 and 18 GHz, neglecting the small differences in the central frequencies. The variability index (V.I.) of a population is defined as:

$$\text{V.I.} = \frac{100}{\langle S\rangle}\sqrt{\frac{\sum_{i=1}^{n}(S_i - \langle S\rangle)^2 - \sum_{i=1}^{n}\sigma_i^2}{n}}, \tag{2.17}$$

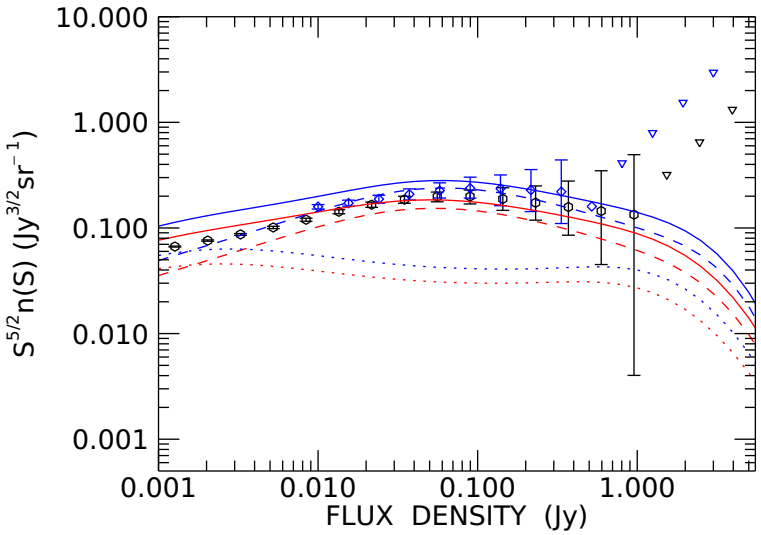

Figure 2.7: Differential source counts at 20 GHz in polarization (black circles) and upper limits (black downward triangles). Ffor comparison, are shown the polarimetric data estimates from the survey (202), shallower than the present one ($S_{20\,\mathrm{GHz}} > 500$ mJy) combined with the full AT20G catalogue (blue diamonds) and upper limits (blue downward triangles). The curves show the model predictions: blue for the 'conservative' case and red for the 'optimistic' case. Solid lines represent the total number counts; dotted lines are for steep-spectrum sources (classified at low frequencies); dashed lines are for flat objects (flat-spectrum radio quasars, i.e. FSRQs and BL Lacs).

$\langle S \rangle$ being the average of the n flux density measurements at a given frequency, S_i, with error σ_i.

In Table 2.12 are reported the mean V.I. in intensity for each frequency and for the time lags that correspond to the intervals between the present observations and the PACO or the AT20G ones. Variability indices were computed for the full sample, for steep- and peaked-spectrum populations. The errors in table are the rms of the V.I. rescaled by the $\sqrt{N}$, where N is the number of objects in the considered class.

For 4 – 5 years time lag, the mean V.I. of steep-spectrum sources increases with frequency, consistently with other results (45). The increase was slightly milder for the full sample because it was not seen in the case of peaked-spectrum sources. No trend with frequency was found for the 8 years lag. Fig. 2.8 reports the variability index against the time lag. On average, there is an increase of the variability index with the time lapse at all the frequencies. Moreover, those that have measurements at the highest frequencies have variability indices typically higher than those associated to lower frequencies.

Sel.	Time (yr)	5.5 GHz	9 GHz	18 GHz	24 GHz	33 GHz	38 GHz
All	4 – 5	14 ± 2	14 ± 2	15 ± 2	16 ± 2	21 ± 2	22 ± 2
	8	36 ± 3	32 ± 3	36 ± 3	–	–	–
Steep	4 – 5	10 ± 2	10 ± 2	12 ± 2	14 ± 2	21 ± 3	24 ± 3
	8	35 ± 5	32 ± 5	38 ± 5	–	–	–
Peaked	4-5	20 ± 3	20 ± 3	18 ± 3	19 ± 3	20 ± 4	19 ± 3
	8	38 ± 5	32 ± 5	31 ± 5	–	–	–
All (pol.)	8	50 ± 7	57 ± 6	53 ± 6	–	–	–

Table 2.12: Mean variability indices in total intensity and in polarization (last row).

Due to the lack of PACO polarization data, V.I. could be estimated only for the 8 year lag (last line of Table 2.12). Also, due to the larger fractional uncertainties, the analysis could be made only for the full sample. The values derived were substantially larger than in total intensity, with no significant frequency dependence.

2.10 Conclusions

The high sensitivity polarimetric observations carried out in 7 bands, centered at 2.1, 5.5, 9, 18, 24, 33 and 38 GHz, of a complete sample of 104 extragalactic sources with $S_{20\mathrm{GHz}} \geq 200$ mJy in the AT20G catalogue, have an r.m.s error in the polarized flux density of 0.6 mJy at $\nu \geq$ 5.5 GHz and 1 mJy at 2.1 GHz because of the heavy RFI contamination.

A 51 sample was observed in a second campaign, while 53 initial sources were re-observed at 5.5 and 9 GHz and only 20% of them were surveyed at 18, 24, 33 and 38 GHz . The previous measurements at 33 and 38 GHz were re-calibrated using the updated model for the flux density absolute calibrator, PKS1934-638, not available for the earlier analysis.

The continuum spectra have been analyzed in view of the GLEAM survey data at 20 frequencies between 72 and 231 MHz, available for 89 ($\simeq$ 86%) of present sources, for which there are the unparalleled coverage of 2.7 decades in frequency.

The total intensity data from 5.5 to 38 GHz could have been interpreted as a single emission region. A joint analysis of the more extended total intensity spectra presented here and of the polarization spectra revealed a more complex astrophysics. About 93% of actual sources

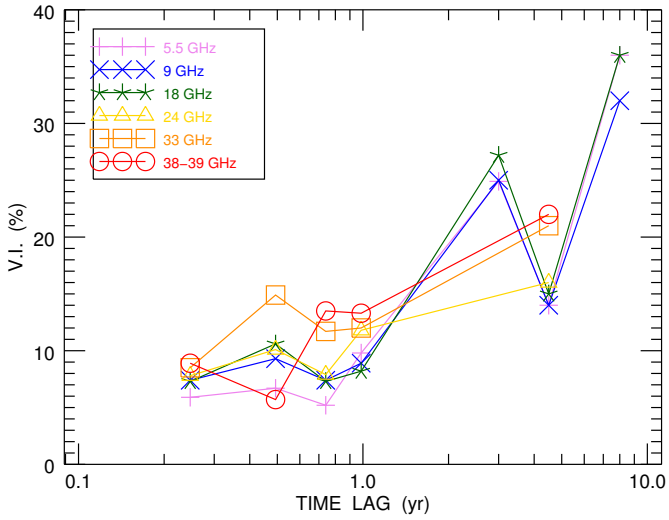

Figure 2.8: Mean variability indices in total intensity *vs.* time lag at the observed frequencies (different colours). Variability measurements for the faint PACO sample are also displayed.

showed clear indications of at least two emission components, one (or sometimes more) dominating the higher frequencies and self-absorbed at few GHz, and another one, generally steeper, emerging at lower frequencies. The most straightforward interpretation of these results is in terms of recurrent activity, with the extension (and, correspondingly, the age) of emission components increasing with decreasing frequency, i.e. with younger components showing up at higher frequencies.

There was no evidence of linear polarization fraction trends with the frequency for the full sample and for the single component (1C) sub-set. However, sources with 2 or 3 components (2-3C) had a polarization fraction minimum at $\simeq$ 9 GHz, consistent with different emission components at lower and higher frequencies. For multi-component (>3C) objects, there was a hint of a *decrease* with increasing frequency of the polarization fraction, although the statistics was very poor.

Further indications of different origins for the low- and high-frequency emissions come from our analysis of rotation measures. The data suggest two regimes for the RM vs λ^2 relation, one at cm-wavelengths, with typical *intrinsic* RM of $\sim$ 90 rad/m^2, and the other for mm-wavelengths with median intrinsic RM $\sim$ 2000 rad/m^2 (but with very large errors). The >3C seem to have very high RMs ($\sim$ 4000 rad/m^2). Even though the statistics is very poor, it

suggests that, at mm wavelengths, the large RMs echo the low polarization fraction.

The high sensitivity polarimetry has allowed a $5\,\sigma$ detection of the weak circular polarization for $\sim 38\%$ of data. The measured values of Stokes' V, while much lower than the linear polarization amplitude, are much higher than expected for the intrinsic circular polarization of synchrotron emission, corresponding to the typical magnetic field intensities in radio emitting regions. This is consistent with previous conclusions in the literature that circular polarization is predominantly produced by Faraday conversion of linear polarization.

Finally, the new estimate of the linear polarization counts at 18 GHz derived from the convolution of the polarization fractions distribution with the model for total intensity source counts, thanks to the high sensitivity of the data, allows to reach deeper polarized flux density levels than obtained so far.

3

Polarization properties of extragalactic sources at Planck frequencies

3.1 Introduction

The detection of the CMB primordial B-mode polarization, as already said, is the current Holy Grail of particle physics and cosmological research, since this signal carries a clean signature of primordial inflation. It is, however, very faint, being generated by tensor perturbations, which are so weak to defy detection so far. The tightest upper limit on the ratio, r, of tensor to scalar fluctuations at the pivot scale of $0.05\,\mathrm{Mpc}^{-1}$ is $r < 0.07$ at the 95% confidence level (35, 238).

The measurements of Galactic (73, 185, 241, 243, 264) and estimates of extragalactic (43, 44, 328, 329) polarized foreground emissions show that, even in the cleanest 70% of the sky, they dominate over both primordial B-modes and instrumental noise of the most sensitive forthcoming or proposed CMB polarization experiments, such as LiteBIRD[1], CORE (104), Probe of Inflation and Cosmic Origin (PICO, one of the 8 Probe-Scale space missions whose study is being funded by NASA)[2], PIXIE (179) and CMB-Stage IV experiment (CMB-S4) (1).

Thus, the capability of future CMB observations to measure or constrain CMB B-mode power spectra will be limited not really by instrument sensitivity, but by the ability of removing foreground contamination with extreme accuracy. To bring the residual contamination below

[1] http://litebird.jp/.
[2] https://zzz.physics.umn.edu/groups/ipsig/cmbprobe2016proposal

noise and/or cosmic variance in multipole bins $\Delta\ell/\ell = 0.3$, foreground cleaning must reach at least the 99.9% level at $\ell \simeq 10$, at least the 99% level at $\ell \simeq 100$ and at least the 90% level at $\ell \simeq 1000$ (104).

Furthermore, the B-mode power spectrum due to gravitational lensing exceeds the one of primordial origin for $\ell \gtrsim 10$ if $r \lesssim 10^{-2}$. Hence the detection of primordial B modes requires a very accurate control of lensing effects which, in turn, are contaminated by fluctuations of unresolved extragalactic sources.

There is no definitive prediction for the magnitude of the tensor-to-scalar ratio, r. For inflationary models driven by a fundamental scalar field, the value of r is related to the total field excursion, i.e. to the inflation field range in Planck units (27, 194). Models currently of special interest (Starobinsky's R^2 and Higgs inflation) predict $r \sim 0.003$ (1, 81, 199). Large-field inflation with super-Planckian field excursions implies even lower values, $r \lesssim 0.001$.

Accurate simulations (280) showed that, for $r \simeq 10^{-3}$, the overall uncertainty on r is dominated by foreground residuals and that unresolved polarized point sources can be the dominant foreground contaminant over a broad range of angular scales ($\ell \gtrsim 50$). An accurate understanding of the polarization properties of extragalactic sources is therefore crucial.

Root-mean-square temperature fluctuations due to unresolved extragalactic sources have a minimum around 120 GHz (98), corresponding to the transition from a dominated radio sources frequency domain to a dusty galaxies one. The main radio source populations in the observational range of CMB experiments (the so-called 'cosmological window') are the compact flat- and inverted- spectrum ones, primarily blazars (BL Lac objects and flat-spectrum radio quasars).

Our understanding of polarization properties of extragalactic radio sources in the 'cosmological window' is still quite poor (131, 329).

Direct WMAP detections in polarization are limited to small numbers of sources (191, 347). *Planck*, owing to its higher sensitivity and angular resolution, has yielded more detections than WMAP. Indeed, the Second *Planck* Catalog of Compact Sources (PCCS2) lists over 120 objects with polarized emission significant at a $> 99.99\%$ level, not including the PCCS2E sub-catalog, whose reliability is unknown (244). These sources are, however, mostly at low Galactic latitudes so that only a minor fraction of them are expected to be extragalactic. The number of detections in the "extra-galactic zone" ($|b| > 30°$) ranges from 28 at 30 GHz to ~ 10 in the channels up to 217 GHz, to 1 at 353 GHz (100); the two highest *Planck* frequencies (545 and 857 GHz) were not polarization sensitive. All detected sources are radio-loud AGNs.

Follow-up polarization measurements at 8.4, 22, and 43 GHz of a complete sample of 199 extragalactic sources stronger than 1 Jy in the 5 yr WMAP catalogue were carried out by (167) and polarimetric observations of 211 radio-loud active galactic nuclei (AGNs) at 86 and 229 GHz were carried out by (6). Their $\geq 3\,\sigma$ detection rate was of 88% at 86 GHz and of 13% at 229 GHz. The sample selection was designed to be flux limited at 1 Jy at 86 GHz; however, 51% of sources were found to have $S_{86} < 1$ Jy and 22% had even $S_{86} < 0.5$ Jy, probably due to variability.

The presented high sensitivity ($\sigma_P \simeq 0.6$ mJy) polarimetric observations at 7 frequencies described in the previous Chapter (133, 134), from 2.1 to 38 GHz, of a complete sample of 104 compact extragalactic radio sources brighter than 200 mJy at 20 GHz, achieved a 5σ detection rate of 90%. Individual sources showed a broad variety of spectral shapes (flat, steep, upturning, peaked, inverted, downturning) both in total intensity and in polarization, but with substantial variations with frequency of the polarization fraction from one object to another. Due to this complexity, extrapolations to frequencies of CMB experiments to mitigate the point source contamination of CMB maps are unreliable.

In the case of star-forming galaxies, the polarized emission above 100 GHz is dominated by dust. At lower frequencies the synchrotron emission takes over but, at such frequencies, the extragalactic sky is by far dominated by radio sources. Polarization properties of dusty galaxies as a whole at (sub-)mm wavelengths are almost completely unexplored. The only published measurement (148) yielded a polarization fraction $\Pi = 0.4\%$ for the prototype starburst galaxy M 82. Integrating the *Planck* dust polarization maps, (100) found an average value of the Stokes Q parameter of about 2.7%. If this is typical for late-type galaxies seen edge-on and the polarization fraction scales as $\cos(\theta)$, θ being the inclination angle, the mean polarization fraction, averaged over all possible inclinations, should be $\simeq 1.4\%$.

It is particularly important to characterize the point source contamination in the 60–120 GHz frequency range, where *Planck* data (238) have shown that the brightness temperature spectra of diffuse polarized foregrounds display a broad minimum (280).

Although the number of sources detected in polarization by *Planck* in the 'extragalactic zone' is quite limited, estimates of the mean polarization fraction of fainter sources can be obtained using stacking techniques, i.e. by co-adding the polarized signal from many objects detected in total intensity but not in polarization, to increase the signal-to-noise (S/N) ratio. A first attempt in this direction was carried out for radio sources (43) and for dusty galaxies (44).

3. POLARIZATION PROPERTIES OF EXTRAGALACTIC SOURCES AT PLANCK FREQUENCIES

In the first case the stacking techniques was applied to the 1560 30 GHz sources in the PCCS2 (244), spanning about a factor of 20 in flux density, and were followed in all *Planck* maps in polarization (at 30, 44, 70, 100, 143, 217 and 353 GHz). The subsample outside the *Planck* GAL60 mask (covering about 40% of the sky, around the Galactic plane) and outside the Magellanic Cloud regions contains 881, likely extragalactic, radio sources while the remaining 679 are probably mostly Galactic.

The application of stacking to high resolution data is relatively straightforward, since one has to deal with only two ingredients, the (faint) signal of sources and the noise. By co-adding measurements at the positions of n sources, the signals add up while Gaussian noise goes down as $n^{-1/2}$. In the case of the low-resolution *Planck* data the situation is much more complicated because each resolution element containing a source also contains other polarized signals: the CMB itself, the diffuse synchrotron and dust emissions from the Galaxy. The Galactic contamination is particularly tricky to deal with because of its highly non-Gaussian statistics and its significant variations on the sky.

Furthermore, the mean polarized flux density, P, is computed from the Stokes parameters Q and U as $P = (Q^2 + U^2)^{1/2}$. But any quadratic sum of this kind is liable to the so-called noise bias (339), indeed the errors on Q and U add a contribution to P. The standard methods to correct for this bias cannot be applied to stacking because sources are not individually detected.

Again, since sources are not detected, the wanted result, i. e. the mean polarization fraction, $\langle\Pi\rangle = \langle P/S\rangle$ where S is the total flux density, cannot be computed directly but is approximated by $\langle P\rangle/\langle S\rangle$. Recent studies (at lower frequencies) do not find evidence of systematic variations of the *mean* polarization fraction with S (133, 153) but, on the other hand, the spectra of polarized emission of individual sources are generally substantially different from those in total intensity (134). Also, for the faintest sources the polarized signal is dominated by other components or by noise, so that it is unrelated to S. The combination of these effects may be a quite delicate point, in particular dealing with flux densities differing by more than one order of magnitude. As described in next section, the described approach does not rely at all on the $\langle\Pi\rangle = \langle P/S\rangle \simeq \langle P\rangle/\langle S\rangle$ approximation.

When applied in this context, stacking techniques typically require simulations to deal with the noise bias. For example, the corresponding correction found for radio sources is less than $\simeq$ 20% when applied to $\sqrt{\langle\Pi^2\rangle}$ but achieve a factor of approximately 3 to 6, depending on frequency, when applied to $\langle\Pi\rangle$ (43). When applied to a sample of 4697 dusty galaxies drawn from the PCCS2 857 GHz catalogue, it was possible to estimate average corrected polarization

fractions and corresponding median values at 217 and 353 GHz, with a tentative detection at 143 GHz (44).

Given the real, substantial difficulty of the problem and the importance of reaching an assessment as solid as possible of the mean polarization properties of extragalactic sources in the *Planck* frequency range, it has been decided to carry out a new investigation adopting an independent approach. In this Chapter, I present a simpler analytical approach and how I controlled the critical aspects.

3.2 Outline of the method

This approach uses the intensity distribution analysis (IDA) (20, 99). Briefly, this method consists of signals measurements in a map at the positions of a given source catalogue. The distribution of signals is compared with that for the 'blank sky', measured at random positions, away from sources (the control fields). If some statistical test detects a significant difference, which means that the source distribution is shifted towards higher values than that of control fields, a signal is detected. For this purpose, it has been used the one-sided Kolmogorov-Smirnov (KS) statistics. The polarized flux density of sources is then estimated as:

$$P = \left(P^2_{\rm src} - P^2_{\rm CF,medn}\right)^{1/2}, \tag{3.1}$$

2014MNRAS.440.3113H where $P_{\rm src}$ is the polarized signal in *Planck* maps at the source position and $P^2_{\rm CF,medn}$ is the median value of P^2 in control fields. The subtraction removes, in a statistical sense, the contributions to P of noise, CMB and polarized Galactic emissions. Thus, it directly corrects for the 'noise bias' without the need of resorting to simulations. Whenever $P^2_{\rm src} < P^2_{\rm CF,medn}$ then $P = 0$. Radio sources listed in PCCS2 have been accounted, selecting those detected at 143 GHz and located at high Galactic latitude ($|b| \geq 20°$), excluding the areas inside the mask adopted for the *Planck* polarization analysis at 100 GHz and high resolution (COM_Mask_Likelihood-polarization-100_2048_R2.00.fits). Sources flagged as extended in the PCCS2 have also been excluded and the analysis have been repeated with a Galactic cut at $|b| = 30°$ obtaining consistent results, but with a poorer statistics. Only the results for the cut at $|b| = 20°$ will be reported in what follows.

At high Galactic latitudes, objects above the the PCCS2 detection limit at 143 GHz are almost exclusively radio sources (215, 221, 265). The contaminating fraction of dusty galaxies or Galactic sources is negligibly small at low frequencies but increases with increasing frequency

because dust emission steeply rises at mm/sub-mm wavelengths. An analysis of the brightest flux density bins at 353 GHz ($S_{353} > 1780$ mJy) has shown that about half of sources are either Galactic HII regions or nearby dusty galaxies. These objects are characterized by a strong up-turn of the spectrum at sub-mm wavelengths due to dust emission. Thus, their contamination of the lower frequency samples is irrelevant. Nevertheless, they have been excluded from all samples.

The *Planck* "light" maps in temperature (T) and in polarization (Stokes' parameters Q and U) with $N_{\rm side} = 1024$ at 30 and 44 GHz, and $N_{\rm side} = 2048$ at higher frequencies were inspected at the source positions. For each source the (positive and negative) signals in all pixels within a circle with FWHM/2 radius have been summed. Temperature and polarization signals, given in temperature units, were converted to flux densities using the unit conversion software provided by the *Planck* Collaboration[1] (266, 267). In this way there was good agreement with the PCCS2 flux densities.

The procedure was repeated for a large number of "control fields". The centers of these fields were required to be separated by at least 2 FWHM from each other and from sources. This could be efficiently implemented using the properties of the Hierarchical Equal Area iso-Latitude Pixelation (HEALPix[2]) (143). It was enough to fix the control field centres at the centres of the $N_{\rm side} = 64$ and of the $N_{\rm side} = 128$ pixels for the frequencies of the Low and the High Frequency Instrument, respectively. They have been selected 26231 and 111442 control fields at the LFI and HFI frequencies.

Since, at variance with the stacking technique, the IDA considers each source individually, it allows us to compute directly the mean and the median P/S ratios. The median was preferred to the mean values because the latter are less stable, being very sensitive to the presence of few objects with exceptionally high polarized flux densities. Analogously to the polarized flux density, the total flux density of sources was estimated subtracting, in statistical sense, the other contributions (mainly due to Galactic emissions) as:

$$S = S_{\rm src} - S_{\rm CF,medn}\,, \tag{3.2}$$

where $S_{\rm src}$ is the signal in *Planck* maps at the source position and $S_{\rm CF,medn}$ is the median value of S in control fields. Thus, the source polarization fraction was estimated by:

$$\Pi = P/S\,, \tag{3.3}$$

[1] http://wiki.cosmos.esa.int/planckpla2015/index.php/Unit_conversion_and_Color_correction

[2] http://healpix.sourceforge.net

with P and S given by Eqs. (3.1) and (3.2), respectively.

In order to investigate the possible flux-density dependence of the median polarization degree on flux density, the selected samples were subdivided at each frequency into flux density bins containing 30 sources each, starting from the 90% completeness limit given by the PCCS2 paper. This left less than 30 objects in the brightest bin with the strongest signal, detectable also with a lower number of sources. Since the removal of dusty sources was done after the definition of the bins, the final number of sources in some bins was consequently slightly smaller than 30. For the source binning, it was used the DETFLUX photometry, as recommended for point sources up to 217 GHz (244), but using APERFLUX, the recommended photometry above 217 GHz, the results at 353 GHz do not change significantly.

For each bin, the polarized signals distribution was compared with that of control fields using the one-sided KS statistics. Generally, no signal was detected for the faintest bins. Whenever a signal was detected, the mean polarized flux density was computed using Eq. (3.1). This reveal another advantage of the analysis by flux density bins over the stacking approach applied to the whole sample in that it allows us to include, for the final estimates, only the flux density bins giving signals; fainter objects, affected by serious limitations because of noise and background signals, can be excluded from the analysis.

While the DETFLUX photomery was used for the binning, for the estimate of the total flux densities used to compute $\Pi_{\rm IDA} = (P/S)_{\rm median}$ was adopted, for uniformity, the same approach as for the polarization signals, i.e. summed signals in pixels within a radius of FWHM/2 from the source position.

3.3 Validation

To validate this approach, was exploited the ground-based polarization measurements by (167) and by (6) at frequencies close to those of a *Planck* channel.

At 43 GHz (167) detected 167 sources. Those detected by *Planck* were divided in total flux density at 44 GHz (244) within the area specified above (135 sources) into bins containing 30 sources each but the brightest bin which contains 15 sources. The KS test detected signal in *Planck* polarization maps for all bins, except for the 1740–3510 mJy one. All detections were highly significant, as shown by the last column of Table 3.1. In this table (and in the following ones), D is the KS statistics, i.e. the largest discrepancy between the cumulative distributions

$S_{\rm range}$ (mJy)	$N_{\rm bin}$	$N_{\rm PCCS2}$	$\Pi_{\rm Jackson}$	$\Pi_{\rm IDA}$	D	Probability
695–958	30	0	0.031	0.043 (+0.013, -0.008)	0.400	6.8×10^{-5}
958–1290	30	0	0.027	0.053 (+0.013, -0.010)	0.433	1.3×10^{-5}
1290–1740	30	0	0.031	0.021 (+0.009, -0.004)	0.467	2.1×10^{-6}
1740–3510	30	1	0.027	—	—	—
3510–23260	15	4	0.031	0.033 (+0.002, -0.009)	0.496	6.2×10^{-4}
695–23260	135	5	0.028	0.023 (+0.006, -0.002)	0.437	5.2×10^{-23}

Table 3.1: Comparison of the median polarization degrees, $\Pi_{\rm IDA} = (P/S)_{\rm median}$, at 44 GHz yielded by the IDA method with those measured by (167) at 43 GHz, within the flux density range $S_{\rm range}$. The errors on $\Pi_{\rm IDA}$ correspond to the 16th and 84th percentiles of the polarization degree distribution divided by $N_{\rm bin}^{1/2}$, $N_{\rm bin}$ being the number of sources in the bin, $N_{\rm PCCS2}$ is the number of them with polarization measurements in the PCCS2, D is the KS statistics. The last column gives the probability of the null hypothesis (the distribution of signals of sources and control fields are drawn from the same parent distribution) given by the one-sided KS test. The bottom line refers to the full sample.

$S_{\rm range}$ (mJy)	$N_{\rm bin}$	$N_{\rm PCCS2}$	$\Pi_{\rm Agudo}$	$\Pi_{\rm IDA}$	D	Probability
300–550	30	0	0.035	0.040 (+0.013, -0.007)	0.400	6.8×10^{-5}
550–800	30	0	0.028	0.023 (+0.018, -0.004)	0.400	6.8×10^{-5}
800-1090	30	1	0.028	0.028 (+0.012, -0.005)	0.400	6.8×10^{-5}
1090–1620	30	2	0.032	0.009 (+0.010, -0.002)	0.467	2.1×10^{-6}
1620–4850	30	5	0.026	0.030 (+0.005, -0.005)	0.436	1.1×10^{-5}
4850–15710	6	5	0.036	0.034 (+0.015, -0.014)	0.827	2.7×10^{-4}
300–15710	156	13	0.030	0.028 (+0.005, -0.002)	0.359	3.7×10^{-18}

Table 3.2: Comparison of the median polarization degrees, Π, at 100 GHz yielded by the IDA method with those measured by (6) at 86 GHz. The columns have the same meaning as in Table 3.1. The bottom line refers to the full sample.

of sources in a bin and of control fields. The probability of the null hypothesis (no difference between the two) was computed approximating the distribution of:

$$X^2 = 4\,D^2\,\frac{mn}{m+n} \tag{3.4}$$

with the chi-square distribution with 2 degrees of freedom (300). Here m and n are the numbers of sources and of control fields, respectively.

The IDA method yielded estimates of the median polarization degrees fully consistent with those measured by (167), within the errors that correspond to the 16th and 84th percentiles of the polarization degree distribution, divided by the square root of the number of sources in the bin (cf. Table 3.1).

Instead, it has been reported (6) a $\geq 3\,\sigma$ linear polarization detections of 183 sources at 86 GHz (88% of the sample detected in total flux density at this frequency) and 23 sources at 229 GHz (13% of those detected in total flux density); 156 of the sources detected in polarization at 86 GHz are listed in the PCCS2 100 GHz catalogue within the area considered here. Again, such sources have been divided in flux density bins of 30 sources each, with the brightest bin containing 6 sources. Highly significant polarization signals are detected for all bins (cf. Table 3.2). Also, in this case the method yielded values of the median polarization degrees in close agreement with the ground-based measurements.

Of the 23 sources detected in polarization at 229 GHz, 18 are within the region considered in the present analysis, but one of them was not detected by *Planck* at 217 GHz. For the remaining 17 sources, the KS test gave a detection probability of 92% (i.e., the probability of the null hypothesis, sources extracted from the same distribution as control fields, of 8%). The median polarization degree measured on *Planck* maps is of 4.8 $(+1.7, -2.7)$% to be compared with 7.9 $(+2.2, -1.8)$% measured for the same sources. Given that only a small fraction of observed sources were detected, it is quite likely that the detected ones, which were strongly variable, were preferentially caught by (6) in a high polarization phase. Hence, it is not surprising that the median value derived from *Planck* maps, which are averages over 5 scans of the sky spanning 2.5 years, is somewhat lower.

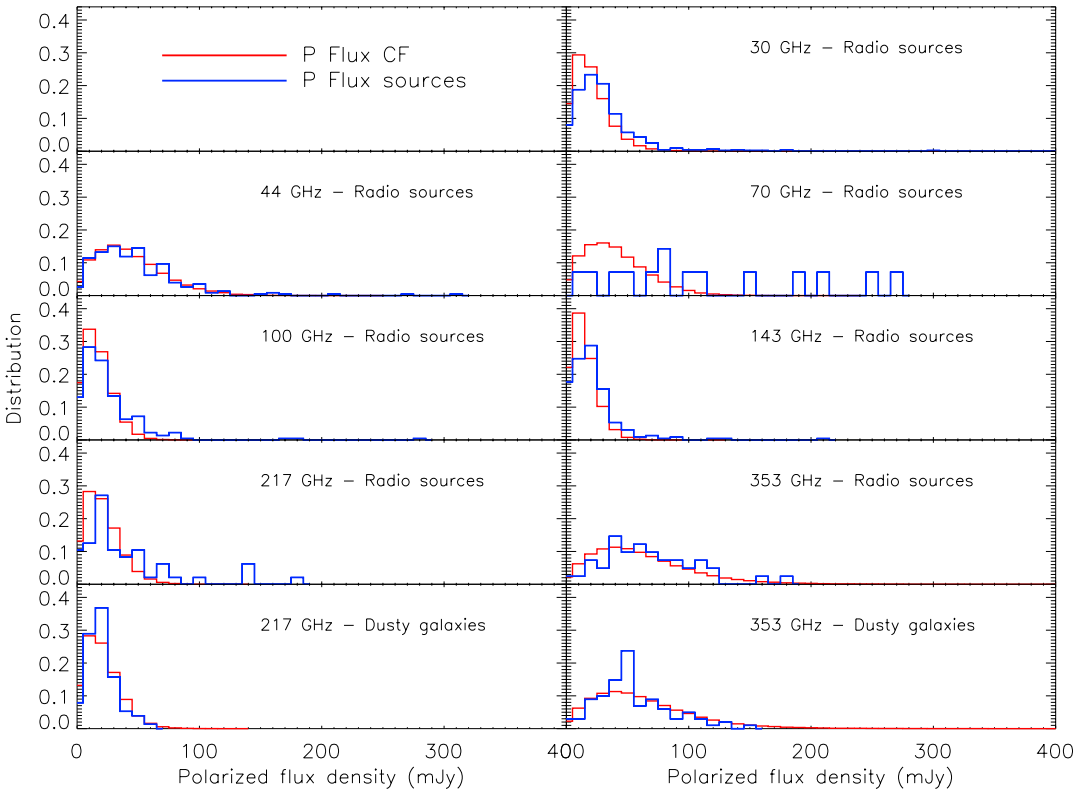

Figure 3.1: Distribution of the polarized signals of PCCS2 radio sources and dusty galaxies compared with those of control fields (signals within a radius of FWHM/2 from the corresponding centers). The total flux density limits for radio sources are those listed in Table 3.7. For dusty galaxies at 353 GHz we have kept the same limit as for radio sources (784 mJy). At 217 GHz, $S_{\rm lim,dusty} = 300$ mJy (see text).

S_{range} (mJy)	N_{bin}	N_{PCCS2}	Π_{IDA}	D	Probability
596–621	29	0	0.054 (+0.017, -0.025)	0.345	1.0×10^{-3}
621–650	30	0	0.059 (+0.009, -0.015)	0.303	4.1×10^{-3}
650–682	30	1	0.038 (+0.014, -0.027)	0.400	6.8×10^{-5}
682–712	30	0	0.010 (+0.024, -0.010)	0.500	3.1×10^{-7}
712–764	30	1	0.036 (+0.021, -0.012)	0.300	4.5×10^{-3}
764–830	30	0	0.044 (+0.012, -0.019)	0.333	1.3×10^{-3}
830–894	30	0	0.042 (+0.010, -0.030)	0.400	6.8×10^{-5}
894–980	29	0	0.026 (+0.009, -0.015)	0.379	2.4×10^{-4}
980–1075	30	1	0.019 (+0.011, -0.019)	0.433	1.3×10^{-5}
1075–1210	30	0	0.036 (+0.007, -0.015)	0.333	1.3×10^{-3}
1210–1370	28	2	0.031 (+0.005, -0.013)	0.321	3.1×10^{-3}
1370–1636	30	5	0.032 (+0.007, -0.006)	0.371	2.6×10^{-4}
1635–2125	30	3	0.025 (+0.004, -0.007)	0.346	7.7×10^{-4}
2125–3800	30	6	0.026 (+0.004, -0.005)	0.440	9.2×10^{-6}
3800–30370	22	16	0.031 (+0.005, -0.005)	0.750	1.8×10^{-11}

Table 3.3: Median polarization degrees, $\Pi_{\text{IDA}} = (P/S)_{\text{median}}$, at 30 GHz of PCCS2 radio sources in the region specified in Sect. 3.2. The columns have the same meaning as in Table 3.1. The first bin is the faintest for which the test detected a significant signal.

S_{range} (mJy)	N_{bin}	N_{PCCS2}	Π_{IDA}	D	Probability
873–945	30	0	0.035 (+0.017, -0.025)	0.400	6.8×10^{-5}
945–1042	30	0	0.038 (+0.016, -0.038)	0.467	2.1×10^{-6}
1042–1162	30	0	0.024 (+0.013, -0.024)	0.433	1.3×10^{-5}
1162–1320	30	0	0.045 (+0.019, -0.024)	0.367	3.2×10^{-4}
1320–1645	30	0	0.021 (+0.008, -0.004)	0.467	2.1×10^{-6}
1645–2100	30	1	—	—	—
2100–3700	30	2	0.003 (+0.008, -0.003)	0.500	3.1×10^{-7}
3700–29204	18	6	0.018 (+0.007, -0.004)	0.508	9.4×10^{-5}

Table 3.4: Same as in Table 3.3 but at 44 GHz.

$S_{\rm range}$ (mJy)	$N_{\rm bin}$	$N_{\rm PCCS2}$	$\Pi_{\rm IDA}$	D	Probability
663–728	30	0	0.037 (+0.016, -0.037)	0.433	1.3×10^{-5}
728–812	30	0	0.023 (+0.015, -0.016)	0.400	6.8×10^{-5}
812–913	30	0	0.010 (+0.009, -0.010)	0.500	3.1×10^{-7}
913–1030	30	1	0.008 (+0.016, -0.008)	0.500	3.1×10^{-7}
1030–1300	30	1	—	—	—
1300–1619	30	3	0.027 (+0.012, -0.019)	0.400	6.8×10^{-5}
1619–2850	30	2	0.028 (+0.005, -0.006)	0.396	8.4×10^{-5}
2850–7714	14	7	0.026 (+0.005, -0.006)	0.621	2.1×10^{-5}

Table 3.5: Same as in Table 3.3 but at 100 GHz.

$S_{\rm range}$ (mJy)	$N_{\rm bin}$	$N_{\rm PCCS2}$	$\Pi_{\rm IDA}$	D	Probability
525–580	30	0	0.005 (+0.021, -0.005)	0.500	3.1×10^{-7}
580–648	30	0	0.029 (+0.012, -0.012)	0.333	1.3×10^{-3}
648–750	30	0	0.002 (+0.012, -0.002)	0.500	3.1×10^{-7}
750–820	29	1	0.040 (+0.005, -0.024)	0.379	2.4×10^{-4}
820–1048	27	2	0.028 (+0.012, -0.016)	0.370	6.1×10^{-4}
1048–1290	30	1	0.043 (+0.007, -0.009)	0.430	1.5×10^{-5}
1290–1650	30	5	0.022 (+0.006, -0.006)	0.294	5.5×10^{-3}
1650–5305	21	6	0.030 (+0.003, -0.009)	0.412	7.9×10^{-4}

Table 3.6: Same as in Table 3.3 but at 143 GHz.

ν (GHz)	$S_{\rm min}$ (mJy)	N	$N_{\rm PCCS2}$	$\Pi_{\rm IDA}$	D	Probability
30	596	438	35	0.032 (+0.003, -0.003)	0.311	8.4×10^{-37}
44	873	228	9	0.021 (+0.006, -0.011)	0.447	5.1×10^{-40}
70	3749	15	4	0.027 (+0.006, -0.006)	0.618	1.0×10^{-5}
100	663	224	14	0.018 (+0.005, -0.005)	0.406	9.0×10^{-33}
143	525	227	15	0.028 (+0.003, -0.005)	0.348	1.5×10^{-24}
217	1085	48	8	0.031 (+0.004, -0.008)	0.292	2.8×10^{-4}
353	784	41	1	0.027 (+0.016, -0.020)	0.415	7.6×10^{-7}

Table 3.7: Median polarization degrees of radio sources at the *Planck* polarization-sensitive frequencies.

3.4 Results

3.4.1 Radio sources

In the region specified in Sect. 3.2 and for more than two flux density bins at 30, 44, 100 and 143 GHz have been detected significant polarization signals of PCCS2 radio sources. The median polarization degrees yielded by the IDA method for each bin are reported in Tables 3.3–3.6, where $\Pi_{\rm IDA}$ was computed using the median of Π, Eq. (3.3), over the considered sample and the errors correspond to the 16th and 84th percentiles of the polarization degree distribution, divided by the square root of the number of sources in the bin.

The first bin in each Table is the faintest one for which has been detected a significant *positive* signal. The significance of the detections (not to be confused with the signal-to-noise ratio) is at least at the $\simeq 3\,\sigma$ level and in most cases is much higher, as shown by the last column of Tables 3.3–3.6, while there is no significant dependence of $\Pi_{\rm IDA}$ on flux density at any frequency.

In Fig. 3.1, the distributions of radio sources polarized signals is compared with those of control fields. The source distributions refer to the total flux densities above the $S_{\rm lim}$ listed in Table 3.7. The shift of the distributions towards higher values of the polarized flux density, compared to control fields, can be perceived by eye.

Table 3.7 and Fig. 3.2 show the median polarization degrees, with their errors, for the full flux density ranges over which a signal was detected, at all the *Planck* polarization sensitive frequencies. The KS test always detects signals with high significance and the estimates have signal-to-noise ratios > 3 except at 44 and 353 GHz. Assuming that $\Pi_{\rm IDA}$ is frequency independent, a minimum χ^2 fit gives $\langle\Pi_{\rm IDA}\rangle = 2.75$ (+0.18, −0.19)% with a reduced χ^2 of 1.2.

The median polarization degree does not show any statistically significant frequency dependence, consistent with other results (26, 133, 134) but not with the increase between 86 and 229 GHz by factors of ~ 1.6 or ~ 2.6 claimed by (6) and by (7), respectively.

These results are in generally good agreement with ground-based high sensitivity polarization measurements at nearby frequencies. At 33 GHz it has been found, for the fainter sample, $\langle\Pi\rangle = 1.85\%$ with first and third quartile values of 1.17% and 3.29%, respectively, to be compared with actual median values at 30 GHz of 3.2%. At 43 GHz has been found found $\Pi_{\rm median} = 2.25\%$; present median value at 44 GHz is 2.1%. At 86 GHz (6) found a median polarization degree, including upper limits, $\Pi_{\rm median} = 2.9\%$ with first and third quartiles of 1.8% and 4.8%, respectively, to be compared with this median value at 100 GHz of 1.8%.

In agreement with what previously found, the average fractional polarization of radio sources derived with stacking techniques is approximately frequency–independent in the *Planck* range and derived weighted *mean* over all the channels is $\Pi = 3.08\%$ (43). Their *median* values, $\Pi = 1.9\%$ are slightly lower, and consistent with the results found here with IDA.

3.4.2 Dusty galaxies

The IDA approach was applied to investigate the polarization properties of dusty galaxies. Samples of these objects within the same area considered for radio sources were extracted from the PCCS2 at 217 and 353 GHz. The selection of dusty galaxies was made taking into account only sources without a counterpart at 143 GHz, where radio sources dominate, as mentioned above.

They have been collected 616 and 678 dusty galaxies brighter than 152 mJy at 217 GHz and than 304 mJy at 353 GHz. As in the case of radio sources, these objects were subdivided in total flux density bins each containing 30 of them, except for the brightest bins which contain 16 and 18 objects, respectively.

The KS test did not detect any significant positive shift of the distribution of polarized flux densities compared to that of control fields. Examples are shown by the bottom panels of Fig. 3.1. At 353 GHz, it was adopted $S_{\rm lim} = 784$ mJy, the same as for radio sources. The 68% and 90% confidence upper limits to the polarization degree are $\Pi_{353,\rm dusty} \lesssim 1.1\%$ and $\lesssim 2.2\%$, respectively. These upper limits are stable varying $S_{\rm lim}$[1].

At 217 GHz there were no objects above 1085 mJy (the limit for radio sources) and only 11 objects above 500 mJy. Thus, the histogram refers to $S_{\rm lim,dusty} = 300$ mJy. The 68% and 90% confidence upper limits are $\Pi_{217,\rm dusty} \lesssim 1.9\%$ and $\lesssim 3.8\%$, respectively. The looser limits at 217 GHz, compared to those at 353 GHz, reflect the weakening of dusty galaxy flux densities. These limits do not vary appreciably when decreasing $S_{\rm lim}$. The number of sources rapidly decreases for higher $S_{\rm lim}$, and the limits become unstable.

Therefore, it is not confirmed the conclusion by (44), who derived *mean* fractional polarizations of $(3.65 \pm 0.66)\%$ and $(3.10 \pm 0.75)\%$, and corresponding *median* values of $(2.0 \pm 0.8)\%$ and $(1.3 \pm 0.7)\%$, at 353 GHz and at 217 GHz, respectively. Note, however, that their median values are consistent with the 68% confidence upper limit at 217 GHz and with the 90% confidence upper limit at 353 GHz found with IDA.

[1] In particular, 68% (respectively 90%) upper limits for $S_{\rm lim}$ between 300 mJy (respectively 500 mJy) and 1200 mJy resulted very stable.

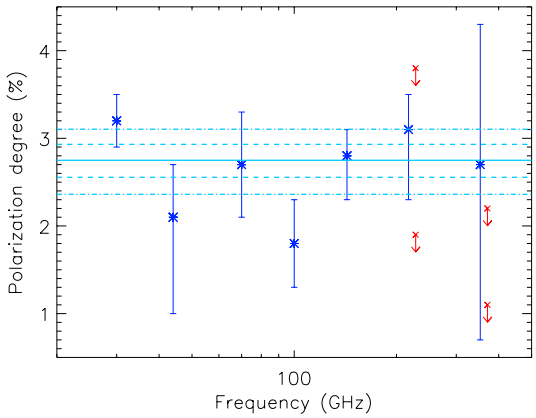

Figure 3.2: Median polarization degrees for radio sources at *Planck* frequencies with their errors (blue data points), and upper limits (90% and 68% confidence) for dusty galaxies (red arrows). The solid blue line shows the minimum χ^2 value of the median polarization degree of radio sources, assumed to be frequency independent. The dashed and dot-dashed lines show the 68% and 95% limits, respectively.

3.4.3 Power spectra

Fig. 3.3 compares the polarization power spectra of radio sources (solid blue lines) and of dusty galaxies (dashed red lines, visible only for $\nu \geq 100$ GHz) with the CMB power spectra. The dot-dashed and dotted green lines show the E-mode and lensing B-mode power spectra for the *Planck* best fit cosmological parameters (252). The dashed green lines show the primordial B-mode power spectra for four values of the tensor to scalar ratio.

The power spectra of sources are the sum of Poisson and clustering contributions. Poisson fluctuations have a white noise power spectrum, independent of the multipole number ℓ:

$$C_{\ell,\mathrm{Poisson}} = \int_0^{S_d} \frac{dN}{dS} S^2 \, dS, \tag{3.5}$$

where $dN(S)/dS$ are the differential number counts per steradian of sources weaker that the detection limit S_d.

In the case of extragalactic radio sources, the contribution of clustering can be neglected (103). To compute the Poisson power spectrum, counts in polarized flux density have been estimated from counts in total flux density, S, adopting a polarization fraction of 2.75%, i.e. setting $S_p = 0.0275\,S$. For the counts in total flux density, models by (102) up to 70 GHz and by (330) at higher frequencies were exploited. In the relevant flux-density range, the slope of the $dN(S)/dS$ of extragalactic radio sources was $\lesssim 2$, so that the largest contribution to

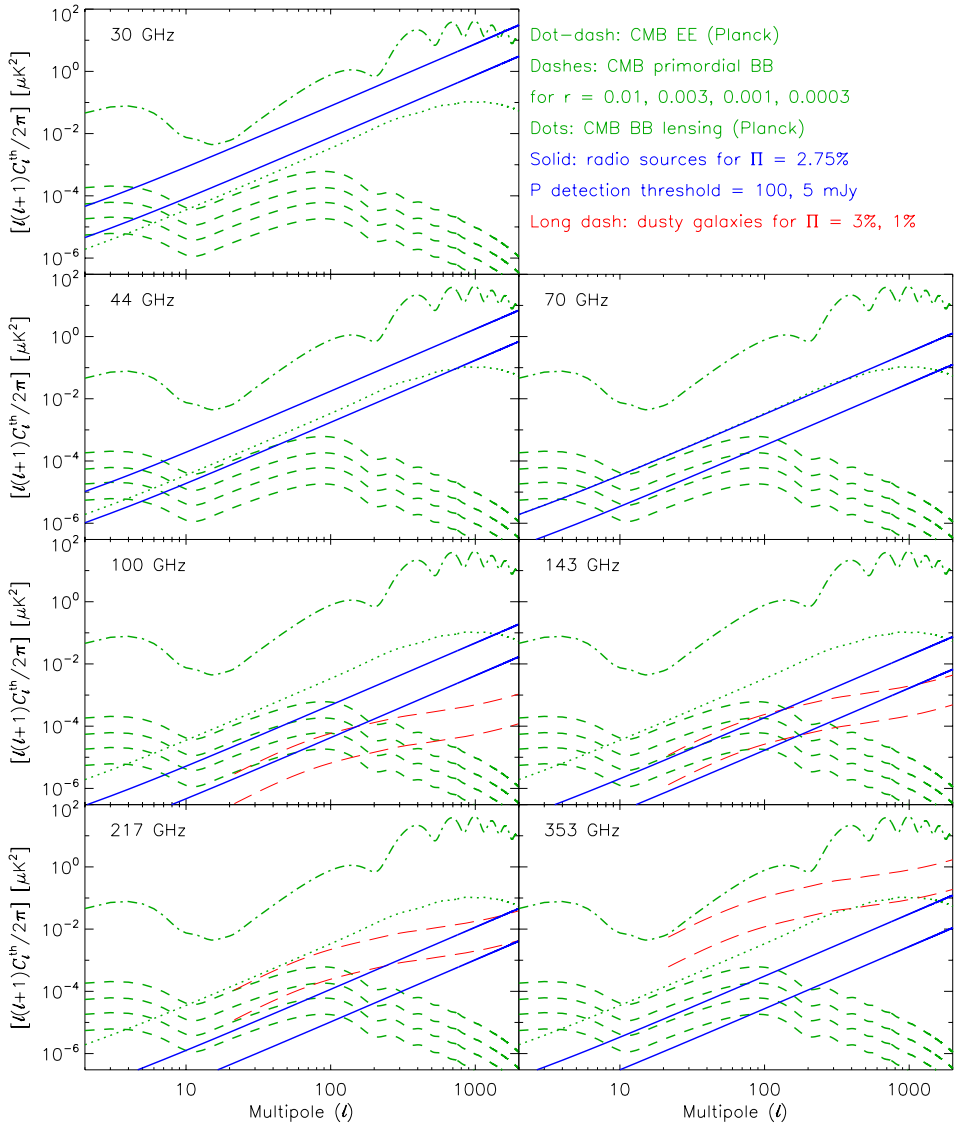

Figure 3.3: Polarization E/B-mode power spectra of radio sources and of dusty galaxies compared with the CMB E-mode and B-mode for four values of the tensor to scalar ratio $r = 0.01, 0.003, 0.001, 0.0003$ (from top to bottom); see text and legend for details. Since unresolved point sources contribute, on average, equally to E- and B-mode, their total power spectra have been divided by a factor of 2.

$C_{\ell,\mathrm{Poisson}}$ comes from flux densities just below the detection limit in polarization. Fig. 3.3 shows two cases, considering values of the polarized flux density limits expected for next generation CMB experiments (100).

Contrariwise, in the case of dusty galaxies the clustering contribution dominates over most of the multipole range of interest here. The power spectrum in polarized flux density have been derived from a model in total flux (57) that accurately reproduce both the *Planck* (247, 269) and the *Herschel* (334) measurements. For these objects, the counts are very steep (slope > 3) so that the main contribution to the power spectrum comes from faint sources, i.e. the power spectrum amplitude is essentially independent on S_d. Again, the power spectra in polarization have been scaled from those in total flux density for two choices of the polarization degree, 3%, close to the mean value found by (44), and 1%, close to this 68% confidence upper limit at 353 GHz. For sake of illustration, it has been applied this approach down to 100 GHz. Note, however, that already at 143 GHz the dusty galaxies in *Planck* maps are too faint to allow the derivation of reasonably accurate constraints on their average polarization degree.

Unresolved point sources contribute, on average, equally to E- and B-mode power spectra. Thus, for comparison with the CMB polarization modes (Fig. 3.3), the total power spectra discussed above have been divided by a factor of 2.

The contamination of CMB polarization maps by extragalactic radio sources was previously discussed (84, 328). Present analysis agrees with their conclusion that these objects are not a strong contaminant to the CMB E-mode polarization, but can constrain the detection of cosmological B-modes if $r \lesssim 0.01$.

Estimates of the power spectrum of dusty galaxies were presented by (84), who assumed an average polarization level of 1%, and by (44). The latter authors used log-normal distributions for the polarization degrees and took into account only the Poisson contributions. Extrapolating to lower frequencies the estimates or the upper limits obtained at 217 and 353 GHz it was found that the contamination by dusty galaxies may be dominant, compared to radio sources, at $\geq$ 217 GHz and the contributions from the two populations may be comparable down to $\simeq$ 100 GHz. Dusty galaxies fade away rapidly at still lower frequencies.

3.5 Conclusions

The estimates of the mean polarization fraction of extragalactic sources (radio-loud AGNs and dusty galaxies) based on data from the *Planck* polarization maps at 30, 44, 70, 100, 143, 217

and 353 GHz have been revised. Although earlier analyses based on stacking techniques were carefully done, there are several tricky aspects and subtleties that call for an independent analysis. This is particularly important in relation to the forthcoming or proposed CMB polarization experiments aimed at detecting primordial B-modes.

The importance of a careful control of foregrounds has been demonstrated by detailed sky simulations (280), which include Galactic and extragalactic polarized emissions in addition to the CMB, based on state-of-the-art observations. These simulations have shown that, for r at the per thousand level (i.e. at the level predicted by models currently of special interest), or less (as in the case of large-field inflation with super-Planckian field excursions), the overall uncertainty on this parameter can be dominated by the contamination of unresolved polarized extragalactic sources. An insufficiently accurate characterization of this component could lead to a bias in the reconstruction of the primordial CMB B-mode signal.

This independent re-analysis overcomes the two most delicate aspects of the application of stacking techniques, i.e. the approximation of the average polarization fraction, $\langle \Pi \rangle = \langle P/S \rangle$, with the ratio of the mean polarized flux density to the mean total flux density, $\langle P \rangle / \langle S \rangle$, and the need of simulations to correct for the noise bias.

This approach considers the objects one by one. This allows to identify the flux density range that contributes significantly to the polarization signal; thus, it is possible to exclude from the analysis fainter objects, that may affect results because of the serious limitation by noise and background signals. For objects above the flux density threshold, the median P/S has been computed directly. The method allows us to detect, on *Planck* maps, mean polarized flux densities at few tens of mJy levels. For comparison, the detection limits in total intensity are at the few to several hundred mJy levels (244). Also, the subtraction of the polarization signal median of control fields removes the contributions of the noise and of the other polarized components (CMB and Galactic emissions), thus removing the noise bias without the need of resorting to simulations.

For radio sources, a median polarization degree, averaged over frequencies, $\Pi_{\rm IDA,median} \simeq 2.75\%$, is in good agreement with (43) as well as with the ground based measurements of a fainter sample at 33 and 38 GHz (134) and of a bright sample at 86 GHz (6). In addition, there is any significant dependence of Π on either flux density or frequency, in agreement with earlier analyses at frequencies of up to 43 GHz but not with the increase of Π from 86 to 229 GHz claimed by (6, 7).

At variance with (44), there is any detection of polarization signal from dusty galaxies, although there is consistency between median values derived with stacking techniques and the upper limits found here with IDA. For these objects, IDA gives 90% confidence upper limit at 353 GHz $\Pi_{\rm dusty} \lesssim 2.2\%$. The upper limit at the same confidence level is looser ($\lesssim 3.8\%$) at 217 GHz, where dusty galaxies are substantially fainter.

The contamination of CMB maps in polarization by extragalactic sources is dominated by radio loud AGNs up to $\simeq$ 100 GHz. The amplitude of their power spectra depends on their detection limit in polarization, S_d. For the values of S_d expected for next generation CMB experiments, it is confirmed that at $\simeq$ 70 GHz, i.e. in correspondence to the minimum Galactic emission, the point source (radio source) contamination is well below primordial E-modes, as found by previous analyses. On the other hand, it is close to the level of lensing B-modes and of primordial B-modes for $r \simeq 0.01$. The contribution of dusty galaxies to the point source power spectra is still poorly constrained, but may be substantial, or even dominant at $\gtrsim$ 100 GHz.

4

Square Kilometre Array and CMB spectral distortions

4.1 Introduction

In the past decades, the present Λ cold dark matter (ΛCDM) cosmological model describing our Universe has been established as the standard model. Its parameters have been measured to high precision, but there are still many fundamental questions in cosmology, as, for example, the physics of the very early Universe, the origin of the cosmic acceleration and the nature of dark matter. The forthcoming radio telescope, the Square Kilometre Array (SKA), in its complete operational mode will be the world's largest observational facility able to open a new frontier in cosmology. The SKA, with its unprecedented sensitivity and resolution, will perform cosmological surveys potentially able to answer to many fundamental questions in cosmology, so representing a step forward in the so called precision cosmology. *Planck* high precision measurements confirmed that only 5% of Universe energy budget is apparently made of ordinary baryonic matter and the remaining 95% of possibly exotic components as dark matter and dark energy. Furthermore, although the CMB has been a powerful observational tool for cosmology in the past decades, the next step towards a precision cosmology requires extra information (348). The SKA, a new technology radio-telescope based on large arrays, will allow us to investigate these and other different cosmological and astrophysical topics and, in combination with future CMB experiments, among others, will contribute to probe various types of dissipation processes relevant at different cosmic epochs.

4.2 The Square Kilometre Array

The SKA will be a giant radio telescope with an effective collecting area of one-million square meters observing in the radio band with different antenna concepts and a continuous frequency coverage from 50 MHz to 14 GHz, allowing all-sky surveys and redshift depth observations (196), or possibly at higher frequencies up to 25 GHz, a range typically accessible from the ground (19). The SKA is planned to be built in two phases, with a first science expected in 2019 and it is foreseen to be fully operational by 2024. The low-frequency part of the observatory will be established in Western Australia, while the mid- and high-frequency part will be developed in Southern Africa where it can be merged with its precursor MeerKAT and connected to the large European and German radio telescopes. The array will be 10–100 times more sensitive than the current facilities and 50 times more sensitive than Jansky Very Large Array (JVLA). The SKA 2 is expected to yield a factor 10 increase in sensitivity over SKA 1. Another fundamental gain of the SKA is the extremely wide FOV, from 200 square degrees at the lowest frequencies to, at least, 1 square degree at 1.4 GHz. The main configuration, in order to achieve high sensitivity and resolution images, can be divided into two main parts: a core that will be densely populated and a central region with logarithmically positioned antennas set in groups along five spiral arms.

Each antenna group will be equipped with single dipoles, small dipoles arrays, or single small telescopes, all allowing a continuous frequency coverage. The high frequency dishes will be either made up by single pixel feeds or, likely, with Phased Array Feeds (PAF). Currently, both phases should consist of three elements: SKA-LOW operating at low frequency, SKA-MID covering the intermediate/high frequency, and SKA-SUR optimized for surveys (168). The SKA1 will host most of the low frequency aperture arrays (SKA1-LOW), a small part of the middle frequency (SKA1-MID) dishes, and the survey aperture arrays (SKA1-SUR), that should be deferred. During the Phase 2 the total array will be completed. A third SKA 3 phase is envisaged and is designed to extend SKA operations to high radio frequencies (> 20 GHz and possibly up to 30 GHz).

The project will consist of two consecutive phases, the Phase 1 (SKA1), able to perform HI intensity mapping surveys and the Phase 2 (SKA2), that will allow to carry out a wide HI galaxy redshift survey, the biggest spectroscopic survey of $\sim$1 billion of galaxies.

Since radio-continuum surveys play an important role in many relevant research fields, various reference surveys have been taken into account as the top priority SKA continuum

science cases (274). The Ultra Deep Survey devoted to trace the Star Formation History of the Universe (SFHU) and the SKA1 extremely high sensitivity at the μJy level and resolution over wide areas (0.5" or lower at $\sim$ 1 GHz) will allow the disentangling of the single radio source populations down to very faint fluxes. Assuming 1 GHz as a reference frequency, the flux limit will be 0.05, 0.2, 1, μJy/beam for the Ultra Deep (1 deg^2 sky coverage), Deep (10–30 deg^2) and Wide (1–5 $\times 10^3$ deg^2) survey, respectively. The different SKA 1 and SKA 2 arrays are characterized by:

- SKA 1 LOW: Low frequency Aperture Array (AA);
- SKA 1 MID: Mid-frequency dish array with high sensitivity single pixel feeds;
- SKA 1 AIP–Survey: Component of SKA 1 delivering high survey speed at mid frequencies, based on Phased Array Feeds (PAF, part of AIP);
- SKA 2 LOW: Low-frequency Aperture Array (AA);
- SKA 2 MID-Dish: Mid-frequency dish array with high sensitivity single pixel feeds, and possibly equipped with PAFs;
- SKA 2 AIP AA: Mid frequency dense Aperture Array (part of AIP);
- SKA2 AIP-PAF: A component of SKA 2 delivering high survey speed at mid frequency, based on PAFs (part of AIP).

In Table 4.1 are reported the main technical specifications of the SKA1-SUR, SKA1-LOW and SKA-MID, while in Fig. 4.1 is schematized the project timeline as six main periods.

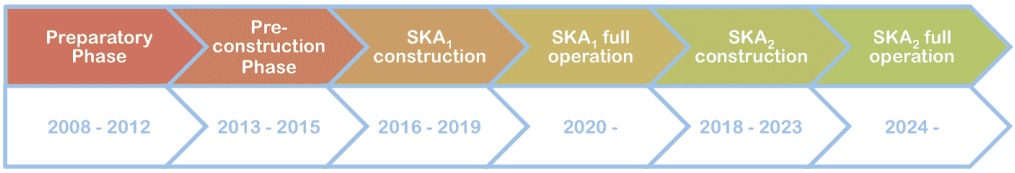

Figure 4.1: SKA overall project timeline.

4.3 The SKA science

The SKA is likely to become one of the leading dark energy (DE) measuring machines, bringing breakthroughs in cosmology by combining CMB (*Planck* outcomes), optical (from LSST,

	SKA1-SUR	SKA1-LOW	SKA-MID
A_{eff}/T_{sys} (m^2/K)	391	1000	1630
FoV (deg^2)	18	27	0.49
Receptor Size (m)	15	35	15
Fiducial frequency (GHz)	1.67	0.11	1.67
Survey Speed FoM ($deg^2m^4K^{-2}$)	$2.75{\cdot}10^6$	$2.70{\cdot}10^7$	$1.30{\cdot}10^6$
Resolution (arcsec)	0.9	11	0.22
Baseline or Size (km)	50	50	200
Frequency Range (GHz)	0.65 – 1.67	0.050 – 0.350	0.35 – 14
Bandwidth (MHz)	500	250	770
Cont. Sensitivity (μJy-$hr^{-1/2}$)	3.72	2.06	0.72
Sensitivity, 100 kHz (μJy-$hr^{-1/2}$)	263	103	63
SEFD (Jy)	7.1	2.8	1.7

Table 4.1: Parameters for SKA (Adapted from SKA-TEL-SKO-DD-001Revision:1, SKA1 System Baseline Design, P. E. Dewdney et al. 2013).

SNAP), optical and near-infrared (from the ESA Euclid mission) and other early 21^{st} century datasets (276). In 2008, the SKA Science and Engineering Committee, SSEC, recognised in the "Precursors" designation the telescopes built on one of the two SKA candidate sites, Australia or South Africa, while in the "Pathfinders" classification all SKA-related technology, science and operations activity telescopes. One of the open key question in cosmology to be explored by the SKA is the probe of the early Universe and, mainly, its reionization history (Epoch of Reionization, EoR) happened soon after the Dark Ages and due to the dawn of galaxies. The SKA offers a unprecedented opportunity to investigate one of its striking exploitation through the redshifted 21-cm line. Being the 21-cm emission line the best way to detect the presence of neutral Hydrogen (HI) and since radio telescopes have a remarkable capability of acquiring images of HI distribution and kinematics in the Universe, a suite of surveys for HI emission is represented by the SKA. Indeed, the radiation from the first galaxies and their descendants permeated the Universe, culminating in the last global phase change of our Universe, which is the epoch of second ionization. This process is fundamentally important, allowing us to study the first galaxies as well as the majority of the baryonic matter spread out between them in the intergalactic medium (IGM). These early epochs correspond to the bulk of our light cone,

enclosing orders of magnitude more linear modes than the much-studied cosmic microwave background. This 21-cm line corresponds to the spin-flip transition in the ground state of neutral hydrogen and, as cosmological probe, the 21-cm signal is usually represented in terms of the offset of the 21-cm brightness temperature from the CMB temperature, T_{CMB}, along the observed line of sight at frequency ν (130):

$$\delta T_b(\nu) = \frac{T_S - T_{CMB}}{1+z}\left(1 - e^{-\tau_{\nu_0}}\right) \tag{4.1}$$

$$\simeq 27 x_{HI}\left(1 - \frac{T_{CMB}}{T_S}\right)(1+\delta_{nl})\left(\frac{H}{dv_r/dr + H}\right)\sqrt{\frac{1+z}{10}\frac{0.15}{\Omega_M h^2}}\left(\frac{\Omega_b h^2}{0.023}\right)\text{mk}, \tag{4.2}$$

where T_S is the gas spin temperature, τ_{ν_0} is the optical depth at the 21-cm frequency ν_0, $\delta_{nl}(\vec{x}, z) \equiv \rho/\bar{\rho} - 1$ is the evolved (Eulerian) density contrast, $H(z)$ is the Hubble parameter, dv_r/dr is the comoving gradient of the line of sight component of the comoving velocity, and all quantities are evaluated at redshift $z = \nu_0/\nu - 1$. The CMB is assumed as a backlight, thus if $T_S < T_{CMB}$ the gas is seen in absorption, while if $T_S > T_{CMB}$ it is seen in emission.

The 21-cm signal is a line transition, which redshifts from the EoR into the FM band. Consequently, each observed frequency corresponds to a redshift slice, making 21-cm interferometry a powerful tomographical probe of early Universe. Actually, Eq. 4.2 shows a dependence on both the IGM temperature (T_S) and ionization (x_{HI}) evolution, as well as fundamental cosmological parameters (H, Ω_M, Ω_b and h^2). With a frequency coverage of $\sim$ 70–200 MHz, SKA-LOW would be able to cover the entire EoR, but, likely, also the epoch of IGM heating.

To deeply understand the 21-cm physical signal there are three main challenges to overcome: an extremely large parameter space, due to our poor understanding of the high-redshift Universe, an enormous dynamic range of the relevant scales, and the treatment of foreground emissions together with their coupling with the instrument.

Theoretically, the early Universe can be modelled via numerical simulations but it requires enormous simulating boxes in order to statistically model ionized regions, distribution of absorption systems and highly biased quasars. Recently, owing to semi-numerical algorithms with $\geq$ 100 realizations of the EoR (351), we were able to conclude that either: (i) the early stages of reionization occurred in a much more homogeneous manner than suggested by fiducial, stellar-driven scenarios and/or (ii) that there is a significant correlation between the cosmic infrared background and the thermal SZ effect.

The Hubble diagram of Type Ia Supernovae (SNeIa), measured by both the Supernova Cosmology Project (234) and the High–z Team (281) up to redshift z ∼ 1, was the first evidence that the Universe is undergoing a phase of accelerated expansion. On the other hand, balloon born experiments, such as BOOMERanG (96) and MAXIMA (306), determined the location of the first and second peak in the anisotropy spectrum of CMB radiation, strongly pointing out that the geometry of the Universe is spatially flat to a good approximation. If combined with constraints coming from galaxy clusters on the matter density parameter Ω_M, these data indicate that the universe is dominated by a non-clustered fluid with negative pressure, generically called DE. Such a fluid should be able to drive the accelerated expansion. The ΛCDM model fails in explaining why the inferred value of Λ is so tiny (120 orders of magnitude lower) compared to the typical vacuum energy values predicted by particle physics and why its energy density is today comparable to the matter density (the so called coincidence problem (337)). The DE nature has led many authors to look for scenarios able to give a quintessential behavior without the need of exotic components. The accelerated expansion can be explained by a single cosmic fluid with an equation of state causing it to act like dark matter (DM) at high densities and DE at low densities. An attractive feature of these models, usually referred to as Unified Dark Energy (UDE) or Unified Dark Matter (UDM) models, is that such an approach naturally solves, at least phenomenologically, the coincidence problem. In this scenario, being the DE a new ingredient of the cosmic Hubble flow, the simplest theoretical model, which is a generalization of the Λ conjecture, is the Quintessential-CDM (QCDM) model, a mechanism that allows an evolving Λ from the past to the present. By means of the Friedman equations, the cosmic acceleration become:

$$H^2 \equiv \left(\frac{\dot{a}}{a}\right)^2 = \frac{8\pi G}{3}(\rho_M + \rho_Q), \tag{4.3}$$

$$2\left(\frac{\ddot{a}}{a}\right) + H^2 = -8\pi G p_Q = -8\pi G w \rho_Q, \tag{4.4}$$

where $w \equiv p/\rho$ is the baryonic factor. Different authors (292) claimed that UDE models are not viable because the growth of density perturbations will lead to matter power spectrum in disagreement with what is observed. This should be an evidence against the parametric density model. Other phenomenological unified models (59) have been proposed where a single fluid with a given energy density assigned by few parameters is able to fit both the SNeIa Hubble diagram and the angular size–redshift relation for ultracompact radio sources. Another possible

approach to the cosmic acceleration is to consider DE and DM as signals of the breakdown of the Einstein General Relativity at some characteristic scale (214), allowing strong field tests of gravity, by using pulsars to challenge Einstein's general relativity and the nature of space and time. The SKA radio-interferometer could result an extremely important tool to remove the degeneracy of models since radio data should contribute to define the energy spectrum of different sources and then contribute to define the standard candles or distance indicators capable of mapping large ranges of redshift.

Finally, SKA has a great advantage to simultaneously measure sky positions and redshifts by detecting the neutral hydrogen with 1.4 GHz emission, a key aspect for controlling systematic errors . Due to these reasons, SKA can be seen as a powerful facility to disentangle among different DE models.

As discussed in Chapter 1, improved CMB temperature and polarization anisotropy experiments could improve current constraints on primordial non-Gaussianities at most by a factor ~ 2. For substantial improvements, it will be necessary to look at different observables and wait for future experiments. LSS could be in principle promising, since it contains more modes than the CMB. Precise primordial bispectrum estimation from LSS surveys is however very hard due to non-linearities from gravitational evolution, galaxy-bias and other effects; whether we will be able to achieve improvements from the LSS bispectrum will strongly depend on how well we can keep all these systematics under control, and it is at present an open question. Two-point function based measurements of large scale signatures arising from scale-dependent halo bias look on the other hand quite promising, and have the potential of achieving $f_{\rm NL} \sim 1$ sensitivity for the local shape (139). It has been pointed out that the study of the bispectrum of 21-cm radiation or measurements of cross-correlations between CMB spectral distortions and temperature anisotropies can, in principle, improve over current bounds by more than one order of magnitude. These are fascinating but futuristic prospects, since high-sensitivity $f_{\rm NL}$ measurements with these techniques will require either full-sky 21-cm surveys with redshift tomography in the $30 \lesssim z \lesssim 100$ range, or high-resolution maps of angular anisotropies of the CMB μ-distortion parameter (216, 228).

In addition, the SKA will provide astronomers insight into other key science questions such as the cradle of life, by studying the habitable segment of proto-planetary disks and to search for prebiotic molecules that indicates primordial Earth-like conditions.

4.4 SKA precursors

Among many different next generations radio telescopes built around the world, two are the official SKA precursors, MeerKAT and ASKAP (Australian SKA Pathfinder).

MeerKAT is the South African SKA pathfinder telescope which, in Phase 1, consists of 64 dishes, each of 13.5-m diameter and equipped with single-pixel receivers, distributed over two components. A dense inner component contains 70% of the dishes with a Gaussian uv-distribution and a dispersion of 300 m and the outer component embodies the remaining 30% dishes, with a Gaussian uv-distribution with a dispersion of 2500 m and a longest baseline of 8 km. A potential future extension (Meerkat Phase 2) could see 7 additional dishes being added to extend the longest baselines to about 16 km. MeerKAT will support a wide range of observing modes, including deep continuum, polarisation and spectral line imaging, pulsar timing, and transient searches. The plan is to provide standard data products, including an imaging pipeline (9).

The Australian SKA Pathfinder (ASKAP) is a new radio telescope being built on the Australian SKA site in Western Australia, at the Murchison Radio-astronomy Observatory. It consists of 36 12-m antennas distributed over a maximum baseline of 6 km diameter area that require a high speed survey instrument, a high dynamic range and an extremely wide field-of-view interferometer with Phased Array Feeds (PAFs). The PAF has a total of 188 elements dual-polarisation pixels, 94 in each of two polarizations operating in a frequency band from 700 MHz to 1.8 GHz and a field of view up to 30 $\deg^2$. ASKAP total collecting area is approximately 4000 square metres and its system temperature is less than 50 K. There are 36 independent beams, each of about 1 square degree, yielded overlapping a 30 square degree field-of-view at 1.4 GHz (145). To guarantee good calibration, the feed and reflector rotate to mimic the effect of an equatorial mount, ensuring a constant position angle of the PAF and sidelobes on the sky. The main characteristic of ASKAP is that some of its technical component will be shared by the SKA, as the sky mount telescopes configuration, the PAF and, in particular, their array set up, the large amount of data transported, digital hardware studies (also in terms of costs and capabilities), instrument calibration, power and communication solutions, system engineering, logistics and, finally, the science case.

4.5 SKA pathfinders

The main SKA pathfinders which are of particular interest for the Italian community are e-MERLIN[1] and LOw Frequency radio ARray (LOFAR[2]).

MERLIN is a cm-wavelength array of seven radio telescopes spread in the UK and connected to the Jodrell Bank Observatory (JBO) central unit by a new dark fibre network. It operates as a high resolution interferometer with a maximum baseline length of 220 km and a unique capability of detecting radio images from 0.01 to 0.15 arcsec resolution at frequencies of 1.5, 5 and 22 GHz (corresponding to L, C and K band).

Telescope main activity is to produce, manage, maintain and extend this new low cost fibre network. The instrument has been largely involved in the e-MERGE Survey programme to exploit the formation and evolution of star forming galaxies and AGN at $z > 5$ in two well studied extragalactic fields with a resolution of 50-200 mas corresponding to < 0.5–1.5 kpc at $z > 5$ providing a truly view of star formation distribution within typical galaxies. e-MERLIN will be able to disentangle the contribution coming from AGN and young forming star.

The LOFAR (33) is a pan European radio phased-array telescope equipped with two types of antenna, one optimised for observations between 30 MHz and 80 MHz and the other between 110 MHz and 240 MHz. The antennas are grouped together in stations a few hundreds meter wide, with 40 stations in The Netherlands distributed over an area of 100 km diameter, and a further eight stations located in Germany, UK, Sweden, and France. The received signals are digitised to form many beams on the sky, making LOFAR an extremely efficient survey instrument.

LOFAR supplies continuum surveys of the radio sky covering the northern half of the sky at high sensitivity and resolution. Three are the main open questions in cosmology and astrophysics that have driven the design of the planned LOFAR surveys: (i) formation of massive galaxies at the epoch of reionization, (ii) magnetic fields and shocked hot gas associated with the first bound clusters of galaxies, (iii) star formation processes in distant galaxies. Other fundamental astrophysical key aspects are the distribution of magnetic fields in the Universe and the comprehension of the cosmic magnetism origin by detecting the linear polarization at low frequencies of the Milky Way, pulsars, nearby galaxies, giant radio galaxies, galaxy groups and filaments.

[1] http://www.e-merlin.ac.uk/
[2] http://www.lofar.org/

	eMERLIN	LOFAR	MeerKAT	ASKAP
A_{eff}/T_{sys} (m^2/K)	60	61	321	65
FoV (deg^2)	0.25	14	0.86	30
Receptor Size (m)	25	39	13.5	12
Fiducial frequency (GHz)	1.4	0.12	1.4	1.4
Survey Speed FoM ($deg^2 m^4 K^{-2}$)	$9.00 \cdot 10^2$	$5.21 \cdot 10^4$	$8.86 \cdot 10^4$	$1.27 \cdot 10^5$
Resolution (arcsec)	$(10\text{-}150) \cdot 10^{-3}$	5	11	7
Baseline or Size (km)	217	100	4	6
Frequency Range (GHz)	1.3-1.8, 4-8, 22-24	0.03 – 0.22	0.7-2.5, 0.7-10	0.7-1.8
Bandwidth (MHz)	400	4	1000	300
Cont. Sensitivity (μJy-$hr^{-1/2}$)	27.11	266.61	3.20	28.89
Sensitivity, 100 kHz (μJy-$hr^{-1/2}$)	1714	1686	320	1582
SEFD (Jy)	46.0	45.2	8.6	42.5

Table 4.2: Parameters for the SKA precursors and pathfinders described in the text (adapted from SKA-TEL-SKO-DD-001Revision:1, SKA1 System Baseline Design, P. E. Dewdney et al. 2013).

Many synchrotron radio sources have steep spectra, therefore they are better studied at low frequencies where their intensity is much larger. Furthermore, Faraday rotation is another important tool for studying cosmic magnetism, being proportional to the wavelength square. Hence, weak fields and low plasma densities, as expected in galaxy halos and filaments, can be measured with much higher precision at long wavelengths. In addition, LOFAR should measure the 21-cm power spectrum during $7 \leq z \leq 12$. Table 4.2 summarizes the main technical specifications of the SKA pathfinders and precursors described above.

4.6 SKA contribution to future CMB spectrum experiments

The CMB spectrum emerges from the thermalization epoch, at $z \sim 10^6 - 10^7$, with a blackbody (BB) shape thanks to the high efficiency of interaction processes in the cosmic plasma able to re-establish the matter-radiation thermal equilibrium even in the presence of a significant departure. After this phase and passing through the recombination epoch, the thermodynamical equilibrium is no longer ensured since the reduced interaction of CMB photons with the plasma, because of the expansion of the Universe and the decrease of electron and photon number densities and temperatures.

The distorted spectra mainly depends on the fractional amount of energy exchanged during the interaction, the epoch and type of the heating or cooling process, and the baryon density. Theoretically, the departure from a perfect BB is predicted by three main unavoidable mechanisms (314):

(*i*) cosmological reionization and related electron heating, which produce physically correlated Comptonization distortion characterized by an (energy) Comptonization parameter, $y \approx 10^{-7} - 10^{-6}$, proportional to the fractional energy exchanged in the interaction, $\Delta\varepsilon/\varepsilon_i \simeq 4y$, and free-free (FF) distortion;

(*ii*) dissipation of primordial perturbations at small scales, damped by photon diffusion and thus invisible in CMB anisotropies, which produces mainly BE-like distorted spectra characterized by a positive chemical potential $\mu_0 \simeq 1.4\Delta\varepsilon/\varepsilon_i \approx 10^{-9} - 10^{-7}$;

(*iii*) BE condensation of CMB photons by colder electrons associated with the matter temperature decrease in the expanding Universe relatively faster than that of radiation giving $\mu_0 \approx -3 \times 10^{-9}$.

The photon occupation number and its evolution at different frequencies and times is described by the complete kinetic Boltzmann equation, very well approximated in terms of the Kompaneets equation . The FF signal associated with cosmological reionization is the most relevant type of low-frequency global spectral distortion (see Figure 4.2). Indeed, the FF term is proportional to the square of baryon density and the structure formation process implies a rate amplification by a factor $\simeq 1 + \sigma^2$ (being σ^2 the matter distribution variance) with respect to the case of homogeneous plasma (327).

Recent limits on CMB spectral distortions and constraints on energy dissipation processes in the plasma (291) ($|\Delta\varepsilon/\varepsilon_i| \lesssim 10^{-4}$ at 95% C.L., the exact value depending on the dissipation epoch and on considering a single process or two different processes jointly) are mainly set by the FIRAS instrument on board the NASA COBE[1] satellite (205) in the wavelength range between 1 cm and 0.5 mm. The measured monopole of the background radiation resulted compatible with a BB spectrum (122) at the current temperature of $T_0 = (2.72548 \pm 0.00057)$ K, because of the Universe expansion, a value that well accounts also for the main (Doppler effect) dipole[2] induced by the solar system velocity ($v \simeq 369$ km/s) relative to the CMB restframe.

[1] http://lambda.gsfc.nasa.gov/product/cobe/

[2] The analysis of the dipole term frequency dependence can be also exploited to study CMB spectral distortions(18, 91), as widely discussed in next chapter.

High accuracy CMB spectrum space experiments, such DIMES (178) ($0.5 \lesssim \lambda \sim 15$ cm) and FIRAS II (126) ($\lambda \lesssim 1$ cm), were proposed to constrain energy exchanges up to 100 times better than FIRAS. Dissipation processes at early times ($z \gtrsim 10^5$), like the ones DIMES is able to probe, result in Bose-Einstein (BE)-like distortions (316), while late epochs mechanisms ($z \lesssim 10^4$) before or after the recombination era generate Comptonization and FF distortions (23). New space missions were proposed to investigate the cosmic origin and its evolution by observing CMB temperature and polarization anisotropies with $\sim$ degree resolution, as in PIXIE (180) and LiteBird, or with arcmin resolution, as in COrE (12), PRISM (12), and COrE+, or in combination with spectrum measurements as in the case of PIXIE and PRISM (see Chapter 1).

In the next chapter, I will discuss further the theoretical aspects of unavoidable CMB spectral distortions, reporting also a concise description of the so-called exotic energy injection processes that might have occurred at different cosmic times and that could be constrained by spectrum measurements from radio to sub-millimeter wavelengths.

The SKA extremely high sensitivity and resolution can contribute to set new constraints on CMB spectral distortions and dissipation processes beyond current limits. In particular, SKA will trace the neutral hydrogen distribution and the neutral-to-ionized transition state at the reionization epoch through the 21-cm line (295). It could trace the development of ionized material directly by looking for FF emission from ionized halos. The expected signal can be derived by reionization models through both semi-analytical methods (219) and numerical simulations (272). Dedicated high resolution sky areas observations allow to distinguish FF distortion by ionized halos rather than by diffuse ionized IGM. SKA2 should be able to detect up to $\sim 10^4$ individual FF emission sources with $z > 5$ in 1 deg^2 discerning ionized halos or diffuse ionized IGM FF distortions.

SKA precise number counts, particularly at frequencies from ~ 1 to few GHz, will be crucial for a precise analysis of CMB spectral distortion experiments, while the precise mapping of individual halos represents an interesting goal for the excellent imaging capabilities of SKA.

4.7 Dark Matter models and free-free emission

Free-free emission from ionized medium can produce a potentially remarkable distortion in the CMB spectrum, particularly at long wavelengths. The baryonic matter variance can be then calculated integrating the corresponding power spectrum over a suitable interval:

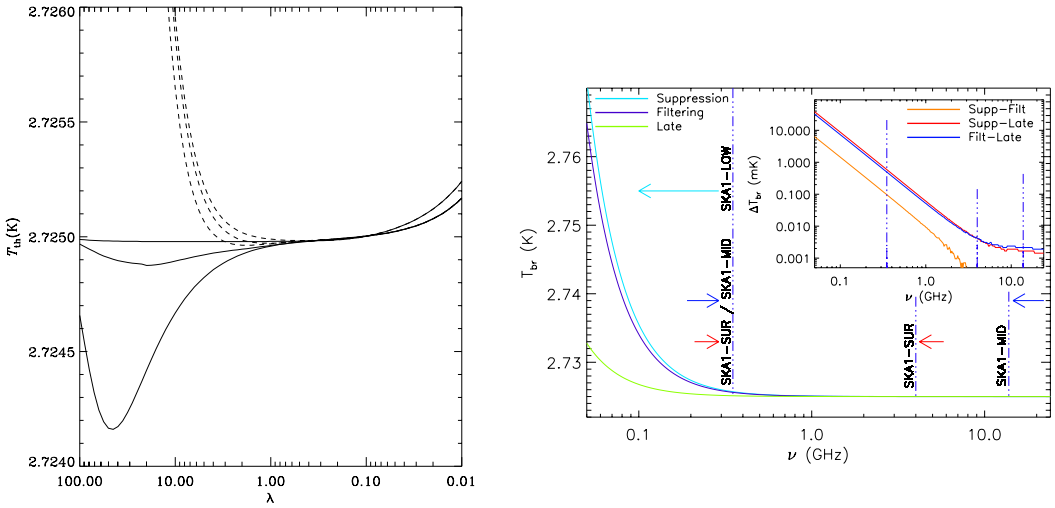

Figure 4.2: Left panel: distorted spectra in equivalent thermodynamic temperature vs. λ (cm) with late energy injection $\Delta\varepsilon/\varepsilon_i \simeq 4y = 5 \times 10^{-6}$ plus an early/intermediate energy injection $\Delta\varepsilon/\varepsilon_i = 5 \times 10^{-6}$ ($\sim$ 20 times smaller than current upper limits) at the "time" Comptonization parameter $y_h = 5, 1, 0.01$ (bottom to top; the cases at $y_h = 5$ and 1 are very similar at short λ; solid lines) plus a FF distortion with $y_B = 10^{-6}$ (dashes). $y_h = y$, but assuming electron temperature equal to the radiation one and computing the integral from the energy injection time to the current time. Right panel: FF distortion in SKA2 frequency range by two astrophysical reionization histories (a *late* phenomenological model is also displayed for comparison). Inset: models absolute differences; vertical lines: ranges of SKA1 configurations.

$$\sigma^2(z) = \frac{1}{2\pi^2} \int P(k,z) k^2 dk \,. \tag{4.5}$$

The matter density contrast depends on the cosmological model and parameters. In particular, the nature of DM particles affects the power spectrum of density perturbations at small scales, with implications for the clumping factor (327).

The CDM standard cosmological model predicts the existence of primordial cold and collisionless particles with negligible small velocity dispersion at the epoch of radiation-matter equilibrium and a derived matter power spectrum supporting small scale structure formation. Warm Dark Matter (WDM) particles have intrinsic thermal velocities, so exhibit larger velocity dispersions with respect to CDM particles and characteristic free streaming scales that contribute to determine clustering properties, as the small scale structures formation suppression. Typical particle masses are in the range of the keV scale ($m_{warm} \sim 1 \div 10\,\mathrm{keV}$) (47), which is intermediate between cold ($\sim 10 \div 10^2\,\mathrm{GeV}$) and hot DM masses ($\sim$ few eV). Sterile

neutrinos or gravitinos are possible candidates for WDM. The suppression of fluctuations due do WDM particles on scales smaller than their free-streaming scale, corresponding to a cut-off of the total matter power at large k, slows down the growth of structure (332) and can be described by the transfer function for different cut-off values. For a given cosmological model, the transfer function describes the effect induced by the free-streaming length on the matter distribution such:

$$T(k) = \left[\frac{P(k)_{WDM}}{P(k)_{CDM}}\right]^{1/2} . \tag{4.6}$$

While the formation of the first generation of stars is affected by the adopted cosmological model, large scale structure distributions are independent of the model (135). The power spectrum drop for WDM models with different particle properties can be approximated by a CDM model with a suitable cut-off k_{max}, typically in the range $\simeq (20 \div 10^3)$. Thus, $\sigma^2(z)$ mainly depends on two crucial parameters, the amplitude and the small scale cut-off of perturbations.

Defining the density as the contribution of a mean term plus a small perturbation

$$\rho = \langle\rho\rangle(1 + \delta\rho/\langle\rho\rangle) \tag{4.7}$$

and averaging over a representative volume of the Universe, I introduce the clumping factor as:

$$\frac{\langle\rho^2\rangle}{\langle\rho\rangle^2} = 1 + \frac{\langle(\delta\rho)^2\rangle}{\langle\rho\rangle^2} = 1 + \sigma^2 > 1 . \tag{4.8}$$

In this context, the clumping factor is a time dependent multiplicative factor to be accounted to modify the bremsstrahlung rate from a homogeneous to an inhomogeneous medium. The complete FF term is then obtained by introducing:

$$\Omega_b^2(z) = \Omega_{b,homog}^2(1 + \sigma^2(z)) , \tag{4.9}$$

where $\Omega_{b,homog}^2$ corresponds to the (standard) homogeneous case[1]. This separation approach, based on the factorization of the square of the baryon density, allows to get the main effect

[1]Note that the density contrasts of free electrons and atoms in different ionization states could be in principle different. Also, inhomogeneities in the medium temperature could be in principle taken into account. On the other hand, being weak the dependence on electron temperature, T_e, of the bremsstrahlung rate $K_B/x_e^3 \propto \phi^{-1/2}$, $x_e = h\nu/(kT_e)$ being a dimensionless photon frequency, and of the term $e^{-x_e} \simeq 1 - x_e$ at low frequencies, where free-free process is particularly relevant, I can neglect to first order this further correction. Higher order corrections could be evaluated from the variances of the various terms. On the basis of the currently available studies on IGM temperature, these corrections are expected to be very small.

from matter density contrast and to couple it with all the other relevant aspects in the thermal and ionization history, with versatility regarding the underlying cosmological model (see (327), where also suitable analytical approximations are reported).

4.7.1 Exploiting various models

In order to investigate the effects triggered by the reionization process and amplified by a non negligible IGM density contrast on diffuse FF emission, I focalized my analysis on three specific reionization models. Two of them, namely suppression (S) (74) and filtering (F) (142), are astrophysical motivated, the other is a phenomenological, late double peaked (L) history (219), considered here for comparison (see (326) and references therein for further details about these models and their parameters). The S and F reionization scenarios can be tuned to match various kinds of astronomical observations (see (295)). Their optical depths, $\tau_S = 0.1017$ and $\tau_F = 0.0631$, are consistent with the WMAP[1] and *Planck* 2013 results (based on WMAP polarization data) and with *Planck* 2015 results[2], respectively. The L scenario can be modelled by means of free quantities describing the electron ionization fraction and electron temperature (its main parameters are set here to have $\tau_L = \tau_S$).

I explore various alternative cosmological models, evaluating the variance first assuming a fixed cut-off value of the matter power spectrum ($k_{max} = 100$). To this aim, I run the original CAMB code[3] with different combinations of cosmological parameters to compute the matter power spectrum in a suitable range of redshifts, $0 < z < 30$, according to the considered reionization histories. The differences between models are typically more evident at small scales and tend to be smaller on intermediate scales. The power spectrum shape depends on the cosmological model and the full set of parameters. Fixing the other parameters, the perturbation amplitude mainly defines the $P(k)$ overall level. Thus, the variance scales quite linearly with the perturbation amplitude as the power spectrum does. The results can be simply extended to different cut-off parameters. Fig. 4.3 shows the evolution of the clumping factor for a set of cosmological parameter of the ΛCDM model consistent with CMB data and for three values of k_{max} (200, 500 and 1000) among those exploited for numerical estimates.

[1] lambda.gsfc.nasa.gov/product/map/
[2] www.cosmos.esa.int/web/planck
[3] http://camb.info/

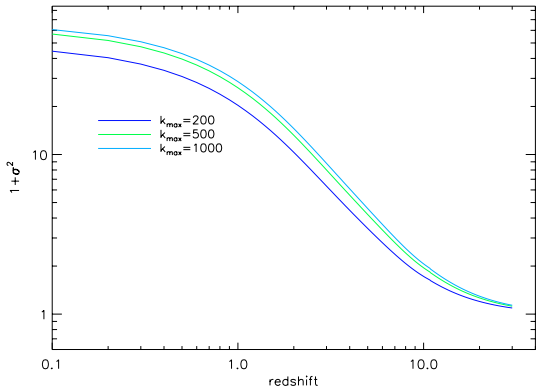

Figure 4.3: Evolution of clumping factor for three values of k_{max}.

4.7.2 Results

At low frequencies, the CMB spectrum can be described in terms of brightness temperature by the relation:

$$T_{br}(x) \simeq \left(\frac{y_B(x)}{x^2} - 2u\phi_i + \phi_i\right) T_r \ , \tag{4.10}$$

where $x = h\nu/(kT_r)$ and $T_r = T_0(1+z)$ are the redshift invariant dimensionless frequency and the redshift dependent CMB effective temperature. Eq. (4.10) holds at any redshift, provided that the coupled free-free and Comptonization distortion parameters, y_B and u, are integrated over the corresponding redshift interval.

Basically, in order to describe the effect induced by FF mechanism in terms of temperature excess at different frequencies, I can rewrite Eq. (4.10) as:

$$\frac{\Delta T_{ff}}{T_r}(x) \simeq \frac{y_B(x)}{x^2} \ , \tag{4.11}$$

where I have defined $\Delta T_{ff} = (T_{br} - T_r\phi_i)$. This is illustrated in Fig. 4.4 for the three considered reionization models and different cut-off parameters.

At wavelengths $\lambda = c/\nu \gtrsim 1.5\,\mathrm{cm}$, y_B can be well described by $y_B(\lambda) \simeq a\log\lambda + b$, where the two parameters a and b are found to be well approximated by a log-log linear dependence on k_{max}, i.e. $\log a \simeq m_a \log k_{max} + n_a$ and $\log b \simeq m_b \log k_{max} + n_b$, with $m_b \simeq m_a = m$, slightly dependent on the model, and with $10^{n_b - n_a}$ independent of the model. Thus, $y_B(\lambda)$ exhibits a simple power law dependence on k_{max}. I find $y_B(\lambda) \simeq Ak_{max}^m(\log\lambda + B)$ with $B = 0.6288$ and $(A, m) = (1.337 \times 10^{-9}, 0.2275)$ for the S model (resp. $(1.078 \times 10^{-9}, 0.2424)$ or

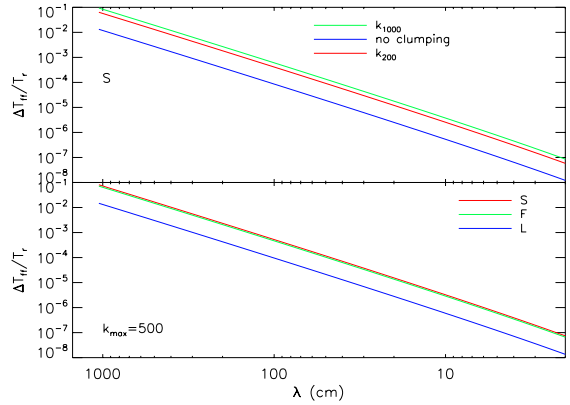

Figure 4.4: Brightness temperature relative excess predicted at current time as function of the wavelength assuming the $y_B(x)$ value properly evaluated at each frequency in the entire range. Upper panel: suppression model for $k_{max} = 200$ and 1000 and without the correction due to the IGM density contrast. Bottom panel: comparison between the three considered reionization histories for $k_{max} = 500$.

$(2.096 \times 10^{-10}, 0.2482)$ for the F and L models). The (weak) dependence of the slope, m, on the model characterizing the dependence of $y_B(\lambda)$ on the cut-off wavenumber, k_{max}, has a physical explanation: m increases with the fractional contribution $\Delta y_B(z)/y_B$ to y_B at low redshifts, as a result of the relative larger relevance of clumping. Remarkably, the value of $m \simeq 0.24$ implies a significant dependence of the free-free signal amplification on k_{max}.

The free-free signal monotonically increases at decreasing frequencies and the same holds for the extragalactic radio sources confusion noise (75).

4.7.3 Astrophysical confusion noise

SKA high sensitivity and resolution can also be used to model the contribution from Galactic emissions and extragalactic foreground, a fundamental step to accurately observe CMB spectral distortions. Extragalactic source contribution is small compared to Galactic radio emission, currently the major astrophysical problem in CMB spectrum experiments, but, differently from the Galactic emission, it cannot be subtracted from the CMB by exploiting its angular correlation properties because of the limited resolution of experiments devoted to CMB monopole temperature, particularly at low frequencies. A direct radio background estimate from precise number counts will certainly improve the robustness of these kinds of analyses.

Even though the radio source background at extremely low brightness temperature is still not well described, recent observations at GHz frequencies (75, 273) have tens of μJy sensitivity

levels. Studying the differential number count of extragalactic sources in various flux densities ranges at 0.153 GHz (342), 0.325 GHz (208), 1.4 GHz and 1.75 GHz, it is possible to estimate their contribution to the radio background. These signals are negligible with respect to the accuracy of current CMB spectrum experiments, in particular at wavelength $\gtrsim 1$ cm but they could be outstanding at the accuracy level potentially achievable with future experiments.

Whether the sources brighter than several tens of nJy have been subtracted from the radio background, T_b comes out to be less than $\sim$ 1 mK at frequencies above $\sim$ 1 GHz, but larger than $\sim$ 10 mK below $\sim$ 0.3 GHz. An estimate of the minimum source detection threshold can be derived by the source confusion noise which, around 1.4 GHz, has been quoted:

$$5\sigma_{conf} \simeq 5 \times 1.2(\nu/3\,\mathrm{GHz})^{-0.7}(\theta/8'')^{10/3}\mu Jy, \tag{4.12}$$

where θ defines the relevant resolution. Thus, the finite angular extension of faint galaxies, $\theta \sim 1''$, implies a "natural confusion limit" of about 10 nJy at frequencies around $\sim$ 1.4 GHz indicating that, for deep surveys, source confusion will not represent a relevant limitation.

At 1 GHz $\lesssim \nu \lesssim$ some GHz ($\lambda \approx 1$ dm) the signal amplitudes derived for CMB distorted spectra sufficiently below FIRAS limits are remarkably larger than the estimates of the background from extragalactic sources fainter than some tens of nJy. Free-free distortion amplitude increases at decreasing frequencies, but source confusion noise may represent a serious problem, maybe by prohibiting the faint detection threshold detection fundamental for a source contribution to the background less than the CMB distortion amplitude.

Accurate absolute measurements with a wide frequency coverage can allow a joint fit of both CMB distorted spectra and astrophysical signals (291), but a direct radio background estimate from precise number counts will certainly improve the robustness of this kind of analyses. The most advantageous frequency range to detect the FF signal should account for a comparison between (at least) these two components, almost isotropic on large angular scales (while Galactic diffuse emissions can be separated exploiting also their remarkable angular pattern and correlation). The best frequencies are found to be around few GHz (50), well above the ones where the redshifted 21-cm line will allow a tomographic view of the reionization history. Therefore, when the astrophysical scenario will be well understood, free-free signatures could be used to test also DM properties through their effect on the power spectrum at small scales.

4.8 SKA contribution to future B-mode projects

The angular power spectrum of the CMB polarized anisotropies can be decomposed into E-modes, mainly generated by scalar perturbations in the primordial universe, and B-modes that could be mainly contributed at large scales (i.e. low multipoles, ℓ) by tensor metric perturbations[1]. As discussed in Chapter 1, discovering primordial B-modes is considered the most ambitious goal of current and future CMB polarization projects (see e.g. (12, 81, 166) and references therein).

Extragalactic radio sources (see e.g. (100) and references therein) are an important, if not dominant, contaminant to the microwave sky in total intensity and in polarization at scales smaller than 30 arcmin up to $\sim$ 100 GHz. As discussed in Chapter 2 and 3 of radio source contribution to the angular power spectrum at high multipoles is fundamental for a precise assessment and subtraction of the lensing B-mode signal. The latter, in turn, improves the detection and the error bar determination of the primordial B-modes at intermediate and large scales. An accurate determination of radio source emission is therefore crucial to measure the CMB angular power spectrum and, in particular, to detect the primordial B-modes, that could be extremely weak for low values of r, and, in general, to accurately characterize them. Correcting the CMB angular power spectrum requires precisely measuring the contribution of radio sources to within several factors below the detection limit of the CMB experiment, which depends on the noise, background and foreground levels varying in different regions of the sky. Indeed, source polarization fluctuations come from the ones below the detection threshold of CMB observations, i.e. they were not observed directly in CMB experiments, that have relatively shallow resolution ($\sim$ arcmin) and sensitivity (of the order of tens to few hundreds of mJy), but are accessible, for instance, to interferometric observations, that have better sensitivity and resolution, being then more suitable for point-like sources. Of course, future CMB surveys will benefit from complementary sensitive polarization measurements at the CMB observing frequency for both generating adequate masks and statistically characterizing source populations to subtract their statistical contribution to the angular power spectrum below the detection thresholds. SKA will allow a deep understanding of polarized sources only up to about 20 GHz, but at the most extreme faint flux densities. The error on the estimate of the source polarization fluctuations based on extrapolation from lower to higher frequencies,

[1] Vector perturbations generate both E- and B-modes, but, except for particular scenarios, they are expected to be typically subdominant.

more suitable for CMB anisotropy experiments, decreases at decreasing flux density detection threshold. Thus, combining ultra-sensitive SKA with observations at millimetre wavelengths will be very important to quantify source contribution to CMB polarization fluctuations at large multipoles, and then to improve lensing and delensing treatment from high to low multipoles.

Besides the SKA continuum surveys, which are described in (274), the deep and ultra-deep surveys are clearly the most relevant ones to determine the very faint source counts, while P(D) methods can be exploited to extract information on number counts below the survey sensitivity (75), particularly in low frequency continuum surveys, dedicated to non-thermal emission in clusters and filaments. The Ultra Deep survey dedicated to the Star Formation History of the Universe (SFHU), with their planned rms sensitivity of some tens of nJy per beam and arcsec or better resolution[1], to be compared, for example, with the sensitivity levels of tens of μJy of current measurement of radio source counts at GHz frequencies (75, 273), will represent a great opportunity for an accurate determination of source number counts and fluctuations down to very faint fluxes. Fig. 4.5 shows a comparison between CMB B-mode angular power spectrum for different values of r, lensing and residual foregrounds. The B-mode angular power spectrum (from the dominant Poissonian term) of radio sources is shown for different detection thresholds in polarized flux density, adopting the number counts model and the median polarization degree, averaged over frequencies, $\Pi_{\rm IDA,median} = 2.75$ %, respectively adopted and found Chapter 3. In spite of unavoidable frequency extrapolation errors (generously accounted in the figure by the very conservative assumed threshold), we expect that SKA characterization of polarization properties of radio sources will make their residual polarization fluctuations almost negligible.

Moreover, SKA will allow a better study of the low frequency tail of Galactic diffuse foregrounds, where polarized synchrotron emission peaks, a key point for B-mode analyses, also because CMB projects are typically focused on higher frequencies. In particular, this will allow us to test Galactic synchrotron emission models, 3D physical models of the Galaxy and the large scale coherent component of the Galactic magnetic field (118, 119, 311, 312, 313), based on advanced numerical codes (308, 335) and including turbulence phenomena (72). For the accurate treatment of foregrounds in cosmology it is also important to improve our understanding of the anomalous microwave emission (AME), well-correlated with far-IR dust emission. It is

[1] According to (75), considering, as example, frequencies around 1.4 GHz, a natural source confusion limit of about 10 nJy is derived, thus indicating that, for surveys with rms sensitivity of tens of nJy, source confusion will not represent a relevant limitation in a wide set of frequencies (50).

produced by rapidly spinning small dust grains having an electric dipole moment and its spectrum is expected to peak in the range 15–50 GHz. The AME polarization degree is currently essentially unknown, although values at the per cent level are typically expected. SKA2 could provide precise mapping on the low frequency tail of this emission.

Fig. 4.5 compares the CMB B-mode angular power spectrum for different values of r with examples of potential residuals from Galactic emission (applying a mask excluding about 27% of the sky highly contaminated by Galactic emission) based on *Planck* 2015 results (238, 243). As well known, polarized dust emission is the most critical foreground for CMB B-mode analyses (36, 241), but for detecting and characterizing B-modes for $r \lesssim$ some $\times 10^{-2}$ the accurate knowledge low frequency polarized foregrounds, synchrotron and AME, is also crucial.

In general, a large sky coverage mapping of above Galactic radio emissions is very important for cosmological applications. Among the SKA continuum surveys (274), I compare the sensitivity (on the same resolution element) of the $\sim$ 75% sky coverage surveys at 1.4 GHz and at 0.12 GHz, planned for 1–2 years of integration and dedicated respectively to strong gravitational lensing and legacy/rare serendipity and to non-thermal emission in clusters and filaments, with that of radio surveys (186) currently adopted as ancillary maps in CMB experiment analyses. The former will have a sensitivity about 20 times better than the available all-sky radio survey at 1.4 GHz, the latter will have sensitivity about 4 times better than the Haslam map at 408 MHz (156), thus representing a significant improvement with respect to current ancillary radio maps.

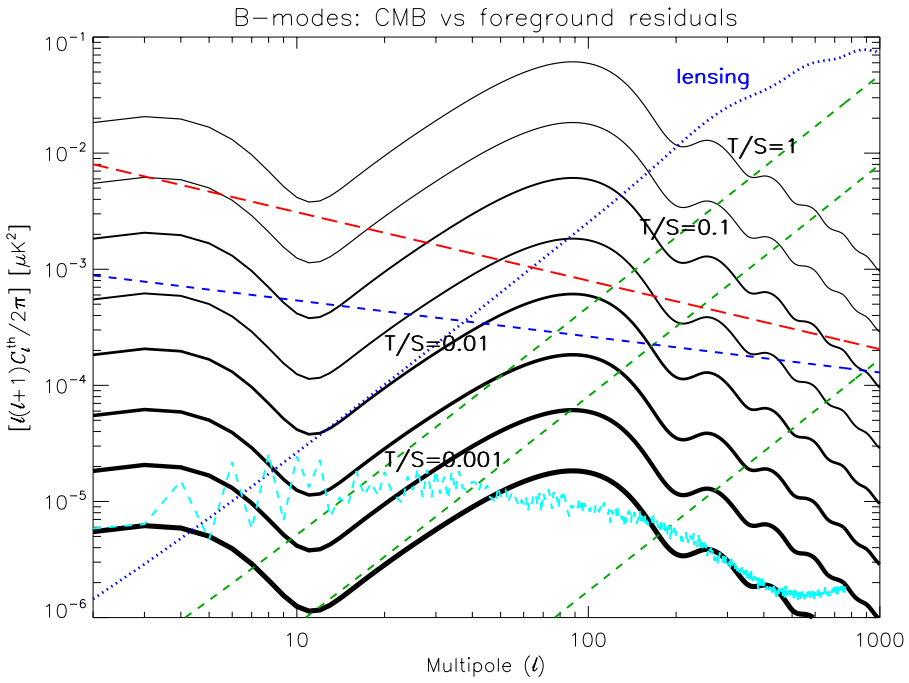

Figure 4.5: The CMB B-mode polarization angular power spectrum for different tensor-to-scalar perturbation ratios (from 1 to 3×10^{-4}; solid black lines), lensing (blue dots), and estimates of potential residual of Galactic foregrounds (at 70 GHz) and angular power spectrum from polarized radio sources (at 100 GHz) below different detection thresholds in polarized flux density (green dashes; from top to bottom, 100 mJy and 10 mJy, representative of thresholds achievable, respectively, in current and future CMB experiments, and 100 μJy representative of potential improvement discussed here). Red long dashes show typical potential residuals from Galactic polarized dust emission extrapolated from 353 GHz assuming an error of 0.01 in the dust grain spectral index. Blue dashes show typical potential residuals from Galactic polarized synchrotron emission extrapolated from 30 GHz assuming an error of 0.02 in the synchrotron emission spectral index. Cyan dashes show an estimate of AME angular power spectrum assuming a polarization degree of 2%. See also the text.

5

Observer peculiar motion effects in microwave and radio surveys

5.1 Introduction

The peculiar motion of an observer with respect to the CMB rest frame gives rise to boosting effects (the largest of which is the CMB dipole, i.e., the multipole $\ell = 1$ anisotropy in the Solar System barycentre frame), which can be explored by future CMB missions. In this Chapter, I focus on peculiar velocity effects and their relevance to the CORE experiment, according to specifications summarised in Table 1.8.

The analysis of cosmic dipoles is of fundamental relevance in cosmology, being related to the isotropy and homogeneity of the Universe at the largest scales. In principle, the observed dipole is a combination of various contributions, including observer motion with respect to the CMB rest frame, the intrinsic primordial (Sachs-Wolfe) dipole and the Integrated Sachs-Wolfe dipole as well as dipoles from astrophysical (extragalactic and Galactic) sources. The interpretation that the CMB dipole is mostly (if not fully) of kinematic origin has strong support from independent studies of the galaxy and cluster distribution, in particular via the measurements of the so-called *clustering dipole*. According to the linear theory of cosmological perturbations, the peculiar velocity of an observer (as imprinted in the CMB dipole) should be related to the observer's peculiar gravitational acceleration via $\vec{v}_{\rm lin} = \beta_{\rm rd}\vec{g}_{\rm lin}$, where $\beta_{\rm rd} \simeq \Omega_{\rm m}^{0.55}/b_{\rm g}$ is also know as the redshift-space distortion parameter ($b_{\rm g}$ and $\Omega_{\rm m}$ being, respectively, the bias of the particular galaxy sample and the matter density parameter at the present time). The peculiar velocity and acceleration of, for instance, the Local Group treated as one system, i.e., as

measured from its barycentre, should thus be aligned and have a specific relation between amplitudes. The former fact has been confirmed from analyses of many surveys over the last three decades, such as IRAS (155, 307), 2MASS (112, 198), or galaxy cluster samples (48, 271). As far as the amplitudes are concerned, the comparison has been used to place constraints on the $\beta_{\rm rd}$ parameter (25, 37, 48, 112, 284), totally independent of those from redshift-space distortions observed in spectroscopic surveys. In this context, confirming the kinematic origin of the CMB dipole, through a comparison accounting for our Galaxy's motion in the Local Group and the Sun's motion in the Galaxy (82, 296), it would provide support for the standard cosmological model, while finding any significant deviations from this assumption could open up the possibility for other interpretations (42, 136, 283, 344).

Cosmic dipole investigations of more general type have been carried out in several frequency domains (140), where the main signal comes from various types of astrophysical sources differently weighted in different shells in redshift. An example are dipole studies in the radio domain, pioneered by (111) and recently revisited by (286) performing a re-analysis of the NRAO VLA Sky Survey (NVSS) and the Westerbork Northern Sky Survey, as well as by (324, 325) using NVSS data alone. Prospects to accurately measure the cosmic radio dipole with the Square Kilometre Array have been studied by (297) while perspectives on future surveys jointly covering microwave/millimeter and far-infrared wavelengths aimed at comparing CMB and CIB dipoles have been presented in (125). For the CMB, space observations represent the best, if not unique, way to precisely measure this large-scale signal. It is then important to consider the expectations from (and the potential issues for) future CMB surveys beyond the already impressive results produced by *Planck*.

In addition to the dipole, due to the combination of observer velocity and Sachs-Wolfe and intrinsic effects, a moving observer will see velocity imprints on the CMB due to Doppler and aberration effects (55, 61), which manifest themselves in correlations between the power at subsequent multipoles of both temperature and polarization anisotropies. Precise measurements of such correlations (11, 184) provide important consistency checks of fundamental principles in cosmology, as well as an alternative and general way to probe observer peculiar velocities (259, 283). This type of analysis can in principle be extended to thermal Sunyaev-Zeldovich (tSZ) (31, 54, 68) and CIB signals. I am going to discuss how these investigations could be improved when applied to data expected from a next generation of CMB missions, exploiting experimental specifications in the range of those foreseen for LiteBIRD (166) and CORE.

Since the results from COBE (41), no substantial improvements have been achieved in the observations of the CMB spectrum at $\nu \gtrsim 30\,\mathrm{GHz}$.[1] Absolute spectral measurements rely on ultra-precise absolute calibration. FIRAS (123) achieved an absolute calibration precision of 0.57 mK, with a typical inter-frequency calibration accuracy of 0.1 mK in one decade of frequencies around 300 GHz. The amplitude and shape of the CIB spectrum, measured by FIRAS (124), is still not well known. Anisotropy missions, like CORE, are not designed to have an independent absolute calibration, but nevertheless can investigate the CMB and CIB spectra by looking at the frequency spectral behaviour of the dipole amplitude (18, 91, 101, 236). Unavoidable spectral distortions are predicted as the result of energy injections in the radiation field occurring at different cosmic times, related to the origin of cosmic structures and to their evolution, or to the different evolution of the temperatures of matter and radiation. For quantitative forecasts I will focus on well-defined types of signal, namely Bose-Einstein (BE) and Comptonization distortions (316, 353); however, one should also be open to the possible presence of unconventional heating sources, responsible in principle for imprints larger than (and spectral shapes different from) those mentioned above, and having parameters that could be constrained through analysis of the CMB spectrum. Deciphering such signals will be a challenge, but holds the potential for important new discoveries and for constraining unexplored processes that cannot be probed by other means. At the same time, a better determination of the CIB intensity greatly contributes to the understanding of the dust-obscured star-formation phase of galaxy evolution.

5.2 Radio dipole

During last years the dipole anisotropy has been intensely investigated (39, 140, 286, 302) also in radio surveys and it seems to be due to the radio-source number counts (111). Conversely, from the anisotropy of those radio number counts it is possible to derive the velocity relative to their rest frame which can be, in principle, compared to the one evaluated from the CMB. Even though the two measurements are in good agreement, a non negligible discrepancy exist. Different analyses have revealed a radio dipole characterized by a similar direction to the CMB dipole but with an amplitude remarkably higher by a factor three or four (286, 302).

[1] For recent observations at long wavelengths, see the results from the ARCADE-2 balloon (298, 303) and from the TRIS experiment (138).

Many authors hypothesize that the radio dipole gets part of its contribution from the Solar System motion with respect to the CMB, the so called kinetic dipole, and an additional part from the uneven galaxy distribution, known as the structure dipole. The amplitude of the kinetic term is given by $d = [2 + x(1 + \alpha)](v/c)$, being α the mean radio sources spectral index and x the power law index of the corresponding number counts. The observed dependence on the lower flux density limit and on the survey frequency band can be the key to disentangle the two dipole constributions.

Recent studies (175, 340) affirm that, on scales of 300 Mpc, the local Universe presents regions of atypical low density galaxies. Unlikely we live in the centre of one void, therefore it must be an offset distance between us and the centre of the void, $\vec{r}_{\rm v}$. An imaginary sphere centred around the Local Group, with a radius $R_{\rm o} > R_{\rm v}$, will enclose more galaxies in one direction than in the other. If the Local Group moves in the direction of the under densities because of gravitational pull, it gives rise to a structural dipole component which affects the evaluation of the radio dipole. Presumably, the presence of local voids can play a role in the amplitude of radio dipole with an additive term to the velocity dipole (285). This extra term, expected to be of the order of $(2.1 \pm 0.1) \times 10^{-3}$ for a void of radius $0.07 R_H$ with R_H the Hubble radius, cannot explain completely the discrepancy.

5.3 The CMB dipole: forecasts for CORE in the ideal case

A relative velocity, $\beta \equiv v/c$, between an observer and the CMB rest frame induces a dipole (i.e., $\ell = 1$ anisotropy) in the temperature of the CMB sky through the Doppler effect. Such a dipole is likely dominated by the velocity of the Solar System, $\vec{\beta}_{\rm S}$, with respect to the CMB (Solar dipole), with a seasonal modulation due to the velocity of the Earth/satellite, $\vec{\beta}_{\rm o}$, with respect to the Sun (orbital dipole). In this work, I neglect the orbital dipole (which may indeed be used for calibration), thus hereafter I will denote with $\vec{\beta}$ the relative velocity of the Solar dipole (52).

It is important to initially forecast the ability to recover the dipole parameters (amplitude and direction) by performing a Markov chain Monte Carlo (MCMC) analysis in the ideal case (i.e., without calibration errors or sky residuals). Results including systematics are given in Sect. 5.5. I test the amplitude of the parameter errors against the chosen sampling resolution and to probe the impact of both instrumental noise and masking of the sky. I consider the "*Planck* common mask 76" (in temperature), which is publicly available from the Planck

Legacy Archive (PLA)[1] (235), and keeps 76 % of the sky, avoiding the Galactic plane and regions at higher Galactic latitudes contaminated by Galactic or extragalactic sources. I exploit here an extension of this mask that excludes all the pixels at $|b| \leq 30°$.[2]

Additionally, I explore the dipole reconstruction ability for different frequency channels, specifically 60, 100, 145, and 220 GHz and I finally investigate the impact of spectral distortions (see Sects. 5.7 and 5.8), treating the specific case of a BE spectrum (with chemical potential $\mu_0 = 1.4 \times 10^{-5}$, which is several times smaller than FIRAS upper limits).

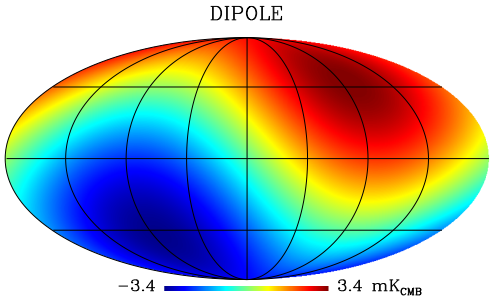

Figure 5.1: Map of the CMB dipole used in the simulations, corresponding to an amplitude $A = 3.3645$ mK and a dipole direction defined by the Galactic coordinates $b_0 = 48.24°$ and $l_0 = 264.00°$. The map is in Galactic coordinates and at a resolution of $\simeq 3.4$ arcmin, corresponding to `HEALPix` $N_{\rm side} = 1024$.

The dipole can be written in the form:

$$d(\hat{n}) = A\,\hat{n} \cdot \hat{n}_0 + T_0, \tag{5.1}$$

where $\hat{n}$ and $\hat{n}_0$ are the unit vectors defined respectively by the Galactic longitudes and latitudes (l, b) and (l_0, b_0). In Fig. 5.1 I show the dipole map used in the simulations, generated assuming the best-fit values of the measured dipole amplitude, $A = (3.3645 \pm 0.002)$ mK, and direction, $l_0 = 264.00° \pm 0.03°$ and $b_0 = 48.24° \pm 0.02°$, found in the *Planck* (combined result from the High Frequency Instrument, HFI, and Low Frequency Instrument, LFI) 2015 release (237, 240, 256). Assuming the dipole to be due to velocity effects only, its amplitude corresponds to $\beta \equiv |\vec{\beta}| \equiv v/c = A/T_0 = 1.2345 \times 10^{-3}$, with $T_0 = 2.72548 \pm 0.00057$ K being the present-day temperature of the CMB (122). In Fig. 5.2 I present the instrumental noise map and the *Planck*

[1] http://pla.esac.esa.int/pla/

[2] When I degrade the *Planck* common mask 76 to lower resolutions I apply a threshold of 0.5 for accepting or excluding pixels, so that the exact sky coverage not excluded by each mask (76–78 %) slightly increases at decreasing $N_{\rm side}$. In the case of the extended masks, typical sky coverage values are 47–48 %.

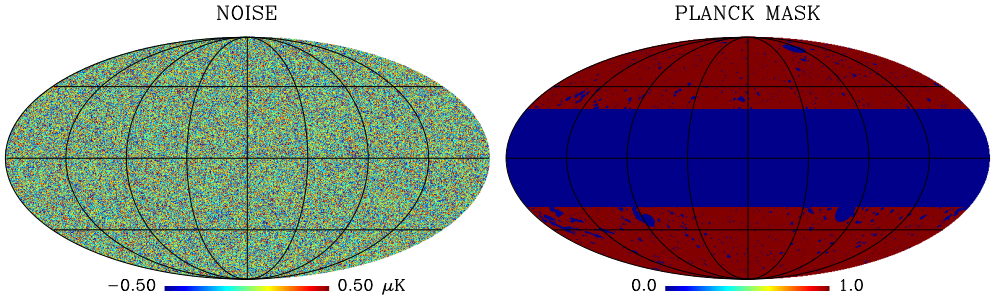

Figure 5.2: Instrumental noise map and *Planck* Galactic mask (extended to cut out ±30° of the Galactic plane) employed in the simulations. The noise map corresponds to 7.5 μK.arcmin, as expected for the 60-GHz band. The Map is in Galactic coordinates and at resolution of $\simeq$ 3.4 arcmin, corresponding to `HEALPix` $N_{\rm side} = 1024$.

Galactic mask employed in the simulations. The noise map corresponds to 7.5 μK.arcmin, as expected for the 60-GHz band.

The likelihoods for the parameters A, l_0, b_0 and T_0 are evaluated using the publicly available `COSMOMC` generic sampler package (157, 189, 213). While the monopole T_0 is not an observable of interest in this context, it is included to be a free parameter in order to verify any degeneracy with the other parameters and for internal consistency checks.

To probe the dependence of the parameter error estimates on the sampling resolution, I investigate the dipole reconstruction at `HEALPix` (143) $N_{\rm side} = 128$, 256, 512, and 1024, eventually including the noise and the Galactic mask. The reference frequency channel for this analysis is the 60-GHz band. The corresponding likelihoods are collected in Appendix 5.A (see Fig. 5.15) for the same representative values of $N_{\rm side}$ (see also Table 5.10 for the corresponding 68% confidence levels).

Fig. 5.4 shows the 1 σ uncertainties on the parameter estimates as functions of the `HEALPix` $N_{\rm side}$ value. I find that the pixelization error due to the finite resolution is dominant over the instrumental noise at any $N_{\rm side}$. This means that dipole estimation is essentially limited by the sampling resolution. As expected, the impact of noise is negligible, although the effect of reducing the effective sky fraction is relevant. Indeed, the presence of the Galactic mask results in larger errors (for all parameters) and introduces a small correlation between the parameters A and b_0, as clearly shown in these plots.

The likelihood results for some of the different frequencies under analysis are collected in Figs. 5.16 of Appendix 5.A (see also Table 5.11 for the 68% confidence levels at the four considered frequencies). I fix the resolution at `HEALPix` $N_{\rm side} = 1024$ and consider both noise

level and choice of Galactic mask. It emerges that the dipole parameter estimates do not significantly change among the frequency channels, which is clearly due to the sub-dominant effect of the noise.

As last ideal case test, I compare the dipole parameter reconstruction between the cases of a pure blackbody (BB) spectrum and a BE-distorted spectrum. The comparison of the likelihoods is presented in Fig. 5.17 of Appendix 5.A (see also Table 5.12 for the corresponding 68% confidence levels). This analysis shows that the parameter errors are not affected by the spectral distortion and that the direction of the dipole is successfully recovered. The difference found in the amplitude value is consistent with the theoretical difference of about 76 nK.

5.4 Parametric model for potential foreground and calibration residuals in total intensity

Previous section points out that in the ideal case of pure noise, i.e., assuming perfect foreground subtraction, calibration and in absence of systematic effects, the sky regions analysed manifest a dominant pixel-sampling limitation over the noise limitation.

Clearly, specific component-separation and calibration methods introduce specific types of residuals. Rather than trying to accurately characterize them (particularly in the view of great efforts carried out in the last decade for specific experiments and the progress that is expected over the coming years), I implemented a toy model to parametrically estimate the potential impact of foreground subtraction residuals and patchy calibration in total intensity (i.e., in temperature). To this aim I exploited some of the publicly available *Planck* results and products accessible at the PLA website[1].

The PLA provides single frequency high resolution ($N_{\rm side} = 2048$) temperature maps of global foregrounds and for the different component separation algorithms. My analysis is based on the `COMMANDER` method but adopting another foreground-separation cleaned map is not relevant for the present purpose. The archive provides also suitable estimates of temperature zodiacal light emission (ZLE) maps from *Planck*-HFI. My aim is to produce templates of potential foreground residuals scalable in amplitude by means of a free parameter. To estimate such emission at the CORE frequencies, without relying on particular sky models, I linearly interpolated in logarithmic scale, i.e., in $\log(\nu)$–$\log(T)$) pixel by pixel the foreground and ZLE maps, and linearly extrapolate the ZLE maps at $\nu < 100$ GHz. Then I derive a template of

[1] https://pla.esac.esa.int/pla/#home

signal sky amplitude at each CORE frequency, adding, for each pixel, the absolute values of these foreground and ZLE maps[1] and of the CMB anisotropy map available at the same resolution in the PLA (specifically used that based on COMMANDER). For this analysis it is not relevant to separate CMB and astrophysical emission at $\ell \geq 3$, then I generate the templates from these maps, extracting the a_{lm} modes for $\ell \leq 2$ only, before degrading them to the desired resolution. Finally, I produce maps of Gaussian random fields at each CORE frequency, with rms amplitude given by these templates, $T_{\rm amp,for}$, multiplied by a free factor, $E_{\rm for}$, which globally characterizes the potential amplitude of foreground residuals after component separation. Clearly, the choice of reasonable values of $E_{\rm for}$ depends on the resolution being considered (or on the adopted pixel size), with the same value of $E_{\rm for}$ but at smaller pixel size implying less contamination at a given angular scale.

Planck maps reveal, at least in temperature, a greater complexity in the sky than obtained by previous experiments. The large number of frequencies of CORE is in fact designed to accurately model foreground emission components with a precision much better than *Planck*'s. Also, at least in total intensity, ancillary information will come in the future from a number of other surveys, ranging from radio to infrared frequencies.

The target for CORE in the separation of diffuse polarized foreground emission corresponds to $E_{\rm for} \simeq 0.01$, i.e., to $\simeq 1\,\%$ precision at angular scales larger than about 1° (i.e., up to multipoles $\ell \lesssim 200$), where the main information on primordial *B*-modes is contained, while at larger multipoles the main limitation comes from lensing subtraction and characterization through control of extragalactic source contributions. Comparing PLA CMB anisotropy maps at $N_{\rm side} = 2048$ for the four component-separation methods and degraded to various resolutions, it emerges that the rms of the difference maps does not scale strongly with the adopted pixel size, at least excluding regions close to the Galactic plane.

For example, outside the *Planck* common mask 76, degrading from $N_{\rm side} = 2048$ to $N_{\rm side} = 256$ or 64, i.e., increasing the pixel linear size by a factor of 8 or 32 (with the exception of the comparison of SEVEM versus SMICA), the rms values of the cross-comparisons range from about 8–9 μK to about 3–5 μK, i.e., a decreases by a factor of only about 2.5. This suggests that, at least for temperature analyses, the angular scale adopted to set $E_{\rm for}$ is not so critical.

[1] Since, here, I am not interested in the separation between the diffuse Galactic emission and ZLE, this assumption is in principle slightly conservative. In practice, separation methods will at least distinguish among these diffuse components, which are typically treated with different approaches, e.g., analysing multi-frequency maps in the case of Galactic emission, and different surveys (or more generally, data taken at different times) for the ZLE.

5.4 Parametric model for potential foreground and calibration residuals in total intensity

Data calibration represents one of the most delicate aspects of CMB experiments. The quality of CMB anisotropy maps does not rely on absolute calibration of the signal (as it would be, for example, in experiments dedicated to absolute measurements of the CMB temperature as the direct determination of the CMB spectrum). However, the achievement of very high accuracy in the relative calibration of the maps (sometimes referred to as absolute calibration of the anisotropy maps), as well as the inter-frequency calibration of the maps, is crucial for the scientific goals achievement of CMB projects. Although this calibration step could in principle benefit from the availability of precise instrumental reference calibrators (implemented for example in FIRAS (206) and foreseen in PIXIE (180), or – but with much less accurate requirements – in *Planck*-LFI (331)), this is not necessary for anisotropy experiments, as shown for example by WMAP and *Planck*-HFI. This represents a huge simplification in the design of anisotropy experiments with respect to absolute temperature ones. *Planck* demonstrated the possibility to achieve relatively calibration of anisotropy data at a level of accuracy of about 0.1 % up to about 300 GHz, while recent analyses of planet flux density measurements and modelling (263) indicate the possibility to achieve a calibration accuracy of $\simeq$ 1 % even above 300 GHz, with only moderate improvements over what is currently realised.

The goal of CORE is to achieve a calibration accuracy level around 0.01 %, while the requirement of 0.1 % is clearly feasible on the basis of current experiments, with some possible relaxation at high frequencies. Methods for improving calibration are fundamental in astrophysical and cosmological surveys, and clearly critical in CMB experiments. In principle, improvements in various directions can be pursued: from a better characterization of all instrument components to cross-correlation between different CMB surveys; from the implementation of external precise artificial calibration sources to the search for a better characterization (and increasing number) of astronomical calibration sources; and, in general, with the improvement of data analysis methods.

To parametrically model potential residuals due to imperfect calibration I reproduce a similar approach to the one applied for the foreground contamination. Calibration uncertainty implies an error proportional to the global effective (anisotropy in my case) signal. Therefore, I produce the same templates adding the foreground, ZLE and CMB anisotropy maps, keeping their signs and maintaining all the a_{lm} modes contained in the maps. The absolute values of these templates are then multiplied by a free parameter, $E_{\rm cal}$ (possibly dependent on frequency), which globally characterizes the amplitude of potential residuals arising from imperfect cali-

bration. From the templates I define the pixel-by-pixel rms amplitudes, adopted to construct maps, $T_{\rm res,cal}$, of Gaussian random fields at each CORE frequency.

Indeed, I might also expect calibration errors to affect the level of foreground residuals. Hence, as a final step, I account for a certain coupling between the two types of residuals in the model. Lastly, I multiply the simulated maps of foreground residuals by $(1 + T_{\rm res,cal}/T_{\rm amp,for})$.

5.5 The CMB dipole: forecasts for CORE including potential residuals

I extend the previous analysis including two sources of systematics, namely the calibration errors and eventual sky foreground residuals. I take into account two pairs of calibration uncertainty and sky residuals (parameterised by $E_{\rm for} = 0.04$ and $E_{\rm cal} = 0.004$, and by $E_{\rm for} = 0.64$ and $E_{\rm cal} = 0.064$) at $N_{\rm side} = 1024$ to explore different resolutions through pixel degradation. Rescaled to $N_{\rm side} = 64$, the two cases correspond to a set-up respectively better and worse by a factor of 4 with respect to the case $E_{\rm cal} = 10^{-3}$ and $E_{\rm for} = 10^{-2}$.

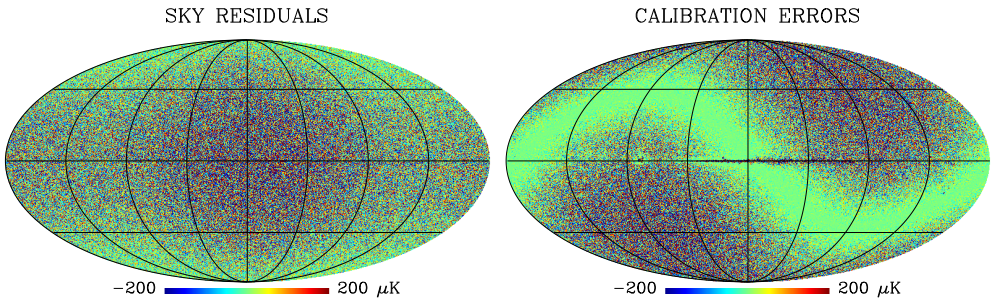

Figure 5.3: Sky residual and calibration error maps (in Galactic coordinates) in the 60-GHz band employed in the simulations. Their amplitudes correspond to the pessimistic case, $E_{\rm for} = 0.64$ and $E_{\rm cal} = 0.064$, for maps at resolution `HEALPix` $N_{\rm side} = 1024$.

In Fig. 5.3 I show the maps used in the simulations (for the 60-GHz band). The amplitudes correspond to the worse expected case; the most optimistic case is not shown, since the amplitude is just rescaled by a factor 16. The corresponding likelihood plots and 68% confidence levels are collected in Appendix 5.A.

The impact of systematic effects on the parameter errors is negligible. Indeed, as shown in Fig. 5.4, calibration errors and sky residuals do not noticeably worsen the $1\,\sigma$ uncertainty

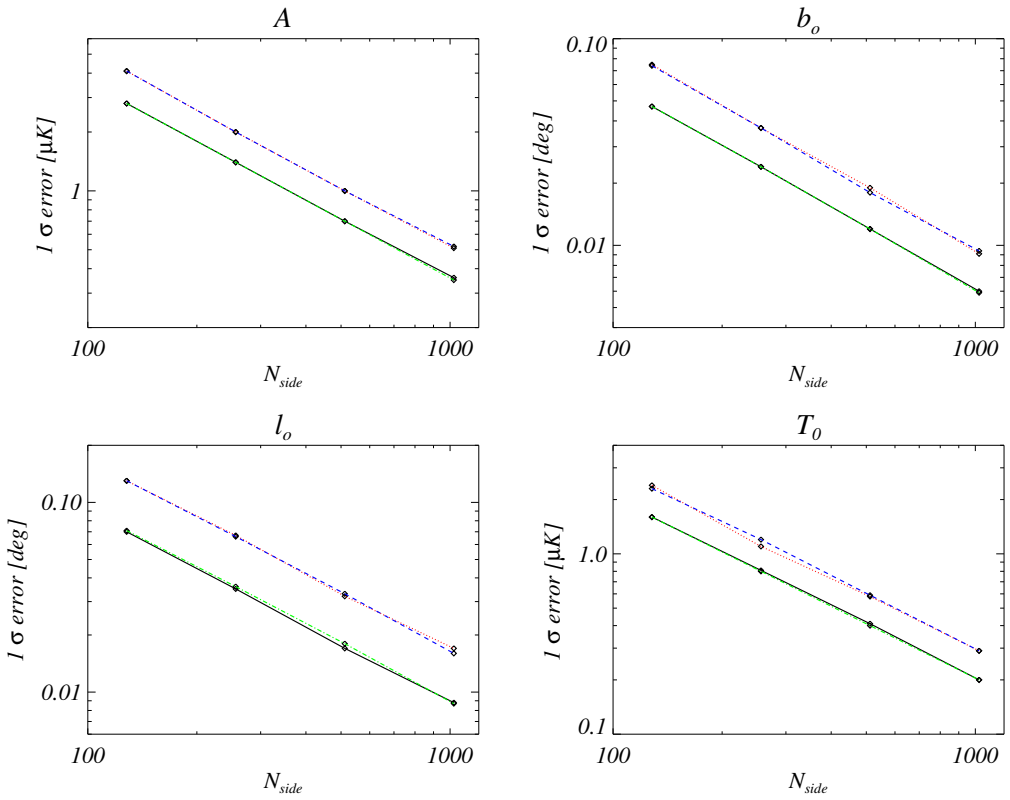

Figure 5.4: $1\,\sigma$ errors as function of `HEALPix` $N_{\rm side}$ values for the parameters A, b_0, l_0, and T_0: dipole-only (solid black line); dipole+noise (green dot-dashed line); dipole+noise+mask (red dotted line); and dipole+noise+mask+systematics (blue dashed line). The chosen frequency channel is 60 GHz and the noise map corresponds to 7.5 μK.arcmin. I adopted the *Planck* Galactic mask extended in order to cut out $\pm 30^\circ$ of the Galactic plane. The systematics correspond to the pessimistic expectation of calibration errors and sky (foreground, etc.) residuals. Notice that the pixelization error, due to the finite map resolution, is dominant over the noise for any $N_{\rm side}$. While the impact of noise and systematics is negligible, the effect of reducing the effective sky fraction is important.

at any sampling resolution. Furthermore, the frequency analysis confirms that the impact of systematic effects is not relevant in any of the bands under consideration (from 60 to 220 GHz).

While the effect of the systematics studied here on the *precision* of the parameter reconstruction is negligible, they may have, instead, a moderate impact on the *accuracy*, introducing a bias in the central values of the estimates. Nonetheless, the bias is usually buried within the $1\,\sigma$ error, with the marginal exception of the estimate of l_0 for the 220-GHz band (in the case of pessimistic systematics).

In conclusion, my results show that the dipole recovery (in both amplitude A and direction

angles b_0 and l_0) is completely dominated by the sky sampling resolution. They also evidence that the noise impact is negligible, the sky fraction reduction due to the Galactic mask impacts on the parameter error amplitude by increasing the $1\,\sigma$ errors on A, b_0 and l_0 by a factor of about 1.5, 1.6, and 1.9, respectively. Moreover, the effect of systematics slightly worsens the accuracy of the MCMC chain without affecting the error estimate.

The main point of this study is that, in order to achieve an increasing precision in the dipole reconstruction, high resolution measurements are required, in particular when a sky mask has to be applied. This is especially relevant for dipole spectral distortion analyses, based on the high-precision, multi-frequency observations that are necessary to study the tiny signals expected.

5.6 Measuring Doppler and aberration effects in different maps

5.6.1 Boosting effects on the CMB fields

As already said, the relative velocity between an observer and the CMB rest frame induces a dipole in the CMB temperature through the Doppler effect. The CMB dipole, however, is completely degenerate with an *intrinsic* dipole, which could be produced by the Sachs-Wolfe effect at the last-scattering surface due to a large-scale dipolar Newtonian potential (283). For ΛCDM such a dipole should be of order of the Sachs-Wolfe plateau amplitude (i.e., 10^{-5}) (113, 354), nevertheless the dipole could be larger in the case of more exotic models. In addition to the dipole, a moving observer will also see velocity imprints at $\ell > 1$ in the CMB due to Doppler and aberration effects (55, 61). Such effects can be measured as correlations among different ℓs, as has been proposed in (11, 184, 222) and subsequently demonstrated in (259).

The aberration effect changes the arrival direction of photons from $\hat{n}'$ to $\hat{n}$, which, at linear order in β, is completely degenerate with a lensing dipole. The Doppler effect modulates the CMB (an effect that is partly degenerate with an intrinsic CMB dipole[1]) changing the specific intensity I' in the CMB rest frame to the intensity I in the observer's frame[2] by a multiplicative direction-dependent factor as (61, 288)

$$I'(\nu', \hat{n}') = I(\nu, \hat{n}) \left(\frac{\nu'}{\nu}\right)^3 , \tag{5.2}$$

[1]It has been shown in (283) that, in the Gaussian case, an intrinsic large scale dipolar potential exactly mimics on large scales a Doppler modulation.

[2]The prime and non-prime is related to the CMB and to the observer frame, respectively, following (259).

where

$$\nu \;=\; \nu'\,\gamma\,(1+\vec{\beta}\cdot\hat{n}')\,, \qquad \hat{n} \;=\; \frac{\hat{n}' + \left[\gamma\beta + (\gamma-1)(\hat{n}'\cdot\hat{\beta})\right]\hat{\beta}}{\gamma(1+\vec{\beta}\cdot\hat{n}')}\,, \tag{5.3}$$

with $\gamma \equiv (1-\vec{\beta}^2)^{-1/2}$. The temperature and polarization fields $X(\hat{n})$ in the CMB rest frame (X stands for T, E or B) are similarly transformed as

$$X'(\hat{n}') \;=\; \gamma X(\hat{n})(1-\vec{\beta}\cdot\hat{n})\,. \tag{5.4}$$

Decomposing Eq. (5.4) into spherical harmonics leads to an effect in the multipole ℓ of order β^ℓ. Although this effect is dominant in the dipole, it also introduces a small, non-negligible correction to the quadrupole, with a different frequency dependence, due to the conversion of intensity to temperature (70, 174, 223, 275). In addition, both aberration and Doppler effects couple multipoles ℓ to $\ell \pm n$ (65, 222). This coupling is largest in the correlation between ℓ and $\ell \pm 1$ (11, 61, 184), which was measured by *Planck* at 2.8 and 4.0 σ significance for the aberration and Doppler effects, respectively (259). These $\mathcal{O}(\beta)$ couplings are present on all scales and the measurability of aberration is mostly limited by cosmic variance, which constrains my ability to assume fully uncorrelated modes for $\ell \neq \ell'$. Hence, in order to improve their measurement, it is important to have as many modes as possible, which drives to cosmic-variance-limited measurements of temperature and polarization up to very high $\ell_{\rm max}$ and coverage of a large fraction of the sky $f_{\rm sky}$. CORE probes a larger $\ell_{\rm max}$ and covers a larger effective $f_{\rm sky}$ than *Planck* (as the extra frequency channels and the better sensitivity allow for an improved capability in doing component separation), hence it should achieve a detection of almost 13 σ even with a 1.2-m telescope, as shown below.

Upon a boost of a CMB map X (61), the $a_{\ell m}$ coefficients of the spherical harmonic decomposition transform as

$$a^X_{\ell m} \;=\; \sum_{\ell'=0}^{\infty} {}_sK_{\ell'\ell m}\, a'^X_{\ell' m}\,, \tag{5.5}$$

where s indicates the spin of the quantity X. For the temperature, and the scalars in general, $s = 0$, while for spin-2 quantities (such as the polarization), $s = 2$.

The kernels ${}_sK_{\ell'\ell m}$ usually cannot be computed analytically and their numerical computation is not trivial, since this involves highly oscillatory integrals (65). However, efficient methods using an operator approach in harmonic space have been developed (85), although for

my estimates more approximate methods will suffice. It was shown in (85, 222) that the kernels can be well approximated by Bessel functions as follows:

$$\begin{aligned} K^X_{(\ell-n)\ell m} &\simeq J_n\left(-2\beta\left[\prod_{k=0}^{n-1}\left[(\ell-k)\ {}_sG_{(\ell-k)m}\right]\right]^{1/n}\right); \\ K^X_{(\ell+n)\ell m} &\simeq J_n\left(2\beta\left[\prod_{k=1}^{n}\left[(\ell+k)\ {}_sG_{(\ell+k)m}\right]\right]^{1/n}\right). \end{aligned} \tag{5.6}$$

Here

$${}_sG_{\ell m} \equiv \sqrt{\frac{\ell^2-m^2}{4\ell^2-1}\left[1-\frac{s^2}{\ell^2}\right]}\,, \tag{5.7}$$

and $n \geq 1$ (where n is the difference in multipole between a pair of coupled multipoles, namely ℓ and $\ell \pm n$). It is also assumed that $\beta \ll 1$, although the formula above can be generalised to large β (85, 222). These kernels couple different multipoles so that, by a Taylor expansion, are derived $\langle a_{\ell m}\ a^*_{(\ell+n)m}\rangle = \mathcal{O}(\beta\ell)^n$. For $\ell \ll 1/\beta$, the most important couplings are between neighbouring multipoles, ℓ and $\ell \pm 1$ (e.g. (61)). One may wonder about the importance of the couplings between non-neighbouring multipoles, i.e., ℓ and $\ell \pm n$, for $\ell \gtrsim 1/\beta$. However, quite surprisingly, for $\ell \gg 1/\beta$ I find that: (1) in the $(\ell, \ell \pm 1)$ correlations, higher order in $\beta\ell$ terms are negligible (65, 222); and (2) most of the correlation seems to remain in the $(\ell, \ell \pm 1)$ coupling. For these reasons, from here on, higher order terms in β and couplings between non-neighbouring multipoles (i.e., $n > 1$) will be ignored.

In order to measure deviations from isotropy due to the proper motion of the observer, the off-diagonal correlations $\langle a^X_{\ell m}\ a^{X*}_{(\ell+1)m}\rangle$ are thus computed. Assuming that in the rest frame the Universe is statistically isotropic and that parity is conserved, then in the boosted frame, for $\ell' = \ell + 1$, one gets (11, 61, 184):

$$a^X_{\ell m} \simeq c^-_{\ell m} a'^X_{(\ell-1)m} + c^+_{\ell m} a'^X_{(\ell+1)m}\,, \tag{5.8}$$

where

$$c^+_{\ell m} = \beta(\ell+2-d)_sG_{(\ell+1)m}\,, \qquad c^-_{\ell m} = -\beta(\ell-1+d)_sG_{\ell m}\,, \tag{5.9}$$

and d parametrizes the Doppler effect of dipolar modulation. It then follows that:

$$\left\langle a^X_{\ell m}\ a^{Y*}_{(\ell+1)m}\right\rangle = \beta\left[(\ell+2-d)\ {}_{s_X}G_{(\ell+1)m}C^{XY}_{\ell+1} - (\ell+d)\ {}_{s_Y}G_{(\ell+1)m}C^{XY}_{\ell}\right] + O(\beta^2)\,. \tag{5.10}$$

For $\ell \gtrsim 20$, ${}_2G_{\ell m} \simeq {}_0G_{\ell m}$. As will be shown, the large scales are not important for measuring the boost, and thus it is not important to keep the indication of the spin. The above equation reduces, then, to:

$$\left\langle a^X_{\ell m}\, a^{Y*}_{(\ell+1)m} \right\rangle = \beta G_{(\ell+1)m} \left[(\ell + 2 - d) C^{XY}_{\ell+1} - (\ell + d) C^{XY}_{\ell} \right] + O(\beta^2)\,, \tag{5.11}$$

where the angular power spectra C^{XY}_ℓ are measured in the CMB rest frame. For CMB temperature and polarization, $d = 1$, as observed from Eqs. (5.2)–(5.3). In this case, no mixing of E- and B-polarization modes occurs, not even at higher orders in β (85, 222). However, for $d \neq 1$, the coupling is non-zero already at first order in β (61, 85). Maps estimated from spectra that are not blackbody have different Doppler coefficients[1], as discusses next.

Practically, temperature and polarization anisotropies cannot be measured directly but *intensity* anisotropies, then converted to temperature and polarization. This distinction (though seeming trivial) is relevant for the Doppler effect, which induces a dipolar modulation of CMB anisotropies, revealing as frequency-dependent factors (224, 259). In particular, such factors are shown to be proportional to a Compton y-type spectrum (exactly like the quadrupole correction (70, 174, 223, 275) and therefore degenerate with the tSZ effect); they are measurable in the *Planck* maps at about $12\,\sigma$ and in the CORE maps even at 25–60 σ (224), depending on the contamination template used to describe the tSZ effect. These S/N ratios are much larger than those derivable in temperature and polarization, so, at first sight, they may appear to represent a better way to measure the boosting effects. However, the peculiar frequency dependence is strictly a consequence of the intensity-to-temperature (or intensity-to-polarization) conversion and thus agnostic to the source of the dipole (224, 259) (i.e., whether it is from our peculiar velocity or is an intrinsic CMB dipole). Accordingly, the frequency-*independent* part of the dipolar modulation signal in Eq. (5.11) (with $d = 1$), which is unlikely to be caused by an intrinsically large CMB dipole (283), is considered in the forecast.

5.6.2 Going beyond the CMB maps

Since CORE will also measure the thermal Sunyaev-Zeldovich effect, the CIB, and the weak lensing signal over a wide multipole range, it is interesting to examine if these maps could also be used to measure the aberration and Doppler couplings.

[1] Note that the kernel defined as in Eq. (5.5) for $d \neq 1$ can be obtained from ${}_sK_{\ell'\ell m}$ using recursions (85).

The intensity of a tSZ Compton-y map is given by:

$$I'_{tSZ}(\nu') \;=\; y \cdot g\left(\frac{h\nu'}{k_{\rm B}T_0}\right) K(\nu')\,, \tag{5.12}$$

where $g(x') = x' \coth(x'/2) - 4$, $K(\nu')$ is the conversion factor that derives from setting $T = T_0 + \delta T$ in the Planck distribution and expanding to first order in δT, and $x' \equiv h\nu'/k_{\rm B}T_0$ (T_0 being the present temperature of the CMB). Explicitly $K(\nu')$ is given by:

$$K(\nu') \;=\; \frac{2\,h(\nu')^3}{c^2}\,\frac{x'\exp(x')}{(\exp(x')-1)^2}\,. \tag{5.13}$$

A boosted observer will see an intensity as defined in Eq. (5.2). Such intensity, expanded at first order in β, will contain Doppler couplings with a non-trivial frequency dependence, similarly to what happens in the case of CMB fluctuations, where frequency-dependent boost factors are generated, as already discussed. For simplicity, only the couplings that retain the same frequency dependence of the original tSZ signal, which come from aberration[1] are analyzed, so setting $d = 0$ in Eq. (5.11).

For the intensity of the CIB map (see Sect. 5.7.2 for further details), is adopted the template obtained by (124),

$$I'_{\rm CIB} \;\propto\; (\nu')^{0.64}\,\frac{(\nu')^3}{\exp\!\left[\frac{h\nu'}{k_{\rm B}\,18.5{\rm K}}\right]-1}\,. \tag{5.14}$$

At low frequencies, the intensity scales as:

$$I'_{\rm CIB} = A_{\rm CIB}\,(\nu')^{2.64}\,, \tag{5.15}$$

where $A_{\rm CIB}$ is a constant related to the amplitude. Thus, in the boosted frame and to lowest order in β,

$$I_{\rm CIB}(\nu) = \left(\frac{\nu}{\nu'}\right)^3 A'_{\rm CIB}\,(\nu')^{2.64} \simeq A'_{\rm CIB}[\gamma(1-\vec{\beta}\cdot\hat{n})]^{-0.36}\nu^{2.64}\,. \tag{5.16}$$

Therefore, the boosted amplitude is $A_{\rm CIB} \equiv A'_{\rm CIB}/[\gamma(1-\vec{\beta}\cdot\hat{n})]^{0.36}$, which implies $d = 0.36$. In this case, working in a low-frequency approximation (relative to the peak of the CIB at around 3000 GHz), there are not frequency-dependent boost factors.

The CMB weak lensing maps can also be used to measure the boost but, since the weak lensing potential estimation involves 4-point correlation functions of the CMB fields, the boost effect is more complex to estimate and requires further study.

[1] Also, sub-leading contributions, namely the kinetic Sunyaev-Zeldovich effect (315) and changes in the tSZ signal induced by the observer motion relative to the CMB rest frame (68), as well as relativistic corrections (116, 346), are specific to each particular cluster. Their inclusion could be considered in more detailed predictions in future, but represent higher-order corrections with respect to the present study.

5.6.3 Estimates of the Doppler and aberration effect

For full-sky experiments, it has been shown in (61) that, under a boost, the corrections to the power spectra are $\mathcal{O}(\beta^2)$, whereas for experiments with partial sky coverage there can be an $\mathcal{O}(\beta)$ correction (170, 192, 233). Nevertheless, even for the partial-sky case, this correction to C_ℓ^{XY} would only propagate at $\mathcal{O}(\beta^2)$ in the correlations above. In what follows, the effect of the sky coverage in the boost corrections will be neglected. Also, going to inspect the $\mathcal{O}(\beta)$ effects only, I disregard each $\mathcal{O}(\beta^2)$ term from the equations.

For the CMB fields, as shown in (11, 222), the fractional uncertainty in the estimator of $\left\langle a^X_{\ell m}\, a^{Y*}_{(\ell+1)m}\right\rangle$ is given by

$$\left.\frac{\delta\beta}{\beta}\right|_{XY} \simeq \left[\sum_\ell \sum_{m=-\ell}^{\ell} \frac{\left\langle a^X_{\ell m}\, a^{Y*}_{(\ell+1)m}\right\rangle^2}{\mathfrak{C}_\ell^{XX}\mathfrak{C}_{\ell+1}^{YY}}\right]^{-1/2} \tag{5.17}$$

(242). Here, $\mathfrak{C}_\ell^{XX} \equiv (C_\ell^{XX} + N^{XX}_{\ell,\rm total})/\sqrt{f_{\rm sky}}$, where $f_{\rm sky}$ is the fraction of the sky covered by the experiment and $N^{XX}_{\ell,\rm total}$ is the effective noise level on the map X. The expression $\mathfrak{C}_\ell^{XX}$ represents the sum of instrumental noise and cosmic variance. The effective noise is obtained by taking the inverse of the sum over the different channels i of the inverse of the individual $N^2_{\ell,i}$ (222),

$$N_{\ell,\rm total} = \left[\sum_i^{\rm nchannel} \frac{1}{N^2_{\ell,i}}\right]^{-1/2}. \tag{5.18}$$

The noise in each channel is given by few times a Gaussian beam characterised by the beam width $\theta_{\rm FWHM}$:

$$N^X_{\ell,i} \;=\; (\sigma^X)^2 \exp\left[\frac{\ell(\ell+1)\theta^2_{\rm FWHM}}{8\ln 2}\right], \tag{5.19}$$

where σ^X is the noise in μK.arcmin for the map X.

For the tSZ signal, the fiducial spectrum obtained in (261) (slightly extrapolated to higher ℓs) is assumed and the (dominant) contribution due to the residual foreground contamination is included in the forecast noise spectrum. For the CIB signal, the spectra from (57) are adopted; the noise is modelled according to the simulations carried out in (100). Also, a 100% correlation of the different CIB channels is conservatively assumed. Since different channels pick up different redshifts, effectively the correlation is not going to be total and some extra signal can be obtained from multiple channels; however, since this makes the analysis much more

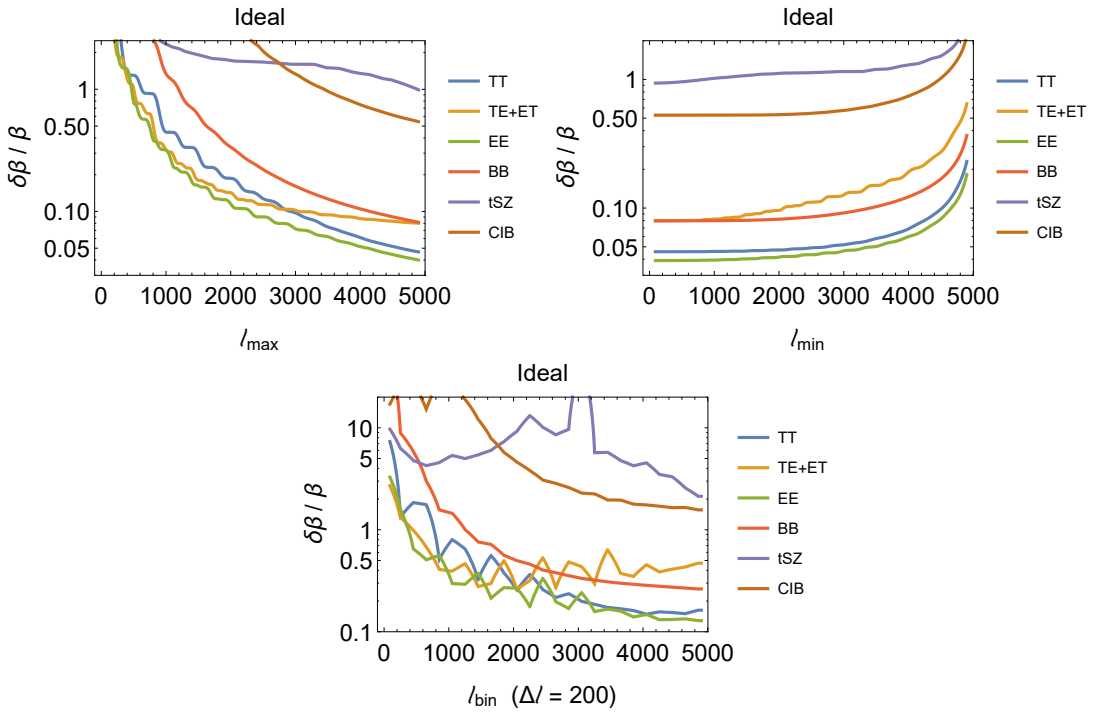

Figure 5.5: Achievable precision in estimating the velocity through aberration and Doppler effects in an ideal experiment (with $f_{\rm sky} = 1$ and limited by cosmic variance only) for different maps. *Left:* as a function of $\ell_{\rm max}$. *Right:* as a function of $\ell_{\rm min}$ (with fixed $\ell_{\rm max} = 5000$). *Bottom:* for individual bins with $\Delta\ell = 200$. It emerges that: (i) the first hundred ℓs are not important for achieving a high S/N; and (ii) the non-CMB diffuse maps exhibit low precision and are not very useful for measuring β. Note that for simplicity no primordial B-modes are assumed (constraints turn out to be very weakly sensitive to this choice).

complex (due to the need to have all the covariance matrices) and since the CIB turns out not to be promising for measuring aberration (see Fig. 5.5), these corrections seem not too critical.

Using Eq. (5.17) for the different maps of different experiments, the detection potentials of CORE (see Table 1.8) are compared with those expected from both *Planck* and LiteBIRD (166). The values of the 2015 release provide the *Planck* specifications, while the LiteBIRD specifications used in this analysis are listed in Table 1.7.

Fig. 5.5 shows the precision that could be reached by an ideal experiment with $f_{\rm sky} = 1$ and limited by cosmic variance only. I present the results for: the range $\ell \in [2, \ell_{\rm max}]$; the range $\ell \in [\ell_{\rm min}, 5000]$; and for individual ℓ bins of width $\Delta\ell = 200$. The signal-to-noise ratios in the tSZ and CIB maps are considerably lower than in the CMB maps, which is due to the fact that the spectra are smoother, as explained later. For instance, for $\ell_{\rm max} = 4000$, in the TT and EE

maps separately S/N > 16, whereas in tSZ and in CIB S/N ≃ 1.

Fig. 5.6 and Table 5.1 summarize the forecasts for CORE, *Planck* and LiteBIRD forecasts. These results differ from the ideal case due to the inclusion of instrumental noise, foreground contamination (in the case of tSZ) and $f_{\rm sky} \neq 1$. The bottom right panel illustrates the precision by combining all temperature and polarization channels assuming a negligible correlation among them (a good approximation, as shown in (11)). The TE and ET correlation functions are shown to be independent in (11) and both carry the same S/N. So I usually present the combined S/N for $TE + ET$, which is $\sqrt{2}$ times their individual S/N values.

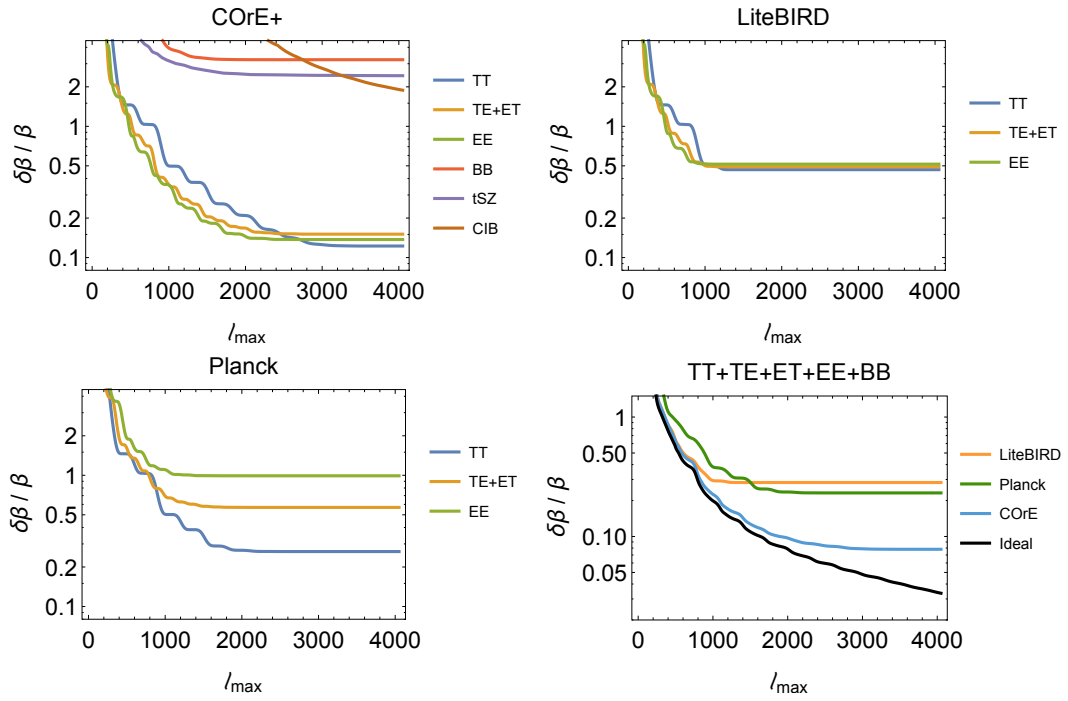

Figure 5.6: Similar to the left panel of Fig. 5.5 but for realistic experiments and assuming $f_{\rm sky} = 0.8$. Bottom right panel gives the precision combining all temperature and polarization maps, also in the case of an ideal experiment (no instrumental noise and $f_{\rm sky} = 1$).

Experiment	Channel [GHz]	$\theta_{\rm FWHM}$ [arcmin]	σ^T [μK.arcmin]	S/N TT	S/N $TE + ET$	S/N EE	S/N Total
Planck	(all)	$\simeq 5.5$	$\simeq 13$	3.8	1.7	1.0	4.3
LiteBIRD	(all)	$\simeq 19$	$\simeq 1.7$	2.0	1.8	1.8	3.3
CORE	60	17.87	7.5	2.1	1.9	1.8	3.4
	70	15.39	7.1	2.5	2.4	2.2	4.1
	80	13.52	6.8	2.8	2.8	2.6	4.8
	90	12.08	5.1	3.5	3.4	3.3	5.9
	100	10.92	5	3.9	3.7	3.7	6.5
	115	9.56	5	4.3	4.2	4.2	7.3
	130	8.51	3.9	5.1	4.9	5.	8.6
	145	7.68	3.6	5.7	5.3	5.5	9.5
	160	7.01	3.7	6.1	5.6	5.8	10.1
	175	6.45	3.6	6.5	5.8	6.1	10.7
	195	5.84	3.5	7.1	6.1	6.5	11.4
	220	5.23	3.8	7.5	6.3	6.7	11.9
	255	4.57	5.6	7.5	5.9	6.2	11.4
	295	3.99	7.4	7.5	5.7	5.8	11.
	340	3.49	11.1	7.	5.1	4.9	9.9
	390	3.06	22	5.8	3.8	3.1	7.6
	450	2.65	45.9	4.5	2.3	1.4	5.3
	520	2.29	116.6	2.9	1.	0.3	3.1
	600	1.98	358.3	1.4	0.3	0.	1.4
	(all)	$\simeq 4.5$	$\simeq 1.4$	8.2	6.6	7.3	12.8
Ideal ($\ell_{\rm max} = 2000$)	(all)	0	0	5.3	7.1	8.7	12.7
Ideal ($\ell_{\rm max} = 3000$)	(all)	0	0	10	9.8	14	21
Ideal ($\ell_{\rm max} = 4000$)	(all)	0	0	16	11.4	19	29
Ideal ($\ell_{\rm max} = 5000$)	(all)	0	0	22	12.6	26	38

Table 5.1: Aberration and Doppler effects with CORE. $f_{\rm sky} = 0.8$ for all experiments (and $f_{\rm sky} = 1$ in the ideal cases) in order to make comparisons simpler. For CORE and LiteBIRD $\sigma^P = \sqrt{2}\sigma^T$, while for *Planck* see the 2015 values. The combined channel estimates are effective values that best approximate Eq. (5.19) in the ℓ range of interest. Note that CORE will have S/N ≥ 5 in 14 different frequency bands. Also, by combining all frequencies, CORE will have similar S/N in TT, $TE + ET$ and EE.

Since the estimators for $\left\langle a^X_{\ell m}\, a^{Y*}_{(\ell+1)m}\right\rangle$ involve a sum over all ℓs and ms and since m enters through $G_{\ell m}$ only, it is useful to use the following approximations, which are valid to very good accuracy for $\ell \gtrsim 20$ (222, 224):

$$\sum_m G_{\ell,m} = 0.39(2\ell+1)\,; \qquad \sum_m [G_{\ell,m}]^2 = 0.408^2(2\ell+1)\,. \tag{5.20}$$

Note that these approximations yield up to 1 %-level accuracy and, removing the sum over ms, they significantly simplify the calculation of the estimators.

The achievable precision in β through this method depends strongly on the shape of the power spectrum – strongly varying spectra give much lower uncertainties compared to smooth spectra. For instance, for the tSZ and CIB maps, many modes are in the cosmic-variance-limited regime, thus one might think that they would yield a good measurement of β. However, since their C_ℓs are smooth functions of ℓ, they do not carry much information on the boost. To understand this and gain some insight, let us approximate Eq. (5.10) by $C_{\ell+1}$ as $C_\ell + \partial C_\ell/\partial\ell$ and add the approximation $\partial C_\ell/\partial\ell \ll C_\ell$ (note, however, that $\ell\partial C_\ell/\partial\ell$ could be comparable to C_ℓ at small scales). This gives:

$$\sum_m \left\langle a^X_{\ell m}\, a^{Y*}_{(\ell+1)m}\right\rangle = 0.39(2\ell+1)\beta\left[(2-2d)C^{XY}_\ell - (\ell+d)\frac{\partial C^{XY}_\ell}{\partial\ell}\right]. \tag{5.21}$$

Assuming the cosmic-variance dominated regime (i.e., $\mathfrak{C}^{XX}_\ell \simeq C^{XX}_\ell$) for $\ell \gtrsim 20$ and putting $X = Y$, we get:

$$\left.\frac{\delta\beta}{\beta}\right|_{XX} \simeq \frac{1}{0.408\beta}\left[\sum_\ell (2\ell+1)\left[(2-2d) - \ell\left(1 - \frac{C^{XX}_{\ell+1}}{C^{XX}_\ell}\right)\right]^2\right]^{-\frac{1}{2}}. \tag{5.22}$$

For the TE case, the formula is less useful. For the CMB temperature and polarization ($d = 1$), only the derivative term survives:

$$\left.\frac{\delta\beta}{\beta}\right|_{XX=TT,EE,BB} \simeq \frac{1}{0.408\beta}\left[\sum_\ell (2\ell+1)\left[\frac{\partial \ln C^{XX}_\ell}{\partial \ln \ell}\right]^2\right]^{-\frac{1}{2}}. \tag{5.23}$$

Note that for the CIB the precision is smaller than for the CMB temperature and polarization, not only because the spectra are smoother, but also because there is a partial cancellation between the two terms in the summand of Eq. (5.22).

This analysis consider only the diffuse background components of the measured maps. Aberration and Doppler effects can in principle also be detected using point sources, since the

boosting effects will change both their number counts, angular distribution, and redshift. For the upcoming CMB experiments, nevertheless, the number density of point sources is probably insufficient for a significant signal, since one needs more than about 10^6 objects to have a detection at more than $1\,\sigma$ (349).

5.7 Differential approach to CMB spectral distortions and the CIB

Using the complete description of the Compton-Getting effect (128) I compute full-sky maps of the expected effect at desired frequency. I start discussing the frequency dependence of the dipole spectrum (18, 91) and then extend the analysis beyond the dipole.

5.7.1 The CMB dipole

The dipole amplitude is directly proportional to the first derivative of the photon occupation number, $\eta(\nu)$, which is related to the thermodynamic temperature, $T_{\rm therm}(\nu)$, i.e., to the temperature of the blackbody having the same $\eta(\nu)$ at the frequency ν, by

$$T_{\rm therm} = \frac{h\nu}{k_{\rm B}\ln(1+1/\eta(\nu))}. \tag{5.24}$$

The difference in $T_{\rm therm}$ measured in the direction of motion and in the perpendicular direction is given by (91):

$$\Delta T_{\rm therm} = \frac{h\nu}{k}\left\{\frac{1}{\ln\left[1+1/\eta(\nu)\right]} - \frac{1}{\ln\left[1+1/\eta(\nu(1+\beta))\right]}\right\}, \tag{5.25}$$

which, to first order, can be approximated by:

$$\Delta T_{\rm therm} \simeq -\frac{x\beta T_0}{(1+\eta)\ln^2(1+1/\eta)}\frac{d\ln\eta}{d\ln x}, \tag{5.26}$$

where $x \equiv h\nu/kT_0$ is the dimensionless frequency.

Fig. 5.7 shows the dipole spectrum derived for two well-defined deviations from the Planck distribution, namely the BE and Comptonization distortions induced by unavoidable energy injections in the radiation field occurring at different cosmic times, early and late, respectively. I briefly discuss below their basic properties and the signal levels expected from different processes.

A BE-like distorted spectrum is produced by two distinct processes. Firstly there is the dissipation of primordial perturbations at small scales (69, 69, 86, 162, 162, 229, 316), damped

by photon diffusion and thus invisible in the CMB anisotropies, which generates a positive chemical potential. Secondly, colder electrons induce Bose condensation of CMB photons as a consequence of the faster decrease of the matter temperature relative to the radiation temperature in an expanding Universe, which generates a negative chemical potential (71, 314).

The photon occupation number of the BE spectrum is given by (316)

$$\eta_{\rm BE} = \frac{1}{e^{x_{\rm e}+\mu} - 1}, \tag{5.27}$$

where μ is the chemical potential that quantifies the fractional energy, $\Delta\epsilon/\varepsilon_{\rm i}$, exchanged in the plasma during the interaction,[1] $x_{\rm e} = x/\phi(z)$, $\phi(z) = T_{\rm e}(z)/T_{\rm CMB}(z)$, with $T_{\rm e}(z)$ being the electron temperature. For a BE spectrum, $\phi = \phi_{\rm BE}(\mu)$. The dimensionless frequency x is redshift invariant, since in an expanding Universe both $T_{\rm CMB}$ and the physical frequency ν scale as $(1 + z)$. For small distortions, $\mu \simeq 1.4\Delta\epsilon/\varepsilon_{\rm i}$ and $\phi_{\rm BE} \simeq (1 - 1.11\mu)^{-1/4}$. The current FIRAS 95 % CL upper limit is $|\mu_0| < 9\times10^{-5}$ (123), where μ_0 is the value of μ at the redshift z_1 corresponding to the end of the kinetic equilibrium era. At earlier times μ can be significantly higher, and the ultimate limits on $\Delta\epsilon/\varepsilon_{\rm i}$ before the thermalization redshift (when any distortion can be erased) comes from cosmological nucleosynthesis.

These two kinds of distortions are characterised by a $|\mu_0|$ value in the range, respectively, $\sim 10^{-9}$–10^{-7} (and in particular $\simeq 2.52 \times 10^{-8}$ for a primordial scalar perturbation spectral index $n_{\rm s} = 0.96$, without running), and $\simeq 3 \times 10^{-9}$. Since very small scales that are not explored by current CMB anisotropy data are relevant in this context, a broad set of primordial spectral indices needs to be explored. A wider range of chemical potentials is found by (67), allowing also for variations in the amplitude of primordial perturbations at very small scales, as motivated by some inflation models.

Cosmological reionization associated with the early stages of structure and star formation is an additional source of photon and energy production. This mechanism induces electron heating that is responsible for Comptonization distortions (352). The characteristic parameter for describing this effect is

$$u(t) = \int_{t_{\rm i}}^{t} [(\phi - \phi_{\rm i})/\phi](k_{\rm B}T_{\rm e}/m_{\rm e}c^2)n_{\rm e}\sigma_{\rm T}c dt\,. \tag{5.28}$$

In the case of small energy injections and integrating over the relevant epochs then $u \simeq (1/4)\Delta\varepsilon/\varepsilon_{\rm i}$. In Eq. (5.28), $\phi_{\rm i} = \phi(z_{\rm i}) = (1 + \Delta\epsilon/\varepsilon_{\rm i})^{-1/4} \simeq 1 - u$ is the ratio between the

[1] Here, the subscript i denotes the initial time of the dissipation process.

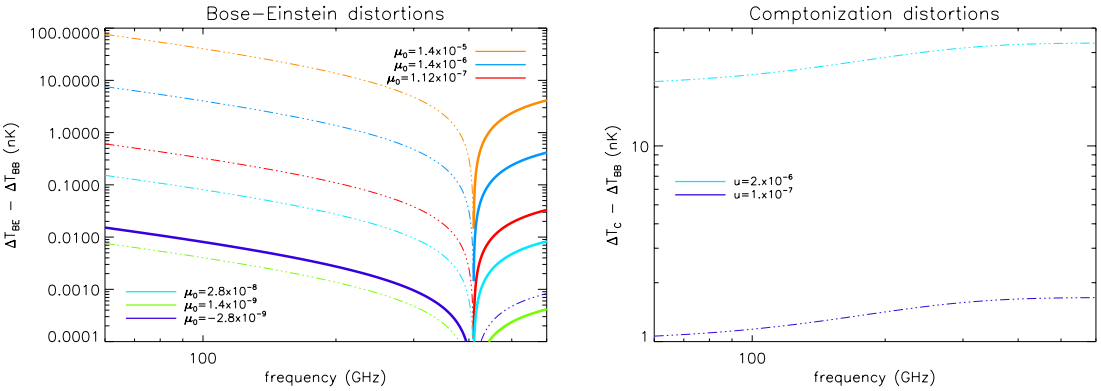

Figure 5.7: Spectrum of dipole (in equivalent thermodynamic, or CMB, temperature) expressed as the difference between that produced by a distorted spectrum and that corresponding to the blackbody at the current temperature T_0. Thick solid lines (or thin three dots-dashes) correspond to positive (or negative) values. *Left*: the case of BE distortions for $\mu_0 = -2.8 \times 10^{-9}$ (representative of adiabatic cooling; green dots, note the opposite signs with respect to the cases with positive μ_0), $\mu_0 = 1.4 \times 10^{-5}$, 1.4×10^{-6} (representative of improvements with respect to FIRAS upper limits), $\mu_0 = 1.12 \times 10^{-7}$, 2.8×10^{-8}, and 1.4×10^{-9} (representative of primordial adiabatic perturbation dissipation). *Right*: the case of Comptonization distortions for $u = 2 \times 10^{-6}$ (upper curves) and $u = 10^{-7}$ (lower curves), representative of imprints by astrophysical or minimal reionization models, respectively.

equilibrium matter temperature and the radiation temperature evaluated at the beginning of the heating process (i.e., at $z_{\rm i}$). The distorted spectrum is then

$$\eta_{\rm C} \simeq \eta_{\rm i} + u \frac{x/\phi_{\rm i} \exp(x/\phi_{\rm i})}{[\exp(x/\phi_{\rm i}) - 1]^2} \left(\frac{x/\phi_{\rm i}}{\tanh(x/2\phi_{\rm i}) - 4} \right), \tag{5.29}$$

where $\eta_{\rm i}$ is the initial photon occupation number (before the energy injection)[1].

Typically, reionization induces Comptonization distortions with *minimal* values $u \simeq 10^{-7}$ (54). In addition to this, the variety of energy injections expected in astrophysical reionization models, including: energy produced by nuclear reactions in stars and/or by nuclear activity that mechanically heats the intergalactic medium (IGM); super-winds from supernova explosions and active galactic nuclei; IGM heating by quasar radiative energy; and shocks associated with structure formation. Together these induce much larger values of u ($\simeq$ several $\times 10^{-6}$) (158, 279), i.e., not much below the current FIRAS 95 % CL upper limit of $|u| < 1.5 \times 10^{-5}$ (123). Free-free signals associated with reionization (327) produce instead the most relevant distortion at the lowest frequencies (below 10 GHz), as discussed in the previous chapter.

[1]Here and in Eq. (5.27) I neglect the effect of photon emission/absorption processes, which is instead remarkable at low frequencies (see (90) and (53)).

It could also be considered the possible presence of unconventional heating sources. Decaying and annihilating particles during the pre-recombination epoch may affect the CMB spectrum, with the exact distorted shape depending on the process timescale and, in some cases, being different from the one produced by energy release. This is especially interesting for decaying particles with lifetimes $t_X \simeq \text{few}\times 10^8$–$10^{11}$ sec (66, 87, 163). Superconducting cosmic strings would also produce copious electromagnetic radiation, creating CMB spectral distortion shapes (226) that would be distinguishable with high accuracy measurements. Evaporating primordial black holes provide another possible source of energy injection, with the shape of the resulting distortion depending on the black hole mass function (60). CMB spectral distortion measurements could also be used to constrain the spin of non-evaporating black holes (230). The CMB spectrum could additionally set constraints on the power spectrum of small-scale magnetic fields (169), the decay of vacuum energy density (22), axions (110), and other new physical processes.

5.7.2 The CIB dipole

Multi-frequency measurements of the dipole spectrum will allow us to constrain the CIB intensity spectrum (18, 91). The spectral shape of the CIB is hard to determine directly because it requires absolute intensity measurements, which are also compromised by Galactic and other foregrounds. Although the dipole amplitude is about 10^{-3} of the monopole, its spatial form is already known and hence this indirect route may provide the most robust measurements of the CIB in the future.

Fig. 5.8 shows the CIB dipole spectrum computed according to Eq. (5.25), using the analytic representation of the CIB spectrum (observed at present time) given in (124):

$$\eta_{\rm CIB} = \frac{c^2}{2h\nu^3} I_{\rm CIB}(\nu) = I_0 \left(\frac{k_{\rm B} T_{\rm CIB}}{h\nu_0}\right)^{k_F} \frac{x_{\rm CIB}^{k_{\rm F}}}{\exp(x_{\rm CIB}) - 1}\,, \tag{5.30}$$

where $T_{\rm CIB} = (18.5 \pm 1.2)\,{\rm K}$, $x_{\rm CIB} = h\nu/k_{\rm B}T_{\rm CIB} = 7.78(\nu/\nu_0)$, $\nu_0 \simeq 3\times 10^{12}\,{\rm Hz}$ and $k_{\rm F} = 0.64 \pm 0.12$. Here I_0 sets the CIB spectrum amplitude, its best-fit value being 1.3×10^{-5} (124). On the other hand, the uncertainty of the CIB amplitude is currently quite high, with I_0 only known to a $1\,\sigma$ accuracy of about 30 %.

The CIB dipole amplitude, in terms of thermodynamic temperature, increases rapidly with frequency, reaching $257\,\mu$K (or $652\,{\rm Jy\,sr^{-1}}$) at 600 GHz and $420\,\mu$K (or $1306\,{\rm Jy\,sr^{-1}}$) at 800 GHz. The measurement of the CIB dipole amplitude will be dependent on systematic effects from

the foreground Galaxy subtraction, which has a similar spectrum to the CIB (125). Although the calibration of the dipole signal at different frequencies is not trivial (since the orbital part of the dipole will be used for calibration), the *Planck* experience is that with sufficient care the limitation is removal of the Galactic signals, not calibration uncertainty. Hence the CIB dipole should be clearly detectable by CORE in its highest frequency bands. Such a detection will provide important constraints on the CIB intensity; its amplitude uncertainty constitutes a major current limitation in the understanding of the dust-obscured star-formation phase of galaxy evolution.

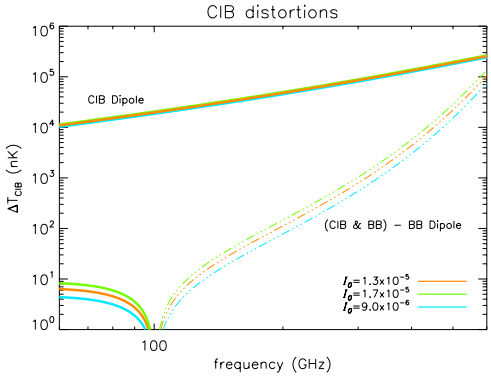

Figure 5.8: Expected behaviour of the dipole spectrum. The upper lines show the spectrum of the (pure) CIB dipole, while the lower lines show the spectrum coming from the dipole pattern computed from the CIB distribution function added to the blackbody (at temperature T_0) distribution function, minus the dipole pattern computed by the blackbody distribution function. Thick solid lines (or thin three dots-dashes) correspond to positive (or negative) values. The analytic representation of the CIB spectrum by (124) is adopted here, considering the best-fit amplitude and the range of $\pm 1\,\sigma$.

5.7.3 Beyond the dipole

Generalizing the considerations of the previous section, I evaluate the effect of peculiar velocity on the whole sky. To achieve this, I generate maps and, using the Lorentz-invariance of the distribution function, I can include all orders of the effect, coupling them with the geometrical properties induced at low multipoles. To compute the maps at each multipole[1] $\ell \geq 1$, I first derive the maps at all angular scales, both for the distorted spectra and for the blackbody at

[1]For the sake of generality and for the purpose of cross-checking, I also include the monopole term, which can be easily subtracted afterwards.

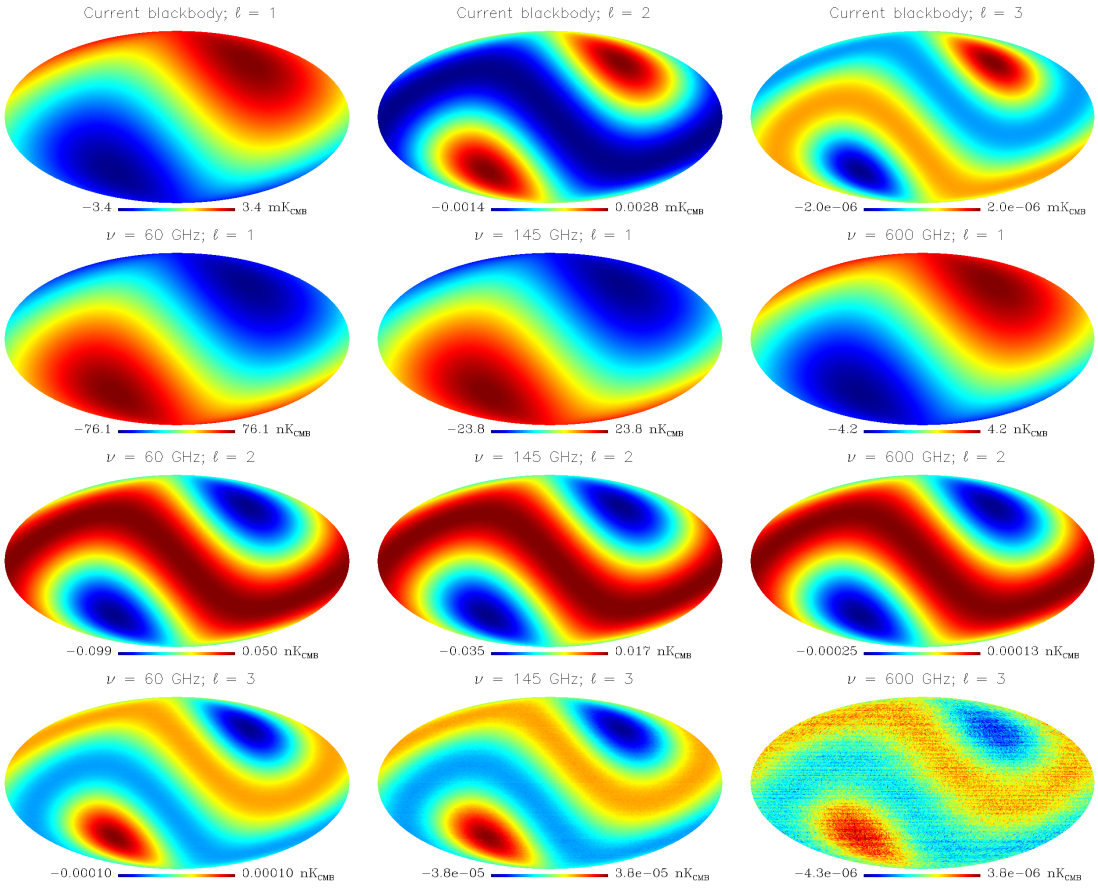

Figure 5.9: *Top row*: maps of the dipole, quadrupole and octupole computed assuming a CMB blackbody spectrum at the current temperature T_0, for reference. In all other cases I provide the maps of the dipole (*second row*), quadrupole (*third row*), and octupole (*bottom row*) at three different frequencies (namely 60, 145, and 600 GHz, from left to right), in terms of the difference between the pattern computed for a BE distortion with $\mu_0 = 1.5 \times 10^{-5}$ and that computed for a blackbody at the present-day temperature T_0.

the current temperature T_0. From the dipole direction found in the *Planck* (HFI+LFI combined) 2015 release and defining the motion vector of the observer, I produce the maps in a pixelization scheme at a given observational frequency ν by computing the photon distribution function, $\eta^{\rm BBdist}$, for each considered type of spectrum at a frequency given by the observational frequency ν but multiplied by the product $(1 - \hat{n} \cdot \vec{\beta})/(1 - \vec{\beta}^2)^{1/2}$ to account for all the possible sky directions with respect to the observer peculiar velocity. Here the notation 'BBdist' stands for BB, CIB, BE, or Comptonization (C). Hence, the map of the observed signal in terms of thermodynamic temperature is given by generalising Eq. (5.24):

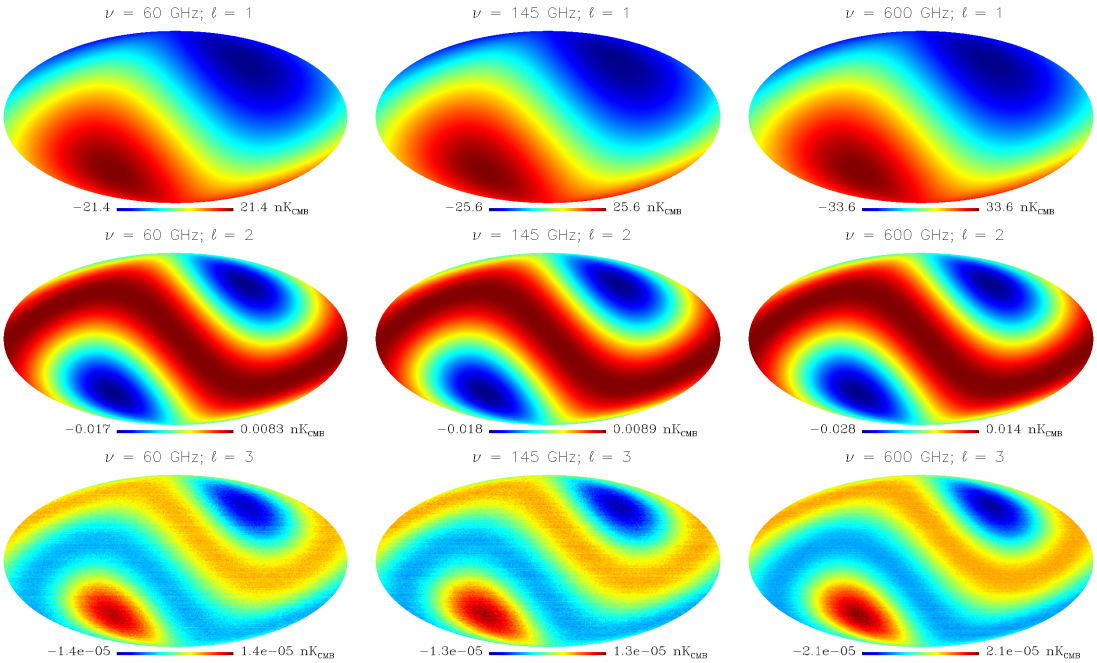

Figure 5.10: The same as in Fig. 5.9, but for the case of a Comptonization distortion with $u = 2 \times 10^{-6}$.

$$T_{\rm therm}^{\rm BB/dist}(\nu, \hat{n}, \vec{\beta}) = \frac{xT_0}{\log(1/(\eta(\nu, \hat{n}, \vec{\beta}))^{\rm BB/dist} + 1)}\,, \tag{5.31}$$

where $\eta(\nu, \hat{n}, \vec{\beta}) = \eta(\nu')$ with $\nu' = \nu(1 - \hat{n} \cdot \vec{\beta})/(1 - \vec{\beta}^2)^{1/2}$.

The `HEALPix` pixelization scheme is adopted to discretize the sky at the desired resolution. I decompose the maps into spherical harmonics and then regenerate them considering the a_{lm} only up to a desired multipole $\ell_{\rm max}$. I start setting $\ell_{\rm max} = 5$ and then iterate the process with a decreasing $\ell_{\rm max}$. The maps containing the power at a single multipole are produced by taking the difference of the map at $\ell_{\rm max}$ from the map at $\ell_{\rm max-1}$. I then compute the difference of maps having specific spectral distortions from the purely blackbody maps. As seen in Figs. 5.9–5.11, the expected signal is important for the dipole, can be considerable for the quadrupole and, depending on the distortion parameters, still not negligible for the octupole (although this will depend on the amplitude relative to experimental noise levels, as discussed below). For higher-order multipoles, the signal is essentially negligible.

Note that the maps present a clear and obvious symmetry with respect to the axis of the

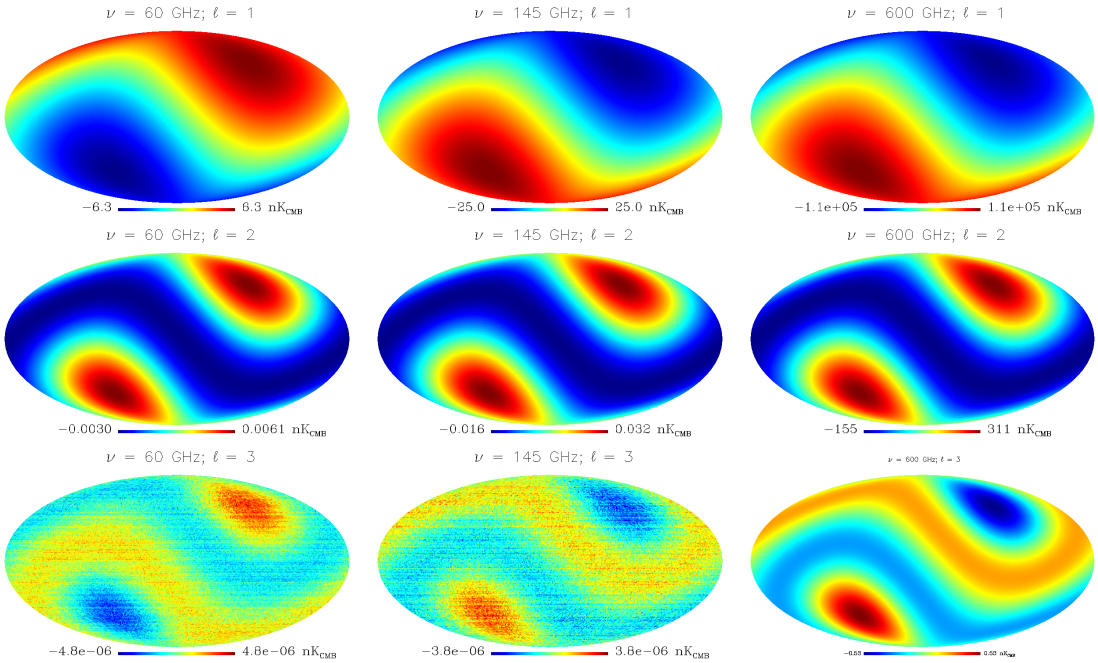

Figure 5.11: The same as in Fig. 5.9, but for the case of the CIB with amplitude set at the best-fit value found by FIRAS. More precisely, I display the temperature pattern of the CIB distribution function added to the blackbody one, minus the temperature pattern coming from the blackbody.

observer's peculiar velocity[1]. This is simply due to the angular dependence in Eq. (5.31). For coordinates in which the positive z-axis is aligned with the dipole, the only angular dependence comes from $\hat{n} \cdot \vec{\beta} \equiv \beta \cos\theta_{\rm d}$. In terms of the spherical harmonic expansion, this implies that higher-order multipoles will appear as polynomial functions of $\cos\theta_{\rm d}$, with different frequency-dependent factors depending on the specific type of spectral distortion being considered.

In the above considerations I assumed that each multipole pattern can be isolated from that of the other multipoles. In reality, a certain leakage is expected (particularly between adjacent multipoles), especially as a result of masking for foregrounds. The sources of astrophysical emission are highly complex, and their geometrical properties mix with their frequency behaviour. Furthermore, in real data analysis, there is an interplay between the determination of the calibration and zero levels of the maps, and this issue is even more critical when data in different frequency domains are used to improve the component-separation process. The analysis

[1]For real experiments, these patterns are weakly modulated (and their perfect symmetry broken) by the second-order ('orbital dipole') effect coming from the Earth's motion around the Sun and (for spacecraft moving around the Earth-Sun L2 point), by the further contribution from motion in the Lissajous orbit.

of these aspects is outside the scope of the present analysis, but deserves further investigation.

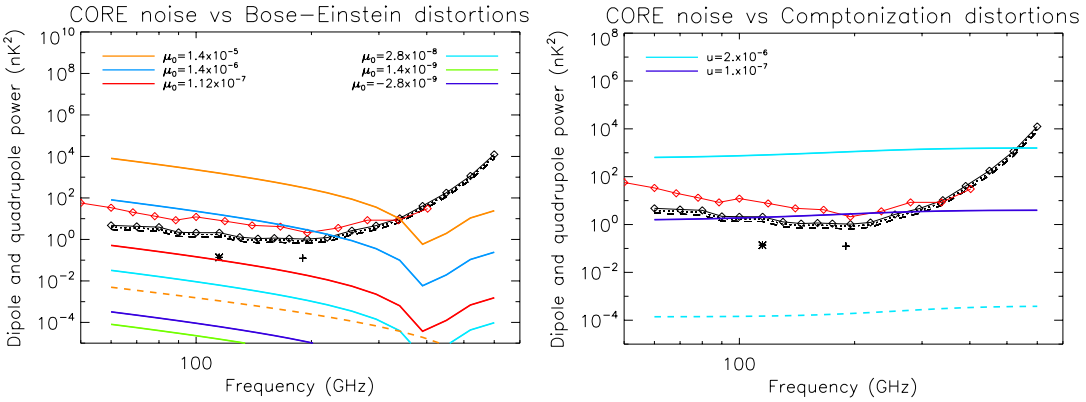

Figure 5.12: Angular power spectrum of the dipole map, derived from the difference between distorted spectra and the current blackbody spectrum versus CORE sensitivity. The CORE white noise power spectrum (independent of multipole, shown as the black upper solid curve and with diamonds for different frequency channels) and its rms uncertainty (for $\ell = 1$, using dots, and for $\ell = 2$, using dashes) are plotted in black. The cross (asterisk) displays aggregated CORE noise from all channels (up to 220 GHz). Are also shown, for comparison, the LiteBIRD white noise power spectrum (red solid curve and diamonds for different frequency channels). *Left*: BE distortions for $\mu_0 = -2.8 \times 10^{-9}$ (representative of adiabatic cooling), $\mu_0 = 1.4 \times 10^{-5}$, 1.4×10^{-6} (representative of improvements with respect to FIRAS upper limits), $\mu_0 = 1.12 \times 10^{-7}$, 2.8×10^{-8}, and 1.4×10^{-9} (representative of primordial adiabatic perturbation dissipation). For $\mu_0 = 1.4 \times 10^{-5}$ I show also the angular power spectrum of the quadrupole map. *Right*: Comptonization distortions for $u = 2 \times 10^{-6}$ (upper solid curve for the dipole map and bottom dashed curve for the quadrupole map) and $u = 10^{-7}$ (lower solid curve for the dipole map), representative of imprints by astrophysical and minimal reionization models, respectively.

5.7.4 Detectability

Here I explore the detectability of the dipolar and quadrupolar signals introduced in Sects. 5.7.1–5.7.3. To this aim, I compare the dipole signal with the noise dipole as a function of frequency. Note that since the prediction includes the specific angular dependence of the dipole, there is no cosmic-variance related component in the noise. The noise for each frequency is determined by Table 1.8, assuming full-sky coverage for simplicity[1].

Fig. 5.12 shows the dipole signal for BE and Comptonization distortions (left and right, respectively), defined as the temperature dipole coming from Eq. (5.31) subtracted from the

[1]Sampling variance, as specified by the adopted masks, will be taken into account in the next section.

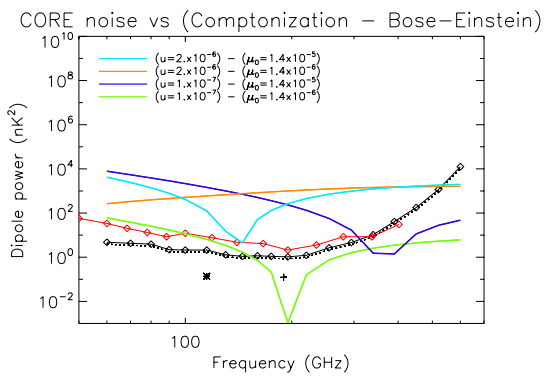

Figure 5.13: The same as in Fig. 5.12, but comparing the two above cases of Comptonization distortions with the two above cases of BE distortions with the largest values of μ_0.

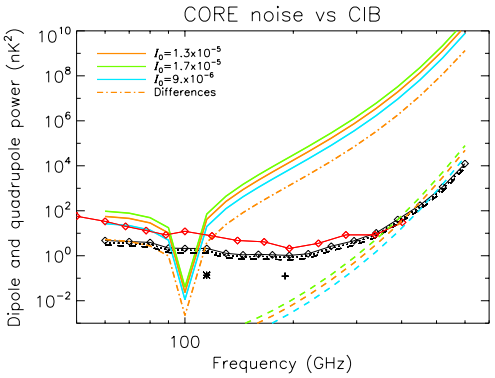

Figure 5.14: The same as in Fig. 5.12, but for the CIB (assuming the model from (124)). Also shown is the quadrupole signal (dashes). The different values of I_0 in Eq. (5.31) are the best-fit values and deviations by $\pm 1\,\sigma$.

CMB dipole (shown as coloured lines). The CORE noise as a function of frequency is reported by black lines. For BE distortions, the signal is clearly above the CORE noise up to about 200 GHz for $\mu_0 \gtrsim 10^{-6}$ and comparable or slightly above the aggregated noise below about 100 GHz for $\mu_0 \gtrsim 10^{-7}$, while for Comptonization distortions, the signal is clearly above the noise up to around 500 GHz for $u \gtrsim 2 \times 10^{-6}$ and comparable to or above the noise between approximately 100 GHz and 300 GHz for $u \gtrsim 10^{-7}$. The analogous analysis for the quadrupole (shown for simplicity only for the largest values of μ_0 and u) indicate that, for CORE sensitivity, noise dominates at any frequency for CMB spectral distortion parameters compatible with FIRAS limits, thus experiments beyond CORE are needed to use the quadrupole pattern to infer constraints on CMB spectral distortions. In Fig. 5.13 I display the dipole signal of the difference between Comptonization and BE distortion maps. Fig. 5.14 presents the size of the dipole signal (the quadrupole is shown as dashed curves) for the CIB (where I have removed the CMB dipole) compared to noise. The signal is always above the noise except at about 100 GHz. Due to the large uncertainty in the amplitude of the CIB spectra (I_0), I also include the deviations of $\pm 1\,\sigma$ from the best-fit value of 1.3×10^{-5} (as well as their difference from the best fit). The signal is orders of magnitude above the noise at high frequencies and moreover, the quadrupole is above the noise at frequencies greater than about 400 GHz, although it is always much smaller than the dipole (since it is suppressed by an extra factor of β).

Comparing Fig. 5.14 with Fig. 5.12, it is evident that the dipole power expected from the

CIB is above those predicted for CMB spectral distortions at $\nu \gtrsim 200\,\mathrm{GHz}$ for the classes of processes and parameter values discussed here. Since the dependence of the quoted power on the CMB spectral distortion parameter is quadratic, the above statement does not hold for larger CMB distortions, even just below the FIRAS limits. Although they are not predicted by standard scenarios, they may be generated by unconventional dissipation processes, such those discussed at the end of Sect. 5.7.1, according to their characteristic parameters.

I computed for analogy the power spectrum sensitivity of LiteBIRD (see Table 1.7): it is similar to that of CORE around 300 GHz and significantly worse at $\nu \lesssim 150\,\mathrm{GHz}$, a range suitable in particular for BE distortions. As discussed in Sects. 5.3 and 5.5, resolution is important to achieve the sky sampling necessary for ultra-accurate dipole analysis, thus adopting a resolution changing from a range of $\simeq$ 2–18 arcmin to a range of $\simeq 0.5^\circ$–1.5° is certainly critical. Furthermore, the number of frequency channels is relevant, in particular (see next section) when one compares between pairs of frequencies, the number of which scales approximately as the square of the number of frequency channels. In addition, a large number of frequency channels and especially the joint analysis of frequencies around 300 GHz and above 400 GHz (not foreseen in LiteBIRD) is crucial for separating the various types of signals, and, in particular, to accurately control the contamination by Galactic dust emission.

The analysis carried out here will be extended to include all frequency information in the following section. This will also include a discussion of the impact of residual foregrounds.

5.8 Simulation results for CMB spectral distortions and CIB intensity

In order to quantify the ideal CORE sensitivity to measure spectral distortion parameters and the CIB amplitude, I carried out some detailed simulations. The idea here is to simulate the sky signal assuming a certain model and to quantify the accuracy level at which (in the presence of noise and of potential residuals) the key input parameters can be recovered. I consider twelve reference cases, physically or observationally motivated, based on considerations and works quoted in Sect. 5.7.2 (cases 2–4) and Sect. 5.7.1 (cases 8–12), namely:

(1) a (reference) blackbody spectrum defined by T_0;
(2) a CIB spectrum at the FIRAS best-fit amplitude;
(3) a CIB spectrum at the FIRAS best-fit amplitude plus 1 σ error;

(4) a CIB spectrum at the FIRAS best-fit amplitude minus 1 σ error;
(5) a BE spectrum with $\mu_0 = 1.12 \times 10^{-7}$, representative of a distortion induced by damping of primordial adiabatic perturbations in the case of relatively high power at small scales;
(6) a BE spectrum with $\mu_0 = 1.4 \times 10^{-5}$, a value 6.4 times smaller than the FIRAS 95 % upper limits;
(7) a BE spectrum with $\mu_0 = 1.4 \times 10^{-6}$, a value 64 times smaller than the FIRAS 95 % upper limits;
(8) a BE spectrum with $\mu_0 = 1.4 \times 10^{-9}$, representative of the typical minimal distortion induced by the damping of primordial adiabatic perturbations;
(9) a BE spectrum with $\mu_0 = 2.8 \times 10^{-8}$, representative of the typical distortion induced by damping of primordial adiabatic perturbations;
(10) a BE spectrum with $\mu_0 = -2.8 \times 10^{-9}$, representative of the typical distortion induced by BE condensation (adiabatic cooling);
(11) a Comptonized spectrum with $u = 10^{-7}$, representative of minimal reionization models;
(12) a Comptonized spectrum with $u = 2 \times 10^{-6}$, representative of typical astrophysical reionization models.

For each model listed I generate both an ideal sky (the "prediction") and a sky with noise realizations ("simulated data") according to the sensitivity of CORE (see Table 1.8), at each of its 19 frequency channels. For a suitable number of cases I repeated the analysis working with maps simply containing only the dipole term and verified that the major contribution to the significance comes from the dipole, i.e., the quadrupole (the only other possibly relevant term) contributes almost negligibly[1], in agreement with Sect. 5.7.4. For the sake of simplicity my noise realizations assume Gaussian white noise. This simulation set consists of 10 realizations for each of the 19 CORE frequencies (giving 190 independent noise realizations). These are generated at $N_{\rm side} = 64$ (roughly 1° resolution). The inclusion of certain systematics is considered in the following subsections. I then compare each theoretical prediction with all maps of our simulated data. I calculate $\Delta\chi^2$ for each combination, summarised in a 12×12 matrix, quantifying the significance level at which each model can be potentially detected or ruled out. The results are reported in terms of $\sqrt{|\Delta\chi^2|}\,\mathrm{sign}(\Delta\chi^2)$, which directly gives the significance in terms of σ levels, since we are dealing with a single parameter at a time[2]

[1] In some cases we found it affects only the last digit (reported in the tables) of the estimated $\sqrt{|\Delta\chi^2|}\,\mathrm{sign}(\Delta\chi^2)$.
[2] The adopted number of realizations allows to provide an estimate the rms of the quoted significance values

I perform the $\sqrt{\Delta\chi^2}$ analysis for three different approaches:

(a) using each of the 19 frequency channels, assuming they are independent;

(b) using the 171 ($19 \times 18/2$) combinations coming from the differences of the maps from pairs of frequency bands;

(c) combining cases (a) and (b) together.

When differences of maps from pairs of frequency bands are included in the analysis, in the corresponding contributions to the χ^2 the variance comes from the sum of the variances at the two considered frequencies.

Approach (a) essentially compares the amplitude of dipole of a distorted spectrum with that of the blackbody, being so sensitive to the overall difference between the two cases, while approach (b) compares the dipole signal at different frequencies for each type of spectrum, being so sensitive to its slope.

5.8.1 Ideal case: perfect calibration and foreground subtraction

Tables 5.2 and 5.13 (and Tables 5.3 and 5.14, Tables 5.4 and 5.15, respectively) report the results of approach a (approach b, and c, respectively) in terms of average and rms of (see Appendix 5.B) $\sqrt{|\Delta\chi^2|}\ \mathrm{sign}(\Delta\chi^2)$.

I find that, in general, the analysis of the difference of pairs of frequency channels (approach b) tends to substantially increase the significance of the recovery of the CIB amplitude, which is due to the very steep frequency shape of the CIB dipole spectrum. For the opposite reason, the same does not occur in general for CMB distortion parameters, and, in particular, approach (b) can make the recovery of the Comptonization distortion more difficult. These results are in agreement with the shapes displayed in Figs. 5.12, 5.13, and 5.14. It is important to note that, in general, the rms values found in approach (b) are larger than those found in approach (a), seemingly relatively more stable. I interpret this as an effect of larger susceptibility of approach (b) to realization combinations. On the other hand, for the estimation of the CIB amplitude this rms amplification does not spoil the improvement in significance. Combining

suitable to check (particularly for some results based, for simplicity, on a single realization) they are not in the tail of distribution, to quantitatively compare pros and cons of the three adopted approaches, and to spot in the results the effects of coupling between signal and noise/residuals realizations. With much more realizations it is obviously possible to refine these estimates, but it is not relevant in this work that deals with wide ranges of residual parameters..

σ **level**	Current	FIRAS CIB amplitude			$(\Delta\varepsilon/\varepsilon_i)_{z_i}$						$(\Delta\varepsilon/\varepsilon_i)_{\rm late}$	
significance	blackbody	(units 10^{-5})			8×10^{-8}	10^{-5}	10^{-6}	10^{-9}	2×10^{-8}	-2×10^{-9}	4×10^{-7}	8×10^{-6}
		$I_0^{\rm bf}$	$+1\,\sigma$	$-1\,\sigma$	μ_0						u	
		1.3	1.7	0.9	1.12×10^{-7}	1.4×10^{-5}	1.4×10^{-6}	1.4×10^{-9}	2.8×10^{-8}	-2.8×10^{-9}	10^{-7}	2×10^{-6}
Case	(1)	(2)	(3)	(4)	(5)	(6)	(7)	(8)	(9)	(10)	(11)	(12)
(1)	0	3650	4740	2540	1.63	175.	17.9	0.0998	0.532	−0.137	7.95	154.
(2)	3650	0	1100	1110	3650	3640	3650	3650	3650	3650	3650	3620
(3)	4740	1100	0	2210	4740	4740	4740	4740	4740	4740	4740	4710
(4)	2540	1110	2200	0	2540	2540	2540	2540	2540	2540	2540	2510
(5)	0.403	3650	4740	2540	0	174.	16.5	0.384	−0.111	0.445	6.83	153.
(6)	174.	3640	4740	2540	173.	0	157.	174.	174.	174.	168.	108.
(7)	17.0	3650	4740	2540	15.6	158.	0	17.0	16.6	17.0	11.8	140.
(8)	−0.0975	3650	4740	2540	1.62	175.	17.9	0	0.514	−0.165	7.93	154.
(9)	−0.346	3650	4740	2540	1.28	175.	17.6	−0.342	0	−0.352	7.66	153.
(10)	0.142	3650	4740	2540	1.67	175.	17.9	0.176	0.567	0	7.98	154.
(11)	7.25	3650	4740	2540	6.22	169.	12.8	7.23	6.98	7.27	0	146.
(12)	153.	3620	4710	2510	152.	108.	140.	153.	153.	153.	145.	0

Table 5.2: Average values of $\sqrt{|\Delta\chi^2|}\ \mathrm{sign}(\Delta\chi^2)$ from a Monte Carlo simulation at $N_{\rm side} = 64$, full-sky coverage, adopting perfect foreground subtraction and calibration, and considering each of the 19 frequency channels.

the two approaches, as in (c), typically results in an overall advantage, with an improvement in significance larger than the possible increasing of the quoted rms. I anticipate that these results will still be valid when including potential residuals, as discussed below.

I remark that in the present analysis both pure theoretical maps and maps polluted with noise are pixelised in the same way. So, the sampling problem discussed in Sects. 5.3 and 5.5 is automatically by-passed. This is not a limitation for the present analysis, given the high resolution achieved by CORE, and because it is clear that we could in principle perform my simulations at the desired resolution. Working at roughly 1° resolution makes the analysis feasible without supercomputing facilities, with no significant loss of information. Nonetheless, I also report some results carried out at higher resolution. In particular, Appendix 5.C presents results of the analysis repeated at $N_{\rm side} = 512$ (i.e., at about 7 arcmin resolution), for a single realization. The results are fully compatible, within the statistical variance, with those derived working at $N_{\rm side} = 64$.

σ **level**	Current	FIRAS CIB amplitude			$(\Delta\varepsilon/\varepsilon_{\rm i})_{z_1}$						$(\Delta\varepsilon/\varepsilon_{\rm i})_{\rm late}$	
significance	blackbody	(units 10^{-5})			8×10^{-8}	10^{-5}	10^{-6}	10^{-9}	2×10^{-8}	-2×10^{-9}	4×10^{-7}	8×10^{-6}
		$I_0^{\rm bf}$	$+1\,\sigma$	$-1\,\sigma$	μ_0						u	
		1.3	1.7	0.9	1.12×10^{-7}	1.4×10^{-5}	1.4×10^{-6}	1.4×10^{-9}	2.8×10^{-8}	-2.8×10^{-9}	10^{-7}	2×10^{-6}
Case	(1)	(2)	(3)	(4)	(5)	(6)	(7)	(8)	(9)	(10)	(11)	(12)
(1)	0	14000	18200	9740	1.96	271.	27.8	0.124	0.666	−0.170	−0.229	43.7
(2)	14000	0	4180	4240	14000	14100	14000	14000	14000	14000	14000	14000
(3)	18200	4190	0	8430	18200	18200	18200	18200	18200	18200	18200	18200
(4)	9740	4240	8420	0	9740	9810	9750	9740	9740	9740	9740	9730
(5)	0.0596	14000	18200	9740	0	269.	25.6	0.0456	−0.249	0.0910	1.44	45.7
(6)	269.	14000	18200	9810	267.	0	242.	269.	269.	269.	271.	312.
(7)	26.0	14000	18200	9750	23.8	244.	0	26.0	25.4	26.1	28.1	69.6
(8)	−0.122	14000	18200	9740	1.93	271.	27.8	0	0.644	−0.205	−0.209	43.7
(9)	−0.386	14000	18200	9740	1.51	271.	27.2	−0.384	0	−0.391	0.228	44.2
(10)	0.178	14000	18200	9740	2.00	271.	27.9	0.220	0.708	0	−0.267	43.6
(11)	2.66	14000	18200	9740	4.69	273.	29.9	2.68	3.11	2.62	0	41.4
(12)	46.4	14000	18200	9730	48.4	314.	72.0	46.4	46.9	46.4	44.1	0

Table 5.3: The same as in Table 5.2, but considering all 171 independent combinations of pairs of different frequency channels.

The matrices reported in each of these tables perhaps require a little more explanation. Firstly, I should point out that the diagonals are zero by construction. I find that the reduced χ^2 ($\chi^2_{\rm r} = \chi^2/(n_{\rm d}-1)$, where $n_{\rm d}$ is the global number of data being treated and the estimate of a single parameter are considered, namely CMB distortion or CIB amplitude), is always extremely close to unity, which is an obvious validation cross-check. Note that, in principle, when potential residuals are included, one should specify the variance pixel-by-pixel in the estimation of χ^2.[1] This requires a precise local characterization of residuals. While this can easily be included by construction in my analyses, I explicitly avoid implementing this in the χ^2 analysis, but instead perform my forecasts assuming knowledge of only the average level

[1]This holds also in the case that the instrument sensitivity varies across the sky because of non-uniform sky coverage from the adopted scanning strategy (an aspect that is not so crucial in the case of the relatively uniform sky coverage expected for CORE (105, 336)) is included in the analysis. Note also that, in principle, pixel-to-pixel correlations introduced by noise correlations and potential residual morphologies should be included in the χ^2. This aspect, although important in the analysis of real data, is outside the scope of the present investigation. Nonetheless, it does not affect the main results of our forecasts.

σ **level**	Current	FIRAS CIB amplitude			$(\Delta\varepsilon/\varepsilon_i)_{z_1}$						$(\Delta\varepsilon/\varepsilon_i)_{\rm late}$	
significance	blackbody	(units 10^{-5})			8×10^{-8}	10^{-5}	10^{-6}	10^{-9}	2×10^{-8}	-2×10^{-9}	4×10^{-7}	8×10^{-6}
		$I_0^{\rm bf}$	$+1\,\sigma$	$-1\,\sigma$	μ_0						u	
		1.3	1.7	0.9	1.12×10^{-7}	1.4×10^{-5}	1.4×10^{-6}	1.4×10^{-9}	2.8×10^{-8}	-2.8×10^{-9}	10^{-7}	2×10^{-6}
Case	(1)	(2)	(3)	(4)	(5)	(6)	(7)	(8)	(9)	(10)	(11)	(12)
(1)	0	14400	18800	10100	2.67	323.	33.1	0.157	0.844	−0.214	7.83	160.
(2)	14500	0	4320	4380	14500	14500	14500	14500	14500	14500	14500	14400
(3)	18800	4330	0	8710	18800	18800	18800	18800	18800	18800	18800	18800
(4)	10100	4380	8710	0	10100	10100	10100	10100	10100	10100	10100	10100
(5)	0.369	14400	18800	10100	0	320.	30.5	0.346	−0.105	0.413	7.24	159.
(6)	321.	14500	18800	10100	318.	0	288.	321.	320.	321.	319.	330.
(7)	31.1	14500	18800	10100	28.5	290.	0	31.0	30.4	31.1	30.5	157.
(8)	−0.153	14400	18800	10100	2.64	323.	33.1	0	0.816	−0.259	7.82	160.
(9)	−0.537	14400	18800	10100	2.07	322.	32.4	−0.532	0	−0.547	7.61	160.
(10)	0.224	14400	18800	10100	2.73	323.	33.1	0.277	0.900	0	7.85	160.
(11)	7.92	14400	18800	10100	8.03	321.	32.5	7.92	7.87	7.93	0	152.
(12)	160.	14400	18800	10000	160.	332.	157.	160.	160.	160.	152.	0

Table 5.4: The same as in Table 5.2, but considering each of the 19 frequency channels independently and all 171 independent combinations of pairs of different frequency channels.

of the residuals in the sky region being considered. Secondly, I note that the matrices are not perfectly symmetric, due to the cross-terms in the squares (from noise and signal) entering into the χ^2. Thirdly, the off-diagonal terms are sometimes negative, but with absolute values compatible with the quoted rms. These second and third effects are clearly statistical in nature.

The results found in this section (see also Appendix 5.C) identify the ideal sensitivity target for CMB spectral distortion parameters and CIB amplitude that are achievable from the dipole frequency behaviour.

Elements[1] (2:4, 2:4) of the matrix quantify the sensitivity to the CIB amplitude. Comparison with FIRAS in terms of the σ level of significance can be extracted directly from the tables; the ideal improvement ranges from a factor of about 1000 to 4000.

The ideal improvement found for CMB spectral distortion parameters is also impressive. Elements (1, 5:10) and (5:10, 1) and elements (1, 11:12) and (11:12, 1) refer to comparisons between the blackbody and BE and Comptonization distortions, respectively. The comparison

[1] I adopt the convention (row index range, column index range).

with FIRAS is simply quoted by the element of the matrix of the table multiplied by the ratio between the FIRAS $1\,\sigma$ upper limit on μ_0 or u and the distortion parameter value considered in the table. The sensitivity on u is clearly enough to disentangle between minimal models of reionization and a variety of astrophysical models that predict larger amounts of energy injection by various types of source. The ideal improvement with respect to FIRAS limits is about 500–600. The level of (negative) BE distortions is much lower, and the same holds also for BE distortions predicted for the damping of primordial adiabatic perturbations. Only weak, tentative constraints on models with high power at small scales could be set with this approach, for a mission with the sensitivity of CORE. Nonetheless, the ideal improvement with respect to FIRAS limits on BE distortions lies in the range 600–1000.

The other elements of the matrix refer to the comparison of distorted spectra; note in particular the elements (6:7, 11:12) and (11:12, 6:7) that show how Comptonization distortions can be distinguished from BE distortions, for the two larger values considered for μ_0, as suggested by Fig. 5.13.

5.8.2 Including potential foreground and calibration residuals

I expect that potential residuals from imperfect foreground subtraction and calibration may affect the results presented in the previous section, depending on their level. To assess this, I have carried out a wide set of simulations in order to quantify the accuracy in recovering the CMB distortion parameters and CIB amplitude under different working assumptions.

Simulations are first performed adopting $E_{\rm for} = 10^{-2}$ and $E_{\rm cal} = 10^{-4}$ (defined by the parametric model introduced in Sect. 5.4) at $N_{\rm side} = 64$, and then adding many tests exploring combinations of possible improvements in foreground characterization (assuming $E_{\rm for} = 10^{-3}$ or $E_{\rm for} = 10^{-2}$, but at larger $N_{\rm side}$), as well as different levels of calibration accuracy (including possible worsening at higher frequencies).

5.8.2.1 Monte Carlo results at about 1° resolution

To understand the typical implications of different assumptions, I first perform a series of Monte Carlo simulations, identical to that described in Sect. 5.8.1, but including potential foreground and calibration residuals, modelled according to Sect. 5.4, assuming $E_{\rm for} = 10^{-2}$ and $E_{\rm cal} = 10^{-4}$. The main results (the average values of $\sqrt{|\Delta\chi^2|}\ \mathrm{sign}(\Delta\chi^2)$) are presented in Ta-

σ **level**	Current	FIRAS CIB amplitude			$(\Delta\varepsilon/\varepsilon_i)_{z_1}$						$(\Delta\varepsilon/\varepsilon_i)_{\rm late}$	
significance	blackbody	(units 10^{-5})			8×10^{-8}	10^{-5}	10^{-6}	10^{-9}	2×10^{-8}	-2×10^{-9}	4×10^{-7}	8×10^{-6}
		$I_0^{\rm bf}$	$+1\,\sigma$	$-1\,\sigma$	μ_0						u	
		1.3	1.7	0.9	1.12×10^{-7}	1.4×10^{-5}	1.4×10^{-6}	1.4×10^{-9}	2.8×10^{-8}	-2.8×10^{-9}	10^{-7}	2×10^{-6}
Case	(1)	(2)	(3)	(4)	(5)	(6)	(7)	(8)	(9)	(10)	(11)	(12)
(1)	0	13.7	17.7	9.61	−0.00676	10.4	0.833	−0.00264	−0.00996	0.00383	0.166	4.83
(2)	12.8	0	4.37	3.48	12.8	16.6	12.8	12.8	12.8	12.8	12.8	13.1
(3)	16.8	3.44	0	7.58	16.8	19.9	16.9	16.8	16.8	16.8	16.8	16.9
(4)	8.75	4.39	8.45	0	8.76	13.7	8.83	8.75	8.75	8.75	8.72	9.47
(5)	0.0391	13.7	17.7	9.61	0	10.3	0.686	0.0385	0.0307	0.0400	0.133	4.76
(6)	10.5	17.3	20.6	14.3	10.4	0	9.41	10.5	10.4	10.5	10.2	6.51
(7)	0.821	13.7	17.7	9.67	0.739	9.39	0	0.821	0.799	0.825	0.611	3.93
(8)	0.00270	13.7	17.7	9.61	−0.00701	10.4	0.830	0	−0.00967	0.00473	0.166	4.83
(9)	0.0139	13.7	17.7	9.61	−0.0100	10.4	0.788	0.0135	0	0.0146	0.163	4.82
(10)	−0.00370	13.7	17.7	9.61	−0.00658	10.4	0.836	−0.00451	−0.0102	0	0.166	4.84
(11)	0.0337	13.7	17.6	9.57	−0.0402	10.2	0.505	0.0330	0.0210	0.0346	0	4.60
(12)	4.56	13.9	17.7	10.1	4.48	6.28	3.57	4.56	4.54	4.56	4.32	0

Table 5.5: Average values of $\sqrt{|\Delta\chi^2|}\,\mathrm{sign}(\Delta\chi^2)$ from a Monte Carlo simulation at $N_{\rm side} = 64$, with full-sky coverage, adopting $E_{\rm for} = 10^{-2}$ and $E_{\rm cal} = 10^{-4}$, and considering each of the 19 frequency channels.

bles 5.5, 5.6, and 5.7, while the corresponding rms values are reported in Appendix 5.D (see Tables 5.17, 5.18, and 5.19).

With these levels of potential residuals, the improvement with respect to FIRAS in the recovery of the CIB amplitude ranges from a factor of approximately 4 (with an rms of about 1 in the estimate of this improvement factor) for approach (a) to a factor of about 15 or 20 (with an rms of about 3) for approaches (b) and (c), respectively.

The improvement found for the recovery of CMB spectral distortion parameters is also very promising. The sensitivity to u improves with respect to FIRAS by a factor of 20 (except for the less stable approach (b)), which is suitable for detecting reionization imprints (of the sort predicted in astrophysical reionization models) at about $5\,\sigma$, while the improvement on BE distortions is about a factor of 40 (approach (c)). Note that these results are derived considering the full sky, and thus I expect to obtain improvements by applying masks to avoid regions with significant potential contamination, as discussed in the next section.

σ **level**	Current	FIRAS CIB amplitude			$(\Delta\varepsilon/\varepsilon_i)_{z_1}$						$(\Delta\varepsilon/\varepsilon_i)_{\rm late}$	
significance	blackbody	(units 10^{-5})			8×10^{-8}	10^{-5}	10^{-6}	10^{-9}	2×10^{-8}	-2×10^{-9}	4×10^{-7}	8×10^{-6}
		$I_0^{\rm bf}$	$+1\,\sigma$	$-1\,\sigma$	μ_0						u	
		1.3	1.7	0.9	1.12×10^{-7}	1.4×10^{-5}	1.4×10^{-6}	1.4×10^{-9}	2.8×10^{-8}	-2.8×10^{-9}	10^{-7}	2×10^{-6}
Case	(1)	(2)	(3)	(4)	(5)	(6)	(7)	(8)	(9)	(10)	(11)	(12)
(1)	0	49.9	64.7	35.0	−0.224	6.67	−0.311	−0.0267	−0.117	0.0379	0.211	1.15
(2)	47.7	0	15.6	13.4	47.7	49.9	47.8	47.7	47.7	47.7	47.6	47.4
(3)	62.4	13.3	0	28.4	62.4	64.5	62.6	62.4	62.4	62.4	62.4	62.2
(4)	32.7	15.8	30.6	0	32.7	35.2	32.9	32.7	32.7	32.7	32.7	32.5
(5)	0.250	49.9	64.7	35.0	0	6.61	−0.324	0.248	0.214	0.253	0.314	1.21
(6)	8.51	52.3	66.9	37.7	8.44	0	7.71	8.51	8.48	8.51	8.54	9.31
(7)	1.15	50.1	64.9	35.2	1.08	5.84	0	1.15	1.13	1.15	1.20	2.06
(8)	0.0268	49.9	64.7	35.0	−0.223	6.67	−0.310	0	−0.114	0.0465	0.212	1.15
(9)	0.121	49.9	64.7	35.0	−0.196	6.66	−0.314	0.118	0	0.127	0.239	1.17
(10)	−0.0378	49.9	64.7	35.0	−0.227	6.67	−0.310	−0.0463	−0.122	0	0.208	1.15
(11)	−0.206	49.9	64.7	35.0	−0.289	6.71	−0.322	−0.207	−0.230	−0.203	0	1.11
(12)	−0.710	49.6	64.4	34.7	−0.706	7.40	−0.391	−0.709	−0.708	−0.711	−0.703	0

Table 5.6: The same as in Table 5.5, but considering all 171 independent combinations of pairs of different frequency channels.

5.8.2.2 Application of masks

I perform some additional tests assuming $E_{\rm for} = 10^{-2}$ and $E_{\rm cal} = 10^{-4}$, but applying appropriate masks to the sky. Clearly, in this way the available statistical information is reduced (as I verified through tests carried out under ideal conditions of perfect foreground subtraction and calibration), but in realistic cases we may expect to improve the quality of results by reducing the impact of potential residuals.

I use the "*Planck* common mask 76" (in temperature) and the extension of this mask that excludes all pixels at $|b| \leq 30°$.[1]

Having already addressed the rms uncertainty in the $\sqrt{|\Delta\chi^2|}\ {\rm sign}(\Delta\chi^2)$ estimates, in this test (as well as in the following ones) I will consider a single realization only, in order to avoid repeating a huge number of unnecessary simulations and omit reporting the results found in the

[1] I also considered a mask that excludes also all pixels within 30° of the Ecliptic plane, to avoid zodiacal-light contamination, but the resulting map has considerably less statistical power due to the low overall sky fraction.

σ **level**	Current	FIRAS CIB amplitude			$(\Delta\varepsilon/\varepsilon_i)_{z_1}$						$(\Delta\varepsilon/\varepsilon_i)_{\rm late}$	
significance	blackbody	(units 10^{-5})			8×10^{-8}	10^{-5}	10^{-6}	10^{-9}	2×10^{-8}	-2×10^{-9}	4×10^{-7}	8×10^{-6}
		$I_0^{\rm bf}$	$+1\,\sigma$	$-1\,\sigma$	μ_0						u	
		1.3	1.7	0.9	1.12×10^{-7}	1.4×10^{-5}	1.4×10^{-6}	1.4×10^{-9}	2.8×10^{-8}	-2.8×10^{-9}	10^{-7}	2×10^{-6}
Case	(1)	(2)	(3)	(4)	(5)	(6)	(7)	(8)	(9)	(10)	(11)	(12)
(1)	0	51.8	67.0	36.3	−0.191	12.4	0.142	−0.0230	−0.101	0.0327	0.309	5.10
(2)	49.4	0	16.2	13.9	49.4	52.6	49.5	49.4	49.4	49.4	49.3	49.2
(3)	64.6	13.7	0	29.4	64.7	67.5	64.8	64.7	64.7	64.6	64.6	64.4
(4)	33.9	16.4	31.8	0	33.9	37.7	34.1	33.9	33.9	33.9	33.9	33.9
(5)	0.222	51.8	67.1	36.3	0	12.3	0.0689	0.220	0.189	0.225	0.402	5.05
(6)	13.5	55.1	70.0	40.2	13.4	0	12.2	13.5	13.5	13.5	13.4	11.4
(7)	1.48	52.0	67.3	36.5	1.38	11.2	0	1.48	1.46	1.49	1.43	4.57
(8)	0.0231	51.8	67.0	36.3	−0.190	12.4	0.142	0	−0.0987	0.0401	0.309	5.10
(9)	0.105	51.8	67.0	36.3	−0.169	12.4	0.123	0.102	0	0.110	0.338	5.09
(10)	−0.0326	51.8	67.0	36.3	−0.193	12.4	0.145	−0.0399	−0.106	0	0.308	5.10
(11)	−0.143	51.7	67.0	36.3	−0.324	12.3	−0.0738	−0.147	−0.200	−0.136	0	4.86
(12)	4.35	51.5	66.8	36.2	4.26	9.77	3.06	4.35	4.33	4.35	4.10	0

Table 5.7: The same as in Table 5.5, but considering each of the 19 frequency channels independently and all 171 independent combinations of pairs of different frequency channels.

less stable approach (b), for the sake of simplicity.

In the case of the extended mask and including also the cross-comparisons between different frequency channels (approach (c)), I find a significant improvement (see Table 5.8) with respect to the results based on the full sky; the significance of the CIB amplitude recovery improves by about 50 % and that on the BE distortion improves by about 20 %. This indicates the relevance of optimising the selection of the sky region for which the analysis is applied, and of comparing results obtained with different masks.

5.8.2.3 Varying assumptions on potential foreground and calibration residuals

I now consider the implications of different levels of potential residuals, evaluating both better and worse cases with respect to the reference case analysed before. Given the results obtained in the previous section the case of the extended mask will be exploited. I present here the main outcomes of this analysis, while the tables with the corresponding numerical results are

σ **level**	Current	FIRAS CIB amplitude			$(\Delta\varepsilon/\varepsilon_{\rm i})_{z_1}$						$(\Delta\varepsilon/\varepsilon_{\rm i})_{\rm late}$	
significance	blackbody	(units 10^{-5})			8×10^{-8}	10^{-5}	10^{-6}	10^{-9}	2×10^{-8}	-2×10^{-9}	4×10^{-7}	8×10^{-6}
		$I_0^{\rm bf}$	$+1\,\sigma$	$-1\,\sigma$	μ_0						u	
		1.3	1.7	0.9	1.12×10^{-7}	1.4×10^{-5}	1.4×10^{-6}	1.4×10^{-9}	2.8×10^{-8}	-2.8×10^{-9}	10^{-7}	2×10^{-6}
Case	(1)	(2)	(3)	(4)	(5)	(6)	(7)	(8)	(9)	(10)	(11)	(12)
(1)	0	73.5	95.1	51.8	0.139	14.8	1.50	0.00844	0.0473	−0.0113	−0.385	5.29
(2)	69.1	0	23.7	19.4	69.1	72.7	69.3	69.1	69.1	69.1	69.0	68.7
(3)	90.6	19.2	0	41.0	90.6	93.9	90.8	90.6	90.6	90.6	90.6	90.2
(4)	47.3	23.8	45.4	0	47.4	51.6	47.6	47.3	47.3	47.3	47.3	47.0
(5)	0.0920	73.5	95.1	51.8	0	14.7	1.38	0.0905	0.0611	0.0950	−0.422	5.22
(6)	14.7	76.9	98.2	55.7	14.6	0	13.3	14.7	14.7	14.7	14.6	12.2
(7)	1.45	73.7	95.3	52.0	1.33	13.3	0	1.45	1.42	1.46	1.22	4.53
(8)	−0.00818	73.5	95.1	51.8	0.138	14.8	1.50	0	0.0457	−0.0137	−0.386	5.29
(9)	−0.0223	73.5	95.1	51.8	0.109	14.8	1.47	−0.0227	0	−0.0213	−0.398	5.27
(10)	0.0121	73.5	95.1	51.8	0.142	14.8	1.50	0.0150	0.0506	0	−0.384	5.29
(11)	0.558	73.5	95.0	51.7	0.541	14.6	1.44	0.558	0.551	0.559	0	5.00
(12)	6.10	73.2	94.7	51.6	6.04	12.6	5.46	6.10	6.08	6.10	5.81	0

Table 5.8: Values of $\sqrt{|\Delta\chi^2|}\ \mathrm{sign}(\Delta\chi^2)$ for a single realization at $N_{\rm side} = 64$, using the *Planck* mask-76 extended to exclude regions at $|b| \leq 30°$. I adopt $E_{\rm for} = 10^{-2}$ and $E_{\rm cal} = 10^{-4}$, and consider each of the 19 frequency channels and all 171 independent combinations of pairs of different frequencies.

reported in Appendix 5.E for sake of completeness.

– **Improving foreground subtraction**

I evaluate the improvement in component separation of total intensity maps by considering the case of $E_{\rm for} = 10^{-3}$. The results, summarised in Table 5.20 (for approach (c)), can be compared with those of Table 5.8. Note the improvement by a factor of approximately 10 in the recovery of the CIB amplitude, in line with that assumed in foreground removal, and by a factor of 5 (or 6) in the recovery of μ_0 (or u), implying that calibration uncertainty is relatively more important for estimating CMB distortion parameters than for estimating the CIB amplitude. Indeed, the CIB is better constrained at higher frequencies, where foregrounds are more relevant.

– **The case of poorer calibration**

I discuss here the degradation in sensitivity entailed by keeping $E_{\rm for} = 10^{-2}$, but replacing CORE's calibration-accuracy goal of $E_{\rm cal} = 10^{-4}$ with $E_{\rm cal} = 10^{-3}$ at $\nu \leq 295\,\mathrm{GHz}$ and $E_{\rm cal} = 10^{-2}$ at $\nu \geq 340\,\mathrm{GHz}$.

The results, summarised in Table 5.21 (for approach (c)), can be compared with those of Table 5.8. In spite of the assumed degradation in calibration accuracy at high frequencies (particularly relevant for the CIB), I determine that the recovery of the CIB amplitude is very weakly affected, while the significance of the μ_0 (or u) determination degrades by factor of approximately 2 (or 25–30 %). This result strengthens the conclusion of the previous subsection that calibration uncertainty is relatively more important for estimating CMB distortion parameters than for the CIB amplitude.

For the assumptions adopted, I derive an improvement with respect to FIRAS by factor of around 20 in the recovery of the CIB amplitude, 15 on the constraints on the Comptonization parameter u (or for its detection, at a level of about 3–4 σ for astrophysical reionization models), and about 24 for the constraints on chemical potential μ_0.

Finally, a worst case scenario with $E_{\rm for} = E_{\rm cal} = 10^{-2}$ is considered. Even in this situation, I obtain an improvement with respect to FIRAS by a factor of 17 in the recovery of the CIB amplitude, and a factor of a few for CMB spectral distortion parameters, specifically around 4 for BE distortions and a marginal detection of astrophysical reionization models for Comptonization distortions.

– **Poorer calibration together with improved foreground subtraction**

At this point, I focus on a combination of the two cases above, i.e., a further improvement in component separation of total intensity maps represented by $E_{\rm for} = 10^{-3}$ and a calibration accuracy parameterised by $E_{\rm cal} = 10^{-3}$ at $\nu \leq 295\,\mathrm{GHz}$ and $E_{\rm cal} = 10^{-2}$ at $\nu \geq 340\,\mathrm{GHz}$.

The results obtained in approach (c) are summarised in Table 5.22. The significance of CIB amplitude recovery is intermediate between the results found in the previous cases, while the degradation due to the poorer calibration is approximately compensated by the improvement due to better foreground subtraction in the case of Comptonization distortions, but only partially compensated in the case of BE distortions.

Overall, the analysis indicates that the relevance of calibration accuracy increases from CIB amplitude to Comptonization-distortion and to BE-distortion recovery, while the rel-

evance of the quality of foreground subtraction increases from BE distortions to Comptonization distortions and to CIB amplitude recovery. This conclusion reflects the increase of the foreground level and of the relative amplitude of the imprints left by the three types of signals at increasing frequencies (for CORE).

– **Varying the reference angular scale**

Lastly, I account for foreground and calibration subtraction errors in the range discussed above, but at smaller angular scales, specifically at $N_{\rm side} = 256$. The corresponding pixel linear size ($\simeq$ 13.7 arcmin) is similar to the FWHM resolution of CORE channels at $\nu \lesssim 80$ GHz that are necessary for the mitigation of low-frequency foreground emission.

With this adopted set-up and considering the most advantageous approach (i.e., approach (c)), assuming a foreground mitigation parameterised by $E_{\rm for} = 10^{-3}$, I get (see Table 5.23) an improvement with respect to FIRAS by a factor of 80–90 for the recovery of CIB amplitude, around 80 on the constraints for the Comptonization parameter u (implying a precise measure of the energy injections associated to astrophysical reionization models), and about 150 on the constraints on chemical potential μ_0. Adopting $E_{\rm for} = 10^{-2}$, the improvement is a factor of 75 for the recovery of CIB amplitude, 50 for the constraints on the Comptonization parameter u, and 80 for the constraints on the chemical potential μ_0.

I further consider the same set-up but at $N_{\rm side} = 128$, i.e., with a pixel side 2 times larger. As expected, the results are intermediate between those derived at $N_{\rm side} = 64$ and 256.

5.8.3 Summary of simulation results

A large set of simulations for different choices of the parameters characterising foreground and calibration residual levels have been presented above. I summarize the main results in Table 5.9 in terms of improvements with respect to FIRAS, in order to parametrically quantify the accuracy required to achieve significant improvements. For other values of $E_{\rm for}$ and $E_{\rm cal}$, I find an almost linear dependence on them for the improvement factor in parameter recovery.

5.9 Discussion and conclusions

I have carried out a detailed investigation of three distinct scientific implications coming from exploitation of the observer's peculiar velocity effects in CORE maps. The determination of

	$E_{\rm cal}$ (%)	$E_{\rm for}$ (%)	CIB amplitude	Bose-Einstein	Comptonization
Ideal case, all sky	-	-	$\simeq 4.4 \times 10^3$	$\simeq 10^3$	$\simeq 6.0 \times 10^2$
All sky	10^{-4}	10^{-2}	$\simeq 15$	$\simeq 42$	$\simeq 18$
P76	10^{-4}	10^{-2}	$\simeq 19$	$\simeq 42$	$\simeq 18$
P76ext	10^{-2}	10^{-2}	$\simeq 17$	~ 4	~ 2
P76ext	10^{-4}	10^{-2}	$\simeq 22$	$\simeq 47$	$\simeq 21$
P76ext	10^{-4}	10^{-3}	$\simeq 2.1 \times 10^2$	$\simeq 2.4 \times 10^2$	$\simeq 1.1 \times 10^2$
P76ext	$10^{-3}_{(\leq 295)}$–$10^{-2}_{(\geq 340)}$	10^{-2}	$\simeq 19$	$\simeq 26$	$\simeq 11$
P76ext	$10^{-3}_{(\leq 295)}$–$10^{-2}_{(\geq 340)}$	10^{-3}	$\simeq 48$	$\simeq 35$	$\simeq 15$
P76ext, $N_{\rm side} = 128$	$10^{-3}_{(\leq 295)}$–$10^{-2}_{(\geq 340)}$	10^{-2}	$\simeq 38$	$\simeq 51$	$\simeq 23$
P76ext, $N_{\rm side} = 128$	$10^{-3}_{(\leq 295)}$–$10^{-2}_{(\geq 340)}$	10^{-3}	$\simeq 43$	$\simeq 87$	$\simeq 39$
P76ext, $N_{\rm side} = 256$	$10^{-3}_{(\leq 295)}$–$10^{-2}_{(\geq 340)}$	10^{-2}	$\simeq 76$	$\simeq 98$	$\simeq 44$
P76ext, $N_{\rm side} = 256$	$10^{-3}_{(\leq 295)}$–$10^{-2}_{(\geq 340)}$	10^{-3}	$\simeq 85$	$\simeq 1.6 \times 10^2$	$\simeq 73$

Table 5.9: Predicted improvement in the recovery of the distortion parameters discussed in the text with respect to FIRAS for different calibration and foreground residual assumptions. This table summarizes the results derived with approach (c). "P06" stands for the *Planck* common mask, while "P06ext" is the extended P06 mask. When not explicitly stated, all values refer to $E_{\rm cal}$ and $E_{\rm for}$ at $N_{\rm side} = 64$.

the CMB dipole amplitude and direction is an important observable in modern cosmology. It provides information on our velocity with respect to the CMB reference frame, which is expected to dominate the effect. Related investigations in other wavebands, which exploit signals from different types of astrophysical sources, probe different shells in redshift, and together provide an important test of fundamental principles in cosmology. In particular, the alignment of the CMB dipole with those independently measured from galaxy and cluster catalogues is regarded as indirect proof of the kinematic origin of the CMB dipole. The specific relation between the amplitudes of the CMB and large-scale structure dipoles, predicted by the linear perturbation theory, has been used to obtain estimates of the redshift-space distortion parameter independent of (but consistent with) those coming from redshift surveys. It is thus important to look for possible departures from a purely kinematic character for the CMB dipole.

In this context, surveys from space are clearly appealing, since they represent the best (and perhaps only) way to precisely measure this large-scale signal.

I performed detailed simulations in the context of a mission like CORE, to understand the expectations, and potential issues arising from future CMB surveys beyond the already excellent results produced by *Planck*. The sampling of the sky turns out to be the main limiting factor for the precise measurement of the dipole direction and (obviously together with calibration) also a crucial limiting factor for the precise measurement of dipole amplitude. I reveal that the recovered uncertainty scales linearly with the map pixel linear size (i.e., inversely with $N_{\rm side}$). Although maps can be oversampled through a proper scanning strategy and by setting the sampling time of the data acquisition well below that corresponding to the beam resolution, it is clear that the experimental resolution plays a crucial role in this respect. Thus, achieving a good angular resolution in future CMB space missions, as proposed for CORE, will be important not only for delensing but also for dipole analyses. The dipole direction determination can be averaged over the various frequency channels, improving accuracy and providing cross-checks for systematics. With the assumption of a pure blackbody, the same holds for the amplitude. However, when searching for dipole spectral signatures, increasing the accuracy at each frequency (which results from a better sky sampling) turns out to be even more important.

An observer moving with respect to the CMB rest frame will also see boosting imprints on the CMB at $\ell > 1$, due to Doppler and aberration effects, which can be measured in harmonic space as correlations between ℓ and $\ell+1$ modes (assuming that the CMB is statistically isotropic in its rest frame). Such a signal can be measured independently in temperature and polarization, which constitutes a new consistency check, with a signal-to-noise ratio of about 8 for TT, 7 for $TE + ET$ and 7 for EE. Overall, CORE can achieve a signal-to-noise ratio of almost 13, which improves on the capabilities of *Planck* (about S/N $\simeq$ 4, only in TT) and is essentially that of an ideal cosmic-variance-limited experiment up to $\ell \simeq 2000$. I stress the importance of performing high-sensitivity measurements at close to arcminute resolution in order to be sensitive to the correlations at high multipoles that yield most of the signal. Since CORE will also provide good measurements of the tSZ effect and the CIB, which are also assumed to be statistically isotropic in the CMB rest frame, boosting effects in these maps have been also investigated. However, the aberration effect on tSZ maps and the boosting effects on the CIB are smaller than in the CMB maps, and the predicted signal-to-noise is less than 1 in both cases.

Beyond FIRAS, great hopes are expected for PIXIE, which has been proposed to NASA to observe CMB polarization and the CMB spectrum with degree resolution and is designed

to have a precision about 10^3 times better than FIRAS, mainly relying on the achievement of extreme quality in its absolute calibration, and a corresponding similar improvement on CMB spectral distortion parameters (180). Note that even if PIXIE fails to fully achieve these ambitious goals, an improvement in calibration precision of even one or two orders of magnitude with respect to FIRAS calibration, in addition to being intrinsically interesting for strengthening the limits on CMB distortion parameters, will imply an analogous improvement for the calibration of other CMB projects. In general, combining results from experiments like PIXIE and CORE will offer a chance to have maps with substantially improved calibration, sensitivity, and resolution.

CMB anisotropy missions will not perform absolute measurements of the CMB spectrum, but can observe the frequency spectral behaviour of the CMB and CIB dipoles. We exploit the sensitivity of an experiment like CORE for the recovery of the parameters u and μ_0 of Comptonization and BE spectral distortions, as well as for the amplitude of the CIB spectrum. Assuming perfect relative calibration and absence of foreground contamination, the CORE sensitivity and frequency coverage, combined with its resolution (to cope with sampling uncertainty), could allow us to achieve an improvement with respect to FIRAS by a factor of around $1\text{–}4 \times 10^3$, 500–600, and 600–1000 in the recovery of the CIB spectrum amplitude, u, and μ_0, respectively; the best results are obtained from the joint information contained in each of the frequency channels independently *and* in all the independent combinations of pairs of different frequencies. Combining pairs of different frequencies turns out to be particularly advantageous for the CIB dipole spectrum, since it exhibits a steeper frequency behaviour.

As expected, foregrounds are critical in both absolute and differential methods. Relative calibration accuracy is an important limiting factor in CMB anisotropy experiments in general and even more so for analyses based on the dipole. In current data analysis pipelines the dipole itself is in fact typically used for calibration, which raises the issue of a circular argument. However, for all-sky mapping experiments (like WMAP and *Planck*), the *orbital* dipole from the Earth and satellite motion is ultimately used for calibration, rather than the CMB dipole itself. Precise calibration is always challenging, and it is unclear what the limiting step will be for any new experiment. Nevertheless, in principle it will be possible to measure the spectrum of the dipole with an anisotropy experiment. In general, improving and extending calibration methods is crucial for these analyses. Various approaches can be integrated into the data reduction design, ranging from a better instrumental characterization to cross-correlation between different CMB surveys and substantial refinements in astronomical calibration sources.

I have carried out a large set of simulations, summarised in Table 5.9, to parametrically quantify the accuracy required to achieve significant improvements with respect to FIRAS.

I find that the importance of the impact of calibration errors decreases from BE distortions to Comptonization distortions and to the CIB amplitude, while the opposite holds for the impact of foreground contamination (in agreement with the increase with frequency of foreground level and of the relative amplitude of the imprints left by the three types of signal). Applying suitable masks also yields an improvement in parameter estimation.

In the case of 1 % accuracy (at a reference scale of about 1°) in both foreground removal and relative calibration (i.e., $E_{\rm for} = E_{\rm cal} = 10^{-2}$), CORE will be able to improve the recovery of the CIB spectrum amplitude of a factor of about 17, to achieve a marginal detection of the energy release associated with astrophysical reionization models, and to improve by a factor of approximately 4 the limits on early energy dissipations. On the other hand, an improvement of a factor of 20 for CIB amplitude, of 10 for u, and of around 25 for the chemical potential μ_0, is found by improving the relative calibration error to $\simeq 0.1\,\%$. Any further improvement in foreground mitigation and calibration will enable still more precise results to be achieved.

Appendices

5.A Likelihoods of CMB dipole parameters

For the sake of completeness, I report here the likelihoods computed for CMB dipole parameters and the confidence levels in their estimation. I limit the presentation here to the lowest and highest resolutions among those exploited in this analysis.

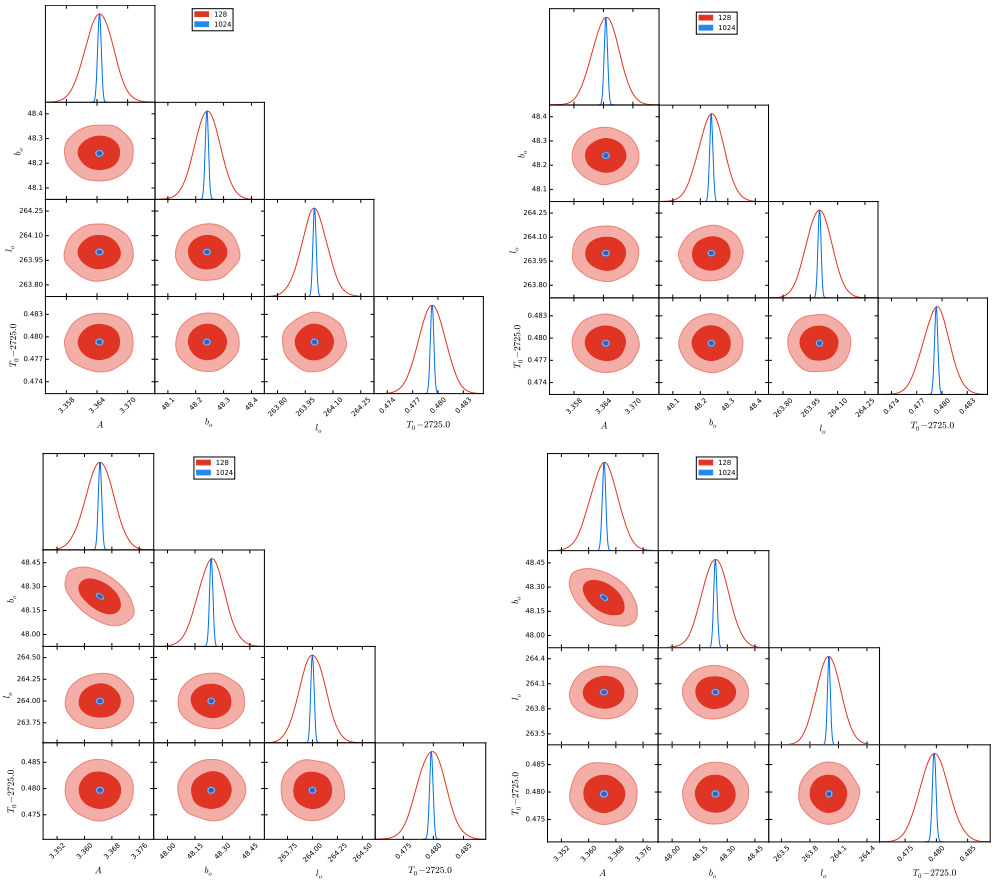

Figure 5.15: Marginalised likelihoods, and 68% and 95% contours of the parameters A, b_0, l_0, and T_0 at $N_{\rm side} = 128$ (red) and at $N_{\rm side} = 1024$ (blue): top left, dipole only; top right, dipole+noise; bottom left, dipole+noise+mask; and bottom right, dipole+noise+mask+systematics. The reference frequency channel is 60 GHz and the noise is 7.5 μK.arcmin. The mask used here is the *Planck* Galactic mask extended to cut out ±30° of the Galactic plane. The level of systematics correspond to the pessimistic expectation of calibration errors and sky residuals.

$N_{\rm side}$ = 128	A(mK)	$b_0(^\circ)$	$l_0(^\circ)$	T_0(mK)
dipole	3.3644 ± 0.0028	48.242 ± 0.047	263.999 ± 0.070	2725.4793 ± 0.0016
dip+noi	3.3644 ± 0.0028	48.240 ± 0.047	263.998 ± 0.071	2725.4793 ± 0.0016
dip+noi+mask	3.3644 ± 0.0041	48.240 ± 0.075	264.00 ± 0.13	2725.4797 ± 0.0024
dip+noi+mask+sys	3.3645 ± 0.0041	48.235 ± 0.074	264.00 ± 0.13	2725.4797 ± 0.0023
$N_{\rm side}$ = 1024	A(mK)	$b_0(^\circ)$	$l_0(^\circ)$	T_0(mK)
dipole	3.36447 ± 0.00036	48.2399 ± 0.0060	264.0002 ± 0.0088	2725.47930 ± 0.00020
dip+noi	3.36450 ± 0.00035	48.2398 ± 0.0059	264.0005 ± 0.0087	2725.47931 ± 0.00020
dip+noi+mask	3.36454 ± 0.00051	48.2387 ± 0.0091	264.000 ± 0.017	2725.47966 ± 0.00029
dip+noi+mask+sys	3.36451 ± 0.00052	48.2352 ± 0.0092	264.000 ± 0.016	2725.47965 ± 0.00029

Table 5.10: 68 % confidence levels of the parameters A, b_0, l_0, and T_0 from Fig. 5.15.

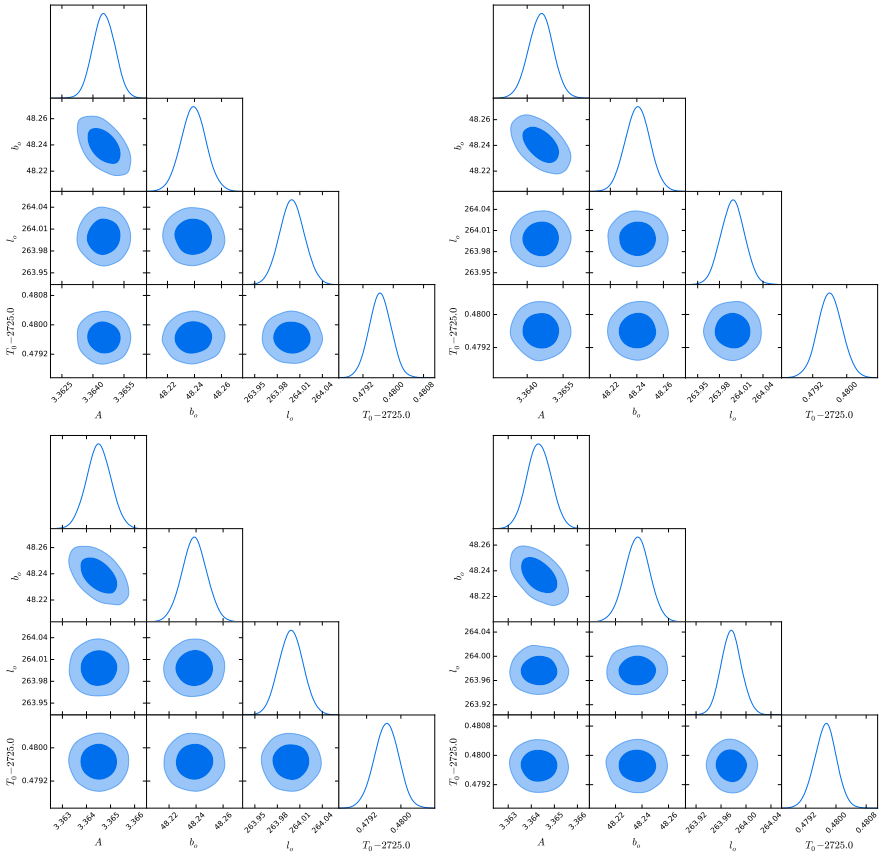

Figure 5.16: Marginalised likelihoods, and 68% and 95% contours of the parameters A, b_0, l_0, and T_0. Input maps are at $N_{\rm side} = 1024$, with noise, mask and residuals (calibration errors and sky residuals). *Top*: 100 GHz with optimistic (left) and pessimistic (right) systematics. *Bottom*: 220 GHz with optimistic (left) and pessimistic (right) systematics.

$N_{\rm side}$ = 1024	A(mK)	$b_0(^\circ)$	$l_0(^\circ)$	T_0(mK)
60 GHz, good sys	3.36454 ± 0.00052	48.2387 ± 0.0093	263.999 ± 0.016	2725.47965 ± 0.00029
60 GHz, bad sys	3.36451 ± 0.00052	48.2352 ± 0.0092	264.000 ± 0.016	2725.47965 ± 0.00029
100 GHz, good sys	3.36453 ± 0.00053	48.2393 ± 0.0093	264.000 ± 0.016	2725.47965 ± 0.00029
100 GHz, bad sys	3.36457 ± 0.00051	48.2406 ± 0.0093	263.998 ± 0.016	2725.47961 ± 0.00029
145 GHz, good sys	3.36452 ± 0.00052	48.2391 ± 0.0093	263.999 ± 0.017	2725.47967 ± 0.00029
145 GHz, bad sys	3.36434 ± 0.00051	48.2391 ± 0.0091	263.996 ± 0.017	2725.47965 ± 0.00029
220 GHz, good sys	3.36451 ± 0.00051	48.2387 ± 0.0092	263.998 ± 0.016	2725.47966 ± 0.00029
220 GHz, bad sys	3.36434 ± 0.00052	48.2364 ± 0.0094	263.977 ± 0.016	2725.47972 ± 0.00029

Table 5.11: 68 % confidence level of the parameters A, b_0, l_0, and T_0 at 60, 100, 145 and 220 GHz (see Fig. 5.16 for the likelihoods at 100 and 220 GHz).

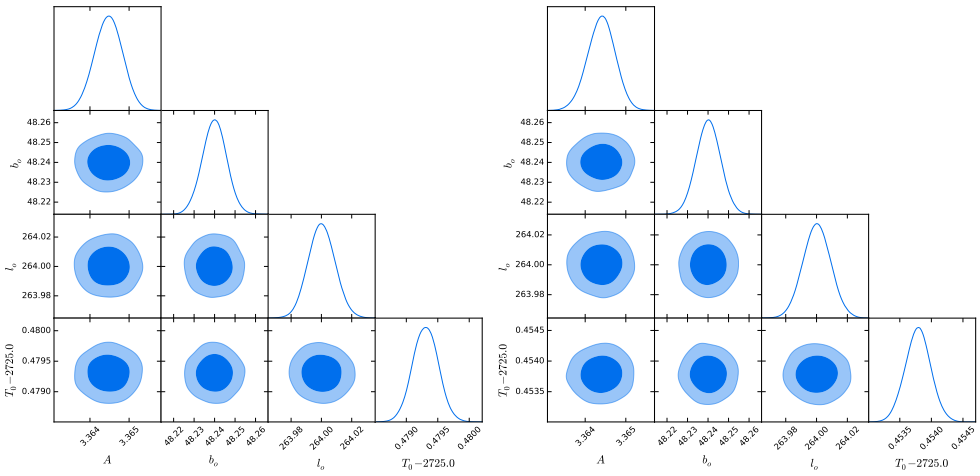

Figure 5.17: Marginalised likelihoods, and 68% and 95% contours of the parameters A, b_0, l_0, and T_0. Input maps are dipole-only, at 60 GHz and at $N_{\rm side}$ = 1024. On the left: blackbody. On the right: Bose-Einstein (chemical potential $\mu_0 = 1.4 \times 10^{-5}$).

$N_{\rm side}$ = 1024	A(mK)	$b_0(^\circ)$	$l_0(^\circ)$	T_0(mK)
blackbody	3.36447 ± 0.00036	48.2399 ± 0.0060	264.0002 ± 0.0088	2725.47930 ± 0.00020
Bose-Einstein	3.36440 ± 0.00034	48.2402 ± 0.0059	264.0002 ± 0.0090	2725.45379 ± 0.00020

Table 5.12: 68 % confidence level of the parameters A, b_0, l_0, and T_0 of Fig. 5.17.

5.B Rms values from Monte Carlo simulations: ideal case

I report the tables with the estimates of the rms of the $\sqrt{|\Delta\chi^2|}\ \mathrm{sign}(\Delta\chi^2)$ quoted from a Monte Carlo simulation at $N_{\rm side} = 64$, using all-sky maps and adopting perfect foreground subtraction and calibration.

Rms of σ level	Current	FIRAS CIB amplitude			$(\Delta\varepsilon/\varepsilon_{\rm i})_{z_{\rm i}}$						$(\Delta\varepsilon/\varepsilon_{\rm i})_{\rm late}$	
significance	blackbody	(units 10^{-5})			8×10^{-8}	10^{-5}	10^{-6}	10^{-9}	2×10^{-8}	-2×10^{-9}	4×10^{-7}	8×10^{-6}
		$I_0^{\rm bf}$	$+1\,\sigma$	$-1\,\sigma$	μ_0						u	
		1.3	1.7	0.9	1.12×10^{-7}	1.4×10^{-5}	1.4×10^{-6}	1.4×10^{-9}	2.8×10^{-8}	-2.8×10^{-9}	10^{-7}	2×10^{-6}
Case	(1)	(2)	(3)	(4)	(5)	(6)	(7)	(8)	(9)	(10)	(11)	(12)
(1)	0	4.83	6.99	3.16	0.872	0.568	0.621	0.129	0.562	0.183	0.976	1.06
(2)	4.22	0	4.22	0.00	4.22	5.27	5.16	4.22	4.22	4.22	5.16	5.16
(3)	6.99	3.16	0	5.16	6.99	4.22	6.99	6.99	6.99	6.99	6.99	6.75
(4)	0.00	3.16	5.16	0	0.00	4.22	3.16	0.00	0.00	0.00	3.16	0.00
(5)	1.06	4.83	6.99	3.16	0	0.675	0.621	1.06	0.976	1.07	1.05	1.06
(6)	0.667	6.75	6.32	4.22	0.738	0	0.823	0.667	0.738	0.568	0.667	1.08
(7)	0.636	4.83	6.75	3.16	0.636	0.675	0	0.636	0.632	0.635	0.657	1.14
(8)	0.129	4.83	6.99	3.16	0.871	0.568	0.610	0	0.549	0.224	0.976	1.06
(9)	0.578	4.83	6.99	3.16	0.813	0.675	0.619	0.564	0	0.606	0.993	1.06
(10)	0.182	4.83	6.99	3.16	0.873	0.667	0.613	0.223	0.587	0	0.974	1.06
(11)	1.04	5.16	6.75	3.16	1.14	0.568	0.620	1.05	1.07	1.04	0	0.994
(12)	0.994	5.16	6.32	3.16	0.919	1.05	1.08	0.994	1.07	0.994	0.966	0

Table 5.13: Rms values of $\sqrt{|\Delta\chi^2|}\ \mathrm{sign}(\Delta\chi^2)$ from a Monte Carlo simulation at $N_{\rm side} = 64$, full sky, adopting perfect foreground subtraction and calibration, and considering each of the 19 frequency channels.

Rms of σ level	Current	FIRAS CIB amplitude			$(\Delta\varepsilon/\varepsilon_i)_{zi}$						$(\Delta\varepsilon/\varepsilon_i)_{late}$	
significance	blackbody	(units 10^{-5})			8×10^{-8}	10^{-5}	10^{-6}	10^{-9}	2×10^{-8}	-2×10^{-9}	4×10^{-7}	8×10^{-6}
		I_0^{bf}	$+1\,\sigma$	$-1\,\sigma$	μ_0						u	
		1.3	1.7	0.9	1.12×10^{-7}	1.4×10^{-5}	1.4×10^{-6}	1.4×10^{-9}	2.8×10^{-8}	-2.8×10^{-9}	10^{-7}	2×10^{-6}
Case	(1)	(2)	(3)	(4)	(5)	(6)	(7)	(8)	(9)	(10)	(11)	(12)
(1)	0.00	31.6	42.2	14.8	2.93	2.67	2.52	0.342	1.52	0.485	2.89	2.18
(2)	31.6	0	6.75	6.67	0.00	51.6	0.00	31.6	0.00	31.6	31.6	31.6
(3)	42.2	5.16	0	8.43	42.2	42.2	31.6	42.2	42.2	42.2	42.2	51.6
(4)	10.8	8.23	11.4	0	10.8	12.9	12.9	10.8	10.8	10.8	11.7	12.9
(5)	3.11	31.6	42.2	14.8	0	2.59	2.53	3.09	2.70	3.15	4.15	2.20
(6)	2.30	51.6	42.2	14.5	2.49	0	2.33	2.33	2.67	2.30	2.50	2.46
(7)	2.59	31.6	31.6	14.5	2.64	2.56	0	2.62	2.60	2.60	2.58	2.31
(8)	0.343	31.6	42.2	14.8	2.91	2.56	2.51	0	1.48	0.594	2.91	2.19
(9)	1.56	31.6	42.2	14.8	2.58	2.59	2.53	1.52	0	1.63	3.29	2.20
(10)	0.484	31.6	42.2	14.8	2.96	2.67	2.53	0.593	1.60	0	2.85	2.18
(11)	2.39	31.6	42.2	14.8	2.93	2.81	2.48	2.40	2.60	2.36	0	2.20
(12)	2.10	31.6	52.7	14.0	2.13	2.59	2.30	2.09	2.12	2.12	2.10	0

Table 5.14: The same as in Table 5.13, but considering all 171 independent combinations of pairs of different frequency channels.

Rms of σ level	Current	FIRAS CIB amplitude			$(\Delta\varepsilon/\varepsilon_i)_{z_1}$						$(\Delta\varepsilon/\varepsilon_i)_{\rm late}$	
significance	blackbody	(units 10^{-5})			8×10^{-8}	10^{-5}	10^{-6}	10^{-9}	2×10^{-8}	-2×10^{-9}	4×10^{-7}	8×10^{-6}
		$I_0^{\rm bf}$	$+1\,\sigma$	$-1\,\sigma$	μ_0						u	
		1.3	1.7	0.9	1.12×10^{-7}	1.4×10^{-5}	1.4×10^{-6}	1.4×10^{-9}	2.8×10^{-8}	-2.8×10^{-9}	10^{-7}	2×10^{-6}
Case	(1)	(2)	(3)	(4)	(5)	(6)	(7)	(8)	(9)	(10)	(11)	(12)
(1)	0	52.7	31.6	31.6	2.69	2.17	2.14	0.340	1.50	0.482	1.40	1.57
(2)	51.6	0	8.43	6.75	51.6	0.00	51.6	51.6	51.6	51.6	51.6	31.6
(3)	31.6	5.16	0	11.0	31.6	52.7	31.6	31.6	31.6	31.6	31.6	51.6
(4)	31.6	6.32	12.6	0	31.6	0.00	0.00	31.6	31.6	31.6	31.6	51.6
(5)	3.10	52.7	31.6	31.6	0	2.28	2.14	3.08	2.68	3.14	2.15	1.40
(6)	2.20	0.00	48.3	31.6	2.21	0	2.17	2.06	2.21	2.20	2.21	2.59
(7)	2.23	51.6	31.6	31.6	2.23	2.27	0	2.22	2.22	2.22	2.57	1.65
(8)	0.340	52.7	31.6	31.6	2.68	2.17	2.12	0	1.46	0.591	1.40	1.57
(9)	1.53	52.7	31.6	31.6	2.40	2.28	2.16	1.49	0	1.61	1.58	1.57
(10)	0.481	52.7	31.6	31.6	2.72	2.31	2.14	0.589	1.57	0	1.38	1.57
(11)	1.48	51.6	31.6	31.6	2.15	2.18	2.48	1.49	1.65	1.46	0	1.57
(12)	1.23	31.6	52.7	51.6	1.58	2.72	1.87	1.23	1.23	1.23	1.23	0

Table 5.15: The same as in Table 5.13, but considering each of the 19 frequency channels and all 171 independent combinations of pairs of different frequency channels.

5.C Ideal case at high resolution

I repeat the same analysis carried out in the previous section, now working at $N_{\rm side} = 512$, i.e., at about 7 arcmin resolution, and considering a single realization. The results are reported in Table 5.16 relative to approach (c).

σ **level**	Current	FIRAS CIB amplitude			$(\Delta\varepsilon/\varepsilon_i)_{z_1}$						$(\Delta\varepsilon/\varepsilon_i)_{\rm late}$	
significance	blackbody	(units 10^{-5})			8×10^{-8}	10^{-5}	10^{-6}	10^{-9}	2×10^{-8}	-2×10^{-9}	4×10^{-7}	8×10^{-6}
		$I_0^{\rm bf}$	$+1\,\sigma$	$-1\,\sigma$	μ_0						u	
		1.3	1.7	0.9	1.12×10^{-7}	1.4×10^{-5}	1.4×10^{-6}	1.4×10^{-9}	2.8×10^{-8}	-2.8×10^{-9}	10^{-7}	2×10^{-6}
Case	(1)	(2)	(3)	(4)	(5)	(6)	(7)	(8)	(9)	(10)	(11)	(12)
(1)	0	14400	18800	10100	−1.39	320.	30.5	−0.326	−1.31	0.467	8.65	161.
(2)	14500	0	4380	4380	14500	14500	14500	14500	14500	14500	14500	14400
(3)	18800	4330	0	8710	18800	18800	18800	18800	18800	18800	18800	18800
(4)	10100	4380	8710	0	10100	10100	10100	10100	10100	10100	10100	10000
(5)	3.90	14400	18800	10100	0	317.	27.9	3.86	3.19	3.97	9.06	160.
(6)	323.	14500	10100	10100	321.	0	291.	323.	323.	323.	322.	332.
(7)	33.8	18800	18800	10100	31.2	288.	0	33.8	33.1	33.8	33.4	158.
(8)	0.329	14400	18800	10100	−1.41	320.	30.4	0	−1.29	0.575	8.66	161.
(9)	1.60	14400	18800	10100	−1.64	319.	29.8	1.55	0	1.69	8.69	160.
(10)	−0.458	14400	18800	10100	−1.35	320.	30.5	−0.559	−1.36	0	8.65	161.
(11)	7.27	14400	18800	10100	6.56	318.	29.7	7.26	7.01	7.30	0	153.
(12)	159.	14500	18800	10000	159.	328.	156.	159.	159.	159.	151.	0

Table 5.16: Values of $\sqrt{|\Delta\chi^2|}\ {\rm sign}(\Delta\chi^2)$ for a single realization at $N_{\rm side} = 512$, for the full sky, adopting perfect foreground subtraction and calibration, and considering each of the 19 frequency channels and all 171 independent combinations of pairs of different frequencies.

5.D Rms values from Monte Carlo simulations: including potential residuals

This appendix reports the tables with the estimates of the rms of the $\sqrt{|\Delta\chi^2|}\,\mathrm{sign}(\Delta\chi^2)$ quoted from a Monte Carlo simulation at $N_{\rm side} = 64$, with all-sky data, and including potential foreground and calibration residuals.

Rms of σ level	Current	FIRAS CIB amplitude			$(\Delta\varepsilon/\varepsilon_i)_{z_1}$						$(\Delta\varepsilon/\varepsilon_i)_{\rm late}$	
significance	blackbody	(units 10^{-5})			8×10^{-8}	10^{-5}	10^{-6}	10^{-9}	2×10^{-8}	-2×10^{-9}	4×10^{-7}	8×10^{-6}
		$I_0^{\rm bf}$	$+1\,\sigma$	$-1\,\sigma$	μ_0						u	
		1.3	1.7	0.9	1.12×10^{-7}	1.4×10^{-5}	1.4×10^{-6}	1.4×10^{-9}	2.8×10^{-8}	-2.8×10^{-9}	10^{-7}	2×10^{-6}
Case	(1)	(2)	(3)	(4)	(5)	(6)	(7)	(8)	(9)	(10)	(11)	(12)
(1)	0	0.798	0.804	0.802	0.274	0.471	0.673	0.0308	0.137	0.0435	0.416	0.469
(2)	0.838	0	0.792	0.973	0.846	0.637	0.819	0.838	0.838	0.838	0.838	0.701
(3)	0.829	0.981	0	0.871	0.829	0.682	0.806	0.829	0.829	0.829	0.823	0.753
(4)	0.859	0.788	0.799	0	0.857	0.578	0.837	0.859	0.860	0.859	0.841	0.667
(5)	0.276	0.798	0.804	0.800	0	0.480	0.746	0.274	0.239	0.280	0.359	0.472
(6)	0.490	0.605	0.657	0.529	0.495	0	0.486	0.490	0.480	0.481	0.484	0.509
(7)	0.788	0.795	0.808	0.768	0.775	0.477	0	0.788	0.784	0.789	0.775	0.474
(8)	0.0308	0.798	0.804	0.802	0.272	0.471	0.673	0	0.134	0.0533	0.415	0.470
(9)	0.138	0.798	0.804	0.802	0.237	0.478	0.702	0.134	0	0.145	0.399	0.469
(10)	0.0435	0.798	0.804	0.802	0.277	0.486	0.670	0.0533	0.144	0	0.418	0.469
(11)	0.455	0.798	0.798	0.784	0.383	0.482	0.768	0.454	0.437	0.457	0	0.469
(12)	0.539	0.709	0.733	0.624	0.542	0.525	0.591	0.539	0.539	0.538	0.543	0

Table 5.17: Rms values of $\sqrt{|\Delta\chi^2|}\,\mathrm{sign}(\Delta\chi^2)$ from a Monte Carlo simulation at $N_{\rm side} = 64$, full sky, adopting $E_{\rm for} = 10^{-2}$ and $E_{\rm cal} = 10^{-4}$, and considering each of the 19 frequency channels.

5.E Results for different assumptions on potential foreground and calibration residuals

I report here some of the results discussed in Sect. 5.8.2.3.

Rms of σ level	Current	FIRAS CIB amplitude			$(\Delta\varepsilon/\varepsilon_i)_{zi}$						$(\Delta\varepsilon/\varepsilon_i)_{late}$	
significance	blackbody	(units 10^{-5})			8×10^{-8}	10^{-5}	10^{-6}	10^{-9}	2×10^{-8}	-2×10^{-9}	4×10^{-7}	8×10^{-6}
		I_0^{bf}	$+1\,\sigma$	$-1\,\sigma$	μ_0						u	
		1.3	1.7	0.9	1.12×10^{-7}	1.4×10^{-5}	1.4×10^{-6}	1.4×10^{-9}	2.8×10^{-8}	-2.8×10^{-9}	10^{-7}	2×10^{-6}
Case	(1)	(2)	(3)	(4)	(5)	(6)	(7)	(8)	(9)	(10)	(11)	(12)
(1)	0	2.69	2.69	2.68	0.332	1.77	1.34	0.0362	0.164	0.0512	0.359	1.54
(2)	2.67	0	2.77	2.88	2.67	2.69	2.67	2.67	2.67	2.67	2.67	2.66
(3)	2.65	2.91	0	2.70	2.64	2.68	2.67	2.65	2.65	2.65	2.65	2.65
(4)	2.69	2.76	2.70	0	2.69	2.72	2.71	2.69	2.69	2.69	2.69	2.68
(5)	0.320	2.69	2.69	2.68	0	1.78	1.28	0.318	0.278	0.324	0.483	1.56
(6)	1.39	2.69	2.71	2.64	1.38	0	1.38	1.39	1.37	1.39	1.38	1.40
(7)	1.08	2.69	2.69	2.68	1.04	1.85	0	1.08	1.08	1.09	1.12	1.59
(8)	0.0362	2.69	2.69	2.68	0.329	1.77	1.34	0	0.160	0.0627	0.361	1.54
(9)	0.161	2.69	2.69	2.68	0.286	1.78	1.33	0.157	0	0.169	0.395	1.55
(10)	0.0512	2.69	2.69	2.68	0.336	1.77	1.35	0.0629	0.172	0	0.355	1.54
(11)	0.360	2.69	2.72	2.67	0.491	1.77	1.38	0.362	0.397	0.356	0	1.51
(12)	1.64	2.69	2.69	2.66	1.68	1.79	2.08	1.64	1.65	1.64	1.60	0

Table 5.18: The same as in Table 5.17, but considering all 171 independent combinations of pairs of different frequency channels.

5.E Results for different assumptions on potential foreground and calibration residuals

Rms of σ level	Current	FIRAS CIB amplitude			$(\Delta\varepsilon/\varepsilon_i)_{z_1}$						$(\Delta\varepsilon/\varepsilon_i)_{\rm late}$	
significance	blackbody	(units 10^{-5})			8×10^{-8}	10^{-5}	10^{-6}	10^{-9}	2×10^{-8}	-2×10^{-9}	4×10^{-7}	8×10^{-6}
		$I_0^{\rm bf}$	$+1\,\sigma$	$-1\,\sigma$	μ_0						u	
		1.3	1.7	0.9	1.12×10^{-7}	1.4×10^{-5}	1.4×10^{-6}	1.4×10^{-9}	2.8×10^{-8}	-2.8×10^{-9}	10^{-7}	2×10^{-6}
Case	(1)	(2)	(3)	(4)	(5)	(6)	(7)	(8)	(9)	(10)	(11)	(12)
(1)	0	2.79	2.82	2.79	0.411	1.10	1.48	0.0458	0.205	0.0647	0.469	0.638
(2)	2.79	0	2.87	3.03	2.79	2.74	2.78	2.79	2.79	2.79	2.79	2.75
(3)	2.77	3.04	0	2.84	2.76	2.75	2.79	2.76	2.76	2.77	2.77	2.75
(4)	2.82	2.86	2.81	0	2.82	2.73	2.82	2.82	2.82	2.82	2.80	2.74
(5)	0.406	2.79	2.79	2.78	0	1.10	1.43	0.404	0.352	0.411	0.534	0.649
(6)	1.02	2.71	2.76	2.62	1.02	0	1.01	1.02	1.02	1.02	1.02	1.34
(7)	1.18	2.79	2.79	2.78	1.14	1.10	0	1.18	1.17	1.18	1.21	0.853
(8)	0.0457	2.79	2.82	2.79	0.409	1.10	1.48	0	0.199	0.0794	0.470	0.638
(9)	0.204	2.79	2.82	2.79	0.356	1.08	1.47	0.199	0	0.214	0.475	0.642
(10)	0.0647	2.79	2.82	2.79	0.417	1.10	1.48	0.0794	0.215	0	0.467	0.637
(11)	0.503	2.81	2.82	2.78	0.547	1.11	1.54	0.503	0.513	0.502	0	0.636
(12)	0.842	2.76	2.78	2.74	0.876	1.55	1.87	0.843	0.849	0.840	0.859	0

Table 5.19: The same as in Table 5.17, but considering each of the 19 frequency channels and all 171 independent combinations of pairs of different frequency channels.

σ **level**	Current	FIRAS CIB amplitude			$(\Delta\varepsilon/\varepsilon_i)_{z_1}$						$(\Delta\varepsilon/\varepsilon_i)_{\rm late}$	
significance	blackbody	(units 10^{-5})			8×10^{-8}	10^{-5}	10^{-6}	10^{-9}	2×10^{-8}	-2×10^{-9}	4×10^{-7}	8×10^{-6}
		$I_0^{\rm bf}$	$+1\,\sigma$	$-1\,\sigma$	μ_0						u	
		1.3	1.7	0.9	1.12×10^{-7}	1.4×10^{-5}	1.4×10^{-6}	1.4×10^{-9}	2.8×10^{-8}	-2.8×10^{-9}	10^{-7}	2×10^{-6}
Case	(1)	(2)	(3)	(4)	(5)	(6)	(7)	(8)	(9)	(10)	(11)	(12)
(1)	0.00	700.	911.	487.	0.859	75.7	7.85	0.0689	0.341	−0.0956	2.35	30.7
(2)	699.	0.00	211.	213.	699.	715.	700.	699.	699.	699.	699.	696.
(3)	910.	211.	0.00	424.	910.	926.	911.	910.	910.	910.	910.	907.
(4)	486.	213.	424.	0.00	486.	504.	487.	486.	486.	486.	486.	483.
(5)	−0.103	700.	911.	487.	0.00	75.1	7.24	−0.122	−0.276	−0.0379	2.19	30.5
(6)	75.1	716.	926.	505.	74.5	0.00	67.6	75.1	75.0	75.1	74.6	69.5
(7)	7.23	701.	912.	488.	6.62	68.2	0.00	7.22	7.07	7.24	7.00	28.7
(8)	−0.0680	700.	911.	487.	0.851	75.7	7.84	0.00	0.331	−0.116	2.35	30.7
(9)	−0.266	700.	911.	487.	0.697	75.6	7.70	−0.262	0.00	−0.275	2.30	30.7
(10)	0.0979	700.	911.	487.	0.875	75.7	7.86	0.121	0.361	0.00	2.35	30.8
(11)	−1.06	700.	911.	487.	−1.04	75.1	7.19	−1.06	−1.09	−1.05	0.00	29.3
(12)	28.5	697.	907.	484.	28.3	69.3	26.4	28.5	28.5	28.5	27.0	0.00

Table 5.20: Values of $\sqrt{|\Delta\chi^2|}\,\mathrm{sign}(\Delta\chi^2)$ for a single realization at $N_{\rm side} = 64$, using *Planck* mask-76 extended to exclude regions at $|b| \le 30°$. I adopt $E_{\rm for} = 10^{-3}$ and $E_{\rm cal} = 10^{-4}$, and consider each of the 19 frequency channels and all 171 independent combinations of pairs of different frequencies.

5.E Results for different assumptions on potential foreground and calibration residuals

σ **level**	Current	FIRAS CIB amplitude			$(\Delta\varepsilon/\varepsilon_i)_{z_1}$						$(\Delta\varepsilon/\varepsilon_i)_{\rm late}$	
significance	blackbody	(units 10^{-5})			8×10^{-8}	10^{-5}	10^{-6}	10^{-9}	2×10^{-8}	-2×10^{-9}	4×10^{-7}	8×10^{-6}
		$I_0^{\rm bf}$	$+1\,\sigma$	$-1\,\sigma$	μ_0						u	
		1.3	1.7	0.9	1.12×10^{-7}	1.4×10^{-5}	1.4×10^{-6}	1.4×10^{-9}	2.8×10^{-8}	-2.8×10^{-9}	10^{-7}	2×10^{-6}
Case	(1)	(2)	(3)	(4)	(5)	(6)	(7)	(8)	(9)	(10)	(11)	(12)
(1)	0	65.2	84.3	46.0	−0.193	7.80	0.376	−0.0227	−0.101	0.0322	0.563	3.96
(2)	61.2	0	20.9	17.1	61.2	63.0	61.3	61.2	61.2	61.2	61.2	60.9
(3)	80.3	17.0	0	36.3	80.3	82.0	80.4	80.3	80.3	80.3	80.2	79.9
(4)	41.9	21.1	40.2	0	41.9	44.0	42.1	41.9	41.9	41.9	41.9	41.7
(5)	0.214	65.2	84.3	46.0	0	7.73	0.286	0.212	0.183	0.217	0.595	3.94
(6)	8.44	67.0	86.0	48.0	8.37	0	7.62	8.44	8.42	8.44	8.39	8.11
(7)	1.09	65.3	84.4	46.1	1.02	6.98	0	1.08	1.07	1.09	1.18	3.84
(8)	0.0228	65.2	84.3	46.0	−0.192	7.80	0.375	0	−0.0980	0.0395	0.563	3.96
(9)	0.103	65.2	84.3	46.0	−0.169	7.78	0.355	0.100	0	0.108	0.570	3.95
(10)	−0.0322	65.2	84.3	46.0	−0.195	7.80	0.378	−0.0394	−0.105	0	0.562	3.96
(11)	−0.517	65.2	84.2	45.9	−0.560	7.71	−0.481	−0.518	−0.529	−0.516	0	3.80
(12)	2.00	64.8	83.9	45.6	1.94	6.61	1.42	1.99	1.98	2.00	1.82	0

Table 5.21: Values of $\sqrt{|\Delta\chi^2|}\ \mathrm{sign}(\Delta\chi^2)$ for a single realization at $N_{\rm side} = 64$, using *Planck* mask-76 extended to exclude regions at $|b| \leq 30°$. I adopt $E_{\rm for} = 10^{-2}$ and $E_{\rm cal} = 10^{-3}$ at $\nu \leq 295\,$GHz and $E_{\rm cal} = 10^{-2}$ at $\nu \geq 340\,$GHz, and consider each of the 19 frequency channels and all 171 independent combinations of pairs of different frequencies.

σ **level**	Current	FIRAS CIB amplitude			$(\Delta\varepsilon/\varepsilon_i)_{z_1}$						$(\Delta\varepsilon/\varepsilon_i)_{\rm late}$	
significance	blackbody	(units 10^{-5})			8×10^{-8}	10^{-5}	10^{-6}	10^{-9}	2×10^{-8}	-2×10^{-9}	4×10^{-7}	8×10^{-6}
		$I_0^{\rm bf}$	$+1\,\sigma$	$-1\,\sigma$	μ_0						u	
		1.3	1.7	0.9	1.12×10^{-7}	1.4×10^{-5}	1.4×10^{-6}	1.4×10^{-9}	2.8×10^{-8}	-2.8×10^{-9}	10^{-7}	2×10^{-6}
Case	(1)	(2)	(3)	(4)	(5)	(6)	(7)	(8)	(9)	(10)	(11)	(12)
(1)	0	161.	209.	112.	−0.601	8.97	−1.83	−0.0680	−0.303	0.0962	0.963	6.15
(2)	157.	0	49.8	46.4	157.	160.	157.	157.	157.	157.	157.	156.
(3)	205.	45.9	0	94.4	205.	208.	205.	205.	205.	205.	205.	204.
(4)	109.	50.2	98.2	0	109.	112.	109.	109.	109.	109.	109.	108.
(5)	0.615	161.	209.	112.	0	8.88	−1.78	0.611	0.531	0.622	1.14	6.17
(6)	13.1	164.	212.	116.	13.1	0	12.0	13.1	13.1	13.2	13.1	13.8
(7)	2.43	161.	209.	113.	2.31	7.81	0	2.43	2.40	2.43	2.59	6.46
(8)	0.0680	161.	209.	112.	−0.598	8.97	−1.83	0	−0.296	0.118	0.966	6.15
(9)	0.305	161.	209.	112.	−0.522	8.95	−1.82	0.297	0	0.320	1.01	6.15
(10)	−0.0961	161.	209.	112.	−0.609	8.97	−1.83	−0.118	−0.318	0	0.959	6.15
(11)	−0.909	161.	209.	112.	−1.09	8.87	−2.07	−0.912	−0.959	−0.904	0	5.91
(12)	1.65	160.	208.	111.	1.48	8.00	−1.60	1.64	1.61	1.65	1.27	0

Table 5.22: Values of $\sqrt{|\Delta\chi^2|}\,\mathrm{sign}(\Delta\chi^2)$ for a single realization at $N_{\rm side} = 64$, using *Planck* mask-76 extended to exclude regions at $|b| \le 30°$. I adopt $E_{\rm for} = 10^{-3}$ and $E_{\rm cal} = 10^{-3}$ at $\nu \le 295\,$GHz and $E_{\rm cal} = 10^{-2}$ at $\nu \ge 340\,$GHz, and consider each of the 19 frequency channels and all 171 independent combinations of pairs of different frequencies.

5.E Results for different assumptions on potential foreground and calibration residuals

σ **level**	Current	FIRAS CIB amplitude			$(\Delta\varepsilon/\varepsilon_i)_{z_1}$						$(\Delta\varepsilon/\varepsilon_i)_{\rm late}$	
significance	blackbody	(units 10^{-5})			8×10^{-8}	10^{-5}	10^{-6}	10^{-9}	2×10^{-8}	-2×10^{-9}	4×10^{-7}	8×10^{-6}
		$I_0^{\rm bf}$	$+1\,\sigma$	$-1\,\sigma$	μ_0						u	
		1.3	1.7	0.9	1.12×10^{-7}	1.4×10^{-5}	1.4×10^{-6}	1.4×10^{-9}	2.8×10^{-8}	-2.8×10^{-9}	10^{-7}	2×10^{-6}
Case	(1)	(2)	(3)	(4)	(5)	(6)	(7)	(8)	(9)	(10)	(11)	(12)
(1)	0	286.	371.	200.	−1.12	48.6	2.74	−0.133	−0.589	0.189	2.12	21.3
(2)	278.	0	88.9	81.7	278.	289.	278.	278.	278.	278.	278.	276.
(3)	363.	81.0	0	167.	363.	373.	364.	363.	363.	363.	363.	361.
(4)	192.	89.7	175.	0	192.	205.	193.	192.	192.	192.	192.	191.
(5)	1.26	286.	371.	200.	0	48.2	2.25	1.25	1.08	1.28	2.38	21.2
(6)	52.1	297.	381.	213.	51.7	0	47.1	52.1	52.0	52.1	51.6	46.2
(7)	6.57	286.	371.	201.	6.15	43.5	0	6.57	6.47	6.58	6.52	19.9
(8)	0.134	286.	371.	200.	−1.12	48.5	2.74	0	−0.574	0.232	2.12	21.3
(9)	0.606	286.	371.	200.	−0.989	48.5	2.62	0.590	0	0.636	2.18	21.3
(10)	−0.189	286.	371.	200.	−1.14	48.6	2.75	−0.231	−0.617	0	2.11	21.3
(11)	−1.60	286.	371.	200.	−2.06	48.0	−0.489	−1.61	−1.74	−1.59	0	20.3
(12)	17.7	284.	369.	199.	17.4	40.4	14.8	17.7	17.6	17.7	16.7	0

Table 5.23: Values of $\sqrt{|\Delta\chi^2|}\,{\rm sign}(\Delta\chi^2)$ for a single realization at $N_{\rm side} = 256$, using *Planck* mask-76 extended to exclude regions at $|b| \leq 30°$. I adopt $E_{\rm for} = 10^{-3}$ and $E_{\rm cal} = 10^{-3}$ at $\nu \leq 295\,{\rm GHz}$ and $E_{\rm cal} = 10^{-2}$ at $\nu \geq 340\,{\rm GHz}$, and consider each of the 19 frequency channels and all 171 independent combinations of pairs of different frequencies.

5. OBSERVER PECULIAR MOTION EFFECTS IN MICROWAVE AND RADIO SURVEYS

Conclusions

Our Universe is well described by a nearly spatially flat, Λ cold dark matter (ΛCDM) model with nearly scale-invariant, adiabatic and Gaussian primordial fluctuations. These theoretical statements, part of the standard cosmological model, have been determined to a high level of precision during the last decades, with observations from various space borne satellites and ground based facilities. On the other hand, there are still many fundamental open questions that remain unsolved by this model. In order to answer these problems and to reach an outstanding degree of precision in the cosmological parameters measure, it is compelling to disentangle all the contaminants which add up to the cosmological signal, and to strongly reduce the instrumental noise. The microwave band have been, and is still now, a powerful observational tool to study the primordial Universe and all the systematic effects affecting observational data and their interpretation. Microwaves observations provide a wealth of cosmological information immersed in the Galactic foregrounds, thermal and kinetic Sunyaev-Zeldovich effects arising from clusters of galaxies and extragalactic point sources emissions. Thus, to unveil all the informations encoded in the CMB and to reveal the finest structures in its anisotropies, it is crucial to disentangle the cosmological signal from all the other sky components. At the same time, a complete knowledge of foregrounds can reveal many astrophysical mechanisms. In order to analyze the main Galactic foregrounds as synchrotron, free free and thermal dust emissions, it is crucial to develop adequate component separation tools and cleaning routines. Indeed, more recently, multifrequency investigations are becoming increasingly of interest. In this thesis, I mainly focused on the fundamental synergy between microwaves and radio frequencies, where the majority of Galactic and extragalactic sources emit.

After the first discovery of CMB total intensity fluctuations as measured by the COsmic Background Explorer (COBE) satellite, the Wilkinson Microwave Anisotropy Probe (WMAP) satellite released all sky CMB observations mapping anisotropies on degree and sub-degree angular scales. The *Planck* mission, with a greater sensitivity and resolution than ever before,

had the goal to study this relic radiation left over from the Big Bang and to look into the evolution since the birth of our Universe, nearly 14 billion years ago.

Recent and forthcoming radio facilities, such as the SKA and its precursors and pathfinders, will be useful for addressing a wide set of topics relevant for cosmology. Among them, the SKA can provide crucial insights into dark matter properties. It provides an opportunity to constrain the dark matter parameter space, to detect and identify a dark matter particle, thus offering the opportunity for astrophysical observations to give a unique and significant contribution to other areas of physics. There are several areas where the SKA observations are expected to contribute to the identification or exclusion of dark matter particle candidates. The interaction of baryons with magnetic fields can potentially lead to direct observations of filaments, and provide greater insight into the production mechanism for high-energy cosmic rays. If the astrophysical scenario can be well understood, free-free emission can be used to test dark matter properties via their effect on the HI power spectrum at small scales, or via synchrotron emission from annihilation products. Significantly enhanced HI mapping will inform our understanding of the dark matter distribution, and detections of fast radio bursts and pulsars could allow us to test current observations, quantum gravity or even string theory. Whether the dark matter is a WIMP, any other particle type, or can be explained by primordial black holes or modifications of gravity, the SKA has the capability to provide groundbreaking new insights into its nature.

In Chapter 1, I present a concise overview of *Planck* Collaboration cosmological results and of astrophysical studies based on *Planck* data in both temperature and polarization recently released. Diffuse astrophysical components (including Galactic emissions, cosmic far infrared background (CIB), y-maps of the thermal Sunyaev-Zeldovich (SZ) effect) and catalogs of many thousands of Galactic and extragalactic radio and far-IR sources, and galaxy clusters detected through the SZ effect are the main astrophysical products of the mission. I discuss the impact of systematics effects, the role of methods to separate the CMB signal from the astrophysical emissions and each different astrophysical component from the others.

I study the impact of the large-angle CMB polarization datasets publicly released by the WMAP and *Planck* satellites on the estimation of cosmological parameters of the ΛCDM model (187). To complement large-angle polarization, I consider the high resolution (or "high-ℓ") CMB datasets from either WMAP or *Planck* as well as CMB lensing as traced by *Planck*'s measured four point correlation function. In the case of WMAP, I compute the large-angle polarization likelihood starting over from low resolution frequency maps and their covariance

matrices, and perform foreground mitigation technique, which includes as a possible alternative *Planck* 353 GHz data to trace polarized dust. The latter choice induces a downward shift in the optical depth τ, roughly of order 2σ, robust to the choice of the complementary high resolution dataset. When the *Planck* 353 GHz is consistently used to minimize polarized dust emission, WMAP and *Planck* 70 GHz large-angle polarization data are in remarkable agreement: by combining them I find $\tau = 0.066^{+0.012}_{-0.013}$, again very stable against the particular choice for high-ℓ data. The amplitude of primordial fluctuations A_s, notoriously degenerate with τ, is the second parameter most affected by the assumptions on polarized dust removal, but the other parameters are also affected, typically between 0.5σ and 1σ. In particular, cleaning dust with *Planck*'s 353 GHz data imposes a 1σ downward shift in the value of the Hubble constant H_0, significantly contributing to the tension reported between CMB based and direct measurements of the present expansion rate. On the other hand, the appearance of the so-called low ℓ anomaly, a well-known tension between the high- and low-resolution CMB anisotropy amplitude, is not significantly affected by the details of large-angle polarization, or by the particular high-ℓ dataset employed.

In Chapter 2, I present high sensitivity ($\sigma_P \simeq 0.6$ mJy) polarimetric observations of a complete sample of 104 compact extragalactic radio sources brighter than 200 mJy at 20 GHz. The observations, carried out with the Australia Telescope Compact Array (ATCA), achieved a 90% detection rate (at 5σ) in polarization. I confirm previous findings in the $5-38$ GHz frequency range also extending the total intensity properties to 70 MHz by including GLEAM data and the polarization properties to 2 GHz with ATCA dedicated observations. The high sensitivity allow us to investigate polarization fractions dependence on frequency for different spectrally-selected populations, the circular polarization and the behaviour of the electron vector position angle (EVPA) with the frequency. I present source counts in polarization down to $\sim$ 1 mJy, hence extending by an order of magnitude the existing estimate. Polarization measurements in six bands between $5.5-38$ GHz, which correspond to the first set of observations described in the text, for 53 of these objects were reported by (132, 133). With ATCA new measurements in the same six bands for another 51 sources and measurements at 2.1 GHz for the full sample of 104 sources have been added. Also, the previous measurements at 18, 24, 33 and 38 GHz were re-calibrated using the updated model for the flux density absolute calibrator, PKS1934-638, not available for the earlier analysis. Among the sample, 89 sources have a counterpart in the 72 to 231 MHz GLEAM survey, providing an unparallel spectral coverage of 2.7 decades of frequency. While the total intensity data from 5.5 to 38 GHz could be interpreted in terms of

single component emission, a joint analysis of more extended total intensity spectra presented here, and of the polarization spectra, reveals that over 90% of our sources show clear indications of at least two emission components, interpreted as an evidence of recurrent activity. This high sensitivity polarimetry has allowed a $5\,\sigma$ detection of weak circular polarization for $\sim 38\%$ of the dataset.

In Chapter 3, I derive the median polarization fraction of extragalactic sources (radio-loud AGNs and dusty galaxies) analyzing *Planck* polarization maps with an original and dedicated implementation of the intensity distribution analysis (IDA) in order to mitigate or overcome the most critical aspects of earlier analyses. Remarkably, an insufficiently accurate characterization of the contamination of unresolved polarized extragalactic sources can seriously bias measurements of the primordial CMB power spectrum if the tensor-to-scalar ratio $r \sim 0.001$ which is predicted by current models of high interest (as Starobinsky's R^2 and Higgs inflation). The median polarization fraction, $\Pi_{\rm median}$, of extragalactic radio sources is found to be $\sim 2.75\%$, with no significant dependence on either frequency or flux density, in good agreement with the earlier estimate and with high-sensitivity measurements in the frequency range 5–40 GHz. No polarization signal is detected in the case of dusty galaxies, and 90% confidence upper limits of $\Pi_{\rm dusty} \lesssim 2.2\%$ at 353 GHz and of $\lesssim 3.8\%$ at 217 GHz are derived.

In Chapter 4, I first briefly describe the SKA facility, its precursors and pathfinders, giving a general overview of their technical performances and scientific goals. Then, I characterize the CMB free-free spectral distortion accounting for the amplification effect coming from clumping factor (327). Indeed, the density contrast of the Universe, parametrized in terms of the matter power spectrum and its variance, can amplify the signal of the free-free process in the plasma. The damping of fluctuations on scales smaller than the DM particle free streaming scale corresponds to a suppression of the total matter power spectrum on large wave numbers k. I derive the time evolution of the matter power spectrum variance for various cosmological models and parameters by numerically computing the power spectrum with a modified version of the Boltzmann code CAMB, for different values of the cut-off parameter k_{max}. Suitable analytical approximations of the numerical results are presented. The clumpiness, associated to the density contrast of the intergalactic medium, increases at decreasing redshift. The analysis is carried out for selected astrophysical and phenomenological cosmological reionization histories, for which I evaluate the impact of the clumping factor on the free-free distortion and discuss the wavelength dependence of the predicted signal. Finally, I address a comparison

with other classes of unavoidable CMB spectral distortions and future observational perspectives. While Comptonization from reionization is dominant at high frequencies, the free-free signal predicted in the considered models contributes to the distortion at a level of few (few tens) per cent at frequencies below $\sim$ 25 GHz ($\sim$ 10 GHz) and represents the main signature below $\sim$ 4 GHz. The cosmological signal from the HI 21-cm background is found to prevail over the free-free distortion in a restricted, model dependent frequency window between ~ 0.1 and $\sim$ 0.2 GHz. Through the comparison between with the confusion noise by extragalactic radio sources, the best frequencies to identify the free-free reionization signal are found to be around few GHz. When the astrophysical scenario will be well understood, free-free signatures could be used to test also DM properties through their effect on the power spectrum at small scales. Finally, I address the SKA contribution to the foregrounds analysis in the context of future CMB projects aimed at the detection of the primordial B-mode angular power spectrum.

In Chapter 5, I discuss the effects on the CMB, CIB and thermal SZ effect due to the observer peculiar motion with respect to the CMB rest frame, which induces boosting effects. After a brief review of the current observational and theoretical status, I investigate the scientific perspectives opened by future CMB space missions, focussing on the Cosmic Origins Explorer (CORE) proposal. The improvements in sensitivity offered by a mission like CORE, together with its high resolution over a wide frequency range, will provide a more accurate estimate of the CMB dipole (52). The extension of boosting effects to polarization and cross-correlations will enable a more robust determination of purely velocity-driven effects that are not degenerate with the intrinsic CMB dipole, allowing us to achieve an overall signal-to-noise ratio of 13; this improves on the *Planck* detection and essentially equals that of an ideal cosmic-variance-limited experiment up to a multipole $\ell \simeq 2000$. Precise inter-frequency calibration will offer the opportunity to constrain or even detect CMB spectral distortions, particularly from the cosmological reionization epoch, because of the frequency dependence of the dipole spectrum, without resorting to precise absolute calibration. The expected improvement with respect to COBE-FIRAS in the recovery of distortion parameters (which could in principle be a factor of several hundred for an ideal experiment with the CORE configuration) ranges from a factor of several up to about 50, depending on the quality of foreground removal and relative calibration. Even in the case of $\simeq$ 1 % accuracy in both foreground removal and relative calibration at an angular scale of 1°, I find that dipole analyses for a mission like CORE will be able to improve the recovery of the CIB spectrum amplitude by a factor $\simeq 17$ in comparison with current results

based on COBE-FIRAS. In addition to the scientific potential of a mission like CORE for these analyses, synergies with other planned and ongoing projects are also discussed.

References

[1] K. N. Abazajian, P. Adshead, Z. Ahmed, S. W. Allen, D. Alonso, K. S. Arnold, C. Baccigalupi, J. G. Bartlett, N. Battaglia, B. A. Benson, C. A. Bischoff, J. Borrill, V. Buza, E. Calabrese, R. Caldwell, J. E. Carlstrom, C. L. Chang, T. M. Crawford, F.-Y. Cyr-Racine, F. De Bernardis, T. de Haan, S. di Serego Alighieri, J. Dunkley, C. Dvorkin, J. Errard, G. Fabbian, S. Feeney, S. Ferraro, J. P. Filippini, R. Flauger, G. M. Fuller, V. Gluscevic, D. Green, D. Grin, E. Grohs, J. W. Henning, J. C. Hill, R. Hlozek, G. Holder, W. Holzapfel, W. Hu, K. M. Huffenberger, R. Keskitalo, L. Knox, A. Kosowsky, J. Kovac, E. D. Kovetz, C.-L. Kuo, A. Kusaka, M. Le Jeune, A. T. Lee, M. Lilley, M. Loverde, M. S. Madhavacheril, A. Mantz, D. J. E. Marsh, J. McMahon, P. D. Meerburg, J. Meyers, A. D. Miller, J. B. Munoz, H. N. Nguyen, M. D. Niemack, M. Peloso, J. Peloton, L. Pogosian, C. Pryke, M. Raveri, C. L. Reichardt, G. Rocha, A. Rotti, E. Schaan, M. M. Schmittfull, D. Scott, N. Sehgal, S. Shandera, B. D. Sherwin, T. L. Smith, L. Sorbo, G. D. Starkman, K. T. Story, A. van Engelen, J. D. Vieira, S. Watson, N. Whitehorn, and W. L. Kimmy Wu. **CMB-S4 Science Book, First Edition**. *ArXiv e-prints*, October 2016. 75, 76

[2] V. Acquaviva, N. Bartolo, S. Matarrese, and A. Riotto. **Gauge-invariant second-order perturbations and non-Gaussianity from inflation**. *Nuclear Physics B*, **667**:119–148, September 2003. 21

[3] J. Adams, B. Cresswell, and R. Easther. **Inflationary perturbations from a potential with a step**. *Phys. Rev. D*, **64**(12):123514, December 2001. 19

[4] G. E. Addison, Y. Huang, D. J. Watts, C. L. Bennett, M. Halpern, G. Hinshaw, and J. L. Weiland. **Quantifying Discordance in the 2015 Planck CMB Spectrum**. *ApJ*, **818**:132, February 2016. 23, 29

[5] P. A. R. Ade, Y. Akiba, A. E. Anthony, K. Arnold, M. Atlas, D. Barron, D. Boettger, J. Borrill, S. Chapman, Y. Chinone, M. Dobbs, T. Elleflot, J. Errard, G. Fabbian, C. Feng, D. Flanigan, A. Gilbert, W. Grainger, N. W. Halverson, M. Hasegawa, K. Hattori, M. Hazumi, W. L. Holzapfel, Y. Hori, J. Howard, P. Hyland, Y. Inoue, G. C. Jaehnig, A. Jaffe, B. Keating, Z. Kermish, R. Keskitalo, T. Kisner, M. Le Jeune, A. T. Lee, E. Linder, E. M. Leitch, M. Lungu, F. Matsuda, T. Matsumura, X. Meng, N. J. Miller, H. Morii, S. Moyerman, M. J. Myers, M. Navaroli, H. Nishino, H. Paar, J. Peloton, E. Quealy, G. Rebeiz, C. L. Reichardt, P. L. Richards, C. Ross, I. Schanning, D. E. Schenck, B. Sherwin, A. Shimizu, C. Shimmin, M. Shimon, P. Siritanasak, G. Smecher, H. Spieler, N. Stebor, B. Steinbach, R. Stompor, A. Suzuki, S. Takakura, T. Tomaru, B. Wilson, A. Yadav, O. Zahn, and Polarbear Collaboration. **Measurement of the Cosmic Microwave Background Polarization Lensing Power Spectrum with the POLARBEAR Experiment**. *Physical Review Letters*, **113**(2):021301, July 2014. 41

[6] I. Agudo, C. Thum, J. L. Gómez, and H. Wiesemeyer. **A simultaneous 3.5 and 1.3 mm polarimetric survey of active galactic nuclei in the northern sky**. *A&A*, **566**:A59, June 2014. xxviii, 62, 77, 81, 82, 83, 87, 92

[7] I. Agudo, C. Thum, V. Ramakrishnan, S. N. Molina, C. Casadio, and J. L. Gomez. **POLAMI: Polarimetric Monitoring of Active Galactic Nuclei at Millimetre Wavelengths. III. Characterisation of total flux density and polarisation variability of relativistic jets**. *ArXiv e-prints*, September 2017. 87, 92

[8] I. Agudo, C. Thum, H. Wiesemeyer, and T. P. Krichbaum. **A 3.5 mm Polarimetric Survey of Radio-loud Active Galactic Nuclei**. *ApJS*, **189**:1–14, July 2010. 62

[9] F. Aharonian, T. G. Arshakian, B. Allen, R. Banerjee, R. Beck, W. Becker, D. J. Bomans, D. Breitschwerdt, M. Brüggen, A. Brunthaler, B. Catinella, D. Champion, B. Ciardi, R. Crocker, M. A. de Avillez, R. J. Dettmar, D. Engels, T. Ensslin, H. Enke, T. Fieseler, L. Gizon, E. Hackmann, B. Hartmann, C. Henkel, M. Hoeft, L. Iapichino, D. Innes, C. James, J. Jasche, D. Jones, V. Kagramanova, G. Kauffmann, E. Keane, J. Kerp, H.-R. Klöckner, K. Kokkotas, M. Kramer, M. Krause, M. Krause, N. Krupp, J. Kunz, C. Lämmerzahl, K. J. Lee, M. List, K. Liu, A. Lobanov, G. Mann, A. Merloni, E. Middelberg, J. Niemeyer, A. Noutsos, V. Perlick, W. Reich, P. Richter, A. Roy, A. Saintonge, G. Schäfer, J. Schaffner-Bielich, E. Schinnerer, D. Schleicher, P. Schneider, D. J. Schwarz, A. Sedrakian, A. Sesana, V. Smolčić, S. Solanki, R. Tuffs, M. Vetter, E. Weber, J. Weller, N. Wex, O. Wucknitz, and M. Zwaan. **Pathway to the Square Kilometre Array - The German White Paper -**. *ArXiv e-prints*, January 2013. 102

[10] G. Aldazabal and A. M. Uranga. **Tachyon-free non-supersymmetric type IIB orientifolds via brane-antibrane systems**. *Journal of High Energy Physics*, **10**:024, October 1999. 18

[11] L. Amendola, R. Catena, I. Masina, A. Notari, M. Quartin, and C. Quercellini. **Measuring our peculiar velocity on the CMB with high-multipole off-diagonal correlations**. *J. Cosmology Astropart. Phys.*, **7**:027, July 2011. 118, 128, 129, 130, 133, 135

[12] P. André, C. Baccigalupi, A. Banday, D. Barbosa, B. Barreiro, J. Bartlett, N. Bartolo, E. Battistelli, R. Battye, G. Bendo, A. Benoît, J.-P. Bernard, M. Bersanelli, M. Béthermin, P. Bielewicz, A. Bonaldi, F. Bouchet, F. Boulanger, J. Brand, M. Bucher, C. Burigana, Z.-Y. Cai, P. Camus, F. Casas, V. Casasola, G. Castex, A. Challinor, J. Chluba, G. Chon, S. Colafrancesco, B. Comis, F. Cuttaia, G. D'Alessandro, A. Da Silva, R. Davis, M. de Avillez, P. de Bernardis, M. de Petris, A. de Rosa, G. de Zotti, J. Delabrouille, F.-X. Désert, C. Dickinson, J. M. Diego, J. Dunkley, T. Ensslin, J. Errard, E. Falgarone, P. Ferreira, K. Ferrière, F. Finelli, A. Fletcher, P. Fosalba, G. Fuller, S. Galli, K. Ganga, J. García-Bellido, A. Ghribi, M. Giard, Y. Giraud-Héraud, J. Gonzalez-Nuevo, K. Grainge, A. Gruppuso, A. Hall, J.-C. Hamilton, M. Haverkorn, C. Hernandez-Monteagudo, D. Herranz, M. Jackson, A. Jaffe, R. Khatri, M. Kunz, L. Lamagna, M. Lattanzi, P. Leahy, J. Lesgourgues, M. Liguori, E. Liuzzo, M. Lopez-Caniego, J. Macias-Perez, B. Maffei, D. Maino, A. Mangilli, E. Martinez-Gonzalez, C. J. A. P. Martins, S. Masi, M. Massardi, S. Matarrese, A. Melchiorri, J.-B. Melin, A. Mennella, A. Mignano, M.-A. Miville-Deschênes, A. Monfardini, A. Murphy, P. Naselsky, F. Nati, P. Natoli, M. Negrello, F. Noviello, C. O'Sullivan, F. Paci, L. Pagano, R. Paladino, N. Palanque-Delabrouille, D. Paoletti, H. Peiris, F. Perrotta, F. Piacentini, M. Piat, L. Piccirillo, G. Pisano, G. Polenta, A. Pollo, N. Ponthieu, M. Remazeilles, S. Ricciardi, M. Roman, C. Rosset, J.-A. Rubino-Martin, M. Salatino, A. Schillaci, P. Shellard, J. Silk, A. Starobinsky, R. Stompor, R. Sunyaev, A. Tartari, L. Terenzi, L. Toffolatti, M. Tomasi, N. Trappe, M. Tristram, T. Trombetti, M. Tucci, R. Van de Weijgaert, B. Van Tent, L. Verde, P. Vielva, B. Wandelt, R. Watson, and S. Withington. **PRISM (Polarized Radiation Imaging and Spectroscopy Mission): an extended white paper**. *J. Cosmology Astropart. Phys.*, **2**:006, February 2014. 30, 106, 113

[13] C. Angelantonj. **Comments on open-string orbifolds with a non-vanishing B_{ab}**. *Nuclear Physics B*, **566**:126–150, 2000. 18

[14] C. Angelantonj, I. Antoniadis, G. D'Appollonio, E. Dudas, and A. Sagnotti. **Type I vacua with brane supersymmetry breaking**. *Nuclear Physics B*, **572**:36–70, April 2000. 18

REFERENCES

[15] I. Antoniadis. **Brane supersymmetry breaking**. *Physics Letters B*, **464**:38–45, October 1999. 18

[16] H. Arkin and R.R. Colton. *Statistical Methods (College Outline)*. Barnes and Noble, fifth edition, 1970. xvii, 64

[17] D. Babich, P. Creminelli, and M. Zaldarriaga. **The shape of non-Gaussianities**. *J. Cosmology Astropart. Phys.*, **8**:009, August 2004. 20

[18] S. A. Balashev, E. E. Kholupenko, J. Chluba, A. V. Ivanchik, and D. A. Varshalovich. **Spectral Distortions of the CMB Dipole**. *ApJ*, **810**:131, September 2015. 105, 119, 138, 141

[19] D. Barbosa, S. Anton, L. Gurvits, and D. Maia. **The Square Kilometre Array: Paving the way for the new 21st century radio astronomy paradigm**. *Astrophysics and Space Science Proceedings*, **25**, 2012. 96

[20] X. Barcons, A. Franceschini, G. de Zotti, L. Danese, and T. Miyaji. **Hard X-Ray Emission from Extragalactic IRAS 12 Micron Sources: Constraints on the Unified Active Galactic Nucleus Model and the Synthesis of the X-Ray Background**. *ApJ*, **455**:480, December 1995. 79

[21] R. B. Barreiro, P. Vielva, C. Hernandez-Monteagudo, and E. Martinez-Gonzalez. **A Linear Filter to Reconstruct the ISW Effect From CMB and LSS Observations**. *IEEE Journal of Selected Topics in Signal Processing*, **2**:747–754, November 2008. 14

[22] J. G. Bartlett and J. Silk. **A Comptonization model for the submillimeter background**. *ApJ*, **353**:399–405, April 1990. 141

[23] J. G. Bartlett and A. Stebbins. **Did the universe recombine?** *ApJ*, **371**:8–13, April 1991. 106

[24] N. Bartolo, E. Komatsu, S. Matarrese, and A. Riotto. **Non-Gaussianity from inflation: theory and observations**. *Phys. Rep.*, **402**:103–266, November 2004. 20

[25] S. Basilakos and M. Plionis. **The PSCz dipole revisited**. *MNRAS*, **373**:1112–1116, December 2006. 118

[26] R. A. Battye, I. W. A. Browne, M. W. Peel, N. J. Jackson, and C. Dickinson. **Statistical properties of polarized radio sources at high frequency and their impact on cosmic microwave background polarization measurements**. *MNRAS*, **413**:132–148, May 2011. 62, 87

[27] D. Baumann and L. McAllister. **A microscopic limit on gravitational waves from D-brane inflation**. *Phys. Rev. D*, **75**(12):123508, June 2007. 76

[28] A. J. Beasley, R. Murowinski, and M. Tarenghi. **The Atacama Large Millimeter/Submillimeter Array: overview and status**. In *Society of Photo-Optical Instrumentation Engineers (SPIE) Conference Series*, **6267** of *Proc. SPIE*, page 626702, June 2006. 43

[29] N. Benitez, R. Dupke, M. Moles, L. Sodre, J. Cenarro, A. Marin-Franch, K. Taylor, D. Cristobal, A. Fernandez-Soto, C. Mendes de Oliveira, J. Cepa-Nogue, L. R. Abramo, J. S. Alcaniz, R. Overzier, C. Hernandez-Monteagudo, E. J. Alfaro, A. Kanaan, J. M. Carvano, R. R. R. Reis, E. Martinez Gonzalez, B. Ascaso, F. Ballesteros, H. S. Xavier, J. Varela, A. Ederoclite, H. Vazquez Ramio, T. Broadhurst, E. Cypriano, R. Angulo, J. M. Diego, A. Zandivarez, E. Diaz, P. Melchior, K. Umetsu, P. F. Spinelli, A. Zitrin, D. Coe, G. Yepes, P. Vielva, V. Sahni, A. Marcos-Caballero, F. Shu Kitaura, A. L. Maroto, M. Masip, S. Tsujikawa, S. Carneiro, J. Gonzalez Nuevo, G. C. Carvalho, M. J. Reboucas, J. C. Carvalho, E. Abdalla, A. Bernui, C. Pigozzo, E. G. M. Ferreira, N. Chandrachani Devi, C. A. P. Bengaly, Jr., M. Campista, A. Amorim, N. V. Asari, A. Bongiovanni, S. Bonoli, G. Bruzual, N. Cardiel, A. Cava, R. Cid Fernandes, P. Coelho, A. Cortesi, R. G. Delgado, L. Diaz Garcia, J. M. R. Espinosa, E. Galliano, J. I. Gonzalez-Serrano, J. Falcon-Barroso, J. Fritz, C. Fernandes, J. Gorgas, C. Hoyos, Y. Jimenez-Teja, J. A. Lopez-Aguerri, C. Lopez-San Juan, A. Mateus, A. Molino, P. Novais, A. OMill, I. Oteo, P. G. Perez-Gonzalez, B. Poggianti, R. Proctor, E. Ricciardelli, P. Sanchez-Blazquez, T. Storchi-Bergmann, E. Telles, W. Schoennell, N. Trujillo, A. Vazdekis, K. Viironen, S. Daflon, T. Aparicio-Villegas, D. Rocha, T. Ribeiro, M. Borges, S. L. Martins, W. Marcolino, D. Martinez-Delgado, M. A. Perez-Torres, B. B. Siffert, M. O. Calvao, M. Sako, R. Kessler, A. Alvarez-Candal, M. De Pra, F. Roig, D. Lazzaro, J. Gorosabel, R. Lopes de Oliveira, G. B. Lima-Neto, J. Irwin, J. F. Liu, E. Alvarez, I. Balmes, S. Chueca, M. V. Costa-Duarte, A. A. da Costa, M. L. L. Dantas, A. Y. Diaz, J. Fabregat, F. Ferrari, B. Gavela, S. G. Gracia, N. Gruel, J. L. L. Gutierrez, R. Guzman, J. D. Hernandez-Fernandez, D. Herranz, L. Hurtado-Gil, F. Jablonsky, R. Laporte, L. L. Le Tiran, J Licandro, M. Lima, E. Martin, V. Martinez, J. J. C. Montero, P. Penteado, C. B. Pereira, V. Peris, V. Quilis, M. Sanchez-Portal, A. C. Soja, E. Solano, J. Torra, and L. Valdivielso. **J-PAS: The Javalambre-Physics of the Accelerated Universe Astrophysical Survey**. *ArXiv e-prints*, March 2014. 14

[30] C. L. Bennett, D. Larson, J. L. Weiland, N. Jarosik, G. Hinshaw, N. Odegard, K. M. Smith, R. S. Hill, B. Gold, M. Halpern, E. Komatsu, M. R. Nolta, L. Page, D. N. Spergel, E. Wollack, J. Dunkley, A. Kogut, M. Limon, S. S. Meyer, G. S. Tucker, and E. L. Wright. **Nine-year Wilkinson Microwave Anisotropy Probe (WMAP) Observations: Final Maps and Results**. *ApJS*, **208**:20, October 2013. 10, 24, 25

[31] J. Bernstein and S. Dodelson. **Aspects of the Zel'dovich-Sunyaev mechanism**. *Phys. Rev. D*, **41**:354–373, January 1990. 118

[32] A. Bernui, T. Villela, C. A. Wuensche, R. Leonardi, and I. Ferreira. **On the cosmic microwave background large-scale angular correlations**. *A&A*, **454**:409–414, August 2006. 17

[33] P. N. Best and t. LOFAR-UK Consortium. **LOFAR-UK White Paper: A Science case for UK involvement in LOFAR**. *ArXiv e-prints*, February 2008. 103

[34] M. Béthermin, E. Daddi, G. Magdis, M. T. Sargent, Y. Hezaveh, D. Elbaz, D. Le Borgne, J. Mullaney, M. Pannella, V. Buat, V. Charmandaris, G. Lagache, and D. Scott. **A Unified Empirical Model for Infrared Galaxy Counts Based on the Observed Physical Evolution of Distant Galaxies**. *ApJ*, **757**:L23, October 2012. xxv, 7

[35] BICEP2 Collaboration and Keck Array Collaboration. **Improved Constraints on Cosmology and Foregrounds from BICEP2 and Keck Array Cosmic Microwave Background Data with Inclusion of 95 GHz Band**. *Physical Review Letters*, **116**(3):031302, January 2016. 75

[36] BICEP2/Keck Collaboration, Planck Collaboration, P. A. R. Ade, N. Aghanim, Z. Ahmed, R. W. Aikin, K. D. Alexander, M. Arnaud, J. Aumont, C. Baccigalupi, and et al. **Joint Analysis of BICEP2/Keck Array and Planck Data**. *Physical Review Letters*, **114**(10):101301, March 2015. 11, 12, 115

[37] M. Bilicki, M. Chodorowski, T. Jarrett, and G. A. Mamon. **Is the Two Micron All Sky Survey Clustering Dipole Convergent?** *ApJ*, **741**:31, November 2011. 118

[38] T. Biswas, A. Mazumdar, and A. Shafieloo. **Wiggles in the cosmic microwave background radiation: Echoes from nonsingular cyclic inflation**. *Phys. Rev. D*, **82**(12):123517, December 2010. 19

[39] C. Blake and J. Wall. **A velocity dipole in the distribution of radio galaxies**. *Nature*, **416**:150–152, March 2002. 119

[40] R. D. Blandford and A. Königl. **Relativistic jets as compact radio sources**. *ApJ*, **232**:34–48, August 1979. 47

[41] N. W. Boggess, J. C. Mather, R. Weiss, C. L. Bennett, E. S. Cheng, E. Dwek, S. Gulkis, M. G. Hauser, M. A. Janssen, T. Kelsall, S. S. Meyer, S. H. Moseley, T. L. Murdock, R. A. Shafer, R. F. Silverberg, G. F. Smoot, D. T. Wilkinson, and E. L. Wright. **The COBE mission - Its design and performance two years after launch**. *ApJ*, **397**:420–429, October 1992. 119

[42] K. Bolejko, M. A. Nazer, and D. L. Wiltshire. **Differential cosmic expansion and the Hubble flow anisotropy**. *J. Cosmology Astropart. Phys.*, **6**:035, June 2016. 118

[43] L. Bonavera, J. González-Nuevo, F. Argüeso, and L. Toffolatti. **Statistics of the fractional polarization of compact radio sources in Planck maps**. *MNRAS*, **469**:2401–2411, August 2017. 75, 77, 78, 88, 92

[44] L. Bonavera, J. González-Nuevo, B. De Marco, F. Argüeso, and L. Toffolatti. **Statistics of the fractional polarization of extragalactic dusty sources in Planck HFI maps**. *MNRAS*, **472**:628–635, November 2017. 75, 77, 79, 88, 91, 93

[45] L. Bonavera, M. Massardi, A. Bonaldi, J. González-Nuevo, G. de Zotti, and R. D. Ekers. **The Planck-ATCA Coeval Observations project: the faint sample**. *MNRAS*, **416**:559–566, September 2011. 49, 58, 71

[46] S. Boughn and R. Crittenden. **A correlation between the cosmic microwave background and large-scale structure in the Universe**. *Nature*, **427**:45–47, January 2004. 13

[47] D. Boyanovsky, H. J. de Vega, and N. G. Sanchez. **Constraints on dark matter particles from theory, galaxy observations, and N-body simulations**. *Phys. Rev. D*, **77**(4):043518, February 2008. 107

[48] E. Branchini and M. Plionis. **Reconstructing Positions and Peculiar Velocities of Galaxy Clusters within 25,000 Kilometers per Second: The Cluster Real Space Dipole**. *ApJ*, **460**:569, April 1996. 118

[49] M. Bucher, B. van Tent, and C. S. Carvalho. **Detecting bispectral acoustic oscillations from inflation using a new flexible estimator**. *MNRAS*, **407**:2193–2206, October 2010. 21

[50] C. Burigana, P. Alexander, C. Baccigalupi, D. S. Barbosa, A. Blanchard, A. De Rosa, G. De Zotti, F. Finelli, A. Gruppuso, M. Jones, S. Matarrese, A. Melchiorri, D. Molinari, M. Negrello, D. Paoletti, F. Perrotta, R. Scaramella, and T. Trombetti. **SKA synergy with Microwave Background studies**. *Advancing Astrophysics with the Square Kilometre Array (AASKA14)*, page 149, April 2015. 112, 114

[51] C. Burigana, E. S. Battistelli, M. Benetti, G. Cabass, P. de Bernardis, S. di Serego Alighieri, E. di Valentino, M. Gerbino, E. Giusarma, A. Gruppuso, M. Liguori, S. Masi, H. U. Norgaard-Nielsen, P. Rosati, L. Salvati, T. Trombetti, and P. Vielva. **Recent results and perspectives on cosmology and fundamental physics from microwave surveys**. *International Journal of Modern Physics D*, **25**:1630016, April 2016. xiv, 14, 18, 19

[52] C. Burigana, C. S. Carvalho, T. Trombetti, A. Notari, M. Quartin, G. De Gasperis, A. Buzzelli, N. Vittorio, G. De Zotti, P. de Bernardis, J. Chluba, M. Bilicki, L. Danese, J. Delabrouille, L. Toffolatti, A. Lapi, M. Negrello, P. Mazzotta, D. Scott, D. Contreras, A. Achucarro, P. Ade, R. Allison, M. Ashdown, M. Ballardini, A. J. Banday, R. Banerji, J. Bartlett, N. Bartolo, S. Basak, M. Bersanelli, A. Bonaldi, M. Bonato, J. Borrill, F. Bouchet, F. Boulanger, T. Brinckmann, M. Bucher, P. Cabella, Z.-Y. Cai, M. Calvo, G. Castellano, A. Challinor, S. Clesse, I. Colantoni, A. Coppolecchia, M. Crook, G. D'Alessandro, J.-M. Diego, A. Di Marco, E. Di Valentino, J. Errard, S. Feeney, R. Fernandez-Cobos, S. Ferraro, F. Finelli, F. Forastieri, S. Galli, R. Genova-Santos, M. Gerbino, J. Gonzalez-Nuevo, S. Grandis, J. Greenslade, S. Hagstotz, S. Hanany, W. Handley, C. Hernandez-Monteagudo, C. Hervias-Caimapo, M. Hills, E. Hivon, K. Kiiveri, T. Kisner, T. Kitching, M. Kunz, H. Kurki-Suonio, L. Lamagna, A. Lasenby, M. Lattanzi, J. Lesgourgues, M. Liguori, V. Lindholm, M. Lopez-Caniego, G. Luzzi, B. Maffei, N. Mandolesi, E. Martinez-Gonzalez, C. J. A. P. Martins, S. Masi, D. McCarthy, A. Melchiorri, J.-B. Melin, D. Molinari, A. Monfardini, P. Natoli, A. Paiella, D. Paoletti, G. Patanchon, M. Piat, G. Pisano, L. Polastri, G. Polenta, A. Pollo, V. Poulin, M. Remazeilles, M. Roman, J.-A. Rubino-Martin, L. Salvati, A. Tartari, M. Tomasi, D. Tramonte, N. Trappe, C. Tucker, J. Valiviita, R. Van de Weijgaert, B. van Tent, V. Vennin, P. Vielva, K. Young, M. Zannoni, and for the CORE Collaboration. **Exploring cosmic origins with CORE: effects of observer peculiar motion**. *ArXiv e-prints*, April 2017. 120, 185

[53] C. Burigana, G. de Zotti, and L. Danese. **Analytical description of spectral distortions of the cosmic microwave background**. *A&A*, **303**:323, November 1995. 140

[54] C. Burigana, L. A. Popa, R. Salvaterra, R. Schneider, T. R. Choudhury, and A. Ferrara. **Cosmic microwave background polarization constraints on radiative feedback**. *MNRAS*, **385**:404–410, March 2008. 118, 140

[55] S. Burles and S. Rappaport. **Detecting the Aberration of the Cosmic Microwave Background**. *ApJ*, **641**:L1–L4, April 2006. 118, 128

[56] G. Cabass, M. Gerbino, E. Giusarma, A. Melchiorri, L. Pagano, and L. Salvati. **Constraints on the early and late integrated Sachs-Wolfe effects from the Planck 2015 cosmic microwave background anisotropies in the angular power spectra**. *Phys. Rev. D*, **92**(6):063534, September 2015. xiv, 15, 16

[57] Z.-Y. Cai, A. Lapi, J.-Q. Xia, G. De Zotti, M. Negrello, C. Gruppioni, E. Rigby, G. Castex, J. Delabrouille, and L. Danese. **A Hybrid Model for the Evolution of Galaxies and Active Galactic Nuclei in the Infrared**. *ApJ*, **768**:21, May 2013. 91, 133

[58] J. R. Callingham, B. M. Gaensler, R. D. Ekers, S. J. Tingay, R. B. Wayth, J. Morgan, G. Bernardi, M. E. Bell, R. Bhat, J. D. Bowman, F. Briggs, R. J. Cappallo, A. A. Deshpande, A. Ewall-Wice, L. Feng, L. J. Greenhill, B. J. Hazelton, L. Hindson, N. Hurley-Walker, D. C. Jacobs, M. Johnston-Hollitt, D. L. Kaplan, N. Kudryavtseva, E. Lenc, C. J. Lonsdale, B. McKinley, S. R. McWhirter, D. A. Mitchell, M. F. Morales, E. Morgan, D. Oberoi, A. R. Offringa, S. M. Ord, B. Pindor, T. Prabu, P. Procopio, J. Riding, K. S. Srivani, R. Subrahmanyan, N. Udaya Shankar, R. L. Webster, A. Williams, and C. L. Williams. **Broadband Spectral Modeling of the Extreme Gigahertz-peaked Spectrum Radio Source PKS B0008-421**. *ApJ*, **809**:168, August 2015. 62

[59] S. Capozziello, V. F. Cardone, E. Elizalde, S. Nojiri, and S. D. Odintsov. **Observational constraints on dark energy with generalized equations of state**. *Phys. Rev. D*, **73**(4):043512, February 2006. 100

[60] B. J. Carr, K. Kohri, Y. Sendouda, and J. Yokoyama. **New cosmological constraints on primordial black holes**. *Phys. Rev. D*, **81**(10):104019, May 2010. 141

[61] A. Challinor and F. van Leeuwen. **Peculiar velocity effects in high-resolution microwave background experiments**. *Phys. Rev. D*, **65**(10):103001, May 2002. 118, 128, 129, 130, 131, 133

[62] X. Chen. **Primordial Non-Gaussianities from Inflation Models**. *Advances in Astronomy*, **2010**:638979, 2010. 20

[63] X. Chen, M.-x. Huang, S. Kachru, and G. Shiu. **Observational signatures and non-Gaussianities of general single-field inflation**. *J. Cosmology Astropart. Phys.*, **1**:002, January 2007. 21

[64] C. Cheung, A. L. Fitzpatrick, J. Kaplan, L. Senatore, and P. Creminelli. **The effective field theory of inflation**. *Journal of High Energy Physics*, **3**:014–014, March 2008. 21

REFERENCES

[65] J. Chluba. **Aberrating the CMB sky: fast and accurate computation of the aberration kernel**. *Mon. Not. Roy. Astron. Soc.*, **415**:3227, 2011. 129, 130

[66] J. Chluba. **Distinguishing different scenarios of early energy release with spectral distortions of the cosmic microwave background**. *MNRAS*, **436**:2232–2243, December 2013. 141

[67] J. Chluba, A. L. Erickcek, and I. Ben-Dayan. **Probing the Inflaton: Small-scale Power Spectrum Constraints from Measurements of the Cosmic Microwave Background Energy Spectrum**. *ApJ*, **758**:76, October 2012. 139

[68] J. Chluba, G. Hütsi, and R. A. Sunyaev. **Clusters of galaxies in the microwave band: Influence of the motion of the Solar System**. *A&A*, **434**:811–817, May 2005. 118, 132

[69] J. Chluba, R. Khatri, and R. A. Sunyaev. **CMB at 2×2 order: the dissipation of primordial acoustic waves and the observable part of the associated energy release**. *MNRAS*, **425**:1129–1169, September 2012. 138

[70] J. Chluba and R. A. Sunyaev. **Superposition of blackbodies and the dipole anisotropy: A possibility to calibrate CMB experiments**. *A&A*, **424**:389–408, September 2004. 129, 131

[71] J. Chluba and R. A. Sunyaev. **The evolution of CMB spectral distortions in the early Universe**. *MNRAS*, **419**:1294–1314, January 2012. 139

[72] J. Cho and A. Lazarian. **Magnetohydrodynamic Turbulence as a Foreground for Cosmic Microwave Background Studies**. *ApJ*, **575**:L63–L66, August 2002. 114

[73] S. K. Choi and L. A. Page. **Polarized galactic synchrotron and dust emission and their correlation**. *J. Cosmology Astropart. Phys.*, **12**:020, December 2015. 75

[74] T. R. Choudhury and A. Ferrara. **Updating reionization scenarios after recent data**. *MNRAS*, **371**:L55–L59, September 2006. 109

[75] J. J. Condon, W. D. Cotton, E. B. Fomalont, K. I. Kellermann, N. Miller, R. A. Perley, D. Scott, T. Vernstrom, and J. V. Wall. **Resolving the Radio Source Background: Deeper Understanding through Confusion**. *ApJ*, **758**:23, October 2012. 111, 114

[76] C. J. Copi, D. Huterer, D. J. Schwarz, and G. D. Starkman. **Uncorrelated universe: Statistical anisotropy and the vanishing angular correlation function in WMAP years 1 3**. *Phys. Rev. D*, **75**(2):023507, January 2007. 17

[77] C. J. Copi, D. Huterer, D. J. Schwarz, and G. D. Starkman. **No large-angle correlations on the non-Galactic microwave sky**. *MNRAS*, **399**:295–303, October 2009. 17

[78] C. J. Copi, D. Huterer, D. J. Schwarz, and G. D. Starkman. **Large-Angle Anomalies in the CMB**. *Advances in Astronomy*, **2010**:847541, 2010. 17

[79] C. J. Copi, D. Huterer, D. J. Schwarz, and G. D. Starkman. **Lack of large-angle TT correlations persists in WMAP and Planck**. *MNRAS*, **451**:2978–2985, August 2015. 17

[80] S. Corder and P. Cox. **Atacama large millimeter/submillimeter array: progress, status, and development**. In *Ground-based and Airborne Telescopes V*, **9145** of *Proc. SPIE*, page 91451V, July 2014. 42

[81] CORE Collaboration, F. Finelli, M. Bucher, A. Achúcarro, M. Ballardini, N. Bartolo, D. Baumann, S. Clesse, J. Errard, W. Handley, M. Hindmarsh, K. Kiiveri, M. Kunz, A. Lasenby, M. Liguori, D. Paoletti, C. Ringeval, J. Väliviita, B. van Tent, V. Vennin, R. Allison, F. Arroja, M. Ashdown, A. J. Banday, R. Banerji, J. G. Bartlett, S. Basak, J. Baselmans, P. de Bernardis, M. Bersanelli, A. Bonaldi, J. Borril, F. R. Bouchet, F. Boulanger, T. Brinckmann, C. Burigana, A. Buzzelli, Z.-Y. Cai, M. Calvo, C. S. Carvalho, G. Castellano, A. Challinor, J. Chluba, I. Colantoni, M. Crook, G. D'Alessandro, G. D'Amico, J. Delabrouille, V. Desjacques, G. De Zotti, J. M. Diego, E. Di Valentino, S. Feeney, J. R. Fergusson, R. Fernandez-Cobos, S. Ferraro, F. Forastieri, S. Galli, J. García-Bellido, G. de Gasperis, R. T. Génova-Santos, M. Gerbino, J. González-Nuevo, S. Grandis, J. Greenslade, S. Hagstotz, S. Hanany, D. K. Hazra, C. Hernández-Monteagudo, C. Hervias-Caimapo, M. Hills, E. Hivon, B. Hu, T. Kisner, T. Kitching, E. D. Kovetz, H. Kurki-Suonio, L. Lamagna, M. Lattanzi, J. Lesgourgues, A. Lewis, V. Lindholm, J. Lizarraga, M. López-Caniego, G. Luzzi, B. Maffei, N. Mandolesi, E. Martínez-González, C. J. A. P. Martins, S. Masi, D. McCarthy, S. Matarrese, A. Melchiorri, J.-B. Melin, D. Molinari, A. Monfardini, P. Natoli, M. Negrello, A. Notari, F. Oppizzi, A. Paiella, E. Pajer, G. Patanchon, S. P. Patil, M. Piat, G. Pisano, L. Polastri, G. Polenta, A. Pollo, V. Poulin, M. Quartin, A. Ravenni, M. Remazeilles, A. Renzi, D. Roest, M. Roman, J. A. Rubiño-Martin, L. Salvati, A. A. Starobinsky, A. Tartari, G. Tasinato, M. Tomasi, J. Torrado, N. Trappe, T. Trombetti, C. Tucker, M. Tucci, J. Urrestilla, R. van de Weygaert, P. Vielva, N. Vittorio, and K. Young. **Exploring Cosmic Origins with CORE: Inflation**. *ArXiv e-prints*, December 2016. 76, 113

[82] S. Courteau and S. van den Bergh. **The Solar Motion Relative to the Local Group**. *AJ*, **118**:337–345, July 1999. 118

[83] R. G. Crittenden and N. Turok. **Looking for a Cosmological Constant with the Rees-Sciama Effect**. *Physical Review Letters*, **76**:575–578, January 1996. 12, 13

[84] A. Curto, M. Tucci, J. González-Nuevo, L. Toffolatti, E. Martínez-González, F. Argüeso, A. Lapi, and M. López-Caniego. **Forecasts on the contamination induced by unresolved point sources in primordial non-Gaussianity beyond Planck**. *MNRAS*, **432**:728–742, June 2013. 91

[85] L. Dai and J. Chluba. **New operator approach to the CMB aberration kernels in harmonic space**. *Phys. Rev. D*, **89**(12):123504, June 2014. 129, 130, 131

[86] R. A. Daly. **Spectral distortions of the microwave background radiation resulting from the damping of pressure waves**. *ApJ*, **371**:14–28, April 1991. 138

[87] L. Danese and C. Burigana. **Theoretical Aspects of the CMB Spectrum**. In J. L. Sanz, E. Martinez-Gonzalez, and L. Cayon, editors, *Present and Future of the Cosmic Microwave Background*, **429** of *Lecture Notes in Physics, Berlin Springer Verlag*, page 28, 1994. 141

[88] L. Danese and G. de Zotti. **The relic radiation spectrum and the thermal history of the Universe**. *Nuovo Cimento Rivista Serie*, **7**:277–362, September 1977. 1

[89] L. Danese and G. de Zotti. **A statistical analysis of the data on the microwave background radiation spectrum**. *A&A*, **68**:157–164, August 1978. 1

[90] L. Danese and G. de Zotti. **On distortions in the Rayleigh-Jeans region of the cosmic background radiation spectrum**. *A&A*, **84**:364, April 1980. 140

[91] L. Danese and G. de Zotti. **Dipole anisotropy and distortions of the spectrum of the cosmic microwave background**. *A&A*, **94**:L33, February 1981. 105, 119, 138, 141

[92] L. Danese and G. de Zotti. **Double Compton process and the spectrum of the microwave background**. *A&A*, **107**:39–42, March 1982. 1

[93] U. H. Danielsson. **Note on inflation and trans-Planckian physics**. *Phys. Rev. D*, **66**(2):023511, July 2002. 19

[94] S. Das, T. Louis, M. R. Nolta, G. E. Addison, E. S. Battistelli, J. R. Bond, E. Calabrese, D. Crichton, M. J. Devlin, S. Dicker, J. Dunkley, R. Dünner, J. W. Fowler, M. Gralla, A. Hajian, M. Halpern, M. Hasselfield, M. Hilton, A. D. Hincks, R. Hlozek, K. M. Huffenberger, J. P. Hughes, K. D. Irwin, A. Kosowsky, R. H. Lupton, T. A. Marriage, D. Marsden, F. Menanteau, K. Moodley, M. D. Niemack, L. A. Page, B. Partridge, E. D. Reese, B. L. Schmitt, N. Sehgal, B. D. Sherwin, J. L. Sievers, D. N. Spergel, S. T. Staggs, D. S. Swetz, E. R. Switzer, R. Thornton, H. Trac, and E. Wollack. **The Atacama Cosmology Telescope: temperature and gravitational lensing power spectrum measurements from three seasons of data**. *J. Cosmology Astropart. Phys.*, **4**:014, April 2014. 12

[95] P. de Bernardis, P. A. R. Ade, J. J. A. Baselmans, E. S. Battistelli, A. Benoit, M. Bersanelli, A. Bideaud, M. Calvo, F. J. Casas, G. Castellano, A. Catalano, I. Charles, I. Colantoni, F. Columbro, A. Coppolecchia, M. Crook, G. D'Alessandro, M. De Petris, J. Delabrouille, S. Doyle, C. Franceschet, A. Gomez, J. Goupy, S. Hanany, M. Hills, L. Lamagna, J. Macias-Perez, B. Maffei, S. Martin, E. Martinez-Gonzalez, S. Masi, D. McCarthy, A. Mennella, A. Monfardini, F. Noviello, A. Paiella, F. Piacentini, M. Piat, G. Pisano, G. Signorelli, C. Y. Tan, A. Tartari, N. Trappe, S. Triqueneaux, C. Tucker, G. Vermeulen, K. Young, M. Zannoni, A. Achúcarro, R. Allison, M. Ashdown, M. Ballardini, A. J. Banday, R. Banerji, J. Bartlett, N. Bartolo, S. Basak, A. Bonaldi, M. Bonato, J. Borrill, F. Bouchet, F. Boulanger, T. Brinckmann, M. Bucher, C. Burigana, A. Buzzelli, Z. Y. Cai, C. S. Carvalho, A. Challinor, J. Chluba, S. Clesse, G. De Gasperis, G. De Zotti, E. Di Valentino, J. M. Diego, J. Errard, S. Feeney, R. Fernandez-Cobos, F. Finelli, F. Forastieri, S. Galli, R. Génova-Santos, M. Gerbino, J. González-Nuevo, S. Hagstotz, J. Greenslade, W. Handley, C. Hernández-Monteagudo, C. Hervias-Caimapo, E. Hivon, K. Kiiveri, T. Kisner, T. Kitching, M. Kunz, H. Kurki-Suonio, A. Lasenby, M. Lattanzi, J. Lesgourgues, A. Lewis, M. Liguori, V. Lindholm, G. Luzzi, C. J. A. P. Martins, A. Melchiorri, J. B. Melin, D. Molinari, P. Natoli, M. Negrello, A. Notari, D. Paoletti, G. Patanchon, L. Polastri, G. Polenta, A. Pollo, V. Poulin, M. Quartin, M. Remazeilles, M. Roman, J. A. Rubiño-Martín, L. Salvati, M. Tomasi, D. Tramonte, T. Trombetti, J. Väliviita, R. Van de Weijgaert, B. van Tent, V. Vennin, P. Vielva, N. Vittorio, and for the CORE collaboration. **Exploring Cosmic Origins with CORE: The Instrument**. *ArXiv e-prints*, May 2017. 37

[96] P. de Bernardis, P. A. R. Ade, J. J. Bock, J. R. Bond, J. Borrill, A. Boscaleri, K. Coble, B. P. Crill, G. De Gasperis, P. C. Farese, P. G. Ferreira, K. Ganga, M. Giacometti, E. Hivon, V. V. Hristov, A. Iacoangeli, A. H. Jaffe, A. E. Lange, L. Martinis, S. Masi, P. V. Mason, P. D. Mauskopf, A. Melchiorri, L. Miglio, T. Montroy, C. B. Netterfield, E. Pascale, F. Piacentini, D. Pogosyan, S. Prunet, S. Rao, G. Romeo, J. E. Ruhl, F. Scaramuzzi, D. Sforna, and N. Vittorio. **A flat Universe from high-resolution maps of the cosmic microwave background radiation**. *Nature*, **404**:955–959, April 2000. 100

[97] P. De Bernardis, M. Bucher, C. Burigana, and L. Piccirillo. **B-Pol: detecting primordial gravitational waves generated during inflation**. *Experimental Astronomy*, **23**:5–16, March 2009. 29

[98] G. De Zotti, G. Castex, J. González-Nuevo, M. Lopez-Caniego, M. Negrello, Z.-Y. Cai, M. Clemens, J. Delabrouille, D. Herranz, L. Bonavera, J.-B. Melin, M. Tucci, S. Serjeant, M. Bilicki, P. Andreani, D. L. Clements, L. Toffolatti, and B. F. Roukema. **Extragalactic sources in Cosmic Microwave Background maps**. *J. Cosmology Astropart. Phys.*, **6**:018, June 2015. 76

[99] G. De Zotti, L. Danese, A. Franceschini, M. Persic, and L. Toffolatti. **Contributions of discrete sources to the X ray background**. In J. Hunt and B. Battrick, editors, *Two Topics in X-Ray Astronomy, Volume 1: X Ray Binaries. Volume 2: AGN and the X Ray Background*, **296** of *ESA Special Publication*, November 1989. 79

[100] G. De Zotti, J. Gonzalez-Nuevo, M. Lopez-Caniego, M. Negrello, J. Greenslade, C. Hernandez-Monteagudo, J. Delabrouille, Z.-Y. Cai, M. Bonato, A. Achucarro, P. Ade, R. Allison, M. Ashdown, M. Ballardini, A. J. Banday, R. Banerji, J. G. Bartlett, N. Bartolo, S. Basak, M. Bersanelli, M. Biesiada, M. Bilicki, A. Bonaldi, J. Borrill, F. Bouchet, F. Boulanger, T. Brinckmann, M. Bucher, C. Burigana, A. Buzzelli, M. Calvo, C. S. Carvalho, M. G. Castellano, A. Challinor, J. Chluba, D. L. Clements, S. Clesse, S. Colafrancesco, I. Colantoni, A. Coppolecchia, M. Crook, G. D'Alessandro, P. de Bernardis, G. de Gasperis, J. M. Diego, E. Di Valentino, J. Errard, S. M. Feeney, R. Fernandez-Cobos, S. Ferraro, F. Finelli, F. Forastieri, S. Galli, R. T. Genova-Santos, M. Gerbino, S. Grandis, S. Hagstotz, S. Hanany, W. Handley, C. Hervias-Caimapo, M. Hills, E. Hivon, K. Kiiveri, T. Kisner, T. Kitching, M. Kunz, H. Kurki-Suonio, G. Lagache, L. Lamagna, A. Lasenby, M. Lattanzi, A. Le Brun, J. Lesgourgues, A. Lewis, M. Liguori, V. Lindholm, G. Luzzi, B. Maffei, N. Mandolesi, E. Martinez-Gonzalez, C. J. A. P. Martins, S. Masi, M. Massardi, D. McCarthy, A. Melchiorri, J.-B. Melin, D. Molinari, A. Monfardini, P. Natoli, A. Notari, A. Paiella, D. Paoletti, R. B. Partridge, G. Patanchon, M. Piat, G. Pisano, L. Polastri, G. Polenta, A. Pollo, V. Poulin, M. Quartin, M. Remazeilles, M. Roman, G. Rossi, B. F. Roukema, J.-A. Rubino-Martin, L. Salvati, D. Scott, S. Serjeant, A. Tartari, L. Toffolatti, M. Tomasi, N. Trappe, S. Triqueneaux, T. Trombetti, M. Tucci, C. Tucker, J. Valiviita, R. van de Weygaert, B. Van Tent, V. Vennin, P. Vielva, N. Vittorio, K. Young, and for the CORE collaboration. **Exploring Cosmic Origins with CORE: Extragalactic sources in Cosmic Microwave Background maps**. *ArXiv e-prints*, September 2016. 37, 76, 77, 91, 113, 133

[101] G. De Zotti, M. Negrello, G. Castex, A. Lapi, and M. Bonato. **Another look at distortions of the Cosmic Microwave Background spectrum**. *J. Cosmology Astropart. Phys.*, **3**:047, March 2016. 119

[102] G. de Zotti, R. Ricci, D. Mesa, L. Silva, P. Mazzotta, L. Toffolatti, and J. González-Nuevo. **Predictions for high-frequency radio surveys of extragalactic sources**. *A&A*, **431**:893–903, March 2005. xxvii, 67, 70, 89

[103] J. Delabrouille, M. Betoule, J.-B. Melin, M.-A. Miville-Deschênes, J. Gonzalez-Nuevo, M. Le Jeune, G. Castex, G. de Zotti, S. Basak, M. Ashdown, J. Aumont, C. Baccigalupi, A. J. Banday, J.-P. Bernard, F. R. Bouchet, D. L. Clements, A. da Silva, C. Dickinson, F. Dodu, K. Dolag, F. Elsner, L. Fauvet, G. Faÿ, G. Giardino, S. Leach, J. Lesgourgues, M. Liguori, J. F. Macías-Pérez, M. Massardi, S. Matarrese, P. Mazzotta, L. Montier, S. Mottet, R. Paladini, B. Partridge, R. Piffaretti, G. Prezeau, S. Prunet, S. Ricciardi, M. Roman, B. Schaefer, and L. Toffolatti. **The pre-launch Planck Sky Model: a model of sky emission at submillimetre to centimetre wavelengths**. *A&A*, **553**:A96, May 2013. 89

[104] J. Delabrouille, P. de Bernardis, F. R. Bouchet, A. Achúcarro, P. A. R. Ade, R. Allison, F. Arroja, E. Artal, M. Ashdown, C. Baccigalupi, M. Ballardini, A. J. Banday, R. Banerji, D. Barbosa, J. Bartlett, N. Bartolo, S. Basak, J. J. A. Baselmans, K. Basu, E. S. Battistelli, R. Battye, D. Baumann, A. Benoît, M. Bersanelli, A. Bideaud, M. Biesiada, M. Bilicki, A. Bonaldi, M. Bonato, J. Borrill, F. Boulanger, T. Brinckmann, M. L. Brown, M. Bucher, C. Burigana, A. Buzzelli, G. Cabass, Z.-Y. Cai, M. Calvo, A. Caputo, C.-S. Carvalho, F. J. Casas, G. Castellano, A. Catalano, A. Challinor, I. Charles, J. Chluba, D. L. Clements, S. Clesse, S. Colafrancesco, I. Colantoni, D. Contreras, A. Coppolecchia, M. Crook, G. D'Alessandro, G. D'Amico, A. da Silva, M. de Avillez, G. de Gasperis, M. De Petris, G. de Zotti, L. Danese, F.-X. Désert, V. Desjacques, E. Di Valentino, C. Dickinson, J. M. Diego, S. Doyle, R. Durrer, C. Dvorkin, H.-K. Eriksen, J. Errard, S. Feeney, R. Fernández-Cobos, F. Finelli, F. Forastieri, C. Franceschet, U. Fuskeland, S. Galli, R. T. Génova-Santos, M. Gerbino, E. Giusarma, A. Gomez, J. González-Nuevo, S. Grandis, J. Greenslade, J. Goupy, S. Hagstotz,

REFERENCES

S. Hanany, W. Handley, S. Henrot-Versillé, C. Hernández-Monteagudo, C. Hervias-Caimapo, M. Hills, M. Hindmarsh, E. Hivon, D. T. Hoang, D. C. Hooper, B. Hu, E. Keihänen, R. Keskitalo, K. Kiiveri, T. Kisner, T. Kitching, M. Kunz, H. Kurki-Suonio, G. Lagache, L. Lamagna, A. Lapi, A. Lasenby, M. Lattanzi, A. M. C. Le Brun, J. Lesgourgues, M. Liguori, V. Lindholm, J. Lizarraga, G. Luzzi, J. F. Macías-Pérez, B. Maffei, N. Mandolesi, S. Martin, E. Martinez-Gonzalez, C. J. A. P. Martins, S. Masi, M. Massardi, S. Matarrese, P. Mazzotta, D. McCarthy, A. Melchiorri, J.-B. Melin, A. Mennella, J. Mohr, D. Molinari, A. Monfardini, L. Montier, P. Natoli, M. Negrello, A. Notari, F. Noviello, F. Oppizzi, C. O'Sullivan, L. Pagano, A. Paiella, E. Pajer, D. Paoletti, S. Paradiso, R. B. Partridge, G. Patanchon, S. P. Patil, O. Perdereau, F. Piacentini, M. Piat, G. Pisano, L. Polastri, G. Polenta, A. Pollo, N. Ponthieu, V. Poulin, D. Prêle, M. Quartin, A. Ravenni, M. Remazeilles, A. Renzi, C. Ringeval, D. Roest, M. Roman, B. F. Roukema, J.-A. Rubino-Martin, L. Salvati, D. Scott, S. Serjeant, G. Signorelli, A. A. Starobinsky, R. Sunyaev, C. Y. Tan, A. Tartari, G. Tasinato, L. Toffolatti, M. Tomasi, J. Torrado, D. Tramonte, N. Trappe, S. Triqueneaux, M. Tristram, T. Trombetti, M. Tucci, C. Tucker, J. Urrestilla, J. Väliviita, R. Van de Weygaert, B. Van Tent, V. Vennin, L. Verde, G. Vermeulen, P. Vielva, N. Vittorio, F. Voisin, C. Wallis, B. Wandelt, I. Wehus, J. Weller, K. Young, M. Zannoni, and for the CORE collaboration. **Exploring Cosmic Origins with CORE: Survey requirements and mission design**. *ArXiv e-prints*, June 2017. 37, 75, 76

[105] J. Delabrouille, P. de Bernardis, F. R. Bouchet, and the CORE Collaboration. **CORE – The Cosmic Origins Explorer**. *A proposal in response to the ESA call for a Medium Size space mission for launch in 2029-2030*, 2016. 37, 152

[106] E. Dudas, N. Kitazawa, S. P. Patil, and A. Sagnotti. **CMB imprints of a pre-inflationary climbing phase**. *J. Cosmology Astropart. Phys.*, **5**:012, May 2012. 17

[107] E. Dudas, N. Kitazawa, and A. Sagnotti. **On climbing scalars in String Theory**. *Physics Letters B*, **694**:80–88, October 2010. 17, 18

[108] G. Efstathiou, Y.-Z. Ma, and D. Hanson. **Large-angle correlations in the cosmic microwave background**. *MNRAS*, **407**:2530–2542, October 2010. 17

[109] G. Efstathiou, W. J. Sutherland, and S. J. Maddox. **The cosmological constant and cold dark matter**. *Nature*, **348**:705–707, December 1990. 1

[110] D. Ejlli and A. D. Dolgov. **CMB constraints on mass and coupling constant of light pseudoscalar particles**. *Phys. Rev. D*, **90**(6):063514, September 2014. 141

[111] G. F. R. Ellis and J. E. Baldwin. **On the expected anisotropy of radio source counts**. *MNRAS*, **206**:377–381, January 1984. 118, 119

[112] P. Erdoğdu, J. P. Huchra, O. Lahav, M. Colless, R. M. Cutri, E. Falco, T. George, T. Jarrett, D. H. Jones, C. S. Kochanek, L. Macri, J. Mader, N. Martimbeau, M. Pahre, Q. Parker, A. Rassat, and W. Saunders. **The dipole anisotropy of the 2 Micron All-Sky Redshift Survey**. *MNRAS*, **368**:1515–1526, June 2006. 118

[113] A. L. Erickcek, S. M. Carroll, and M. Kamionkowski. **Superhorizon perturbations and the cosmic microwave background**. *Phys. Rev. D*, **78**(8):083012, October 2008. 128

[114] H. K. Eriksen, J. B. Jewell, C. Dickinson, A. J. Banday, K. M. Górski, and C. R. Lawrence. **Joint Bayesian Component Separation and CMB Power Spectrum Estimation**. *ApJ*, **676**:10–32, March 2008. 24

[115] H. K. Eriksen, I. J. O'Dwyer, J. B. Jewell, B. D. Wandelt, D. L. Larson, K. M. Górski, S. Levin, A. J. Banday, and P. B. Lilje. **Power Spectrum Estimation from High-Resolution Maps by Gibbs Sampling**. *ApJS*, **155**:227–241, December 2004. 24

[116] R. Fabbri. **Spectrum of the Sunyaev-Zel'dovich effect for high electron temperatures**. *Ap&SS*, **77**:529–537, July 1981. 132

[117] J. S. Farnes, B. M. Gaensler, and E. Carretti. **VizieR Online Data Catalog: Polarized NVSS sources SEDs (Farnes+, 2014)**. *VizieR Online Data Catalog*, **221**, May 2014. 60

[118] L. Fauvet, J. F. Macías-Pérez, J. Aumont, F. X. Désert, T. R. Jaffe, A. J. Banday, M. Tristram, A. H. Waelkens, and D. Santos. **Joint 3D modelling of the polarized Galactic synchrotron and thermal dust foreground diffuse emission**. *A&A*, **526**:A145, February 2011. 114

[119] L. Fauvet, J. F. Macías-Pérez, and F. X. Désert. **Model of the polarized foreground diffuse Galactic emissions from 33 to 353 GHz**. *Astroparticle Physics*, **36**:57–63, August 2012. 114

[120] J. R. Fergusson, M. Liguori, and E. P. S. Shellard. **General CMB and primordial bispectrum estimation: Mode expansion, map making, and measures of F_{NL}**. *Phys. Rev. D*, **82**(2):023502, July 2010. 21

[121] J. R. Fergusson, M. Liguori, and E. P. S. Shellard. **The CMB bispectrum**. *J. Cosmology Astropart. Phys.*, **12**:032, December 2012. 21

[122] D. J. Fixsen. **The Temperature of the Cosmic Microwave Background**. *ApJ*, **707**:916–920, December 2009. 105, 121

[123] D. J. Fixsen, E. S. Cheng, J. M. Gales, J. C. Mather, R. A. Shafer, and E. L. Wright. **The Cosmic Microwave Background Spectrum from the Full COBE FIRAS Data Set**. *ApJ*, **473**:576, December 1996. 119, 139, 140

[124] D. J. Fixsen, E. Dwek, John C. Mather, C. L. Bennett, and R. A. Shafer. **The Spectrum of the extragalactic far infrared background from the COBE FIRAS observations**. *Astrophys. J.*, **508**:123, 1998. xxi, xxii, 119, 132, 141, 142, 147

[125] D. J. Fixsen and A. Kashlinsky. **Probing the Universe's Tilt with the Cosmic Infrared Background Dipole**. *ApJ*, **734**:61, June 2011. 118, 142

[126] D. J. Fixsen and J. C. Mather. **The Spectral Results of the Far-Infrared Absolute Spectrophotometer Instrument on COBE**. *ApJ*, **581**:817–822, December 2002. 106

[127] R. Flauger, L. McAllister, E. Pajer, A. Westphal, and G. Xu. **Oscillations in the CMB from axion monodromy inflation**. *J. Cosmology Astropart. Phys.*, **6**:009, June 2010. 19

[128] M. A. Forman. **The Compton-Getting effect for cosmic-ray particles and photons and the Lorentz-invariance of distribution functions**. *Planet. Space Sci.*, **18**:25–31, January 1970. 138

[129] M. Frommert and T. A. Ensslin. **Ironing out primordial temperature fluctuations with polarization: optimal detection of cosmic structure imprints**. *MNRAS*, **395**:1837–1844, June 2009. 14

[130] S. R. Furlanetto, S. P. Oh, and F. H. Briggs. **Cosmology at low frequencies: The 21 cm transition and the high-redshift Universe**. *Phys. Rep.*, **433**:181–301, October 2006. 99

[131] V. Galluzzi and M. Massardi. **The polarimetric multi-frequency radio sources properties**. *International Journal of Modern Physics D*, **25**:1640005, March 2016. 76

[132] V. Galluzzi, M. Massardi, A. Bonaldi, V. Casasola, L. Gregorini, T. Trombetti, C. Burigana, M. Bonato, G. De Zotti, R. Ricci, J. Stevens, R. D. Ekers, L. Bonavera, S. di Serego Alighieri, E. Liuzzo, M. Lopez-Caniego, R. Paladino, L. Toffolatti, M. Tucci, and J. R. Callingham. **Characterization of polarimetric and total intensity behaviour of a complete sample of PACO radio sources in the radio bands**. *ArXiv e-prints*, November 2017. 50, 183

[133] V. Galluzzi, M. Massardi, A. Bonaldi, V. Casasola, L. Gregorini, T. Trombetti, C. Burigana, G. De Zotti, R. Ricci, J. Stevens, R. D. Ekers, L. Bonavera, S. di Serego Alighieri, E. Liuzzo, M. López-Caniego, A. Mignano, R. Paladino, L. Toffolatti, and M. Tucci. **Multifrequency polarimetry of a complete sample of PACO radio sources**. *MNRAS*, **465**:4085–4098, March 2017. 58, 77, 78, 87, 183

[134] V. Galluzzi, M. Massardi, and A. et al. Bonaldi. **Characterization of polarimetric and total intensity behaviour of a complete sample of PACO radio sources in the radio bands**. MNRAS, submitted, 2017. 77, 78, 87, 92

[135] L. Gao and T. Theuns. **Lighting the Universe with Filaments**. *Science*, **317**:1527, September 2007. 108

[136] C. García-García, A. L. Maroto, and P. Martín-Moruno. **Cosmology with moving bimetric fluids**. *J. Cosmology Astropart. Phys.*, **12**:022, December 2016. 118

[137] E. M. George, C. L. Reichardt, K. A. Aird, B. A. Benson, L. E. Bleem, J. E. Carlstrom, C. L. Chang, H.-M. Cho, T. M. Crawford, A. T. Crites, T. de Haan, M. A. Dobbs, J. Dudley, N. W. Halverson, N. L. Harrington, G. P. Holder, W. L. Holzapfel, Z. Hou, J. D. Hrubes, R. Keisler, L. Knox, A. T. Lee, E. M. Leitch, M. Lueker, D. Luong-Van, J. J. McMahon, J. Mehl, S. S. Meyer, M. Millea, L. M. Mocanu, J. J. Mohr, T. E. Montroy, S. Padin, T. Plagge, C. Pryke, J. E. Ruhl, K. K. Schaffer, L. Shaw, E. Shirokoff, H. G. Spieler, Z. Staniszewski, A. A. Stark, K. T. Story, A. van Engelen, K. Vanderlinde, J. D. Vieira, R. Williamson, and O. Zahn. **A Measurement of Secondary Cosmic Microwave Background Anisotropies from the 2500 Square-degree SPT-SZ Survey**. *ApJ*, **799**:177, February 2015. 12

[138] M. Gervasi, M. Zannoni, A. Tartari, G. Boella, and G. Sironi. **TRIS. II. Search for CMB Spectral Distortions at 0.60, 0.82, and 2.5 GHz**. *ApJ*, **688**:24–31, November 2008. 119

[139] T. Giannantonio, C. Porciani, J. Carron, A. Amara, and A. Pillepich. **Constraining primordial non-Gaussianity with future galaxy surveys**. *MNRAS*, **422**:2854–2877, June 2012. 101

[140] C. Gibelyou and D. Huterer. **Dipoles in the sky**. *MNRAS*, **427**:1994–2021, December 2012. 118, 119

[141] N. Y. Gnedin. **Effect of Reionization on Structure Formation in the Universe**. *ApJ*, **542**:535–541, October 2000. 27

[142] N. Y. Gnedin and X. Fan. **Cosmic Reionization Redux**. *ApJ*, **648**:1–6, September 2006. 109

[143] K. M. Górski, E. Hivon, A. J. Banday, B. D. Wandelt, F. K. Hansen, M. Reinecke, and M. Bartelmann. **HEALPix: A Framework for High-Resolution Discretization and Fast Analysis of Data Distributed on the Sphere**. *ApJ*, **622**:759–771, April 2005. 80, 122

[144] K.M. Gorski, Eric Hivon, A.J. Banday, B.D. Wandelt, F.K. Hansen, et al. **HEALPix - A Framework for high resolution discretization, and fast analysis of data distributed on the sphere**. *Astrophys.J.*, **622**:759–771, 2005. 24

[145] F. Govoni, M. Murgia, H. Xu, H. Li, M. L. Norman, L. Feretti, G. Giovannini, and V. Vacca. **Polarization of cluster radio halos with upcoming radio interferometers**. *A&A*, **554**:A102, June 2013. 102

[146] B. R. Granett, M. C. Neyrinck, and I. Szapudi. **An Imprint of Superstructures on the Microwave Background due to the Integrated Sachs-Wolfe Effect**. *ApJ*, **683**:L99, August 2008. 14

[147] J. K. Grant, A. R. Taylor, J. M. Stil, T. L. Landecker, R. Kothes, R. R. Ransom, and D. Scott. **The DRAO Planck Deep Fields: The Polarization Properties of Radio Galaxies at 1.4 GHz**. *ApJ*, **714**:1689–1701, May 2010. 49

[148] J. S. Greaves and W. S. Holland. **Submillimetre polarization of M82 and the Galactic Center: Implications for CMB polarimetry**. In S. Cecchini, S. Cortiglioni, R. Sault, and C. Sbarra, editors, *Astrophysical Polarized Backgrounds*, **609** of *American Institute of Physics Conference Series*, pages 267–270, March 2002. 77

[149] A. Gruppuso. **Two-point correlation function of Wilkinson Microwave Anisotropy Probe 9-yr data**. *MNRAS*, **437**:2076–2082, January 2014. 17

[150] A. Gruppuso, N. Kitazawa, N. Mandolesi, P. Natoli, and A. Sagnotti. **Pre-inflationary relics in the CMB?** *Physics of the Dark Universe*, **11**:68–73, March 2016. 17

[151] A. Gruppuso, P. Natoli, F. Paci, F. Finelli, D. Molinari, A. De Rosa, and N. Mandolesi. **Low variance at large scales of WMAP 9 year data**. *J. Cosmology Astropart. Phys.*, **7**:047, July 2013. 17

[152] A. Gruppuso and A. Sagnotti. **Observational hints of a pre-inflationary scale?** *International Journal of Modern Physics D*, **24**:1544008–469, September 2015. 17

[153] C. A. Hales, R. P. Norris, B. M. Gaensler, and E. Middelberg. **ATLAS 1.4 GHz data release 2 - II. Properties of the faint polarized sky**. *MNRAS*, **440**:3113–3139, June 2014. 49, 78

[154] D. Hanson, S. Hoover, A. Crites, P. A. R. Ade, K. A. Aird, J. E. Austermann, J. A. Beall, A. N. Bender, B. A. Benson, L. E. Bleem, J. J. Bock, J. E. Carlstrom, C. L. Chang, H. C. Chiang, H.-M. Cho, A. Conley, T. M. Crawford, T. de Haan, M. A. Dobbs, W. Everett, J. Gallicchio, J. Gao, E. M. George, N. W. Halverson, N. Harrington, J. W. Henning, G. C. Hilton, G. P. Holder, W. L. Holzapfel, J. D. Hrubes, N. Huang, J. Hubmayr, K. D. Irwin, R. Keisler, L. Knox, A. T. Lee, E. Leitch, D. Li, C. Liang, D. Luong-Van, G. Marsden, J. J. McMahon, J. Mehl, S. S. Meyer, L. Mocanu, T. E. Montroy, T. Natoli, J. P. Nibarger, V. Novosad, S. Padin, C. Pryke, C. L. Reichardt, J. E. Ruhl, B. R. Saliwanchik, J. T. Sayre, K. K. Schaffer, B. Schulz, G. Smecher, A. A. Stark, K. T. Story, C. Tucker, K. Vanderlinde, J. D. Vieira, M. P. Viero, G. Wang, V. Yefremenko, O. Zahn, and M. Zemcov. **Detection of B-Mode Polarization in the Cosmic Microwave Background with Data from the South Pole Telescope**. *Physical Review Letters*, **111**(14):141301, October 2013. 41

[155] R. T. Harmon, O. Lahav, and E. J. A. Meurs. **The dipole anisotropy of a new, colour-selected, IRAS galaxy sample**. *MNRAS*, **228**:5P–10P, September 1987. 118

[156] C. G. T. Haslam, C. J. Salter, H. Stoffel, and W. E. Wilson. **A 408 MHz all-sky continuum survey. II - The atlas of contour maps**. *A&AS*, **47**:1, January 1982. 24, 115

[157] W.K. Hastings. **Monte Carlo samping methods using Markov chains and their applications**. *Biometrika*, **57**:97–109, 1970. 122

[158] J. C. Hill, N. Battaglia, J. Chluba, S. Ferraro, E. Schaan, and D. N. Spergel. **Taking the Universe's Temperature with Spectral Distortions of the Cosmic Microwave Background**. *Physical Review Letters*, **115**(26):261301, December 2015. 140

[159] G. Hinshaw, A. J. Branday, C. L. Bennett, K. M. Gorski, A. Kogut, C. H. Lineweaver, G. F. Smoot, and E. L. Wright. **Two-Point Correlations in the COBE DMR Four-Year Anisotropy Maps**. *ApJ*, **464**:L25, June 1996. 17

[160] G. Hinshaw, D. Larson, E. Komatsu, D. N. Spergel, C. L. Bennett, J. Dunkley, M. R. Nolta, M. Halpern, R. S. Hill, N. Odegard, L. Page, K. M. Smith, J. L. Weiland, B. Gold, N. Jarosik, A. Kogut, M. Limon, S. S. Meyer, G. S. Tucker, E. Wollack, and E. L. Wright. **Nine-year Wilkinson Microwave Anisotropy Probe (WMAP) Observations: Cosmological Parameter Results**. *ApJS*, **208**:19, October 2013. 17, 22

REFERENCES

[161] W. Hu. **Dark synergy: Gravitational lensing and the CMB**. *Phys. Rev. D*, **65**(2):023003, January 2002. 12

[162] W. Hu, D. Scott, and J. Silk. **Power spectrum constraints from spectral distortions in the cosmic microwave background**. *ApJ*, **430**:L5–L8, July 1994. 138

[163] W. Hu and J. Silk. **Thermalization constraints and spectral distortions for massive unstable relic particles**. *Physical Review Letters*, **70**:2661–2664, May 1993. 141

[164] W. Hu and M. White. **A CMB polarization primer**. *New A*, **2**:323–344, October 1997. 2

[165] N. Hurley-Walker, J. R. Callingham, P. J. Hancock, T. M. O. Franzen, L. Hindson, A. D. Kapińska, J. Morgan, A. R. Offringa, R. B. Wayth, C. Wu, Q. Zheng, T. Murphy, M. E. Bell, K. S. Dwarakanath, B. For, B. M. Gaensler, M. Johnston-Hollitt, E. Lenc, P. Procopio, L. Staveley-Smith, R. Ekers, J. D. Bowman, F. Briggs, R. J. Cappallo, A. A. Deshpande, L. Greenhill, B. J. Hazelton, D. L. Kaplan, C. J. Lonsdale, S. R. McWhirter, D. A. Mitchell, M. F. Morales, E. Morgan, D. Oberoi, S. M. Ord, T. Prabu, N. U. Shankar, K. S. Srivani, R. Subrahmanyan, S. J. Tingay, R. L. Webster, A. Williams, and C. L. Williams. **GaLactic and Extragalactic All-sky Murchison Widefield Array (GLEAM) survey - I. A low-frequency extragalactic catalogue**. *MNRAS*, **464**:1146–1167, January 2017. 49

[166] H. Ishino, Y. Akiba, K. Arnold, D. Barron, J. Borrill, R. Chendra, Y. Chinone, S. Cho, A. Cukierman, et al. **LiteBIRD: lite satellite for the study of B-mode polarization and inflation from cosmic microwave background radiation detection**. In *Society of Photo-Optical Instrumentation Engineers (SPIE) Conference Series*, **9904** of *Proc. SPIE*, page 99040X, July 2016. 113, 118, 134

[167] N. Jackson, I. W. A. Browne, R. A. Battye, D. Gabuzda, and A. C. Taylor. **High-frequency radio polarization measurements of WMAP point sources**. *MNRAS*, **401**:1388–1398, January 2010. xxviii, 77, 81, 82, 83

[168] M. Jarvis, D. Bacon, C. Blake, M. Brown, S. Lindsay, A. Raccanelli, M. Santos, and D. J. Schwarz. **Cosmology with SKA Radio Continuum Surveys**. *Advancing Astrophysics with the Square Kilometre Array (AASKA14)*, page 18, April 2015. 96

[169] K. Jedamzik, V. Katalinić, and A. V. Olinto. **Limit on Primordial Small-Scale Magnetic Fields from Cosmic Microwave Background Distortions**. *Physical Review Letters*, **85**:700–703, July 2000. 141

[170] D. Jeong, J. Chluba, L. Dai, M. Kamionkowski, and X. Wang. **Effect of aberration on partial-sky measurements of the cosmic microwave background temperature power spectrum**. *Phys. Rev. D*, **89**(2):023003, January 2014. 133

[171] S. Johnston, M. Bailes, N. Bartel, C. Baugh, M. Bietenholz, C. Blake, R. Braun, J. Brown, S. Chatterjee, J. Darling, A. Deller, R. Dodson, P. G. Edwards, R. Ekers, S. Ellingsen, I. Feain, B. M. Gaensler, M. Haverkorn, G. Hobbs, A. Hopkins, C. Jackson, C. James, G. Joncas, V. Kaspi, V. Kilborn, B. Koribalski, R. Kothes, T. L. Landecker, E. Lenc, J. Lovell, J.-P. Macquart, R. Manchester, D. Matthews, N. M. McClure-Griffiths, R. Norris, U.-L. Pen, C. Phillips, C. Power, R. Protheroe, E. Sadler, B. Schmidt, I. Stairs, L. Staveley-Smith, J. Stil, R. Taylor, S. Tingay, A. Tzioumis, M. Walker, J. Wall, and M. Wolleben. **Science with the Australian Square Kilometre Array Pathfinder**. *PASA*, **24**:174–188, December 2007. 45

[172] M. Johnston-Hollitt and R. D. Ekers. **Faraday Rotation Measures through the Cores of Southern Galaxy Clusters**. *ArXiv Astrophysics e-prints*, November 2004. 65, 66

[173] M. Kamionkowski. **Matter-microwave correlations in an open universe**. *Phys. Rev. D*, **54**:4169–4170, September 1996. 12

[174] M. Kamionkowski and L. Knox. **Aspects of the cosmic microwave background dipole**. *Phys. Rev. D*, **67**(6):063001, March 2003. 129, 131

[175] R. C. Keenan, A. J. Barger, and L. L. Cowie. **Evidence for a ˜300 Megaparsec Scale Under-density in the Local Galaxy Distribution**. *ApJ*, **775**:62, September 2013. 120

[176] N. Kitazawa and A. Sagnotti. **Pre-inflationary clues from String Theory?** *J. Cosmology Astropart. Phys.*, **4**:017, April 2014. 17

[177] N. Kitazawa and A. Sagnotti. **A string-inspired model for the low-ell CMB**. *Modern Physics Letters A*, **30**:1550137, July 2015. 17

[178] A. Kogut. **Diffuse Microwave Emission Survey**. *ArXiv Astrophysics e-prints*, July 1996. 106

[179] A. Kogut, J. Chluba, D. J. Fixsen, S. Meyer, and D. Spergel. **The Primordial Inflation Explorer (PIXIE)**. In *Society of Photo-Optical Instrumentation Engineers (SPIE) Conference Series*, **9904** of *Proc. SPIE*, page 99040W, July 2016. 75

[180] A. Kogut, D. J. Fixsen, D. T. Chuss, J. Dotson, E. Dwek, M. Halpern, G. F. Hinshaw, S. M. Meyer, S. H. Moseley, M. D. Seiffert, D. N. Spergel, and E. J. Wollack. **The Primordial Inflation Explorer (PIXIE): a nulling polarimeter for cosmic microwave background observations**. *J. Cosmology Astropart. Phys.*, **7**:025, July 2011. 106, 125, 163

[181] A. J. Kogut, D. T. Chuss, J. L. Dotson, E. Dwek, D. J. Fixsen, M. Halpern, G. F. Hinshaw, S. Meyer, S. H. Moseley, M. D. Seiffert, D. N. Spergel, and E. Wollack. **The Primordial Inflation Explorer (PIXIE)**. In *American Astronomical Society Meeting Abstracts #223*, **223** of *American Astronomical Society Meeting Abstracts*, page 439.01, January 2014. 34

[182] A. J. Kogut, D. T. Chuss, J. L. Dotson, D. J. Fixsen, M. Halpern, G. F. Hinshaw, S. M. Meyer, S. H. Moseley, M. D. Seiffert, D. N. Spergel, and E. J. Wollack. **The Primordial Inflation Explorer (PIXIE) Mission**. In *Space Telescopes and Instrumentation 2010: Optical, Infrared, and Millimeter Wave*, **7731** of *Proc. SPIE*, page 77311S, July 2010. 33

[183] E. Komatsu, D. N. Spergel, and B. D. Wandelt. **Measuring Primordial Non-Gaussianity in the Cosmic Microwave Background**. *ApJ*, **634**:14–19, November 2005. 21

[184] A. Kosowsky and T. Kahniashvili. **Signature of Local Motion in the Microwave Sky**. *Physical Review Letters*, **106**(19):191301, May 2011. 118, 128, 129, 130

[185] N. Krachmalnicoff, C. Baccigalupi, J. Aumont, M. Bersanelli, and A. Mennella. **Characterization of foreground emission on degree angular scales for CMB B-mode observations. Thermal dust and synchrotron signal from Planck and WMAP data**. *A&A*, **588**:A65, April 2016. 75

[186] L. La Porta, C. Burigana, W. Reich, and P. Reich. **The impact of Galactic synchrotron emission on CMB anisotropy measurements. I. Angular power spectrum analysis of total intensity all-sky surveys**. *A&A*, **479**:641–654, March 2008. 115

[187] M. Lattanzi, C. Burigana, M. Gerbino, A. Gruppuso, N. Mandolesi, P. Natoli, G. Polenta, L. Salvati, and T. Trombetti. **On the impact of large angle CMB polarization data on cosmological parameters**. *J. Cosmology Astropart. Phys.*, **2**:041, February 2017. 23, 182

[188] R. Laureijs, J. Amiaux, S. Arduini, J. . Augueres, J. Brinchmann, R. Cole, M. Cropper, C. Dabin, L. Duvet, A. Ealet, and et al. **Euclid Definition Study Report**. *ArXiv e-prints*, October 2011. 14

[189] A. Lewis and S. Bridle. **Cosmological parameters from CMB and other data: A Monte Carlo approach**. *Phys. Rev. D*, **66**(10):103511, November 2002. 15, 122

[190] H. Li and J.-Q. Xia. **Constraints on dark energy parameters from correlations of CMB with LSS**. *J. Cosmology Astropart. Phys.*, **4**:026, April 2010. 13

[191] M. López-Caniego, M. Massardi, J. González-Nuevo, L. Lanz, D. Herranz, G. De Zotti, J. L. Sanz, and F. Argüeso. **Polarization of the WMAP Point Sources**. *ApJ*, **705**:868–876, November 2009. 76

[192] T. Louis, E. Grace, M. Hasselfield, M. Lungu, L. Maurin, G. E. Addison, P. A. R. Ade, S. Aiola, R. Allison, et al. **The Atacama Cosmology Telescope: Two-Season ACTPol Spectra and Parameters**. *ArXiv e-prints*, October 2016. 133

[193] LSST Dark Energy Science Collaboration. **Large Synoptic Survey Telescope: Dark Energy Science Collaboration**. *ArXiv e-prints*, November 2012. 14

[194] D. H. Lyth. **What Would We Learn by Detecting a Gravitational Wave Signal in the Cosmic Microwave Background Anisotropy?** *Physical Review Letters*, **78**:1861–1863, March 1997. 76

[195] Y. E. Lyubarsky and R. A. Sunyaev. **The spectral features in the microwave background spectrum due to energy release in the early universe**. *A&A*, **123**:171–183, July 1983. 1

[196] R. Maartens, F. B. Abdalla, M. Jarvis, and M. G. Santos. **Overview of Cosmology with the SKA**. *Advancing Astrophysics with the Square Kilometre Array (AASKA14)*, page 16, April 2015. 96

[197] J. Maldacena. **Non-gaussian features of primordial fluctuations in single field inflationary models**. *Journal of High Energy Physics*, **5**:013, May 2003. 21

[198] A. H. Maller, D. H. McIntosh, N. Katz, and M. D. Weinberg. **The Clustering Dipole of the Local Universe from the Two Micron All Sky Survey**. *ApJ*, **598**:L1–L5, November 2003. 118

[199] J. Martin, C. Ringeval, and V. Vennin. **Encyclopædia Inflationaris**. *Physics of the Dark Universe*, **5**:75–235, December 2014. 76

[200] E. Martinez-Gonzalez, J. L. Sanz, and J. Silk. **Anisotropies in the microwave sky due to nonlinear structures**. *ApJ*, **355**:L5–L9, May 1990. 12

[201] M. Massardi, A. Bonaldi, L. Bonavera, G. De Zotti, M. Lopez-Caniego, and V. Galluzzi. **The Planck-ATCA Co-eval Observations project: analysis of radio source properties between 5 and 217 GHz**. *MNRAS*, **455**:3249–3262, January 2016. 49

[202] M. Massardi, S. G. Burke-Spolaor, T. Murphy, R. Ricci, M. López-Caniego, M. Negrello, R. Chhetri, G. De Zotti, R. D. Ekers, R. B. Partridge, and E. M. Sadler. **A polarization survey of bright extragalactic AT20G sources**. *MNRAS*, **436**:2915–2928, December 2013. xvii, 48, 68, 71

[203] M. Massardi, R. D. Ekers, T. Murphy, R. Ricci, E. M. Sadler, S. Burke, G. de Zotti, P. G. Edwards, P. J. Hancock, C. A. Jackson, M. J. Kesteven, E. Mahony, C. J. Phillips, L. Staveley-Smith, R. Subrahmanyan, M. A. Walker, and W. E. Wilson. **The Australia Telescope 20-GHz (AT20G) Survey: the Bright Source Sample**. *MNRAS*, **384**:775–802, February 2008. 51

[204] M. Massardi, V. Galluzzi, R. Paladino, and C. Burigana. **Polarization of extragalactic radio sources: CMB foregrounds and telescope calibration issues**. *International Journal of Modern Physics D*, **25**:1640009, March 2016. 48

[205] J. C. Mather, E. S. Cheng, R. E. Eplee, Jr., R. B. Isaacman, S. S. Meyer, R. A. Shafer, R. Weiss, E. L. Wright, C. L. Bennett, N. W. Boggess, E. Dwek, S. Gulkis, M. G. Hauser, M. Janssen, T. Kelsall, P. M. Lubin, S. H. Moseley, Jr., T. L. Murdock, R. F. Silverberg, G. F. Smoot, and D. T. Wilkinson. **A preliminary measurement of the cosmic microwave background spectrum by the Cosmic Background Explorer (COBE) satellite**. *ApJ*, **354**:L37–L40, May 1990. 105

[206] J. C. Mather, D. J. Fixsen, R. A. Shafer, C. Mosier, and D. T. Wilkinson. **Calibrator Design for the COBE Far-Infrared Absolute Spectrophotometer (FIRAS)**. *ApJ*, **512**:511–520, February 1999. 125

[207] T. Matsumura, Y. Akiba, J. Borrill, Y. Chinone, M. Dobbs, H. Fuke, A. Ghribi, M. Hasegawa, K. Hattori, M. Hattori, M. Hazumi, W. Holzapfel, Y. Inoue, K. Ishidoshiro, H. Ishino, H. Ishitsuka, K. Karatsu, N. Katayama, I. Kawano, A. Kibayashi, Y. Kibe, K. Kimura, N. Kimura, K. Koga, M. Kozu, E. Komatsu, A. Lee, H. Matsuhara, S. Mima, K. Mitsuda, K. Mizukami, H. Morii, T. Morishima, S. Murayama, M. Nagai, R. Nagata, S. Nakamura, M. Naruse, K. Natsume, T. Nishibori, H. Nishino, A. Noda, T. Noguchi, H. Ogawa, S. Oguri, I. Ohta, C. Otani, P. Richards, S. Sakai, N. Sato, Y. Sato, Y. Sekimoto, A. Shimizu, K. Shinozaki, H. Sugita, T. Suzuki, A. Suzuki, O. Tajima, S. Takada, S. Takakura, Y. Takei, T. Tomaru, Y. Uzawa, T. Wada, H. Watanabe, M. Yoshida, N. Yamasaki, T. Yoshida, and K. Yotsumoto. **Mission Design of LiteBIRD**. *Journal of Low Temperature Physics*, **176**:733–740, September 2014. 35

[208] T. Mauch, H.-R. Klöckner, S. Rawlings, M. Jarvis, M. J. Hardcastle, D. Obreschkow, D. J. Saikia, and M. A. Thompson. **A 325-MHz GMRT survey of the Herschel-ATLAS/GAMA fields**. *MNRAS*, **435**:650–662, October 2013. 112

[209] T. Mauch, T. Murphy, H. J. Buttery, J. Curran, R. W. Hunstead, B. Piestrzynski, J. G. Robertson, and E. M. Sadler. **SUMSS: a wide-field radio imaging survey of the southern sky - II. The source catalogue**. *MNRAS*, **342**:1117–1130, July 2003. xvi, 61

[210] N. M. McClure-Griffiths, J. M. Dickey, B. M. Gaensler, A. J. Green, J. A. Green, and M. Haverkorn. **The Australia Telescope Compact Array H I Survey of the Galactic Center**. *ApJS*, **199**:12, March 2012. 45

[211] A. Mennella, M. Bersanelli, R. C. Butler, A. Curto, F. Cuttaia, R. J. Davis, J. Dick, M. Frailis, S. Galeotta, A. Gregorio, H. Kurki-Suonio, C. R. Lawrence, S. Leach, J. P. Leahy, S. Lowe, D. Maino, N. Mandolesi, M. Maris, E. Martínez-González, P. R. Meinhold, G. Morgante, D. Pearson, F. Perrotta, G. Polenta, T. Poutanen, M. Sandri, M. D. Seiffert, A.-S. Suur-Uski, D. Tavagnacco, L. Terenzi, M. Tomasi, J. Valiviita, F. Villa, R. Watson, A. Wilkinson, A. Zacchei, A. Zonca, B. Aja, E. Artal, C. Baccigalupi, A. J. Banday, R. B. Barreiro, J. G. Bartlett, N. Bartolo, P. Battaglia, K. Bennett, A. Bonaldi, L. Bonavera, J. Borrill, F. R. Bouchet, C. Burigana, P. Cabella, B. Cappellini, X. Chen, L. Colombo, M. Cruz, L. Danese, O. D'Arcangelo, R. D. Davies, G. de Gasperis, A. de Rosa, G. de Zotti, C. Dickinson, J. M. Diego, S. Donzelli, G. Efstathiou, T. A. Ensslin, H. K. Eriksen, M. C. Falvella, F. Finelli, S. Foley, C. Franceschet, E. Franceschi, T. C. Gaier, R. T. Génova-Santos, D. George, F. Gómez, J. González-Nuevo, K. M. Górski, A. Gruppuso, F. K. Hansen, D. Herranz, J. M. Herreros, R. J. Hoyland, N. Hughes, J. Jewell, P. Jukkala, M. Juvela, P. Kangaslahti, E. Keihänen, R. Keskitalo, V.-H. Kilpia, T. S. Kisner, J. Knoche, L. Knox, M. Laaninen, A. Lähteenmäki, J.-M. Lamarre, R. Leonardi, J. León-Tavares, P. Leutenegger, P. B. Lilje, M. López-Caniego, P. M. Lubin, M. Malaspina, D. Marinucci, M. Massardi, S. Matarrese, F. Matthai, A. Melchiorri, L. Mendes, M. Miccolis, M. Migliaccio, S. Mitra, A. Moss, P. Natoli, R. Nesti, H. U. Nørgaard-Nielsen, L. Pagano, R. Paladini, D. Paoletti, B. Partridge, F. Pasian, V. Pettorino, D. Pietrobon, M. Pospieszalski, G. Prézeau, M. Prina, P. Procopio, J.-L. Puget, C. Quercellini, J. P. Rachen, R. Rebolo, M. Reinecke, S. Ricciardi, G. Robbers, G. Rocha, N. Roddis, J. A. Rubino-Martín, M. Savelainen, D. Scott, R. Silvestri, A. Simonetto, P. Sjoman, G. F. Smoot, C. Sozzi, L. Stringhetti, J. A. Tauber, G. Tofani, L. Toffolatti, J. Tuovinen, M. Türler, G. Umana, L. Valenziano,

REFERENCES

J. Varis, P. Vielva, N. Vittorio, L. A. Wade, C. Watson, S. D. M. White, and F. Winder. **Planck early results. III. First assessment of the Low Frequency Instrument in-flight performance**. *A&A*, **536**:A3, December 2011. 3

[212] D. Mesa, C. Baccigalupi, G. De Zotti, L. Gregorini, K.-H. Mack, M. Vigotti, and U. Klein. **Polarization properties of extragalactic radio sources and their contribution to microwave polarization fluctuations**. *A&A*, **396**:463–471, December 2002. 49

[213] N. Metropolis, A. W. Rosenbluth, M. N. Rosenbluth, A. H. Teller, and E. Teller. **Equation of State Calculations by Fast Computing Machines**. *J. Chem. Phys.*, **21**:1087–1092, June 1953. 122

[214] J. P. Mimoso, F. S. N. Lobo, and S. Capozziello. **Extended Theories of Gravity with Generalized Energy Conditions**. In *Journal of Physics Conference Series*, **600** of *Journal of Physics Conference Series*, page 012047, April 2015. 101

[215] L. M. Mocanu, T. M. Crawford, J. D. Vieira, K. A. Aird, M. Aravena, J. E. Austermann, B. A. Benson, M. Béthermin, L. E. Bleem, M. Bothwell, J. E. Carlstrom, C. L. Chang, S. Chapman, H.-M. Cho, A. T. Crites, T. de Haan, M. A. Dobbs, W. B. Everett, E. M. George, N. W. Halverson, N. Harrington, Y. Hezaveh, G. P. Holder, W. L. Holzapfel, S. Hoover, J. D. Hrubes, R. Keisler, L. Knox, A. T. Lee, E. M. Leitch, M. Lueker, D. Luong-Van, D. P. Marrone, J. J. McMahon, J. Mehl, S. S. Meyer, J. J. Mohr, T. E. Montroy, T. Natoli, S. Padin, T. Plagge, C. Pryke, A. Rest, C. L. Reichardt, J. E. Ruhl, J. T. Sayre, K. K. Schaffer, E. Shirokoff, H. G. Spieler, J. S. Spilker, B. Stalder, Z. Staniszewski, A. A. Stark, K. T. Story, E. R. Switzer, K. Vanderlinde, and R. Williamson. **Extragalactic Millimeter-wave Point-source Catalog, Number Counts and Statistics from 771 deg^2 of the SPT-SZ Survey**. *ApJ*, **779**:61, December 2013. 79

[216] J. B. Muñoz, Y. Ali-Haïmoud, and M. Kamionkowski. **Primordial non-gaussianity from the bispectrum of 21-cm fluctuations in the dark ages**. *Phys. Rev. D*, **92**(8):083508, October 2015. 101

[217] D. Munshi and A. Heavens. **A new approach to probing primordial non-Gaussianity**. *MNRAS*, **401**:2406–2418, February 2010. 21

[218] T. Murphy, E. M. Sadler, R. D. Ekers, M. Massardi, P. J. Hancock, E. Mahony, R. Ricci, S. Burke-Spolaor, M. Calabretta, R. Chhetri, G. de Zotti, P. G. Edwards, J. A. Ekers, C. A. Jackson, M. J. Kesteven, E. Lindley, K. Newton-McGee, C. Phillips, P. Roberts, R. J. Sault, L. Staveley-Smith, R. Subrahmanyan, M. A. Walker, and W. E. Wilson. **The Australia Telescope 20 GHz Survey: the source catalogue**. *MNRAS*, **402**:2403–2423, March 2010. 49

[219] P. Naselsky and L.-Y. Chiang. **Late reionizations of the Universe and their manifestation in the WMAP and future Planck data**. *MNRAS*, **347**:795–801, January 2004. 106, 109

[220] P. Natoli, M. Ashdown, R. Banerji, J. Borrill, A. Buzzelli, G. de Gasperis, J. Delabrouille, E. Hivon, D. Molinari, G. Patanchon, L. Polastri, M. Tomasi, F. R. Bouchet, S. Henrot-Versillé, D. T. Hoang, R. Keskitalo, K. Kiiveri, T. Kisner, V. Lindholm, D. McCarthy, F. Piacentini, O. Perdereau, G. Polenta, M. Tristram, A. Achucarro, P. Ade, R. Allison, C. Baccigalupi, M. Ballardini, A. J. Banday, J. Bartlett, N. Bartolo, S. Basak, J. Baselmans, D. Baumann, M. Bersanelli, A. Bonaldi, M. Bonato, F. Boulanger, T. Brinckmann, M. Bucher, C. Burigana, Z.-Y. Cai, M. Calvo, C.-S. Carvalho, G. Castellano, A. Challinor, J. Chluba, S. Clesse, I. Colantoni, A. Coppolecchia, M. Crook, G. D'Alessandro, P. de Bernardis, G. De Zotti, E. Di Valentino, J.-M. Diego, J. Errard, S. Feeney, R. Fernandez-Cobos, F. Finelli, F. Forastieri, S. Galli, R. Genova-Santos, M. Gerbino, J. Gonzalez-Nuevo, S. Grandis, J. Greenslade, A. Gruppuso, S. Hagstotz, S. Hanany, W. Handley, C. Hernandez-Monteagudo, C. Hervias-Caimapo, M. Hills, E. Keihänen, T. Kitching, M. Kunz, H. Kurki-Suonio, L. Lamagna, A. Lasenby, M. Lattanzi, J. Lesgourgues, A. Lewis, M. Liguori, M. López-Caniego, G. Luzzi, B. Maffei, N. Mandolesi, E. Martinez-Gonzalez, C. J. A. P. Martins, S. Masi, A. Melchiorri, J.-B. Melin, M. Migliaccio, A. Monfardini, M. Negrello, A. Notari, L. Pagano, A. Paiella, D. Paoletti, M. Piat, G. Pisano, A. Pollo, V. Poulin, M. Quartin, M. Remazeilles, M. Roman, G. Rossi, J.-A. Rubino-Martin, L. Salvati, G. Signorelli, A. Tartari, D. Tramonte, N. Trappe, T. Trombetti, C. Tucker, J. Valiviita, R. Van de Weijgaert, B. van Tent, V. Vennin, P. Vielva, N. Vittorio, C. Wallis, K. Young, M. Zannoni, and for the CORE collaboration. **Exploring cosmic origins with CORE: mitigation of systematic effects**. *ArXiv e-prints*, July 2017. 38

[221] M. Negrello, M. Clemens, J. Gonzalez-Nuevo, G. De Zotti, L. Bonavera, G. Cosco, G. Guarese, L. Boaretto, S. Serjeant, L. Toffolatti, A. Lapi, M. Bethermin, G. Castex, D. L. Clements, J. Delabrouille, H. Dole, A. Franceschini, N. Mandolesi, L. Marchetti, B. Partridge, and A. Sajina. **The local luminosity function of star-forming galaxies derived from the Planck Early Release Compact Source Catalogue**. *MNRAS*, **429**:1309–1323, February 2013. 79

[222] A. Notari and M. Quartin. **Measuring our peculiar velocity by "predeboosting" the CMB**. *J. Cosmology Astropart. Phys.*, **2**:026, February 2012. 128, 129, 130, 131, 133, 137

[223] A. Notari and M. Quartin. **On the proper kinetic quadrupole CMB removal and the quadrupole anomalies**. *J. Cosmology Astropart. Phys.*, **6**:047, June 2015. 129, 131

[224] A. Notari and M. Quartin. **CMB all-scale blackbody distortions induced by linearizing temperature**. *Phys. Rev. D*, **94**(4):043006, August 2016. 131, 137

[225] N. Oppermann, H. Junklewitz, M. Greiner, T. A. Ensslin, T. Akahori, E. Carretti, B. M. Gaensler, A. Goobar, L. Harvey-Smith, M. Johnston-Hollitt, L. Pratley, D. H. F. M. Schnitzeler, J. M. Stil, and V. Vacca. **Estimating extragalactic Faraday rotation**. *A&A*, **575**:A118, March 2015. 66

[226] J. P. Ostriker and C. Thompson. **Distortion of the cosmic background radiation by superconducting strings**. *ApJ*, **323**:L97–L101, December 1987. 141

[227] A. G. Pacholczyk. **Circular repolarization in compact radio sources**. *MNRAS*, **163**:29P, 1973. 67

[228] E. Pajer and M. Zaldarriaga. **New Window on Primordial Non-Gaussianity**. *Physical Review Letters*, **109**(2):021302, July 2012. 101

[229] E. Pajer and M. Zaldarriaga. **A hydrodynamical approach to CMB μ-distortion from primordial perturbations**. *J. Cosmology Astropart. Phys.*, **2**:036, February 2013. 138

[230] P. Pani and A. Loeb. **Constraining primordial black-hole bombs through spectral distortions of the cosmic microwave background**. *Phys. Rev. D*, **88**(4):041301, August 2013. 141

[231] B. Partridge, M. López-Caniego, R. A. Perley, J. Stevens, B. J. Butler, G. Rocha, B. Walter, and A. Zacchei. **Absolute Calibration of the Radio Astronomy Flux Density Scale at 22 to 43 GHz Using Planck**. *ApJ*, **821**:61, April 2016. 51

[232] A. Pasetto, A. Kraus, K.-H. Mack, G. Bruni, and C. Carrasco-González. **A study of a sample of high rotation-measure AGNs through multifrequency single-dish observations**. *A&A*, **586**:A117, February 2016. 63

[233] T. S. Pereira, A. Yoho, M. Stuke, and G. D. Starkman. **Effects of a Cut, Lorentz-Boosted sky on the Angular Power Spectrum**. *ArXiv e-prints*, September 2010. 133

[234] S. Perlmutter, G. Aldering, G. Goldhaber, R. A. Knop, P. Nugent, P. G. Castro, S. Deustua, S. Fabbro, A. Goobar, D. E. Groom, I. M. Hook, A. G. Kim, M. Y. Kim, J. C. Lee, N. J. Nunes, R. Pain, C. R. Pennypacker, R. Quimby, C. Lidman, R. S. Ellis, M. Irwin, R. G. McMahon, P. Ruiz-Lapuente, N. Walton, B. Schaefer, B. J. Boyle, A. V. Filippenko, T. Matheson, A. S. Fruchter, N. Panagia, H. J. M. Newberg, W. J. Couch, and T. S. C. Project. **Measurements of Ω and Λ from 42 High-Redshift Supernovae**. *ApJ*, **517**:565–586, June 1999. 100

[235] Planck Collaboration. **Planck 2015 Release Explanatory Supplement**. *ESA*, 2015. 121

[236] Planck Collaboration. **Dipole-modulated Compton-*y* signature**. in prep., 2017. 119

[237] Planck Collaboration, R. Adam, P. A. R. Ade, N. Aghanim, Y. Akrami, M. I. R. Alves, F. Argüeso, M. Arnaud, F. Arroja, M. Ashdown, and et al. **Planck 2015 results. I. Overview of products and scientific results**. *A&A*, **594**:A1, September 2016. xiii, xiv, xxv, 6, 7, 9, 10, 11, 22, 24, 121

[238] Planck Collaboration, R. Adam, P. A. R. Ade, N. Aghanim, M. I. R. Alves, M. Arnaud, M. Ashdown, J. Aumont, C. Baccigalupi, A. J. Banday, and et al. **Planck 2015 results. X. Diffuse component separation: Foreground maps**. *A&A*, **594**:A10, September 2016. 11, 75, 77, 115

[239] Planck Collaboration, R. Adam, P. A. R. Ade, N. Aghanim, M. Arnaud, M. Ashdown, J. Aumont, C. Baccigalupi, A. J. Banday, R. B. Barreiro, and et al. **Planck 2015 results. IX. Diffuse component separation: CMB maps**. *A&A*, **594**:A9, September 2016. 13, 24

[240] Planck Collaboration, R. Adam, P. A. R. Ade, N. Aghanim, M. Arnaud, M. Ashdown, J. Aumont, C. Baccigalupi, A. J. Banday, R. B. Barreiro, et al. **Planck 2015 results. VIII. High Frequency Instrument data processing: Calibration and maps**. *A&A*, **594**:A8, August 2016. 121

[241] Planck Collaboration, R. Adam, P. A. R. Ade, N. Aghanim, M. Arnaud, J. Aumont, C. Baccigalupi, A. J. Banday, R. B. Barreiro, J. G. Bartlett, and et al. **Planck intermediate results. XXX. The angular power spectrum of polarized dust emission at intermediate and high Galactic latitudes**. *A&A*, **586**:A133, February 2016. 11, 26, 75, 115

[242] Planck Collaboration, P. A. R. Ade, N. Aghanim, Y. Akrami, P. K. Aluri, M. Arnaud, M. Ashdown, J. Aumont, C. Baccigalupi, A. J. Banday, and et al. **Planck 2015 results. XVI. Isotropy and statistics of the CMB**. *A&A*, **594**:A16, September 2016. 17, 133

[243] Planck Collaboration, P. A. R. Ade, N. Aghanim, M. I. R. Alves, M. Arnaud, M. Ashdown, J. Aumont, C. Baccigalupi, A. J. Banday, R. B. Barreiro, and et al. **Planck 2015 results. XXV. Diffuse low-frequency Galactic foregrounds**. *A&A*, **594**:A25, September 2016. 11, 75, 115

[244] Planck Collaboration, P. A. R. Ade, N. Aghanim, F. Argüeso, M. Arnaud, M. Ashdown, J. Aumont, C. Baccigalupi, A. J. Banday, R. B. Barreiro, and et al. **Planck 2015 results. XXVI. The Second Planck Catalogue of Compact Sources**. *A&A*, **594**:A26, September 2016. xiii, 8, 76, 78, 81, 92

[245] Planck Collaboration, P. A. R. Ade, N. Aghanim, C. Armitage-Caplan, M. Arnaud, M. Ashdown, F. Atrio-Barandela, J. Aumont, C. Baccigalupi, A. J. Banday, and et al. **Planck 2013 results. XVI. Cosmological parameters**. *A&A*, **571**:A16, November 2014. 1, 17

[246] Planck Collaboration, P. A. R. Ade, N. Aghanim, C. Armitage-Caplan, M. Arnaud, M. Ashdown, F. Atrio-Barandela, J. Aumont, C. Baccigalupi, A. J. Banday, and et al. **Planck 2013 results. XXIV. Constraints on primordial non-Gaussianity**. *A&A*, **571**:A24, November 2014. 21

[247] Planck Collaboration, P. A. R. Ade, N. Aghanim, C. Armitage-Caplan, M. Arnaud, M. Ashdown, F. Atrio-Barandela, J. Aumont, C. Baccigalupi, A. J. Banday, and et al. **Planck 2013 results. XXX. Cosmic infrared background measurements and implications for star formation**. *A&A*, **571**:A30, November 2014. 9, 91

[248] Planck Collaboration, P. A. R. Ade, N. Aghanim, M. Arnaud, F. Arroja, M. Ashdown, J. Aumont, C. Baccigalupi, M. Ballardini, A. J. Banday, and et al. **Planck 2015 results. XVII. Constraints on primordial non-Gaussianity**. *A&A*, **594**:A17, September 2016. 21

[249] Planck Collaboration, P. A. R. Ade, N. Aghanim, M. Arnaud, F. Arroja, M. Ashdown, J. Aumont, C. Baccigalupi, M. Ballardini, A. J. Banday, and et al. **Planck 2015 results. XX. Constraints on inflation**. *A&A*, **594**:A20, September 2016. 19, 20

[250] Planck Collaboration, P. A. R. Ade, N. Aghanim, M. Arnaud, M. Ashdown, J. Aumont, C. Baccigalupi, M. Baker, A. Balbi, A. J. Banday, and et al. **Planck early results. I. The Planck mission**. *A&A*, **536**:A1, December 2011. 3, 9

[251] Planck Collaboration, P. A. R. Ade, N. Aghanim, M. Arnaud, M. Ashdown, J. Aumont, C. Baccigalupi, A. Balbi, A. J. Banday, R. B. Barreiro, and et al. **Planck early results. VII. The Early Release Compact Source Catalogue**. *A&A*, **536**:A7, December 2011. 3

[252] Planck Collaboration, P. A. R. Ade, N. Aghanim, M. Arnaud, M. Ashdown, J. Aumont, C. Baccigalupi, A. J. Banday, R. B. Barreiro, J. G. Bartlett, and et al. **Planck 2015 results. XIII. Cosmological parameters**. *A&A*, **594**:A13, September 2016. xiii, 5, 12, 17, 18, 22, 89

[253] Planck Collaboration, P. A. R. Ade, N. Aghanim, M. Arnaud, M. Ashdown, J. Aumont, C. Baccigalupi, A. J. Banday, R. B. Barreiro, J. G. Bartlett, and et al. **Planck 2015 results. XV. Gravitational lensing**. *A&A*, **594**:A15, September 2016. 13

[254] Planck Collaboration, P. A. R. Ade, N. Aghanim, M. Arnaud, M. Ashdown, J. Aumont, C. Baccigalupi, A. J. Banday, R. B. Barreiro, N. Bartolo, and et al. **Planck intermediate results. XXV. The Andromeda galaxy as seen by Planck**. *A&A*, **582**:A28, October 2015. 11

[255] Planck Collaboration, P. A. R. Ade, N. Aghanim, M. Arnaud, M. Ashdown, J. Aumont, C. Baccigalupi, A. J. Banday, R. B. Barreiro, N. Bartolo, and et al. **Planck 2015 results. XXI. The integrated Sachs-Wolfe effect**. *A&A*, **594**:A21, September 2016. 13

[256] Planck Collaboration, P. A. R. Ade, N. Aghanim, M. Ashdown, J. Aumont, C. Baccigalupi, A. J. Banday, R. B. Barreiro, N. Bartolo, P. Battaglia, et al. **Planck 2015 results. V. LFI calibration**. *A&A*, **594**:A5, August 2016. 121

[257] Planck Collaboration, N. Aghanim, Y. Akrami, M. Ashdown, J. Aumont, M. Ballardini, A. J. Banday, R. B. Barreiro, N. Bartolo, S. Basak, K. Benabed, M. Bersanelli, P. Bielewicz, A. Bonaldi, L. Bonavera, J. R. Bond, J. Borrill, F. R. Bouchet, C. Burigana, E. Calabrese, J.-F. Cardoso, A. Challinor, H. C. Chiang, L. P. L. Colombo, C. Combet, B. P. Crill, A. Curto, F. Cuttaia, P. de Bernardis, A. de Rosa, G. de Zotti, J. Delabrouille, E. Di Valentino, C. Dickinson, J. M. Diego, O. Doré, A. Ducout, X. Dupac, S. Dusini, G. Efstathiou, F. Elsner, T. A. Ensslin, H. K. Eriksen, Y. Fantaye, F. Finelli, F. Forastieri, M. Frailis, E. Franceschi, A. Frolov, S. Galeotta, S. Galli, K. Ganga, R. T. Génova-Santos, M. Gerbino, J. González-Nuevo, K. M. Górski, A. Gruppuso, J. E. Gudmundsson, D. Herranz, E. Hivon, Z. Huang, A. H. Jaffe, W. C. Jones, E. Keihänen, R. Keskitalo, K. Kiiveri, J. Kim, T. S. Kisner, L. Knox, N. Krachmalnicoff, M. Kunz, H. Kurki-Suonio, G. Lagache, J.-M. Lamarre, A. Lasenby, M. Lattanzi, C. R. Lawrence, M. Le Jeune, F. Levrier, A. Lewis, P. B. Lilje, M. Lilley, V. Lindholm, M. López-Caniego, P. M. Lubin, Y.-Z. Ma, J. F. Macías-Pérez, G. Maggio, D. Maino, N. Mandolesi, A. Mangilli, M. Maris, P. G. Martin, E. Martínez-González,

REFERENCES

S. Matarrese, N. Mauri, J. D. McEwen, P. R. Meinhold, A. Mennella, M. Migliaccio, M. Millea, M.-A. Miville-Deschênes, D. Molinari, A. Moneti, L. Montier, G. Morgante, A. Moss, A. Narimani, P. Natoli, C. A. Oxborrow, L. Pagano, D. Paoletti, G. Patanchon, L. Patrizii, V. Pettorino, F. Piacentini, L. Polastri, G. Polenta, J.-L. Puget, J. P. Rachen, B. Racine, M. Reinecke, M. Remazeilles, A. Renzi, M. Rossetti, G. Roudier, J. A. Rubiño-Martín, B. Ruiz-Granados, L. Salvati, M. Sandri, M. Savelainen, D. Scott, C. Sirignano, G. Sirri, L. Stanco, A.-S. Suur-Uski, J. A. Tauber, D. Tavagnacco, M. Tenti, L. Toffolatti, M. Tomasi, M. Tristram, T. Trombetti, J. Valiviita, F. Van Tent, P. Vielva, F. Villa, N. Vittorio, B. D. Wandelt, I. K. Wehus, M. White, A. Zacchei, and A. Zonca. **Planck intermediate results. LI. Features in the cosmic microwave background temperature power spectrum and shifts in cosmological parameters**. *ArXiv e-prints*, August 2016. 23, 29

[258] Planck Collaboration, N. Aghanim, B. Altieri, M. Arnaud, M. Ashdown, J. Aumont, C. Baccigalupi, A. J. Banday, R. B. Barreiro, N. Bartolo, E. Battaner, A. Beelen, K. Benabed, A. Benoit-Lévy, J.-P. Bernard, M. Bersanelli, M. Bethermin, P. Bielewicz, L. Bonavera, J. R. Bond, J. Borrill, F. R. Bouchet, F. Boulanger, C. Burigana, E. Calabrese, R. Canameras, J.-F. Cardoso, A. Catalano, A. Chamballu, R.-R. Chary, H. C. Chiang, P. R. Christensen, D. L. Clements, S. Colombi, F. Couchot, B. P. Crill, A. Curto, L. Danese, K. Dassas, R. D. Davies, R. J. Davis, P. de Bernardis, A. de Rosa, G. de Zotti, J. Delabrouille, J. M. Diego, H. Dole, S. Donzelli, O. Doré, M. Douspis, A. Ducout, X. Dupac, G. Efstathiou, F. Elsner, T. A. Ensslin, E. Falgarone, I. Flores-Cacho, O. Forni, M. Frailis, A. A. Fraisse, E. Franceschi, A. Fresjsel, B. Frye, S. Galeotta, S. Galli, K. Ganga, M. Giard, E. Gjerløw, J. González-Nuevo, K. M. Górski, A. Gregorio, A. Gruppuso, D. Guéry, F. K. Hansen, D. Hanson, D. L. Harrison, G. Helou, C. Hernández-Monteagudo, S. R. Hildebrandt, E. Hivon, M. Hobson, W. A. Holmes, W. Hovest, K. M. Huffenberger, G. Hurier, A. H. Jaffe, T. R. Jaffe, E. Keihänen, R. Keskitalo, T. S. Kisner, R. Kneissl, J. Knoche, M. Kunz, H. Kurki-Suonio, G. Lagache, J.-M. Lamarre, A. Lasenby, M. Lattanzi, C. R. Lawrence, E. Le Floc'h, R. Leonardi, F. Levrier, M. Liguori, P. B. Lilje, M. Linden-Vørnle, M. López-Caniego, P. M. Lubin, J. F. Macías-Pérez, T. MacKenzie, B. Maffei, N. Mandolesi, M. Maris, P. G. Martin, C. Martinache, E. Martínez-González, S. Masi, S. Matarrese, P. Mazzotta, A. Melchiorri, A. Mennella, M. Migliaccio, A. Moneti, L. Montier, G. Morgante, D. Mortlock, D. Munshi, J. A. Murphy, P. Natoli, M. Negrello, N. P. H. Nesvadba, D. Novikov, I. Novikov, A. Omont, L. Pagano, F. Pajot, F. Pasian, O. Perdereau, L. Perotto, F. Perrotta, V. Pettorino, F. Piacentini, M. Piat, S. Plaszczynski, E. Pointecouteau, G. Polenta, L. Popa, G. W. Pratt, S. Prunet, J.-L. Puget, J. P. Rachen, W. T. Reach, M. Reinecke, M. Remazeilles, C. Renault, I. Ristorcelli, G. Rocha, G. Roudier, B. Rusholme, M. Sandri, D. Santos, G. Savini, D. Scott, L. D. Spencer, V. Stolyarov, R. Sunyaev, D. Sutton, J.-F. Sygnet, J. A. Tauber, L. Terenzi, L. Toffolatti, M. Tomasi, M. Tristram, M. Tucci, G. Umana, L. Valenziano, J. Valiviita, I. Valtchanov, B. Van Tent, J. D. Vieira, P. Vielva, L. A. Wade, B. D. Wandelt, I. K. Wehus, N. Welikala, A. Zacchei, and A. Zonca. **Planck intermediate results. XXVII. High-redshift infrared galaxy overdensity candidates and lensed sources discovered by Planck and confirmed by Herschel-SPIRE**. *A&A*, **582**:A30, October 2015. xiii, 9

[259] Planck Collaboration, N. Aghanim, C. Armitage-Caplan, M. Arnaud, M. Ashdown, F. Atrio-Barandela, J. Aumont, C. Baccigalupi, A. J. Banday, R. B. Barreiro, et al. **Planck 2013 results. XXVII. Doppler boosting of the CMB: Eppur si muove**. *A&A*, **571**:A27, November 2014. 118, 128, 129, 131

[260] Planck Collaboration, N. Aghanim, M. Arnaud, M. Ashdown, J. Aumont, C. Baccigalupi, A. J. Banday, R. B. Barreiro, J. G. Bartlett, N. Bartolo, and et al. **Planck 2015 results. XI. CMB power spectra, likelihoods, and robustness of parameters**. *A&A*, **594**:A11, September 2016. 22, 23, 24

[261] Planck Collaboration, N. Aghanim, M. Arnaud, M. Ashdown, J. Aumont, C. Baccigalupi, A. J. Banday, R. B. Barreiro, J. G. Bartlett, N. Bartolo, et al. **Planck 2015 results. XXII. A map of the thermal Sunyaev-Zeldovich effect**. *A&A*, **594**:A22, September 2016. 133

[262] Planck Collaboration, N. Aghanim, M. Ashdown, J. Aumont, C. Baccigalupi, M. Ballardini, A. J. Banday, R. B. Barreiro, N. Bartolo, S. Basak, R. Battye, K. Benabed, J.-P. Bernard, M. Bersanelli, P. Bielewicz, J. J. Bock, A. Bonaldi, L. Bonavera, J. R. Bond, J. Borrill, F. R. Bouchet, F. Boulanger, M. Bucher, C. Burigana, R. C. Butler, E. Calabrese, J.-F. Cardoso, J. Carron, A. Challinor, H. C. Chiang, L. P. L. Colombo, C. Combet, B. Comis, A. Coulais, B. P. Crill, A. Curto, F. Cuttaia, R. J. Davis, P. de Bernardis, A. de Rosa, G. de Zotti, J. Delabrouille, J.-M. Delouis, E. Di Valentino, C. Dickinson, J. M. Diego, O. Doré, M. Douspis, A. Ducout, X. Dupac, G. Efstathiou, F. Elsner, T. A. Ensslin, H. K. Eriksen, E. Falgarone, Y. Fantaye, F. Finelli, F. Forastieri, M. Frailis, A. A. Fraisse, E. Franceschi, A. Frolov, S. Galeotta, S. Galli, K. Ganga, R. T. Génova-Santos, M. Gerbino, T. Ghosh, J. González-Nuevo, K. M. Górski, S. Gratton, A. Gruppuso, J. E. Gudmundsson, F. K. Hansen, G. Helou, S. Henrot-Versillé, D. Herranz, E. Hivon, Z. Huang, S. Ilić, A. H. Jaffe, W. C. Jones, E. Keihänen, R. Keskitalo, T. S. Kisner, L. Knox, N. Krachmalnicoff, M. Kunz, H. Kurki-Suonio, G. Lagache, J.-M. Lamarre, M. Langer, A. Lasenby, M. Lattanzi, C. R. Lawrence, M. Le Jeune, J. P. Leahy, F. Levrier, M. Liguori, P. B. Lilje, M. López-Caniego, Y.-Z. Ma, J. F. Macías-Pérez, G. Maggio, A. Mangilli, M. Maris, P. G. Martin, E. Martínez-González, S. Matarrese, N. Mauri, J. D. McEwen, P. R. Meinhold, A. Melchiorri, A. Mennella, M. Migliaccio, M.-A. Miville-Deschênes, D. Molinari, A. Moneti, L. Montier, G. Morgante, A. Moss, S. Mottet, P. Naselsky, P. Natoli, C. A. Oxborrow, L. Pagano, D. Paoletti, B. Partridge, G. Patanchon, L. Patrizii, O. Perdereau, L. Perotto, V. Pettorino, F. Piacentini, S. Plaszczynski, L. Polastri, G. Polenta, J.-L. Puget, J. P. Rachen, B. Racine, M. Reinecke, M. Remazeilles, A. Renzi, G. Rocha, M. Rossetti, G. Roudier, J. A. Rubiño-Martín, B. Ruiz-Granados, L. Salvati, M. Sandri, M. Savelainen, D. Scott, G. Sirri, R. Sunyaev, A.-S. Suur-Uski, J. A. Tauber, M. Tenti, L. Toffolatti, M. Tomasi, M. Tristram, T. Trombetti, J. Valiviita, F. Van Tent, L. Vibert, P. Vielva, F. Villa, N. Vittorio, B. D. Wandelt, R. Watson, I. K. Wehus, M. White, A. Zacchei, and A. Zonca. **Planck intermediate results. XLVI. Reduction of large-scale systematic effects in HFI polarization maps and estimation of the reionization optical depth**. *A&A*, **596**:A107, December 2016. xiii, 5, 23, 24, 27

[263] Planck Collaboration, Y. Akrami, M. Ashdown, J. Aumont, C. Baccigalupi, M. Ballardini, A. J. Banday, R. B. Barreiro, N. Bartolo, S. Basak, et al. **Planck intermediate results. LII. Planet flux densities**. *accepted by A&A*, December 2016. 125

[264] Planck Collaboration Int. L. **Planck intermediate results. L. Evidence of spatial variation of the polarized thermal dust spectral energy distribution and implications for CMB B-mode analysis**. *A&A*, **599**:A51, March 2017. 75

[265] Planck Collaboration Int. VII. **Planck intermediate results. VII. Statistical properties of infrared and radio extragalactic sources from the Planck Early Release Compact Source Catalogue at frequencies between 100 and 857 GHz**. *A&A*, **550**:A133, February 2013. 79

[266] Planck Collaboration IX. **Planck 2013 results. IX. HFI spectral response**. *A&A*, **571**:A9, November 2014. 80

[267] Planck Collaboration V. **Planck 2013 results. V. LFI calibration**. *A&A*, **571**:A5, November 2014. 80

[268] Planck Collaboration XV. **Planck 2013 results. XV. CMB power spectra and likelihood**. *Astron.Astrophys.*, **571**:A15, 2014. 22, 23

[269] Planck Collaboration XVIII. **Planck early results. XVIII. The power spectrum of cosmic infrared background anisotropies**. *A&A*, **536**:A18, December 2011. 91

[270] Planck HFI Core Team, P. A. R. Ade, N. Aghanim, R. Ansari, M. Arnaud, M. Ashdown, J. Aumont, A. J. Banday, M. Bartelmann, J. G. Bartlett, E. Battaner, K. Benabed, A. Benoît, J.-P. Bernard, M. Bersanelli, R. Bhatia, J. J. Bock, J. R. Bond, J. Borrill, F. R. Bouchet, F. Boulanger, T. Bradshaw, E. Bréelle, M. Bucher, P. Camus, J.-F. Cardoso, A. Catalano, A. Challinor, A. Chamballu, J. Charra, M. Charra, R.-R. Chary, C. Chiang, S. Church, D. L. Clements, S. Colombi, F. Couchot, A. Coulais, C. Cressiot, B. P. Crill, M. Crook, P. de Bernardis, J. Delabrouille, J.-M. Delouis, F.-X. Désert, K. Dolag, H. Dole, O. Doré, M. Douspis, G. Efstathiou, P. Eng, C. Filliard, O. Forni, P. Fosalba, J.-J. Fourmond, K. Ganga, M. Giard, D. Girard, Y. Giraud-Héraud, R. Gispert, K. M. Górski, S. Gratton, M. Griffin, G. Guyot, J. Haissinski, D. Harrison, G. Helou, S. Henrot-Versillé, C. Hernández-Monteagudo, S. R. Hildebrandt, R. Hills, E. Hivon, M. Hobson, W. A. Holmes, K. M. Huffenberger, A. H. Jaffe, W. C. Jones, J. Kaplan, R. Kneissl, L. Knox, G. Lagache, J.-M. Lamarre, P. Lami, A. E. Lange, A. Lasenby, A. Lavabre, C. R. Lawrence, B. Leriche, C. Leroy, Y. Longval, J. F. Macías-Pérez, T. Maciaszek, C. J. MacTavish, B. Maffei, N. Mandolesi, R. Mann, B. Mansoux, S. Masi, T. Matsumura, P. McGehee, J.-B. Melin, C. Mercier, M.-A. Miville-Deschênes, A. Moneti, L. Montier, D. Mortlock, A. Murphy, F. Nati, C. B. Netterfield, H. U. Nørgaard-Nielsen, C. North, F. Noviello, D. Novikov, S. Osborne, C. Paine, F. Pajot, G. Patanchon, T. Peacocke, T. J. Pearson, O. Perdereau, L. Perotto, F. Piacentini, M. Piat, S. Plaszczynski, E. Pointecouteau, R. Pons, N. Ponthieu, G. Prézeau, S. Prunet, J.-L. Puget, W. T. Reach, C. Renault, I. Ristorcelli, G. Rocha, C. Rosset, G. Roudier, M. Rowan-Robinson, B. Rusholme, D. Santos, G. Savini, B. M. Schaefer, P. Shellard, L. Spencer, J.-L. Starck, P. Stassi, V. Stolyarov, R. Stompor, R. Sudiwala, R. Sunyaev, J.-F. Sygnet, J. A. Tauber, C. Thum, J.-P. Torre, F. Touze, M. Tristram, F. van Leeuwen, L. Vibert, D. Vibert, L. A. Wade, B. D. Wandelt, S. D. M. White, H. Wiesemeyer, A. Woodcraft, V. Yurchenko, D. Yvon, and A. Zacchei. **Planck early results. IV. First assessment of the High Frequency Instrument in-flight performance**. *A&A*, **536**:A4, December 2011. 3

[271] M. Plionis and V. Kolokotronis. **The X-Ray Cluster Dipole**. *ApJ*, **500**:1–7, June 1998. 118

[272] P. P. Ponente, J. M. Diego, R. K. Sheth, C. Burigana, S. R. Knollmann, and Y. Ascasibar. **The cosmological free-free signal from galaxy groups and clusters**. *MNRAS*, **410**:2353–2362, February 2011. 106

[273] I. Prandoni, L. Gregorini, P. Parma, H. R. de Ruiter, G. Vettolani, M. H. Wieringa, and R. D. Ekers. **The ATESP radio survey. III. Source counts**. *A&A*, **365**:392–399, January 2001. 111, 114

[274] I. Prandoni and N. Seymour. **Revealing the Physics and Evolution of Galaxies and Galaxy Clusters with SKA Continuum Surveys**. *Advancing Astrophysics with the Square Kilometre Array (AASKA14)*, page 67, April 2015. 97, 114, 115

[275] M. Quartin and A. Notari. **Improving Planck calibration by including frequency-dependent relativistic corrections**. *J. Cosmology Astropart. Phys.*, **9**:050, September 2015. 129, 131

[276] S. Rawlings, F. B. Abdalla, S. L. Bridle, C. A. Blake, C. M. Baugh, L. J. Greenhill, and J. M. van der Hulst. **Galaxy evolution, cosmology and dark energy with the Square Kilometer Array**. *New A Rev.*, **48**:1013–1027, December 2004. 98

[277] D. P. Rayner, R. P. Norris, and R. J. Sault. **Radio circular polarization of active galaxies**. *MNRAS*, **319**:484–496, December 2000. 51, 67

[278] M. J. Rees and D. W. Sciama. **Large-scale Density Inhomogeneities in the Universe**. *Nature*, **217**:511–516, February 1968. 12

[279] A. Refregier, E. Komatsu, D. N. Spergel, and U.-L. Pen. **Power spectrum of the Sunyaev-Zel'dovich effect**. *Phys. Rev. D*, **61**(12):123001, June 2000. 140

[280] M. Remazeilles, A. J. Banday, C. Baccigalupi, S. Basak, A. Bonaldi, G. De Zotti, J. Delabrouille, C. Dickinson, H. K. Eriksen, J. Errard, R. Fernandez-Cobos, U. Fuskeland, C. Hervías-Caimapo, M. López-Caniego, E. Martinez-González, M. Roman, P. Vielva, I. Wehus, A. Achucarro, P. Ade, R. Allison, M. Ashdown, M. Ballardini, R. Banerji, N. Bartolo, J. Bartlett, D. Baumann, M. Bersanelli, M. Bonato, J. Borrill, F. Bouchet, F. Boulanger, T. Brinckmann, M. Bucher, C. Burigana, A. Buzzelli, Z.-Y. Cai, M. Calvo, C.-S. Carvalho, G. Castellano, A. Challinor, J. Chluba, S. Clesse, I. Colantoni, A. Coppolecchia, M. Crook, G. D'Alessandro, P. de Bernardis, G. de Gasperis, J.-M. Diego, E. Di Valentino, S. Feeney, S. Ferraro, F. Finelli, F. Forastieri, S. Galli, R. Genova-Santos, M. Gerbino, J. González-Nuevo, S. Grandis, J. Greenslade, S. Hagstotz, S. Hanany, W. Handley, C. Hernandez-Monteagudo, M. Hills, E. Hivon, K. Kiiveri, T. Kisner, T. Kitching, M. Kunz, H. Kurki-Suonio, L. Lamagna, A. Lasenby, M. Lattanzi, J. Lesgourgues, A. Lewis, M. Liguori, V. Lindholm, G. Luzzi, B. Maffei, C. J. A. P. Martins, S. Masi, D. McCarthy, J.-B. Melin, A. Melchiorri, D. Molinari, A. Monfardini, P. Natoli, M. Negrello, A. Notari, A. Paiella, D. Paoletti, G. Patanchon, M. Piat, G. Pisano, L. Polastri, G. Polenta, A. Pollo, V. Poulin, M. Quartin, J.-A. Rubino-Martin, L. Salvati, A. Tartari, M. Tomasi, D. Tramonte, N. Trappe, T. Trombetti, C. Tucker, J. Valiviita, R. Van de Weijgaert, B. van Tent, V. Vennin, N. Vittorio, K. Young, M. Zannoni, and for the CORE collaboration. **Exploring Cosmic Origins with CORE: B-mode Component Separation**. *ArXiv e-prints*, April 2017. 37, 76, 77, 92

[281] A. G. Riess, A. V. Filippenko, P. Challis, A. Clocchiatti, A. Diercks, P. M. Garnavich, R. L. Gilliland, C. J. Hogan, S. Jha, R. P. Kirshner, B. Leibundgut, M. M. Phillips, D. Reiss, B. P. Schmidt, R. A. Schommer, R. C. Smith, J. Spyromilio, C. Stubbs, N. B. Suntzeff, and J. Tonry. **Observational Evidence from Supernovae for an Accelerating Universe and a Cosmological Constant**. *AJ*, **116**:1009–1038, September 1998. 100

[282] A. G. Riess, L. M. Macri, S. L. Hoffmann, D. Scolnic, S. Casertano, A. V. Filippenko, B. E. Tucker, M. J. Reid, D. O. Jones, J. M. Silverman, R. Chornock, P. Challis, W. Yuan, P. J. Brown, and R. J. Foley. **A 2.4% Determination of the Local Value of the Hubble Constant**. *ApJ*, **826**:56, July 2016. 28

[283] O. Roldan, A. Notari, and M. Quartin. **Interpreting the CMB aberration and Doppler measurements: boost or intrinsic dipole?** *J. Cosmology Astropart. Phys.*, **6**:026, June 2016. 118, 128, 131

[284] M. Rowan-Robinson, J. Sharpe, S. J. Oliver, O. Keeble, A. Canavezes, W. Saunders, A. N. Taylor, H. Valentine, C. S. Frenk, G. P. Efstathiou, R. G. McMahon, S. D. M. White, W. Sutherland, H. Tadros, and S. Maddox. **The IRAS PSCz dipole**. *MNRAS*, **314**:375–397, May 2000. 118

[285] M. Rubart, D. Bacon, and D. J. Schwarz. **The cosmic radio dipole and local structure effects**. In A. Heavens, J.-L. Starck, and A. Krone-Martins, editors, *Statistical Challenges in 21st Century Cosmology*, **306** of *IAU Symposium*, pages 182–184, May 2014. 120

[286] M. Rubart and D. J. Schwarz. **Cosmic radio dipole from NVSS and WENSS**. *A&A*, **555**:A117, July 2013. 118, 119

[287] M. Ruszkowski and M. C. Begelman. **Circular Polarization from Stochastic Synchrotron Sources**. *ApJ*, **573**:485–495, July 2002. 67

[288] G. B. Rybicki and A. P. Lightman. *Radiative Processes in Astrophysics*. Wiley, June 1986. 128

[289] R. K. Sachs and A. M. Wolfe. **Perturbations of a Cosmological Model and Angular Variations of the Microwave Background**. *ApJ*, **147**:73, January 1967. 12

[290] A. Sajina, B. Partridge, T. Evans, S. Stefl, N. Vechik, S. Myers, S. Dicker, and P. Korngut. **High-frequency Radio Spectral Energy Distributions and Polarization Fractions of Sources in an Atacama Cosmology Telescope Survey Field**. *ApJ*, **732**:45, May 2011. 62

REFERENCES

[291] R. Salvaterra and C. Burigana. **A joint study of early and late spectral distortions of the cosmic microwave background and of the millimetric foreground**. *MNRAS*, **336**:592–610, October 2002. 105, 112

[292] H. B. Sandvik, M. Tegmark, M. Zaldarriaga, and I. Waga. **The end of unified dark matter?** *Phys. Rev. D*, **69**(12):123524, June 2004. 100

[293] D. Sarkar, D. Huterer, C. J. Copi, G. D. Starkman, and D. J. Schwarz. **Missing power vs low-ell alignments in the cosmic microwave background: No correlation in the standard cosmological model**. *Astroparticle Physics*, **34**:591–594, March 2011. 17

[294] R. J. Sault, P. J. Teuben, and M. C. H. Wright. **A Retrospective View of MIRIAD**. In R. A. Shaw, H. E. Payne, and J. J. E. Hayes, editors, *Astronomical Data Analysis Software and Systems IV*, **77** of *Astronomical Society of the Pacific Conference Series*, page 433, 1995. 51

[295] R. Schneider, R. Salvaterra, T. R. Choudhury, A. Ferrara, C. Burigana, and L. A. Popa. **Detectable signatures of cosmic radiative feedback**. *MNRAS*, **384**:1525–1532, March 2008. 106, 109

[296] R. Schönrich. **Galactic rotation and solar motion from stellar kinematics**. *MNRAS*, **427**:274–287, November 2012. 118

[297] D. J. Schwarz, D. Bacon, S. Chen, C. Clarkson, D. Huterer, M. Kunz, R. Maartens, A. Raccanelli, M. Rubart, and J. L. Starck. **Testing foundations of modern cosmology with SKA all-sky surveys**. *Advancing Astrophysics with the Square Kilometre Array (AASKA14)*, page 32, April 2015. 118

[298] M. Seiffert, D. J. Fixsen, A. Kogut, S. M. Levin, M. Limon, P. M. Lubin, P. Mirel, J. Singal, T. Villela, E. Wollack, and C. A. Wuensche. **Interpretation of the ARCADE 2 Absolute Sky Brightness Measurement**. *ApJ*, **734**:6, June 2011. 119

[299] G. Shiu and J. Xu. **Effective field theory and decoupling in multifield inflation: An illustrative case study**. *Phys. Rev. D*, **84**(10):103509, November 2011. 19

[300] S. Siegel and N.J. Castellan. *Nonparametric statistics for the behavioral sciences*. McGraw–Hill, Inc., second edition, 1988. 83

[301] E. Silverstein and D. Tong. **Scalar speed limits and cosmology: Acceleration from D-cceleration**. *Phys. Rev. D*, **70**(10):103505, November 2004. 21

[302] A. K. Singal. **Large Peculiar Motion of the Solar System from the Dipole Anisotropy in Sky Brightness due to Distant Radio Sources**. *ApJ*, **742**:L23, December 2011. 119

[303] J. Singal, D. J. Fixsen, A. Kogut, S. Levin, M. Limon, P. Lubin, P. Mirel, M. Seiffert, T. Villela, E. Wollack, and C. A. Wuensche. **The ARCADE 2 Instrument**. *ApJ*, **730**:138, April 2011. 119

[304] D. N. Spergel, L. Verde, H. V. Peiris, E. Komatsu, M. R. Nolta, C. L. Bennett, M. Halpern, G. Hinshaw, N. Jarosik, A. Kogut, M. Limon, S. S. Meyer, L. Page, G. S. Tucker, J. L. Weiland, E. Wollack, and E. L. Wright. **First-Year Wilkinson Microwave Anisotropy Probe (WMAP) Observations: Determination of Cosmological Parameters**. *ApJS*, **148**:175–194, September 2003. 17

[305] A. A. Starobinskiĭ. **Spectrum of adiabatic perturbations in the universe when there are singularities in the inflaton potential**. *ZhETF Pisma Redaktsiiu*, **55**:477, May 1992. 19

[306] R. Stompor, M. Abroe, P. Ade, A. Balbi, D. Barbosa, J. Bock, J. Borrill, A. Boscaleri, P. de Bernardis, P. G. Ferreira, S. Hanany, V. Hristov, A. H. Jaffe, A. T. Lee, E. Pascale, B. Rabii, P. L. Richards, G. F. Smoot, C. D. Winant, and J. H. P. Wu. **Cosmological Implications of the MAXIMA-1 High-Resolution Cosmic Microwave Background Anisotropy Measurement**. *ApJ*, **561**:L7–L10, November 2001. 100

[307] M. A. Strauss, A. Yahil, M. Davis, J. P. Huchra, and K. Fisher. **A redshift survey of IRAS galaxies. V - The acceleration on the Local Group**. *ApJ*, **397**:395–419, October 1992. 118

[308] A. W. Strong and I. V. Moskalenko. **Propagation of Cosmic-Ray Nucleons in the Galaxy**. *ApJ*, **509**:212–228, December 1998. 114

[309] R. Subrahmanyan, R. D. Ekers, L. Saripalli, and E. M. Sadler. **ATLBS: the Australia Telescope Low-Brightness Survey**. *MNRAS*, **402**:2792–2806, March 2010. 49

[310] S. Sugimoto. **Anomaly Cancellations in the Type I D9-D9 System and the USp(32) String Theory**. *Progress of Theoretical Physics*, **102**:685–699, September 1999. 18

[311] X. H. Sun and W. Reich. **Simulated square kilometre array maps from Galactic 3D-emission models**. *A&A*, **507**:1087–1105, November 2009. 114

[312] X.-H. Sun and W. Reich. **The Galactic halo magnetic field revisited**. *Research in Astronomy and Astrophysics*, **10**:1287–1297, December 2010. 114

[313] X. H. Sun, W. Reich, A. Waelkens, and T. A. Enßlin. **Radio observational constraints on Galactic 3D-emission models**. *A&A*, **477**:573–592, January 2008. 114

[314] R. A. Sunyaev and R. Khatri. **Unavoidable CMB Spectral Features and Blackbody Photosphere of Our Universe**. *International Journal of Modern Physics D*, **22**:1330014, June 2013. 105, 139

[315] R. A. Sunyaev and I. B. Zeldovich. **The velocity of clusters of galaxies relative to the microwave background - The possibility of its measurement**. *MNRAS*, **190**:413–420, February 1980. 132

[316] R. A. Sunyaev and Y. B. Zeldovich. **The interaction of matter and radiation in the hot model of the Universe, II**. *Ap&SS*, **7**:20–30, April 1970. 106, 119, 138, 139

[317] M. Tarenghi. **The Atacama Large Millimeter/Submillimeter Array: overview and status**. *Ap&SS*, **313**:1–7, January 2008. 43

[318] J. A. Tauber, H. U. Norgaard-Nielsen, P. A. R. Ade, J. Amiri Parian, T. Banos, M. Bersanelli, C. Burigana, A. Chamballu, D. de Chambure, P. R. Christensen, O. Corre, A. Cozzani, B. Crill, G. Crone, O. D'Arcangelo, R. Daddato, D. Doyle, D. Dubruel, G. Forma, R. Hills, K. Huffenberger, A. H. Jaffe, N. Jessen, P. Kletzkine, J. M. Lamarre, J. P. Leahy, Y. Longval, P. de Maagt, B. Maffei, N. Mandolesi, J. Martí-Canales, A. Martín-Polegre, P. Martin, L. Mendes, J. A. Murphy, P. Nielsen, F. Noviello, M. Paquay, T. Peacocke, N. Ponthieu, K. Pontoppidan, I. Ristorcelli, J.-B. Riti, L. Rolo, C. Rosset, M. Sandri, G. Savini, R. Sudiwala, M. Tristram, L. Valenziano, M. van der Vorst, K. van't Klooster, F. Villa, and V. Yurchenko. **Planck pre-launch status: The optical system**. *A&A*, **520**:A2, September 2010. 3

[319] A. R. Taylor, J. M. Stil, J. K. Grant, T. L. Landecker, R. Kothes, R. I. Reid, A. D. Gray, D. Scott, P. G. Martin, A. I. Boothroyd, G. Joncas, F. J. Lockman, J. English, A. Sajina, and J. R. Bond. **Radio Polarimetry of the ELAIS N1 Field: Polarized Compact Sources**. *ApJ*, **666**:201–211, September 2007. 49

[320] M. Tegmark and A. de Oliveira-Costa. **How to measure CMB polarization power spectra without losing information**. *Phys. Rev. D*, **64**(6):063001, September 2001. 25

[321] The COrE Collaboration, C. Armitage-Caplan, M. Avillez, D. Barbosa, A. Banday, N. Bartolo, R. Battye, J. Bernard, P. de Bernardis, S. Basak, M. Bersanelli, P. Bielewicz, A. Bonaldi, M. Bucher, F. Bouchet, F. Boulanger, C. Burigana, P. Camus, A. Challinor, S. Chongchitnan, D. Clements, S. Colafrancesco, J. Delabrouille, M. De Petris, G. De Zotti, C. Dickinson, J. Dunkley, T. Ensslin, J. Fergusson, P. Ferreira, K. Ferriere, F. Finelli, S. Galli, J. Garcia-Bellido, C. Gauthier, M. Haverkorn, M. Hindmarsh, A. Jaffe, M. Kunz, J. Lesgourgues, A. Liddle, M. Liguori, M. Lopez-Caniego, B. Maffei, P. Marchegiani, E. Martinez-Gonzalez, S. Masi, P. Mauskopf, S. Matarrese, A. Melchiorri, P. Mukherjee, F. Nati, P. Natoli, M. Negrello, L. Pagano, D. Paoletti, T. Peacocke, H. Peiris, L. Perroto, F. Piacentini, M. Piat, L. Piccirillo, G. Pisano, N. Ponthieu, C. Rath, S. Ricciardi, J. Rubino Martin, M. Salatino, P. Shellard, R. Stompor, L. T. J. Urrestilla, B. Van Tent, L. Verde, B. Wandelt, and S. Withington. **COrE (Cosmic Origins Explorer) A White Paper**. *ArXiv e-prints*, February 2011. 30

[322] The Polarbear Collaboration: P. A. R. Ade, Y. Akiba, A. E. Anthony, K. Arnold, M. Atlas, D. Barron, D. Boettger, J. Borrill, S. Chapman, Y. Chinone, M. Dobbs, T. Elleflot, J. Errard, G. Fabbian, C. Feng, D. Flanigan, A. Gilbert, W. Grainger, N. W. Halverson, M. Hasegawa, K. Hattori, M. Hazumi, W. L. Holzapfel, Y. Hori, J. Howard, P. Hyland, Y. Inoue, G. C. Jaehnig, A. H. Jaffe, B. Keating, Z. Kermish, R. Keskitalo, T. Kisner, M. Le Jeune, A. T. Lee, E. M. Leitch, E. Linder, M. Lungu, F. Matsuda, T. Matsumura, X. Meng, N. J. Miller, H. Morii, S. Moyerman, M. J. Myers, M. Navaroli, H. Nishino, A. Orlando, H. Paar, J. Peloton, D. Poletti, E. Quealy, G. Rebeiz, C. L. Reichardt, P. L. Richards, C. Ross, I. Schanning, D. E. Schenck, B. D. Sherwin, A. Shimizu, C. Shimmin, M. Shimon, P. Siritanasak, G. Smecher, H. Spieler, N. Stebor, B. Steinbach, R. Stompor, A. Suzuki, S. Takakura, T. Tomaru, B. Wilson, A. Yadav, and O. Zahn. **A Measurement of the Cosmic Microwave Background B-mode Polarization Power Spectrum at Sub-degree Scales with POLARBEAR**. *ApJ*, **794**:171, October 2014. 12

[323] S. J. Tingay and M. de Kool. **An Investigation of Synchrotron Self-absorption and Free-Free Absorption Models in Explanation of the Gigahertz-peaked Spectrum of PKS 1718-649**. *AJ*, **126**:723–733, August 2003. 62

[324] P. Tiwari and P. Jain. **Dipole anisotropy in integrated linearly polarized flux density in NVSS data**. *MNRAS*, **447**:2658–2670, March 2015. 118

[325] P. Tiwari, R. Kothari, A. Naskar, S. Nadkarni-Ghosh, and P. Jain. **Dipole anisotropy in sky brightness and source count distribution in radio NVSS data**. *Astroparticle Physics*, **61**:1–11, February 2015. 118

[326] T. Trombetti and C. Burigana. **Imprints on CMB Angular Power Spectrum Modes from Cosmological Reionization**. *Journal of Modern Physics*, **3**(12):1918–1944, 2012. 9, 109

[327] T. Trombetti and C. Burigana. **Semi-analytical description of clumping factor and cosmic microwave background free-free distortions from reionization**. *MNRAS*, **437**:2507–2520, January 2014. 105, 107, 109, 140, 184

[328] M. Tucci, E. Martínez-González, L. Toffolatti, J. González-Nuevo, and G. De Zotti. **Predictions on the high-frequency polarization properties of extragalactic radio sources and implications for polarization measurements of the cosmic microwave background**. *MNRAS*, **349**:1267–1277, April 2004. 49, 62, 75, 91

[329] M. Tucci and L. Toffolatti. **The Impact of Polarized Extragalactic Radio Sources on the Detection of CMB Anisotropies in Polarization**. *Advances in Astronomy*, **2012**:624987, December 2012. 62, 68, 75, 76

[330] M. Tucci, L. Toffolatti, G. de Zotti, and E. Martínez-González. **High-frequency predictions for number counts and spectral properties of extragalactic radio sources. New evidence of a break at mm wavelengths in spectra of bright blazar sources**. *A&A*, **533**:A57, September 2011. 89

[331] L. Valenziano, F. Cuttaia, A. De Rosa, L. Terenzi, A. Brighenti, G. P. Cazzola, A. Garbesi, S. Mariotti, G. Orsi, et al. **Planck-LFI: design and performance of the 4 Kelvin Reference Load Unit**. *Journal of Instrumentation*, **4**:T12006, December 2009. 125

[332] M. Viel, J. Lesgourgues, M. G. Haehnelt, S. Matarrese, and A. Riotto. **Constraining warm dark matter candidates including sterile neutrinos and light gravitinos with WMAP and the Lyman-α forest**. *Phys. Rev. D*, **71**(6):063534, March 2005. 108

[333] P. Vielva, E. Martínez-González, and M. Tucci. **Cross-correlation of the cosmic microwave background and radio galaxies in real, harmonic and wavelet spaces: detection of the integrated Sachs-Wolfe effect and dark energy constraints**. *MNRAS*, **365**:891–901, January 2006. 13

[334] M. P. Viero, L. Wang, M. Zemcov, G. Addison, A. Amblard, V. Arumugam, H. Aussel, M. Béthermin, J. Bock, A. Boselli, V. Buat, D. Burgarella, C. M. Casey, D. L. Clements, A. Conley, L. Conversi, A. Cooray, G. De Zotti, C. D. Dowell, D. Farrah, A. Franceschini, J. Glenn, M. Griffin, E. Hatziminaoglou, S. Heinis, E. Ibar, R. J. Ivison, G. Lagache, L. Levenson, L. Marchetti, G. Marsden, H. T. Nguyen, B. O'Halloran, S. J. Oliver, A. Omont, M. J. Page, A. Papageorgiou, C. P. Pearson, I. Pérez-Fournon, M. Pohlen, D. Rigopoulou, I. G. Roseboom, M. Rowan-Robinson, B. Schulz, D. Scott, N. Seymour, D. L. Shupe, A. J. Smith, M. Symeonidis, M. Vaccari, I. Valtchanov, J. D. Vieira, J. Wardlow, and C. K. Xu. **HerMES: Cosmic Infrared Background Anisotropies and the Clustering of Dusty Star-forming Galaxies**. *ApJ*, **772**:77, July 2013. 91

[335] A. Waelkens, T. Jaffe, M. Reinecke, F. S. Kitaura, and T. A. Ensslin. **Simulating polarized Galactic synchrotron emission at all frequencies. The Hammurabi code**. *A&A*, **495**:697–706, February 2009. 114

[336] C. G. R. Wallis, M. L. Brown, R. A. Battye, and J. Delabrouille. **Optimal scan strategies for future CMB satellite experiments**. *MNRAS*, **466**:425–442, April 2017. 152

[337] Q. Wang, Z. Zhu, and W. G. Unruh. **How the huge energy of quantum vacuum gravitates to drive the slow accelerating expansion of the Universe**. *Phys. Rev. D*, **95**(10):103504, May 2017. 100

[338] J. F. C. Wardle and D. C. Homan. **Theoretical Models for Producing Circularly Polarized Radiation in Extragalactic Radio Sources**. *Ap&SS*, **288**:143–153, March 2003. 67

[339] J. F. C. Wardle and P. P. Kronberg. **The linear polarization of quasi-stellar radio sources at 3.71 and 11.1 centimeters**. *ApJ*, **194**:249–255, December 1974. 52, 78

[340] J. R. Whitbourn and T. Shanks. **The local hole revealed by galaxy counts and redshifts**. *MNRAS*, **437**:2146–2162, January 2014. 120

[341] R. Wielebinski. **The 408 MHz all-sky survey**. *A&A*, **500**:245–246, June 2009. 10

[342] W. L. Williams, H. T. Intema, and H. J. A. Röttgering. **T-RaMiSu: the Two-meter Radio Mini Survey. I. The Boötes Field**. *A&A*, **549**:A55, January 2013. 112

[343] W. E. Wilson, R. H. Ferris, P. Axtens, A. Brown, E. Davis, G. Hampson, M. Leach, P. Roberts, S. Saunders, B. S. Koribalski, J. L. Caswell, E. Lenc, J. Stevens, M. A. Voronkov, M. H. Wieringa, K. Brooks, P. G. Edwards, R. D. Ekers, B. Emonts, L. Hindson, S. Johnston, S. T. Maddison, E. K. Mahony, S. S. Malu, M. Massardi, M. Y. Mao, D. McConnell, R. P. Norris, D. Schnitzeler, R. Subrahmanyan, J. S. Urquhart, M. A. Thompson, and R. M. Wark. **The Australia Telescope Compact Array Broad-band Backend: description and first results**. *MNRAS*, **416**:832–856, September 2011. 45

[344] D. L. Wiltshire, P. R. Smale, T. Mattsson, and R. Watkins. **Hubble flow variance and the cosmic rest frame**. *Phys. Rev. D*, **88**(8):083529, October 2013. 118

REFERENCES

[345] A. Wootten and A. R. Thompson. **The Atacama Large Millimeter/Submillimeter Array**. *IEEE Proceedings*, **97**:1463–1471, August 2009. 42

[346] E. L. Wright. **Distortion of the microwave background by a hot intergalactic medium**. *ApJ*, **232**:348–351, September 1979. 132

[347] E. L. Wright, X. Chen, N. Odegard, C. L. Bennett, R. S. Hill, G. Hinshaw, N. Jarosik, E. Komatsu, M. R. Nolta, L. Page, D. N. Spergel, J. L. Weiland, E. Wollack, J. Dunkley, B. Gold, M. Halpern, A. Kogut, D. Larson, M. Limon, S. S. Meyer, and G. S. Tucker. **Five-Year Wilkinson Microwave Anisotropy Probe Observations: Source Catalog**. *ApJS*, **180**:283–295, February 2009. 76

[348] D. Yamauchi, K. Ichiki, K. Kohri, T. Namikawa, Y. Oyama, T. Sekiguchi, H. Shimabukuro, K. Takahashi, T. Takahashi, S. Yokoyama, and K. Yoshikawa. **Cosmology with the Square Kilometre Array by SKA-Japan**. *PASJ*, **68**:R2, December 2016. 95

[349] M. Yoon and D. Huterer. **Kinematic Dipole Detection with Galaxy Surveys: Forecasts and Requirements**. *ApJ*, **813**:L18, November 2015. 138

[350] A. Zacchei, D. Maino, C. Baccigalupi, M. Bersanelli, A. Bonaldi, L. Bonavera, C. Burigana, R. C. Butler, F. Cuttaia, G. de Zotti, J. Dick, M. Frailis, S. Galeotta, J. González-Nuevo, K. M. Górski, A. Gregorio, E. Keihänen, R. Keskitalo, J. Knoche, H. Kurki-Suonio, C. R. Lawrence, S. Leach, J. P. Leahy, M. López-Caniego, N. Mandolesi, M. Maris, F. Matthai, P. R. Meinhold, A. Mennella, G. Morgante, N. Morisset, P. Natoli, F. Pasian, F. Perrotta, G. Polenta, T. Poutanen, M. Reinecke, S. Ricciardi, R. Rohlfs, M. Sandri, A.-S. Suur-Uski, J. A. Tauber, D. Tavagnacco, L. Terenzi, M. Tomasi, J. Valiviita, F. Villa, A. Zonca, A. J. Banday, R. B. Barreiro, J. G. Bartlett, N. Bartolo, L. Bedini, K. Bennett, P. Binko, J. Borrill, F. R. Bouchet, M. Bremer, P. Cabella, B. Cappellini, X. Chen, L. Colombo, M. Cruz, A. Curto, L. Danese, R. D. Davies, R. J. Davis, G. de Gasperis, A. de Rosa, G. de Troia, C. Dickinson, J. M. Diego, S. Donzelli, U. Dörl, G. Efstathiou, T. A. Enßlin, H. K. Eriksen, M. C. Falvella, F. Finelli, E. Franceschi, T. C. Gaier, F. Gasparo, R. T. Génova-Santos, G. Giardino, F. Gómez, A. Gruppuso, F. K. Hansen, R. Hell, D. Herranz, W. Hovest, M. Huynh, J. Jewell, M. Juvela, T. S. Kisner, L. Knox, A. Lähteenmäki, J.-M. Lamarre, R. Leonardi, J. León-Tavares, P. B. Lilje, P. M. Lubin, G. Maggio, D. Marinucci, E. Martínez-González, M. Massardi, S. Matarrese, M. T. Meharga, A. Melchiorri, M. Migliaccio, S. Mitra, A. Moss, H. U. Nørgaard-Nielsen, L. Pagano, R. Paladini, D. Paoletti, B. Partridge, D. Pearson, V. Pettorino, D. Pietrobon, G. Prézeau, P. Procopio, J.-L. Puget, C. Quercellini, J. P. Rachen, R. Rebolo, G. Robbers, G. Rocha, J. A. Rubiño-Martín, E. Salerno, M. Savelainen, D. Scott, M. D. Seiffert, J. I. Silk, G. F. Smoot, J. Sternberg, F. Stivoli, R. Stompor, G. Tofani, L. Toffolatti, J. Tuovinen, M. Türler, G. Umana, P. Vielva, N. Vittorio, C. Vuerli, L. A. Wade, R. Watson, S. D. M. White, and A. Wilkinson. **Planck early results. V. The Low Frequency Instrument data processing**. *A&A*, **536**:A5, December 2011. 3

[351] O. Zahn, A. Lidz, M. McQuinn, S. Dutta, L. Hernquist, M. Zaldarriaga, and S. R. Furlanetto. **Simulations and Analytic Calculations of Bubble Growth during Hydrogen Reionization**. *ApJ*, **654**:12–26, January 2007. 99

[352] Y. B. Zel'dovich, A. F. Illarionov, and R. A. Sunyaev. **The Effect of Energy Release on the Emission Spectrum in a Hot Universe**. *Soviet Journal of Experimental and Theoretical Physics*, **35**:643, 1972. 139

[353] Y. B. Zeldovich and R. A. Sunyaev. **The Interaction of Matter and Radiation in a Hot-Model Universe**. *Ap&SS*, **4**:301–316, July 1969. 119

[354] J. P. Zibin and D. Scott. **Gauging the cosmic microwave background**. *Phys. Rev. D*, **78**(12):123529, December 2008. 128